

---

Doctoral

Engineering

---

2018

## Optical Whispering Gallery Mode Cylindrical Micro-Resonator Devices for Sensing Applications

Vishnu Kavungal

Technological University Dublin, vishnu.kavungal@tudublin.ie

Follow this and additional works at: <https://arrow.tudublin.ie/engdoc>

---

### Recommended Citation

Kavungal, V. (2018) *Optical whispering gallery mode cylindrical micro-resonator devices for sensing applications*. Doctoral thesis, DIT, 2018. doi.org/10.21427/7rh5-qn67

This Theses, Ph.D is brought to you for free and open access by the Engineering at ARROW@TU Dublin. It has been accepted for inclusion in Doctoral by an authorized administrator of ARROW@TU Dublin. For more information, please contact [yvonne.desmond@tudublin.ie](mailto:yvonne.desmond@tudublin.ie), [arrow.admin@tudublin.ie](mailto:arrow.admin@tudublin.ie), [brian.widdis@tudublin.ie](mailto:brian.widdis@tudublin.ie).



This work is licensed under a [Creative Commons Attribution-Noncommercial-Share Alike 3.0 License](https://creativecommons.org/licenses/by-nc-sa/3.0/)

# **Optical whispering gallery mode cylindrical micro-resonator devices for sensing applications**

A thesis

Submitted for the degree of Doctor of Philosophy

By

**VISHNU KAVUNGAL**



School of Electrical and Electronic Engineering

Faculty of Engineering

Dublin Institute of Technology

**Supervisors: Prof. Yuliya Semenova, Prof. Gerald Farrell and**

**Dr. Qiang Wu**

Dublin, Ireland

September 2018

**To my father, my mother with all my love**

**In memory of my father**

## **Abstract**

Whispering gallery mode (WGM) micro-resonators are devices attractive for many practical applications including optical sensing, micro-lasers, optical switches, tunable filters and many others. Their popularity is due to the high Q-factors and the exceptional sensitivity of their optical properties to the resonator's size, refractive index as well the properties of the surrounding medium. The main focus of this thesis is on the cylindrical WGM micro-resonators due to the simplicity of their fabrication and light coupling that they offer in comparison with other WGM devices.

At first, an in-depth experimental investigation of the WGM effect in different types of cylindrical micro-resonators was carried out in order to establish the influence of the resonator's geometry and coupling conditions on the resulting WGM spectrum. As one of the outcomes of this study, a novel method for geometrical profiling of asymmetries in thin microfiber tapers with submicron accuracy has been proposed and demonstrated. The submicron accuracy of the proposed method has been verified by SEM studies. The method can be applied as a quality control tool in fabrication of microfiber based devices and sensors or for fine-tuning of microfiber fabrication setups. The study also resulted in better understanding of the optimum conditions for excitation of WGMs in cylindrical fiber resonators, the influence of the tilt angle between the micro-cylinder and the coupling fiber taper.

A novel strain sensor formed by a polymer-wire cylindrical micro-resonator has been developed. Accurate and repeatable measurements of strain have been demonstrated experimentally with the proposed sensor for the upper range of limit of detection up to 3250  $\mu\epsilon$ . Practical packaging method for the proposed strain

sensor on a glass microscope slide has also been realized making the sensor portable and easy to use.

A study of thermo-optic tuning of the WGMs in a nematic liquid crystal-filled hollow cylindrical microresonator has been carried out. A simple and robust packaging has been realized with the proposed tunable device to ensure its stable and repeatable operation. The demonstrated thermo-optic method for the WGMs tuning is potentially useful for many tunable photonic devices.

Two novel all-fiber magnetic-field sensors have been designed based on photonic crystal fibers infiltrated with a magnetic fluid and a ferronematic liquid crystal utilizing the magnetic field tunability of WGM resonances. The highest experimentally demonstrated magnetic field sensitivity was 110 pm/mT in the range of magnetic fields from 0 to 40 mT.

Finally, a packaged inline cascaded optical micro-resonators (ICOMRs) design is proposed for coupling multiple micro-resonators to a single fiber and simultaneous sensing of multiple parameters (strain, temperature, humidity, or refractive index) at multiple points in space has been demonstrated. The proposed design principle can find applications in quasi-distributed sensing, optical coding, optical logic gates and wavelength division multiplexed optical communications systems.

## Declaration

I certify that this thesis which I now submit for examination for the award of PhD, is entirely my own work and has not been taken from the work of others save and to the extent that such work has been cited and acknowledged within the text of my work.

This thesis was prepared according to the regulations for postgraduate study by research of the Dublin Institute of Technology and has not been submitted in whole or in part for an award in any other Institute or University.

The work reported in this thesis conforms to the principles and requirements of Institute's guidelines for ethics in research.

The Institute has permission to keep, to lend or to copy this thesis in whole or in part, on condition that any such use of the material of the thesis be duly acknowledged.

Signature:

A handwritten signature in black ink, appearing to read 'Vishnu', written over a horizontal line.

Date: 03/09/2018

Candidate: Vishnu Kavungal

## **Acknowledgements**

The work presented in this thesis has been carried out within the Photonics Research Centre (PRC) of the Dublin Institute of Technology.

There are numerous people without whose support this thesis would be impossible. Firstly, I would like to express the sincerest gratitude to my supervisor, Prof. Yuliya Semenova for giving me this opportunity to further my education. I also want to thank her for all her guidance, support and patience during my doctoral studies, and for allowing me the freedom to pursue my own ideas and interests. Her caring and friendly nature gave me lots of strength during the hard days of my PhD life. Her brilliant method of article and report edits, supervision and presentation ideas will strongly contribute to my future professional life.

I am deeply indebted to Prof. Gerald Farrell, Director and Dean of College of Engineering and Built Environment for his guidance, comments, encouragement and willingness to serve as my associate supervisor in his busy scheduled of administrative work. The articles and thesis edits days were the million-euro lessons for shaping my professional life as a researcher.

I am grateful to Dr. Qiang Wu, Associate Professor of Photonics, Department of Mathematics, Physics and Electrical Engineering, Northumbria University, Newcastle, UK for his guidance, critical comments, prompt response of the article edits, and willingness to serve as my associate supervisor. His hard-working personality and critical thinking will definitely influence my future professional life.

I also want to gratefully acknowledge the financial support of Dublin Institute of Technology under Fiosraigh Scholarship Programme.



I am grateful to Prof. Michael Conlon, Head of Electrical and Electronic Engineering, for the financial support during the overrunning days of my PhD life.

My sincere thanks to Dr. Aseel Mahmood, Laser and Optoelectronics Research Center, Ministry of Science and Technology, Baghdad, Iraq for her research collaborations, friendships, discussion, food, horror and sad stories of Iraq wars.

Thank you, Prof. Changyu Shen, Institute of Optoelectronic Technology, China Jiliang University for your friendship, discussion, research collaborations during my PhD days.

I am deeply indebted to my fellow colleagues for providing a stimulating environment in the office and lab. Many thanks to Dr. Manjusha Ramakrishnan, Mr. Arun Kumar Mallik, Mr. Dejun Lu, Mr. Wei Han, Mrs. Fangfang Wei, and Mr. Xiaokang Lian for being quite considerate and accommodating.

Many thanks to my friends and senior PhD holders in the PRC, Dr. Sunish Mathews, Dr. Jinesh Mathew, Dr. Ginu Rajan, Dr. Youqiao Ma, Dr. Lin Bo for their friendship, help, and advice during the early days of my PhD.

I would like to also extend my sincere thanks to the staff of graduate research school, Dublin Institute of Technology for their administrative assistance, and support.

A special thank goes to my M. Sc classmate Dr. Sijo Joseph, for his assistance in theoretical simulations and many valuable discussions that facilitated my research.

My sincere thanks to Prof. M. Kailasnath, Prof. V. P. N. Nampoori, Prof. M. K. Jayaraj, Cochin University of Science and Technology, Kerala, India who inspired and support me to reach this level.

Many thanks to my friends in Ireland Mr. Sony Vijayan, Dr. Sithara Pavithran, Mr. Sobin George, Mr. Graceson Antony, Mr. Shaban Muhammad, Mr. Sandeepan

Pathra, Mr. Chittesh, Mr. Sony Koshi, Mrs. Daiva, Mr. Giffin Mathew, Mr. Cyril Joy, Mr. Rony, and Mr. Akash Thomas especially for the occasional dinner parties, which made my life more enjoyable in Ireland.

I would like to express my gratitude and deep love to my parents who raised me and trust me with their endless love. My father is the evertime hero in my life, who has dedicated his life to the family. He was a teacher, actor, painter, sculpture, writer, singer and a great man. After my father, my mother gave me strength to live further. She took care of all my sorrows and ignited my educational dreams. I am so fortunate to be your son.

I express my thanks and love to my sister, brother-in-law, and my niece, who always trust, support, care and encouraged me.

Finally, my wife, Dr. Deepthy. R. Chandran, the mother of my child. I don't know how to express my thanks and love to you. Many thanks for being patience with me for the las two years. You gave me the most beautiful gift of my life, my son, Megharoopan, the hopes and happiness of my life!

# List of publications

## Journal papers

1. **V. Kavungal**, A. K. Mallik, G. Farrell, Q. Wu, and Y. Semenova, "Strain-induced spectral tuning of the whispering gallery modes in a cylindrical micro-resonator formed by a polymer optical fiber," *Applied Optics*, **56**, 1339-1345 (2017).
2. **V. Kavungal**, G. Farrell, Q. Wu, A. K. Mallik, and Y. Semenova, "A packaged whispering gallery mode strain sensor based on a polymer-wire cylindrical micro resonator," *Journal of Lightwave Technology*, **36**, 1757-1765 (2018).
3. **V. Kavungal**, G. Farrell, Q. Wu, A. K. Mallik, and Y. Semenova, "Thermo-optic tuning of a packaged whispering gallery mode resonator filled with nematic liquid crystal," *Optics Express*, **26**, 8431-8442 (2018).
4. **V. Kavungal**, G. Farrell, Q. Wu, A. K. Mallik, and Y. Semenova, "Studies of geometrical profiling in fabricated tapered optical fibers using whispering gallery modes spectroscopy," *Optical Fiber Technology*, **41**, 82-88 (2018).
5. **V. Kavungal**, G. Farrell, Q. Wu, A. K. Mallik, and Y. Semenova, "A comprehensive experimental study of whispering gallery modes in a cylindrical micro-resonator excited by a tilted fiber taper," *Microwave and Optical Technology Letters*, **60**, 1495-1504 (2018).
6. A. Mahmood, **V. Kavungal**, S. S. Ahmed, G. Farrell, Y. Semenova, "Magnetic field sensor based on whispering gallery modes in photonic crystal fiber infiltrated with magnetic fluids," *Optics Letters*, **40**, 4983-4986 (2015).
7. A. Ibrahim, **V. Kavungal**, S. Ahmed, P. Kopcanskya, V. Zavisova, G. Farrell, Y. Semenova, "Magnetic field sensing using whispering-gallery modes in a cylindrical microresonator infiltrated with ferronematic liquid crystal," *Optics Express*, **25**, 12195-12202 (2017).
8. A. K. Mallik, D. Liu, **V. Kavungal**, Q. Wu, G. Farrell, and Y. Semenova, "Agarose coated spherical micro resonator for humidity measurements," *Optics Express*, **24**, 21216-21227 (2016).
9. A. K. Mallik, G. Farrell, D. Liu, **V. Kavungal**, Q. Wu, and Y. Semenova, "Silica gel coated spherical micro resonator for ultra-high sensitivity detection of ammonia gas concentration in air," *Scientific Report*, **8:1620**, 1-10 (2018).

10. A. K. Mallik, G. Farrell, D. Liu, **V. Kavungal**, Q. Wu, and Y. Semenova, “A coated spherical micro-resonator for measurement of water vapor concentration at sub-ppm levels in very low humidity environments,” *Journal of Lightwave Technology*, **36**, 2667-2674 (2018).
11. A. K. Mallik, G. Farrell, D. Liu, **V. Kavungal**, Q. Wu, and Y. Semenova, “Whispering gallery mode micro resonators for multi-parameter sensing applications,” *Optics Express* (Accepted for publication).
12. **V. Kavungal**, G. Farrell, Q. Wu, A. K. Mallik, C. Shen and Y. Semenova, “Packaged inline cascaded optical microresonators for multi-parameter sensing,” In preparation, (2018).

### **Conference proceedings**

1. **V. Kavungal**, G. Farrell, Q. Wu, A. K. Mallik, and Y. Semenova, “Temperature compensated strain sensor based on an inline cascade of optical microresonators,” The 26th international conference on Optical Fiber Sensors (September 24-28, 2018, Lausanne, Switzerland) [Poster presentation].
2. **V. Kavungal**, G. Farrell, Q. Wu, A. K. Mallik, and Y. Semenova, “Real time observation of whispering gallery mode (WGM) eclipse in liquid flowing capillary tube resonator,” International OSA network of student’s conference 2017 (11-14th September 2017, Kerala, India) [Oral presentation].
3. **V. Kavungal**, A. K. Malik, G. Farrell, Q. Wu, and Y. Semenova, “Tunable whispering gallery mode cylindrical micro resonator based on a section of a polymer optical fiber,” 13th International Conference on Fiber Optics and Photonics, (Optical Society of America, 2016), paper Th3A.67 [Poster presentation].
4. **V. Kavungal**, Q. Wu, G. Farrell, C. L. Linslal, M. Kailasnath and Y. Semenova, “Checking diameter uniformity in a prepared graded index polymer optical fiber using a Whispering Gallery Mode technique,” 24th International Conference on Plastic Optical Fibers, (22-24 September 2015, Nuremberg, Germany) [Oral presentation].
5. **V. Kavungal**, Q. Wu, G. Farrell and Y. Semenova, “Studies of symmetries in fabricated tapered optical fibers using whispering gallery modes,” Photonics Ireland 2015, (2- 4th September 2015, Cork, Ireland) [Poster presentation].

6. **V. Kavungal**, Q. Wu, G. Farrell, and Y. Semenova, "Studies of effective coupling conditions for a microsphere-tapered fiber system for generating whispering gallery modes," 12th International Conference on Fiber Optics and Photonics, (Optical Society of America, 2014), paper S5A.11 [Poster presentation].
7. **V. Kavungal**, L. Bo, Q. Wu, M. Teng, C. Yu, G. Farrell, Y. Semenova, "Study of whispering gallery modes in a cylindrical microresonator excited by a tilted fiber taper", 23rd International Conference on Optical Fibre Sensors, Proc. SPIE 9157 (2 -6<sup>th</sup> June 2014) [Poster presentation].
8. **V. Kavungal**, L. Bo, G. Farrell and Y. Semenova, "Influence of the radius of a spherical micro-resonator on its whispering gallery mode spectrum," Photonics Ireland 2013, (2-6<sup>th</sup> September 2013 Belfast, UK) [Poster presentation].
9. Y. Semenova, **V. Kavungal**, Q. Wu, and G. Farrell, "Submicron accuracy fiber taper profiling using whispering gallery modes in a cylindrical fiber micro-resonator," Proc. SPIE 9634, 24th International Conference on Optical Fibre Sensors (28<sup>th</sup> September 2015) [Poster presentation].
10. A. Mahmood, **V. Kavungal**, S. S. Ahmed, G. Farrell and Y. Semenova, "Photonic crystal fibre WGM resonators for magnetic field sensing," Photonics Ireland 2015, (2-4<sup>th</sup> September 2015, Cork, Ireland) [Poster presentation].
11. A. Mahmood, **V. Kavungal**, S. S. Ahmed, P. Kopcansky, V. Zavisova, G. Farrell and Y. Semenova, "Whispering gallery modes in a ferronematic-infiltrated fibre micro-resonator for magnetic field sensing," European Conference on Liquid Crystals, (7-11<sup>th</sup> September 2015, Manchester, UK) [Poster presentation].
12. A. K. Mallik, D. Liu, **V. Kavungal**, X. Lian, G. Farrell, Q. Wu, Y. Semenova, "Compact relative humidity sensor based on an Agarose hydrogel coated silica microsphere resonator," Proceedings of SPIE Vol. 10323, 103230C (2017) [Oral presentation].
13. A. K. Mallik, G. Farrell, D. Liu, **V. Kavungal**, Q. Wu, Y. Semenova, "Porous silica coated spherical microresonator for vapor phase sensing of ammonia at a sub-ppm level," Proceedings of SPIE, Vol. 9916, 99161Y (2016) [Poster presentation]

# Contents

<b>Abstract</b> .....	<b>IV</b>
<b>Declaration</b> .....	<b>VI</b>
<b>Acknowledgements</b> .....	<b>VII</b>
<b>List of publications</b> .....	<b>X</b>
<b>Contents</b> .....	<b>XIII</b>
<b>List of Figures</b> .....	<b>XVII</b>
<b>List of Tables</b> .....	<b>XXVI</b>
<b>List of Abbreviations</b> .....	<b>XXVII</b>
<b>Chapter 1: Introduction</b> .....	<b>1</b>
1.1 Background to the research.....	1
1.1.1 Whispering gallery mode (WGM) resonators: advantages, applications and analytical foundation.....	1
1.1.2 Types of WGM micro-resonators.....	5
1.1.3 Cylindrical WGM micro-resonators .....	6
1.1.4 Liquid core optical ring resonators .....	9
1.1.5 Fundamentals of WGMs in cylindrical micro-resonators.....	9
1.1.6 Light coupling into WGM resonators .....	12
1.1.7 Properties of optical micro-resonators .....	16
1.2 Research Motivation .....	19
1.3 Aim and objectives of the research .....	21
1.4 Research Methodology.....	22
1.5 Thesis layout .....	25
1.6 References .....	27
<b>Chapter 2: Excitation of WGMs from silica fiber based cylindrical microresonators and its application in geometrical profiling</b> .....	<b>40</b>

2.1	A comprehensive experimental study of whispering gallery modes in a cylindrical micro-resonator excited by a tilted fiber taper .....	41
2.1.1	Introduction .....	42
2.1.2	Properties of WGM resonances .....	45
2.1.3	Experimental arrangement, results, and discussion .....	48
2.1.4	Conclusions .....	64
2.2	Studies of geometrical profiling in fabricated tapered optical fibers using whispering gallery modes spectroscopy .....	65
2.2.1	Introduction .....	65
2.2.2	Theoretical background .....	68
2.2.3	Experiments and discussion .....	72
2.2.4	Conclusions .....	84
2.3	References .....	85
<b>Chapter 3: WGMs of polymer cylindrical microresonators for strain tunable devices and strain sensors .....</b>		<b>94</b>
3.1	Strain induced spectral tuning of the whispering gallery modes in a cylindrical micro-resonator formed by a polymer optical fiber .....	95
3.1.1	Introduction .....	96
3.1.2	Experimental arrangements .....	98
3.1.3	The effect of strain on the WGM resonance wavelength .....	100
3.1.4	Polarization effects .....	108
3.1.5	Conclusions .....	111
3.2	A packaged whispering gallery mode strain sensor based on a polymer-wire cylindrical micro resonator .....	112
3.2.1	Introduction .....	112
3.2.2	Sensing principle, operation and fabrication .....	115
3.2.3	Strain sensor packaging experiment .....	122
3.2.4	Before/after packaging performance comparison .....	128

3.2.5	Analysis of the performance of the packaged strain sensor .....	129
3.2.6	Studies of factors affecting the performance of packaged sensor .	132
3.2.7	Conclusions .....	136
3.3	References .....	138
<b>Chapter 4: Temperature and magnetic field sensors based on LCORR cylindrical microresonators.....</b>		<b>145</b>
4.1	Thermo-optic tuning of a packaged whispering gallery mode resonator filled with nematic liquid crystal.....	146
4.1.1	Introduction .....	146
4.1.2	Experimental details, results and discussions .....	150
4.1.3	Summary .....	164
4.2	Magnetic-field sensor based on whispering gallery modes in a photonic crystal fiber infiltrated with magnetic fluid .....	165
4.2.1	Introduction .....	165
4.2.2	Operational principles .....	168
4.2.3	Experimental details, results and discussions .....	170
4.2.4	Conclusions .....	177
4.3	Magnetic field sensing using whispering-gallery modes in a cylindrical microresonator infiltrated with ferronematic liquid crystal. ....	178
4.3.1	Introduction .....	179
4.3.2	Experimental details.....	181
4.3.3	Results and discussion .....	183
4.3.4	Conclusions .....	191
4.4	References .....	192
<b>Chapter 5: Coupling of multiple WGM microresonators for novel sensing applications .....</b>		<b>201</b>
5.1	Packaged inline cascaded optical micro-resonators for multi-	



parameter sensing.....	202
5.1.1 Introduction.....	203
5.1.2 Fabrication of the proposed ICOMRs.....	204
5.1.3 Initial Feasibility Experiments.....	206
5.1.4 Multi-parameter sensing using ICOMRs.....	209
5.1.5 Conclusions.....	213
5.2 Temperature compensated strain sensor based on an inline cascade of optical microresonators.....	214
5.2.1 Introduction.....	215
5.2.2 Fabrication of the ICOMR based strain sensor.....	216
5.2.3 Strain measurement.....	218
5.2.4 Conclusions.....	222
5.3 References.....	223
<b>Chapter 6: Conclusions and Future Work.....</b>	<b>227</b>
6.1 Conclusions from the research.....	227
6.2 Future Work.....	235
6.3 References.....	237
<b>Appendix A: Statement of Contribution.....</b>	<b>238</b>
<b>Appendix B: Studies of Effective Coupling conditions for a Microsphere-Tapered Fiber System for Generating Whispering Gallery Modes.....</b>	<b>240</b>

## List of Figures

<b>Figure 1.</b> Number of articles on WGM resonators published between 1996 and 2017. The data were gathered from the Web of Science database (www.webofknowledge.com). Term “whispering gallery mode” was applied as the keyword.....	2
<b>Figure 2.</b> Some examples of different micro-resonator shapes: (a) micro-sphere [53], (b) micro-disk [54], and (c) micro-toroid [55].....	5
<b>Figure 3.</b> Comparison of experimentally observed WGM spectra of spherical and cylindrical silica micro-resonators: (a) spherical micro-resonator with a radius of 44.3 $\mu\text{m}$ ; (b) cylindrical micro-resonator of 62.5 $\mu\text{m}$ radius; (c) cylindrical micro-resonator of 11 $\mu\text{m}$ radius. ....	8
<b>Figure 4.</b> (a) First order and (b) second order radial electric field profiles (S(R), Eq. (1.3)) for a layered cylindrical microresonator with an outer diameter and wall thickness of 50 $\mu\text{m}$ and 2 $\mu\text{m}$ respectively [65].....	12
<b>Figure 5.</b> Schematic representation of a tapered fiber.....	13
<b>Figure 6.</b> Schematic diagram of a tapered fiber coupled to a cylindrical micro-resonator. ....	14
<b>Figure 7.</b> Block diagram of an experimental set-up to study the response of the fabricated WGM based sensors/tunable devices.....	24
<b>Figure 8.</b> Schematic diagram of the microfibre fabrication setup based on the microheater brushing technique. ....	50
<b>Figure 9.</b> Experimental setup for observation of the transmission spectrum of WGMs in a cylindrical micro-resonator excited by a fiber taper. ....	51
<b>Figure 10.</b> Microphotograph of the micro-cylinder resonator in perpendicular position with respect to the tapered fiber. ....	52
<b>Figure 11.</b> WGM transmission spectra excited in the cylindrical fiber resonator with a diameter of 240 $\mu\text{m}$ for different tapered fiber diameters. ....	53

<b>Figure 12.</b> SEM image of the waist portion of the tapered optical fiber.....	54
<b>Figure 13.</b> WGM spectra for cylindrical micro-resonators with different diameters: (a) 240 $\mu\text{m}$ (b) 125 $\mu\text{m}$ (c) 36 $\mu\text{m}$ and (d) 8 $\mu\text{m}$ .....	56
<b>Figure 14.</b> Variation of (a) free spectral range (FSR), (b) full width at half minimum (FWHM) and quality factor (Q-factor) of the WGM resonances for different diameter resonators with curve fit.....	57
<b>Figure 15.</b> Microscopic image of the micro-cylinder with the tapered optical fiber. ....	59
<b>Figure 16.</b> (a) WGM spectrum generated by a 240 $\mu\text{m}$ diameter cylindrical micro- resonator (normal to the taper, $\theta = 0$ ). (b) Lorentzian fit of one of the WGM peaks, estimated Q factor is $1.83 \times 10^4$ .....	61
<b>Figure 17.</b> (a) Transmission spectra of the tapered fiber in contact with the micro-cylinder for different tilt angles with respect to the perpendicular position; (b) overall average loss of the transmission spectrum and extinction ratio of the WGM dip (for peak p2) with the increase in the tilt angle; (c) The broadening of the WGM dip and blue shift experienced on a selected WGM dip with the increase of the tilt angle. ....	63
<b>Figure 18.</b> Schematic diagram of tapered fiber coupled cylindrical resonator.....	69
<b>Figure 19.</b> (a) Relationship between the transmission power of the tapered fiber coupled with the cylindrical microresonator with the resonator internal loss coefficient ( $\alpha$ ) and, transmission loss coefficient ( $ t $ ) with its transmission power. (b) The simulated transmission spectrum of the tapered fiber at critical coupling. ....	70
<b>Figure 20.</b> Schematic diagram of the microfibre fabrication setup using the microheater brushing technique. ....	74
<b>Figure 21.</b> Schematic of the experimental setup for whispering gallery mode spectroscopy.....	75

<b>Figure 22.</b> Experimental WGM spectrum of the delivery fiber and a simulated spectrum using Eq. 2.11. ....	77
<b>Figure 23.</b> SEM images of the uniform waist portions of the tapered optical fibers.....	78
<b>Figure 24.</b> Experimentally calculated FSR and diameter vs position of the delivery fiber for a taper with a nominal waist diameter of 11.2 $\mu\text{m}$ (Taper 1) and 35.5 $\mu\text{m}$ (Taper 2) measured by WGM spectroscopy. Zero position corresponds to the center of the taper. ....	80
<b>Figure 25.</b> (a) FSR and experimental diameter vs position of the delivery fiber for an asymmetrical taper with a minimum waist region effective diameter $\sim 41 \mu\text{m}$ . The experimental diameter is calculated by the WGM spectroscopy method. (b) Comparison of two experimental profiles for tapered optical fibers drawn under different conditions. ....	82
<b>Figure 26.</b> Comparison of variation in left and right-hand side transition regions of a symmetrical and an asymmetrical fiber taper. ....	83
<b>Figure 27.</b> Schematic diagram of the experimental setup for studies of the tunability of WGMs in the POF resonator under the influence of applied strain.....	99
<b>Figure 28.</b> (a) Whispering gallery modes spectrum generated by the POF MR, (b) Lorentzian fittings of the spectral dips p1. The dip has the central wavelength at 1500.71 nm, and its FWHM and the corresponding Q-factor are 0.072 nm and $2.09 \times 10^4$ respectively.....	100
<b>Figure 29.</b> Evolution of the tapered fiber transmission spectrum under the influence of the increasing axial strain, followed by the strain decrease back to the unstrained position. For illustrative purposes each consecutive spectrum is plotted with an artificial offset of 30 dB compared to the prior spectrum. The arrows indicate the resonant wavelength shift direction.....	101
<b>Figure 30.</b> Wavelength shift of the selected WGM resonances as a function of increasing axial strain: (a) dip p2 and (b) dip p3 (as depicted in Fig.	

29). The measured wavelength shift (scatter data) is linearly fitted (solid line). Linear fitting of the wavelength response data indicates that the linear regression coefficient is greater than 0.99 for both p2 and p3 dips. The slopes of the linear dependencies are  $-0.64 \text{ pm}/\mu\epsilon$  for p2 and  $-66 \text{ pm}/\mu\epsilon$  for p3 respectively..... 104

**Figure 31.** Wavelength shifts of the selected WGM resonances as a function of decreasing axial strain: (a) dip p2 and (b) dip p3. The measured wavelength shift (scatter data) is linearly fitted (solid line). Linear fitting of the wavelength response data indicates that the linear regression coefficient is greater than 0.99 for both p2 and p3 dips. The slopes of the linear dependences are  $0.63 \text{ pm}/\mu\epsilon$  for p2 and  $0.64 \text{ pm}/\mu\epsilon$  for p3 respectively. .... 105

**Figure 32.** Selected WGM resonances during the strain increase (S. I) (black) and strain decrease (S. D) (red) cycles: (a) dip p2 and (b) dip p3. Inset figures show the discrepancies in WGM wavelengths during the increase and decrease cycles. .... 107

**Figure 33.** WGM resonant spectra from the POF MR with different input light polarizations..... 109

**Figure 34.** Selected WGM resonances during the strain increase (black) and strain decrease (red) cycles with different input light polarization. Here linearly polarized input light is rotated by angle (a)  $0^\circ$ , (b)  $7.22^\circ$ , and (c)  $14.44^\circ$  respectively. (d) Sensitivity of the increase and decrease cycles of the axial tensile strain. .... 110

**Figure 35.** (a) Transmission spectrum of tapered fiber coupled with a  $230 \mu\text{m}$  diameter cylindrical polymer wire resonator. (b) Selected single resonance dip along with the Lorentzian fit..... 118

**Figure 36.** Shift in the selected dip of WGM transmission spectrum with increasing axial strain..... 120

**Figure 37.** Theoretically calculated and experimentally measured wavelength shift as a function of axial strain for a selected WGM dip. .... 122

**Figure 38.** Schematic of the packaging process: (1) Capillary tube attached on the glass substrate, (2) inserting polymer-wire into the capillary tube, and (3) attaching the polymer wire on to the glass substrate using UV glue..... 125

**Figure 39.** (a)-(b) Illustration of the packaging process..... 127

**Figure 40.** Photograph of the packaged strain sensor..... 128

**Figure 41.** (a) Transmission spectrum of the tapered fiber before and after packaging (b) selected single resonance dip. .... 129

**Figure 42.** Schematic diagram of the strain sensing experiments using the packaged strain sensor. .... 130

**Figure 43.** Experimental results for the packaged sensor: (a) & (b) wavelength shift of a selected WGM resonance versus applied increasing (decreasing) strain and (c) & (d) corresponding WGM resonance shifts versus applied strain. .... 131

**Figure 44.** Experimental setup for vibration tests (a) General view; (b) Top view of the vibrational platform..... 133

**Figure 45.** Selected single transmission WGM dip of the packaged strain sensor at before and after vibration..... 133

**Figure 46.** (a) Selected WGM resonance with different applied temperature, and (b) linear fit of the measured resonance wavelength shift data... 136

**Figure 47.** Schematic of the packaging process: (a) Capillary tube attached to the glass substrate, (b) Maximizing the coupling efficiency between the tapered optical fiber and capillary tube resonator, and (c) Immobilizing the coupled system on a glass substrate. .... 152

**Figure 48.** (a) Selected WGM resonance dip of the packaged device before and after the vibration test. (b) Experimental set up for vibration tests..... 153

**Figure 49.** Experimental WGM spectra of the air core and liquid crystal filled thin-walled micro-capillary..... 154

**Figure 50.** Transmission spectra of the LC-filled WGM resonator with (a) increasing and (b) decreasing temperature. There is an average spectral shift of 3.23 nm for the temperature change from of 26 to 40 °C..... 156

**Figure 51.** Spectral shift experienced by a selected WGM resonance [p2 in Figure 50] with increasing and decreasing temperature. .... 158

**Figure 52.** The resonance wavelength [p2] plotted against time as the temperature was cycled, for elevated temperatures of 35°C and 45°C from room temperature. .... 159

**Figure 53.** (a) Selected WGM resonance dip of an air-core capillary tube resonator with increasing temperature. (b) Linear fit of the measured resonance wavelength data with increasing temperature. .... 160

**Figure 54.** Schematic representation of WGMs localization. (a) Inner cladding has low RI - WGMs form at the outer wall and have evanescent field extending toward the inner (holey) cladding region; (b) Inner cladding has higher RI - WGMs exist at both outer surface of the fiber and in the vicinity of the holey cladding..... 170

**Figure 55.** Schematic diagram of the experimental setup for the magnetic field sensor characterization..... 171

**Figure 56.** Experimental data and their Lorentzian fitting for selected WGM resonances for the spectra generated by an LMA-10 resonator without a ferrofluid and after its infiltration with the MF containing 10 nm diameter nanoparticles in the absence of magnetic field. .... 172

**Figure 57.** (a) WGM spectra generated by the LMA-10 PCF infiltrated with the MF containing 5 nm diameter nanoparticles in the absence of magnetic field (0 mT) and at 38.7 mT; (b) WGM spectra generated by the LMA-10 PCF infiltrated with the MF containing 10 nm diameter nanoparticles in the absence of magnetic field (0 mT) and at 57.3 mT.

The arrows indicate the direction of the spectral shift with the increase of the magnetic field. ....	174
<b>Figure 58.</b> Selected WGM resonance wavelength versus applied magnetic field: a) 5 nm diameter nanoparticles sample and b) 10 nm diameter nanoparticles sample. ....	175
<b>Figure 59.</b> Evolution of a single fundamental WGM dip under the influence of magnetic field. ....	176
<b>Figure 60.</b> TEM images of (a) spherical magnetic nanoparticles, (b) rod-like magnetic nanoparticles, (c) polarizing microscope images of empty and infiltrated PCF in crossed polarizers, and (d) SEM image of the PM-1550- 01-PCF cross section. ....	182
<b>Figure 61.</b> Schematic diagram of the experimental setup for the magnetic field sensor characterization.....	183
<b>Figure 62.</b> Experimental WGM transmission spectra and corresponding Lorentzian fitting to estimate the Q-factor for the sample resonators infiltrated with rod-like particles containing ferronematic LC in the absence of magnetic field and at room temperature. ....	184
<b>Figure 63.</b> Experimental WGM transmission spectra and corresponding Lorentzian fitting to estimate the Q-factor for the sample resonators infiltrated with spherical particles containing ferronematic LC in the absence of magnetic field and at room temperature. ....	185
<b>Figure 64.</b> WGM spectra at different values of the applied magnetic field for the PM-1550-01-PCF infiltrated samples with (a) rod-like and (b) spherical particles.....	186
<b>Figure 65.</b> Dependence of selected WGM resonant wavelengths and extinction ratio versus applied magnetic field: (a) rod-like particles containing sample and (b) spherical particles containing sample.....	188
<b>Figure 66.</b> The SEM image of the cross section of 50 $\mu\text{m}$ tapered PM- 1550-01-PCFs.....	189



<b>Figure 67.</b> Selected WGM resonance wavelength versus applied magnetic field for the tapered sensors (50 $\mu\text{m}$ diameter): (a) rod-like particles sample and (b) spherical particles sample.....	190
<b>Figure 68.</b> Schematic diagrams illustrating the ICOCR packaging steps: (a) cylindrical micro-resonators attached to glass substrates; (b) three tapered sections fabricated along the single optical fiber and (c) packaged ICOMR formed by three resonators. ....	208
<b>Figure 69.</b> Transmission spectra for ICOCRs formed by (a) two $\sim 20 \mu\text{m}$ diameter resonators and (b) three $\sim 15 \mu\text{m}$ diameter resonators. Each graph illustrates the individual and combined WGM spectra.....	209
<b>Figure 70.</b> Optical microscope image of PDMS coated micro-fiber. One division of the scale in the image is equaling to $1.67 \mu\text{m}$ .....	210
<b>Figure 71.</b> WGM spectra for the PDMS-coated micro-resonator, POF micro-resonator and the resulting ICOMRs. ....	211
<b>Figure 72.</b> Transmission spectra of the ICOMR at different temperatures and applied strain values.....	212
<b>Figure 73.</b> Spectral shift of selected resonance troughs for (a) POF micro-cylinder vs. applied strain and (b) PDMS-coated silica micro-cylinder vs temperature.....	213
<b>Figure 74.</b> (a) Schematic diagram of the experimental setup. (b) Transmission spectra of the ICOCR and each of the MRs separately.....	218
<b>Figure 75.</b> Selected part of the transmission spectrum of the ICOMR with strain decrease. (b) Selected WGM resonance wavelength shift as a function of applied strain. The slope of the linear fit to the measured data of the WGM trough from the MR1 resonator is $3.3 \text{ pm}/\mu\epsilon$ . ....	221
<b>Figure 76.</b> Selected resonance wavelength as a function of temperature increase. (b) Resonance wavelength shift with temperature increase.	

Here the measured wavelength (scatter data) is fitted with polynomial fit  
(solid curve). .....222

## List of Tables

<b>Table 1.</b> Comparison of measured fiber diameter using WGMs and SEM microscopic method.....	81
<b>Table 2.</b> Sensitivity comparison of WGM temperature sensors.....	163

## List of Abbreviations

DL	Detection Limit
FSR	Free Spectral Range
FWHM	Full Width at Half Maximum
FESEM	Field Emission Scanning Electron Microscope
FPC	Fiber Polarization Controller
GIPOF	Graded Index Polymer Optical Fiber
ICOMR	Inline Cascaded Optical Microresonator
LCORR	Liquid Core Optical Ring Resonators
LC	Liquid Crystal
MR	Micro-resonator
MF	Magnetic Fluid
NLC	Nematic Liquid Crystal
OSA	Optical Spectrum Analyser
OFRR	Optofluidic Ring Resonators
PC	Personal Computer
POF	Polymer Optical Fiber
PCF	Photonic Crystal Fiber
PMMA	Polymethyl methacrylate
PDMS	Polydimethylsiloxane
PM-PCF	Polarization Maintaining Photonic Crystal Fiber
Q	Quality factor
RI	Refractive Index
RIU	Refractive Index Unit

SLD	Super Luminescent Diode
SMF	Single Mode Fiber
SEM	Scanning Electron Microscope
S	Sensitivity
TIR	Total Internal Reflection
TEM	Transmission Electron Microscope
TE	Transverse Electrical
TM	Transverse Magnetic
UV	Ultraviolet
WGM	Whispering Gallery Mode

# Chapter 1

---

---

## Introduction

---

---

This thesis presents the outcomes of a number of interconnected investigations of various optical sensors and tunable devices based on the effect of whispering gallery modes (WGMs) in both solid and hollow cylindrical micro-resonators. The thesis consists of a series of six linked journal publications and a conference proceeding prepared within the duration of the Ph. D research period.

This chapter introduces the background, motivation, objectives of the research and provides an overview of the thesis layout.

### 1.1 Background to the research

#### 1.1.1 Whispering gallery mode (WGM) resonators: advantages, applications and analytical foundation

Optical whispering gallery mode (WGM) resonators are monolithic micron-sized transparent dielectric structures in which the closed trajectories of light are supported by total internal reflections from the circular boundaries [1]. The ability to confine light by means of resonance in a small cavity with low mode volumes and high quality factors (Q) makes them attractive in many photonic applications such as all-optical switches [2–4], modulators [5–7], all-optical signal processing [8–10], biochemical sensing [11–13], slow-light structures or optical buffers [14–20], wavelength division-multiplexed (WDM) optical filters for

optical networks and on-chip optical interconnects [21–26], ultralow-threshold microlasers [27,28], enhancement of Raman processes [29] as well as Raman lasing [30–32], and in fundamental experiments in quantum physics [33, 34]. Research interest in this area is confirmed by data from the Web of Science that shows that there has been a rapid increase in publications. Figure 1 shows the number of publications related to optical WGM resonators during last 20 years (gathered from the Web of Science database).

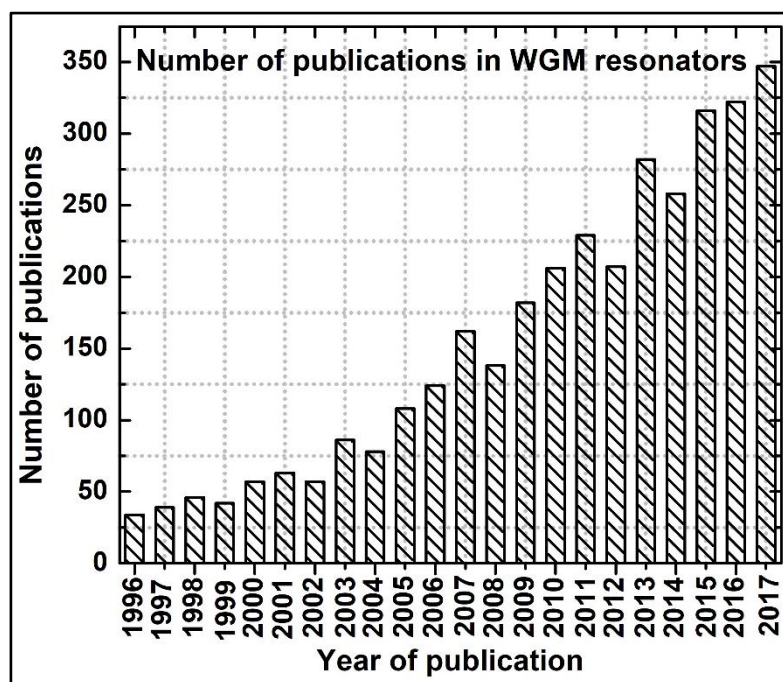


**Figure 1.** Number of articles on WGM resonators published between 1996 and 2017. The data were gathered from the Web of Science database ([www.webofknowledge.com](http://www.webofknowledge.com)). Term “whispering gallery mode” was applied as the keyword.

The exceptional sensitivity of the characteristics of the confined light to the size and the optical properties of the cavity as well as its surrounding medium makes the WGM resonators suitable for applications in optical sensors and various tunable devices. Any perturbation to the resonator’s morphology (shape, size or refractive index) will lead to a spectral shift of the WGM resonances. This property can be utilized in tunable devices where the WGM spectrum could be tuned by

varying any of the resonator's parameters and in optical sensors where detecting any changes in the WGM spectrum can be related to changes in a given environmental parameter following appropriate calibration. This thesis will focus on the applications of WGM resonances both in optical sensing and for the design of novel optical tunable devices.

WGM resonances were first observed for acoustic waves and studied by Lord Rayleigh who described this effect for sound waves propagating in the dome of St. Paul's cathedral in London. In the circular dome structure, a whisper at one side is clearly audible at the other side of the dome, but it can't be heard near the center of the dome. In effect, the sound waves are propagating close to the curved wall of the dome via multiple reflections.

Optical WGMs in dielectric particles were first theoretically investigated by Mie in 1908 during his light scattering experiments and color effects associated with the colloidal gold particles [35]. Part of Mie's work was based on earlier studies of light scattering by Thomson, Alfred Clebsch, Ludwig Lorenz and Peter Debye. Optical WGMs are confined by the continuous total internal reflections (TIR) at the interface of the particles and their surrounding medium. In many ways these electromagnetic modes were similar to Lord Rayleigh's experiments with the sound waves hence the modes were referred to as optical WGMs and the dielectric cavities received the name of optical WGM resonators.

Optical modes in WGM structures have well-defined optical paths that only specific light wavelengths can be coupled to and, subsequently, be guided by TIR. Inside the resonator, light is reflected over and over creating a 10 to 100-meter-long optical path within a tiny device of the size of a grain of sand or less than the diameter of a human hair. In geometrical optics, the resonance condition for the



reflected light rays inside the WGM resonator can be represented by a simple approximation:

$$2\pi a n_{\text{eff}} = l\lambda \quad (1.1)$$

where  $a$  is the radius of the resonator,  $\lambda$  is the wavelength of light in free space,  $n_{\text{eff}}$  is the effective refractive index of the resonator, and  $l$  is an integer number which represents the number of wavelengths around the circumference of the resonator (also called an azimuthal quantum number of the resonator) [36]. On resonance, the circulating light will constructively interfere in phase after each round trip where the phase is an integer multiple of  $2\pi$ . According to the resonance condition either a change in the length of the optical path or the refractive index of the resonator will introduce a change in the resonant wavelength [36]:

$$\frac{\Delta\lambda}{\lambda} = \frac{\Delta a}{a} + \frac{\Delta n}{n} \quad (1.2)$$

Thanks to this property WGM resonators are widely utilized in optical sensing and in various tunable photonic devices, such as optical filters, lasers, switches etc.

Compared to other conventional optical resonators WGM microresonators have several advantages, including their small size, light weight, immunity to electromagnetic interference, low intrinsic losses, high Q-factors and good mechanical stability (due to their monolithic nature). In sensing applications WGM resonators can offer high sensitivity down to single molecule detection [37], label-free detection capability, and compatibility with other optical techniques such as Raman spectroscopy [29], microdroplet [38], and fluorescence techniques [39]. In tunable devices applications WGM spectra can be engineered as well as dynamically tuned by variety of methods (e.g., by means of strain, temperature,

refractive index changes, electric or magnetic fields). Light coupling into WGM resonators can be realized by using various techniques (channel waveguide couplers [39], tapered optical fiber couplers [40], prism couplers [41], and angle polished fibers [42] or polished half block fibers [43]) and the light coupling efficiency depends on the distance between the resonator and the evanescent coupler.

### 1.1.2 Types of WGM micro-resonators

In the last 25 years WGM cavities of a wide variety of shapes fabricated by a range of methods have been studied extensively, including fused silica microspheres [40], micro-droplets [38], micro-disks [41], micro-toroids [42], micro-rings [43], micro-cylinder [44] and some special resonator structures such as micro-bubbles [45], micro-spheroids [46], micro-pillbox [47], micro-gear [48], doughnut-shaped [49], micro-coil [50], wheel shaped [51] and sausage shaped micro-structures [52].

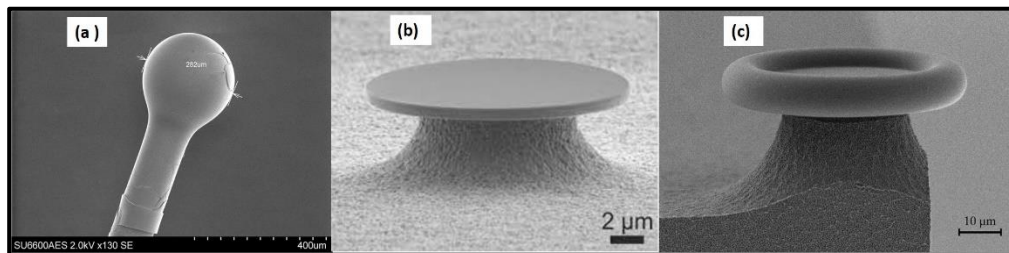


**Figure 2.** Some examples of different micro-resonator shapes: (a) micro-sphere [53], (b) micro-disk [54], and (c) micro-toroid [55].

The micro-sphere, micro-disk, and micro-toroid resonators (Fig. 2) are the most widely used because of their typically high-quality factors and extremely small mode volumes compared to other WGM resonator structures. However, such resonators also have some limitations.

Firstly, fabrication of the micro-resonators with complex shapes (e.g., micro-disks

or micro-goblets) typically requires expensive micro-fabrication facilities. In addition, achieving sufficiently low surface roughness with photo-lithographic methods is difficult. Surface roughness needs to be avoided as it increases scattering loss.

In the context of portable devices design, spherical resonators are not a good choice due to the difficulties in light coupling and packaging. For example, in the case of light coupling with fiber tapers, even a small misalignment between the fiber taper and the sphere's equator or the presence of weak vibrations could result in significant variation in the WGM spectrum. Moreover, spherical and microbottle resonators typically produce very dense spectra with a small free spectral range (FSR) that can limit the range of tunability or sensing range of the devices fabricated on their basis.

### **1.1.3 Cylindrical WGM micro-resonators**

Cylindrical micro-resonators are the simplest form of micro-resonators, as they can be easily fabricated from coating-stripped commercial optical fibers offering the advantages of simplicity and potentially low cost. The stripped-off surface of such cylindrical micro-resonators has a high degree of smoothness without the need for complex micro-fabrication equipment. Commercial optical fibers are highly uniform in diameter, allowing large numbers of identical resonators to be fabricated easily and providing a high degree of repeatability. In addition, the alignment for optimal coupling of the excitation light into the fiber resonator depends on only one angular degree of freedom, as opposed to two degrees of freedom for the more complex spherical structures.

The main disadvantage of an infinitely long cylindrical micro-resonator is its relatively low Q-factor. In a cylindrical structure the coupled beam spreads along

the cylinder's length and eventually vanishes even if there is no material loss. Despite their typically low Q-factors (in the order of  $10^3$  or less) cylindrical micro-resonators found several important applications in photonics. For example, M. Mariano *et al.* demonstrated that an array of low-Q cylindrical microfibers at the surface of organic solar cells can significantly improve their light harvesting capacity [56]. Moreover, numerous experimental studies of the micro-cylinder and micro-capillary resonators' transmission spectra demonstrated that the Q-factor of the cylindrical micro-cavity can be made as high as the Q-factor of a spherical cavity (circa  $10^7$ ) by introducing local diameter variation(s) along its axial direction [44]. The theoretical explanation of this effect was proposed by M. Sumetsky in 2010 [57].

WGM spectra of cylindrical micro-resonators have larger FSRs due to possessing fewer radial and transverse modes than those of a micro-sphere. As an illustration, Figure 3 shows experimentally measured WGM spectra excited by a spherical (a) and cylindrical (b, c) micro-resonators within a range of wavelengths from 1500 nm to 1600 nm. The spherical micro-resonator has a radius of 44.3  $\mu\text{m}$ . From Figure 3(a) one can see that the modes are densely "packed" with an intermodal spacing of 1.3 nm and the estimated Q-factor of the modes is in the order of  $\sim 10^4$ . Figure 3(b) shows the WGM spectrum for a cylindrical micro-resonator with a 62.5  $\mu\text{m}$  radius, made from a section of a standard singlemode telecommunications fiber (SMF 28) while Figure 3(c) shows the WGM spectrum excited by a cylindrical micro-resonator of the 11  $\mu\text{m}$  radius made from an asymmetrically tapered section of the SMF 28 fiber. In the first case the FSR of the spectrum is 4.32 nm and in the latter case the FSR is 39.2 nm. The Q-factor of the WGMs from the conventional fiber is in the order of  $\sim 10^3$  and that from the asymmetric fiber

taper is in the order of  $\sim 10^4$ , which is as high as the Q-factor for the spherical micro-resonator shown in Figure 3(a).

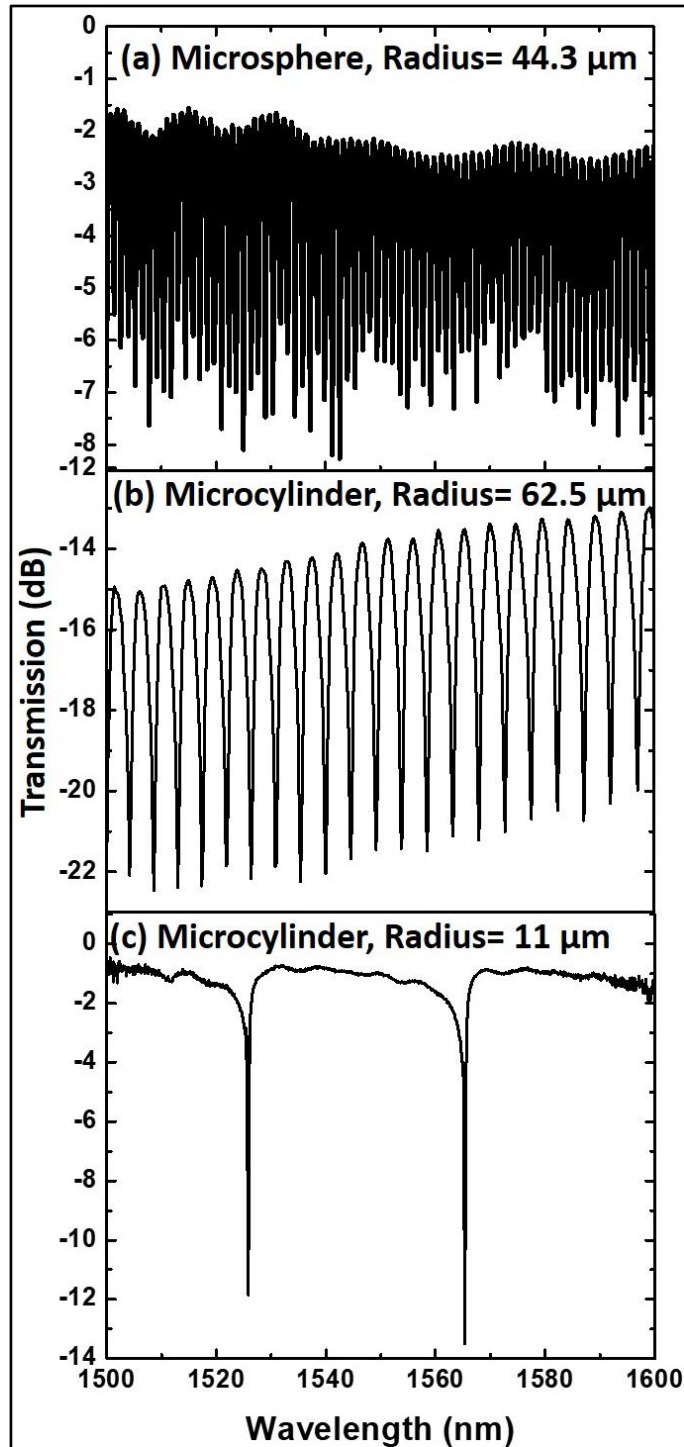


**Figure 3.** Comparison of experimentally observed WGM spectra of spherical and cylindrical silica micro-resonators: (a) spherical micro-resonator with a radius of 44.3  $\mu\text{m}$ ; (b) cylindrical micro-resonator of 62.5  $\mu\text{m}$  radius; (c) cylindrical micro-resonator of 11  $\mu\text{m}$  radius.

As expected, the WGMs of the tapered fiber based cylindrical micro-resonator are strongly localized due to the nanoscale diameter variations as a result of fiber tapering, leading to the higher Q-factor compared with that of the cylindrical resonator made from a conventional fiber [58], without tapering.

The main focus of the research described in this thesis is on the cylindrical micro-resonators and hollow cylindrical micro-resonators, fabricated from sections of polymer fibers, tapered silica fibers, capillaries and photonic crystal fibers.

#### **1.1.4 Liquid core optical ring resonators**

Hollow cylindrical micro-resonators, also known as the liquid core optical ring resonators (LCORR), are typically made from a section of a tapered silica capillary tube. The first LCORR structure was introduced by I. White *et al.* in 2006 and it has since been used in various sensing applications including detection of DNA, viruses, proteins and cancer biomarkers [59]. The LCORR structures have been of a particular interest in sensing since they allow for an easy integration of the solid resonator with various liquid analytes or liquids acting as transducers (e.g., magnetic liquids or liquid crystals). Alternative approaches to integration of liquids with solid WGM resonators involve encapsulation of the fluid inside the resonator which can be fabricated in the shape of a tube, a bubble, or photonic crystal fiber. The research in this thesis includes work on the photonic crystal fiber and capillary tube based thin-walled hollow cylindrical micro-resonators for the development of novel sensors and tunable devices.

#### **1.1.5 Fundamentals of WGMs in cylindrical micro-resonators**

Many theoretical studies reported in the literature aimed to explain the propagation of WGMs both in solid and hollow- or layered cylindrical micro-resonators using numerical and approximate analytical methods based on Lorenz-Mie-Debye

theory [35,60]. For example, the field distribution of the WGMs in a radially nonuniform two-layer cylindrical dielectric micro-resonator was studied in [61], quantum theory of WGMs in a cylindrical optical micro-cavity was reported in [62], simulation of WGMs of dielectric cylinders using the nonstandard finite difference time domain method was reported in [63] and light propagation and calculation of resonant modes in LCORR was reported in [59, 64]. More recently, a theoretical investigation of the light propagation in capillary-type micro-fluidic sensors based on WGMs was presented in [65].

WGMs in a spherical micro-resonator are conventionally described in terms of three integers which are used to characterize the radial, polar and azimuthal components of the electromagnetic field in the micro-sphere [66]. Cylindrical micro-resonators can be characterized by a similar set of numbers but without that associated with the polar component of the field, so that WGMs can be assumed to propagate in a 2-D cross section of the cylinder. The parameters required to describe the cylindrical resonances are the number of intensity maxima in the radial direction ( $n$ ), the number of wavelengths that fit around the cylinder for a given resonance ( $l$ ), and the  $Q$ -factor that describes how well the mode is able to trap the radiation. The polarization can be either transverse electric (TE) or transverse magnetic (TM). Polarizations of the modes are defined with respect to the WGM propagation plane such that TE resonances have their electric field component parallel to the cylinder axis and TM modes have the magnetic field component parallel to the cylinder axis. The radial distribution of TE modes across various boundaries of the layered micro-cylinder is given by [65]:

$$S(R) = \begin{cases} A_l J_l(m_1 k_0 r), & r \leq b \\ B_l H_l^{(2)}(m_2 k_0 r) + C_l H_l^{(1)}(m_2 k_0 r), & b < r \leq a \\ D_l H_l^{(1)}(m_3 k_0 r), & r > a \end{cases} \quad (1.3)$$

where  $J_l$ ,  $H_l^{(1)}$  and  $H_l^{(2)}$  are the  $l^{\text{th}}$  Bessel function of the first kind,  $l^{\text{th}}$  Hankel function of first kind and  $l^{\text{th}}$  Hankel function of the second kind respectively. Here  $m_1$ ,  $m_2$ , and  $m_3$  are the refractive index of the inner cylinder's layer, outer layer, and the surrounding medium. The outer and inner radii of the layered cylinder are  $a$  and  $b$ , respectively.  $k_0$  and  $l$  are the wave vector in vacuum and the azimuthal mode number.  $A_l$ ,  $B_l$ ,  $C_l$ , and  $D_l$  are the proportionality constants found from the boundary conditions for the electric field across various boundaries of the layered structure.

According to the boundary conditions, the eigen equation of the layered microcylinder can be written as [65]:

$$\frac{m_3 H_l^{(1)'}(m_3 k_0 a)}{m_2 H_l^{(1)}(m_3 k_0 a)} = \frac{B_l H_l^{(2)'}(m_2 k_0 a) + H_l^{(1)'}(m_2 k_0 a)}{B_l H_l^{(2)}(m_2 k_0 a) + H_l^{(1)}(m_2 k_0 a)} \quad (1.4)$$

Where the prime symbol indicates the derivatives of the functions with respect to the argument. By solving Eq. (1.4) the resonant wavelengths of the WGMs and the azimuthal and radial quantization numbers,  $n$  and  $l$ , can be determined.

Figure 4 (a, b) shows first and second order radial electric field profiles for TE modes of a layered cylindrical micro-resonator simulated in accordance with Eq. (1.3). The outer diameter and thickness of the hollow cylinder are 50  $\mu\text{m}$  and 2  $\mu\text{m}$  respectively. The resonant wavelengths of the modes are close to 0.8  $\mu\text{m}$ .

Further analysis shows that a discrete set of valid eigenvalues emerges for a cylinder with a fixed diameter, and that a larger resonator supports more modes.

Experimental visualization of the field intensity distributions inside the cylindrical micro-cavity was reported by Klunder *et al.* [67,68] and Balistreri *et al.* [69,70], and those were in line with the theoretically calculated results. The experimental mappings by Klunder *et al.* of the WGMs intensity distributions were carried out



by looking directly into the microcavity by means of a photon scanning tunneling microscope with a spatial resolution of 50 nm.

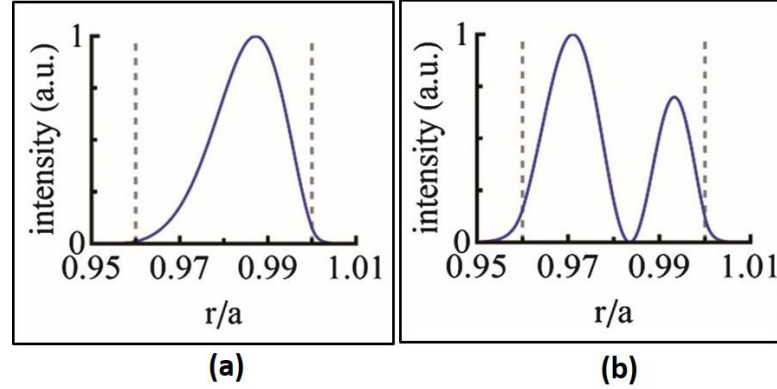


**Figure 4.** (a) First order and (b) second order radial electric field profiles ( $S(R)$ , Eq. (1.3)) for a layered cylindrical microresonator with an outer diameter and wall thickness of 50  $\mu\text{m}$  and 2  $\mu\text{m}$  respectively [65].

### 1.1.6 Light coupling into WGM resonators

There are several methods of light coupling in and out of a WGM resonator including a free space coupling and a guided wave coupling. For free space coupling WGMs are excited using a focused laser beam illuminating the resonator and the scattered light is collected using a collimator to a detector [71–73]. For the guided wave coupling, the most commonly used method is evanescent-wave coupling either from an adjacent guiding structure such as a tapered optical fiber coupler [74], a polished fiber half block coupler [75], eroded monomode optical fiber [76], a channel waveguide coupler [77], coupler utilizing frustrated total internal reflections such in a prism [78] or an angle-polished fiber [79].

Tapered optical fibers have become a popular choice for excitation of WGM resonances for many practical applications after J. C. Knight *et al.* showed in 1997 that high-Q WGMs could be easily and efficiently excited in micro-spherical

resonators by an adiabatic optical fiber taper [80]. This approach offers an ultra-high coupling efficiency of up to 99% [81].

A tapered fiber can be formed by heating and stretching a section of a standard optical fiber to a narrow thread. A typical optical fiber taper, shown schematically in Figure 5, consists of a non-tapered portion followed by a transition region where the radius of the fiber decreases with distance. The uniform thin portion after the transition region is known as the taper waist. In the waist region the fiber core no longer exists, and the light travels in the fundamental mode along the waveguide formed by the silica waist surrounded by air. If the waist is small, the fundamental mode will have an evanescent tail extending significantly into the free space surrounding the taper, and the propagation constant of the mode will be a function of the waist radius. The taper waist is followed by a second transition region of increasing diameter and ends with another non-tapered region. The light remaining in the waist is returned to the guided mode in the fiber core when reaching the other end of the waist. The optical properties of the tapered micro-fibers strongly depend on the geometry of both the transition and waist regions. In this research, only adiabatic tapers [82] were used for excitation of WGMs in cylindrical micro-resonators. That means the fiber tapering process was carried out in such a way that fiber diameter within its transition region changed slowly as a function of fiber length. Using adiabatic tapers ensures low transmission loss and small inter-mode coupling.

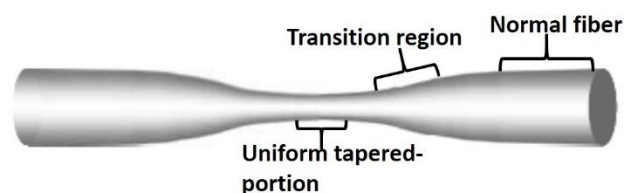


**Figure 5.** Schematic representation of a tapered fiber.

The phase matching condition for the light propagating in the tapered fiber and the resonator can be achieved by optimizing the diameter of the taper waist and the gap between the fiber taper and the resonator [81].

Figure 6 illustrates schematically the optical power exchange between a tapered fiber and a resonator in a lossless system. To explain power exchange in detail, assume that a single unidirectional mode of the resonator is excited and that the coupling is lossless, the interaction in the system can be described by the following matrix [83]:

$$\begin{pmatrix} b_1 \\ b_2 \end{pmatrix} = \begin{pmatrix} t & \kappa \\ -\kappa^* & t^* \end{pmatrix} \begin{pmatrix} a_1 \\ a_2 \end{pmatrix} \quad (1.5)$$

Where the complex mode amplitudes  $a_i$  and  $b_i$  are normalized so that their squared magnitude corresponds to the modal power.

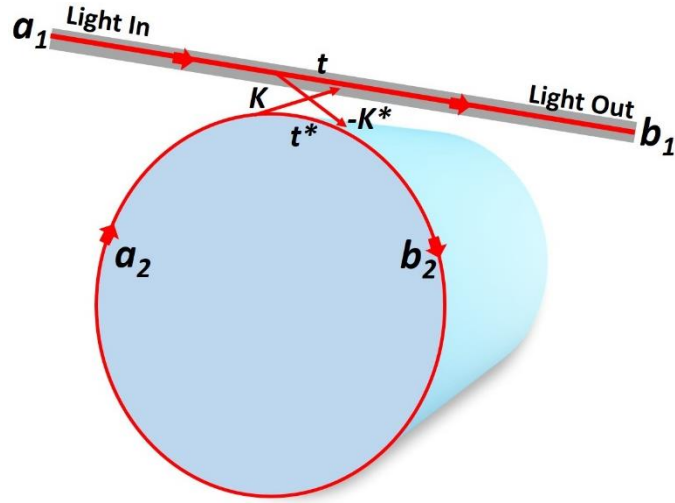


**Figure 6.** Schematic diagram of a tapered fiber coupled to a cylindrical micro-resonator.

Here  $t$  represents the transmission coefficient of the system, which is related to the coupling coefficient ( $\kappa$ ) by the equation:

$$|\kappa^2| + |t^2| = 1 \quad (1.6)$$

The matrix relation (1.5) can be re-written as:

$$b_1 = a_1 t + a_2 \kappa \quad (1.7)$$

$$b_2 = -a_1 \kappa^* + a_2 t^* \quad (1.8)$$

With a normalized input wave of  $a_1=1$ , the transmission around the resonator's circumference is

$$a_2 = \alpha e^{i\theta} b_2 \quad (1.9)$$

where  $\alpha$  is the loss coefficient of the resonator and  $\theta$  is the circulation phase shift

given by  $\theta = \frac{4\pi^2 R n_{eff}}{\lambda}$ , where  $n_{eff}$  is the effective refractive index of the mode that

propagates along a circular path within the cavity,  $R$  is the radius of the cylindrical micro-cavity, and  $\lambda$  is the resonance wavelength.

Substituting equation (1.8) into equation (1.9):

$$a_2 = \frac{-\alpha \kappa^*}{-\alpha t^* + e^{-i\theta}} \quad (1.10)$$

Substituting equation (1.9) into equation (1.7):

$$b_1 = \frac{-\alpha + t e^{-i\theta}}{-\alpha t^* + e^{-i\theta}} \quad (1.11)$$

If  $t = |t| e^{i\varphi_t}$ , where  $\varphi_t$  is a phase offset due to coupling to the tapered fiber, the total circulating power inside the cylinder is

$$|a_2|^2 = \frac{\alpha^2 |\kappa|^2}{1 + \alpha^2 |t|^2 - 2\alpha |t| \cos(\theta - \varphi_t)} \quad (1.12)$$

At resonance  $\varphi_t=0$  and the phase acquired by the wave after a complete round trip is an integer multiple of  $2\pi$ ,  $\theta = m2\pi$  where  $m$  is an integer. Thus, at resonance:

$$|a_2|^2 = \frac{\alpha^2 (1 - |t|)^2}{(1 - \alpha |t|)^2} \quad (1.12a)$$

Similarly, the total transmitted power in the tapered fiber past the resonator can be written as:

$$|b_1|^2 = \frac{\alpha^2 - 2\alpha|t|\cos(\theta - \varphi_t) + |t|^2}{1 - 2\alpha|t|\cos(\theta - \varphi_t) + \alpha^2|t|^2} \quad (1.13)$$

$$|b_1|^2 = \frac{(\alpha - |t|)^2}{(1 - \alpha|t|)^2} \quad (1.13a)$$

- **Critical coupling:** When the internal losses within the resonator are equal to the coupling losses ( $\alpha=t$ ), 100% of the light propagating in the tapered fiber is coupled into the resonator and is dissipated inside the resonator. In this case narrow WGM resonances in the transmission spectrum of the fiber taper are observed with zero transmission at the resonant wavelengths ( $|b_1|^2=0$ ), and the condition is known as the critical coupling.
- **Under-coupling:** If the internal loss within the resonator is less than the coupling loss ( $\alpha<t$ ), all the incident light is unable to couple into the resonator. As a result of this small and sharp non-zero wide WGM resonances are observed in the taper's transmission spectrum, and this case is known as under-coupling.
- **Over-coupling:** If the intrinsic resonator losses are greater than the tapered fiber induced losses ( $\alpha>t$ ), all the tapered fiber incident light is coupled into the resonator but a part of the light is coupled back into the tapered fiber and the case is called over-coupling.

### 1.1.7 Properties of optical micro-resonators

- **Quality factor:** The quality factor (Q- factor) is a dimensionless quantity which characterizes the temporal confinement of light in the cavity. The Q-factor of a cavity is the function of the total energy stored in the cavity ( $U$ ) and

the energy dissipated per cycle:

$$Q \equiv 2\pi \times \frac{\text{Energy Stored}}{\text{Energy Dissipated per Cycle}} = \omega_0 \times \frac{\text{Energy Stored}}{\text{Power Loss}} \quad (1.14)$$

The quality factor  $Q$  can be determined from the WGM spectrum as

$$Q = \frac{\omega_0}{\delta\omega} = \frac{\lambda_0}{\delta\lambda} \quad (1.15)$$

- **Photon lifetime:** For a WGM of frequency  $\omega_0$  (or vacuum wavelength  $\lambda_0$ ), the time dependence of the energy stored in the cavity is:

$$U(t) = U(t_0) e^{-\left(\frac{\omega_0}{Q}\right)t} = U(t_0) e^{-t/\tau_{ph}} \quad (1.16)$$

Where  $\tau_{ph} = \frac{Q}{\omega_0} = \frac{1}{\delta\omega}$  is the cavity photon lifetime defined as the time after which the energy is  $1/e$  of its original value, and where  $\delta\omega$  is the full width at half maximum (FWHM) of the WGM resonance in angular frequency units.

- **Optical losses:** There are two main loss mechanisms in WGM resonators, namely intrinsic and extrinsic losses. Intrinsic losses relate to the physical properties of the optical resonator such as curvature of the resonator, absorption by the resonator material, scattering at the resonator's surface, and any surface contamination on the resonator. Extrinsic losses are produced by the environment surrounding the resonator and are mainly due to the external power losses caused by the coupling to the tapered fiber (coupling loss). The final resulting Q-factor ( $Q_{load}$ ) is a sum of all of these components:

$$Q_{tot}^{-1} = Q_{in}^{-1} + Q_{ext}^{-1} = Q_{rad}^{-1} + Q_{abs}^{-1} + Q_{scatt}^{-1} + Q_{cont}^{-1} + Q_{ext}^{-1} \quad (1.17)$$

Here  $Q_{rad}$ ,  $Q_{abs}$ ,  $Q_{scatt}$ , and  $Q_{cont}$  are the radiation limited, material absorption limited, surface scattering limited and resonator contamination limited Q-factors. The size and the structure of the resonator play a role in determining the dominant loss mechanism. For example, in a smaller resonator the radiative

loss is the main loss factor while in the case of a larger resonator surface scattering and material absorption will dominate.

- **Free spectral range (FSR):** Free spectral range (FSR) is the distance between two successive resonant modes along the wavelength/frequency axis. FSR of the resonator is inversely proportional to the size of the resonator, which means that larger resonators have smaller FSRs and smaller resonators have larger FSRs. A simple approximation can be obtained for the FSR from the propagation constant and neglecting the wavelength dependency of the refractive index as follows:

$$\text{FSR} = \frac{\lambda^2}{Ln_{\text{eff}}} = \frac{\lambda^2}{2\pi Rn_{\text{eff}}} \quad (1.18)$$

Where  $\lambda$  is the central wavelength of the spectrum,  $R$  is the radius of the resonator, and  $n_{\text{eff}}$  is the effective refractive index of the resonator.

- **Finesse:** The light circulation time in the cavity normalized to one optical round trip is called the cavity finesse. The finesse is measured by the ratio of the WGM modes spacing (FSR) to the mode bandwidth (FWHM):

$$\text{Finesse } (F) = \frac{\text{FSR}}{\text{FWHM}} = \frac{\lambda Q}{2\pi n_{\text{eff}} R} \quad (1.19)$$

- **Mode Volume:** The spatial confinement of light in the cavity is termed as mode volume. A WGM optical microresonator can confine light in a low mode volume which results in high optical energy density inside the cavity. The mode volume,  $V$ , of a spherical microresonator is given by [1]:

$$V = 3.4\pi^{3/2} \left( \frac{\lambda}{2\pi n} \right)^3 l^{11/6} \sqrt{l-m+1} \quad (1.20)$$

Where  $\lambda$  is the wavelength of light and  $l$  is the azimuthal quantum number of the mode.

## 1.2 Research Motivation

As discussed in the above sections, cylindrical WGM micro-resonators have several potential advantages in sensing and tunable device applications. However, several existing gaps in knowledge currently prevent their wider use in practical devices.

One of such obstacles is the lack of simple and effective packaging method which would allow one to eliminate the need for bulky and expensive micro-positioning equipment which currently forms an integral part of WGM based devices in laboratory conditions, and to enable long term mechanical stability and reduced weight required for practical devices.

Development of the packaging method is linked to a number of related challenges. One of such challenges is the development of an efficient and robust light coupling method. While excitation of WGMs using evanescent field of a tapered fiber is a highly efficient method, commonly used in laboratory conditions, there is a lack of knowledge on how vibrations and taper angular misalignment, which are almost unavoidable during packaging, would affect the coupling conditions and mechanical stability of the device. Moreover, the influences of the tapered fiber shape and its waist diameter on the WGM spectrum of the cylindrical micro-resonator are other important issues that to date have mostly been studied theoretically, with only a few experimental works published to date.

Several earlier studies [84–92] suggested that the exceptional sensitivity of WGMs resonances to the shape and diameter of the micro-cylinder could be applied for measurement of optical fiber diameter variations during their fabrication. However, using this technique for geometrical profiling of thin microfiber tapers has not yet been fully explored and could become a powerful non-destructive tool



for monitoring and troubleshooting of fiber tapers fabrication and the characterisation of their asymmetries and geometrical profiles.

Numerous WGM strain sensors based on spherical and bubble micro-resonators made from silica and polymer materials have been proposed in the literature. However, practical applications of such sensors are limited due to the difficulties in maintaining the precise alignment between the resonator and the fiber taper, independent of applied strain and external vibrations. WGM strain sensors based on polymer optical fibers offer the advantages of higher sensitivity due to a lower young's modules and better mechanical stability compared to silica fiber based resonators and less rigid requirements to the alignment precision compared to spherical WGM sensors. Therefore, there is a need to explore the use of polymer micro-cylinders as the basis for novel high sensitivity WGM strain sensors and tunable devices.

In order to increase the tunable range of a device or sensitivity of a sensor to a specific parameter, WGM micro-resonators are often combined with various materials such as conjugated polymers, liquids *etc.* For this, liquid core optical ring resonator (LCORR) structures are particularly attractive since they can significantly simplify such integration of the solid resonator with liquids acting as transducers, for example, magnetic fluids or liquid crystals. For example, silica capillary tube based LCORRs for refractive index sensing [64,93–95] and bio sensing [96] have been proposed recently. The research presented in this thesis will focus on the development of thermo-optically tunable WGM devices and WGM magnetic field sensors utilising cylindrical capillary and photonic crystal fiber micro-resonators.

Finally, one of the key requirements to any WGM-based sensor or tunable device is the ability to effectively differentiate between the influence of the target physical parameter or control signal and the influences of various environmental factors such as temperature, humidity, etc. This requires some means to stabilize the operating conditions of the device or, alternatively, additional independent sensors for monitoring the environmental influences and elimination of environmental errors by calibration. Since introducing of such additional sensors increases the cost of the device, there is a growing interest in multi-parametric sensors, which can offer simultaneous measurement and detection of several parameters using a common interrogator.

Most of the WGM multi-parametric sensors proposed to date were realized as integrated photonic circuits or involved coupling of multiple resonators to a single fiber taper, where the former solution suffers from high cost and the latter from a limit on the number of resonators that could be coupled to the same taper without cross-coupling. Therefore, there is a need for a new multi-parameter sensor design and coupling approach capable of overcoming the above shortcomings.

### **1.3 Aim and objectives of the research**

In line with the motivation outlined in the previous section the core aim of the research presented in this thesis is:

**To investigate and address several key aspects related to the development of novel sensors and tunable devices based on cylindrical WGM micro-resonators with the intention of moving such structures closer to practical applications.**

The specific objectives of the research that seek to meet the above aim are as follows:

- Carry out an in-depth investigation of the WGMs effect in different types of cylindrical micro-resonators (including fiber-based, capillary and LCORR) in order to establish the influence of the resonator's geometry and coupling conditions on the resulting WGM spectrum.
- Develop novel applications of the WGM effect in cylindrical micro-resonators for non-destructive geometrical profiling of tapered optical fibers with submicron accuracy.
- Develop a simple and robust packaging method for practical WGM sensors and tunable devices.
- Explore the use of polymer fibers and polymer wires as the basis for novel high sensitivity WGM strain sensors and wide tunable range WGM tunable devices (e.g., tunable filters) and corresponding packaging techniques.
- Develop and demonstrate novel WGM magnetic field sensors and tunable thermo-optic devices based on cylindrical LCORR structures filled with magnetic fluids and liquid crystals.
- Develop and demonstrate a novel approach to coupling of multiple cylindrical micro-resonators for sensing of more than one parameter simultaneously.

## **1.4 Research Methodology**

This thesis is presented as a series of linked journal publications contained within the core chapters of the thesis. Given the requirements for journal papers, a description of the methodology may not always be presented. This section therefore provides a brief overview of the methodology employed in this research. The methodology employed throughout the research undertaken typically consisted of a sequence of steps as follows:

**1. Carrying out an in-depth analysis of the physical phenomenon using existing published knowledge as a foundation**

Such studies were undertaken a number of times over the course of the research, most frequently involving an investigation: a) of methods for excitation of WGMs in cylindrical micro-resonators, b) of dependence of the WGM spectrum on the diameter of the resonator considering relevant different geometries, c) of methods for enhancing the sensitivity of WGM sensors and d) of multi-parameter sensing with WGM resonators.

**2. Carrying out numerical simulations for predicting /verifying experimental results**

This involved the development of a Matlab based simulation platform to determine the position and the corresponding polarization state of WGM resonance modes within the transmission spectrum of a coupling fiber, modelling of the WGM spectrum of cylindrical micro-resonators using coupled mode theory, and analysis of the axial strain effect on the spectral positions of the WGM resonances. All numerical simulations were performed on a personal computer with Intel(R) Core (TM) i5-2450M CPU @ 2.50GHz, 8GB RAM, x64-based processor and a 64-bit OS.

**3. Utilizing and customizing existing techniques for fabrication of tapered optical fibers, cylindrical micro-resonators and LCORRs**

In this thesis several types of cylindrical micro-resonator structures were investigated, including tapered optical fibers with various waist diameters and shapes, cylindrical silica micro-resonators of various diameters, thin-walled silica capillary micro-resonators, and photonic crystal fiber resonators. This typically involved reducing the diameters of commercially available optical fibers or

capillaries by tapering using the customized microheater brushing technique described in [97], developed and available in-house.

Both laboratory samples and commercially available plastic optical fibers were used for the development of WGM based strain tunable/sensing devices. The polymer wire resonators were fabricated by heating and stretching of a polymethyl methacrylate (PMMA) rod to a diameter of 230  $\mu\text{m}$  at a temperature of 180°C.

Infiltration of the silica capillary and photonic crystal fiber resonators with liquid materials (commercial nematic liquid crystal MLC 7012 (Licrystal), laboratory-made ferronematic liquid crystal samples and commercial magnetic fluids from Cytodiagnostics Inc.) was carried out relying on capillary forces at normal atmospheric pressure or using a micro-syringe pump, with the choice dependent on the nature of the resonator.

#### **4. Experimental characterization of the micro-resonators, analysis of the data and comparison with the results of numerical modeling**

##### **a) WGM spectral characterization**

Schematic of a typical experimental setup for characterization of the WGM tunable devices and sensors is shown in Figure 7.

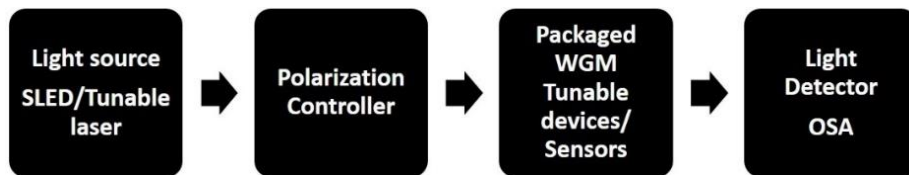


**Figure 7.** Block diagram of an experimental set-up to study the response of the fabricated WGM based sensors/tunable devices.

It consisted of a light source SLED (Thorlabs), an in-line fiber polarization controller (FPC 30, Thorlabs), connected to the input of the WGM device whose output is observed at the detector, an optical spectrum analyser (OSA,

86142B, Agilent) with a resolution of 10  $\mu\text{m}$ .

**b) Characterization of strain response**

A 25 mm long translation stage (PT1/M from Thorlabs, Inc) with 10  $\mu\text{m}$  resolution was used to apply different axial strains to the micro-cylinder samples. The applied strain value in each case was determined using the measured distance between two fixed ends of the sensor probe and the value of the elongation controlled by the translation stage. The minimum strain resolution thus depended on the resolution of the translation stage.

**c) Temperature control**

Temperature experiments were performed within the range from 25°C (room temperature) to 50°C in 1°C steps by placing the packaged device on a controlled hot stage. In some cases, the temperature was also decreased in 1°C steps back to room temperature. The hot stage temperature was measured by a thermocouple (Digital Scientific K-type Thermocouple Thermometer) with 0.1°C measurement resolution.

**d) Magnetic field control**

A rectangular permanent magnet with dimensions of 200"×0.5"×0.25" was used to generate a magnetic field for the characterization of a magnetic field sensor based on a photonic crystal fiber resonator. The magnetic field strength was controlled by changing the distance between the sensor fiber and the magnet. A Gaussmeter probe (RS, GM08) was used as a reference to measure the magnetic field strength in the vicinity of the sensor fiber.

## **1.5 Thesis layout**

This thesis consists of a series of six linked journal publications and a conference proceeding prepared within the duration of the PhD research period. All the above-

mentioned publications are first-author publications by the author of this thesis. As the research was carried out within a research group, there are several authors for each publication. A signed statement from all the co-authors is included in Appendix A, confirming that the first author undertook all aspects of the research described in each paper, including preparation and submission of the paper, with the support and advice of the co-authors. In addition, two second-author publications have been included in Chapter 4 along with the primary first-author paper due to the significant contributions by the author of this thesis toward the proposed sensor concepts and design of the experiments presented in these two second author publications, and due to the direct relevance of these papers to one of the thesis objectives.

**Chapter 1** is introduction chapter which provides the research background, motivation, research objectives and outlines the layout of the thesis.

**Chapter 2** presents the results of experimental studies on the excitation of WGM resonances in cylindrical micro-resonators made from commercial and tapered optical fibers with different diameters. The study also focuses on the influence of the resonator's tilt angle on the excitation of WGMs. A new method for geometrical profiling of optical fiber tapers and the detection of asymmetries in the fabricated thin microfiber tapers is also presented.

**Chapter 3** presents an investigation of the proposed strain-assisted technique for spectral tuning of WGMs in a polymer cylindrical micro-resonator. Axial tensile strain applied to a polymer micro-resonator results in a strong linear shift of the WGM spectrum allowing the design of highly sensitive strain sensors. Finally, a novel and robust packaging method for the WGM based devices is described and the performance of the packaged strain sensor is evaluated.

**Chapter 4** presents several novel tunable WGM devices and sensors based on LCORR structures incorporated with electro-optic and magneto-optic liquid materials. A novel nematic liquid crystal filled packaged capillary tube WGM device for temperature tuning applications is proposed and discussed along with two all fiber magnetic field sensors designed using magnetic fluid and ferronematic liquid crystals filled photonic crystal fiber micro-resonators.

**Chapter 5** proposes and demonstrates a novel design principle and fabrication method for creating multiple-resonator WGM arrays. The proposed design involves an inline cascade of optical micro-resonators (ICOMR) coupled to multiple tapered sections along a single optical fiber. The multi-resonators array can be used for multi-point sensing or sensing of more than one physical parameter simultaneously.

**Chapter 6** summarizes the main conclusions and key results of this thesis and presents a brief overview of possible future research directions.

Appendix B presents a related conference publication focusing on the investigation of excitation of WGMs in a spherical micro-resonator by a tapered optical fiber coupled under various excitation conditions.

## **1.6 References**

1. B. Matsko and V. S. Ilchenko, "Optical resonators with whispering-gallery modes - Part I: Basics," *IEEE J. Sel. Top. Quantum Electron.* **12**, 3–14 (2006).
2. M. Först, J. Niehusmann, T. Plötzing, J. Bolten, T. Wahlbrink, C. Moormann, and H. Kurz, "High-speed all-optical switching in ion-implanted silicon-on-insulator microring resonators," *Opt. Lett.* **32**, 2046–2048 (2007).
3. V. R. Almeida and M. Lipson, "Optical bistability on a silicon chip," *Opt. Lett.* **29**, 2387-2389 (2004).



4. Y. Dumeige and P. Féron, “Dispersive tristability in microring resonators,” *Phys. Rev. E.* **72**, 1–8 (2005).
5. P. Rabiei, W. H. Steier, C. Zhang, and L. R. Dalton, “Polymer micro-ring filters and modulators,” *J. Light. Technol.* **20**, 1968–1975 (2002).
6. Q. Xu, B. Schmidt, S. Pradhan, and M. Lipson, “Micrometre-scale silicon electro-optic modulator,” *Nature*, **435**, 325–327 (2005).
7. H. Tazawa, Y. H. Kuo, I. Dunayevskiy, J. Luo, A. K. Y. Jen, H. R. Fetterman, and W. H. Steier, “Ring resonator-based electrooptic polymer traveling-wave modulator,” *J. Light. Technol.* **24**, 3514–3519 (2006).
8. T. A. Ibrahim, K. Amarnath, L. C. Kuo, R. Grover, V. Van, and P.-T. Ho, “Photonic logic NOR gate based on two symmetric microring resonators,” *Opt. Lett.* **29**, 2779-2781 (2004).
9. T. A. Ibrahim, R. Grover, L.-C. Kuo, S. Kanakaraju, L. C. Calhoun, and P.-T. Ho, “All-optical AND/NAND logic gates using semiconductor microresonators,” *IEEE Photon. Technol. Lett.* **15**, 1422–1424 (2003).
10. V. Van, T. A. Ibrahim, P. P. Absil, F. G. Johnson, R. Grover, and P.-T. Ho, “Optical signal processing using nonlinear semiconductor microring resonators,” *IEEE J. Sel. Top. Quantum Electron.* **8**, 705–713 (2002).
11. Y. Chao and L. J. Guo, “Biochemical sensors based on polymer microrings with sharp asymmetrical resonance,” *Appl. Phys. Lett.* **83**, 1527–1529 (2003).
12. A. Yalçın, K. C. Papat, J. C. Aldridge, T. A. Desai, J. Hryniewicz, N. Chbouki, B. E. Little, O. King, V. Van, S. Chu, D. Gill, M. Anthes-Washburn, M. S. Ünlü, and B. B. Goldberg, “Optical sensing of biomolecules using microring resonators,” *IEEE J. Sel. Top. Quantum Electron.* **12**, 148–154 (2006).

13. K. De Vos, I. Bartolozzi, E. Schacht, P. Bienstman, and R. Baets, "Silicon-on-Insulator microring resonator for sensitive and label-free biosensing," *Opt. Express*, **15**, 7610-7615 (2007).
14. J. K. S. Poon, J. Scheuer, Y. Xu, and A. Yariv, "Designing coupled-resonator optical waveguide delay lines," *J. Opt. Soc. Am. B* **21**, 1665-1673 (2004).
15. F. Xia, L. Sekaric, and Y. Vlasov, "Ultracompact optical buffers on a silicon chip," *Nat. Photonics*, **1**, 65–71 (2007).
16. F. Morichetti, A. Melloni, A. Breda, A. Canciamilla, C. Ferrari, and M. Martinelli, "A reconfigurable architecture for continuously variable optical slow-wave delay lines," *Opt. Express*, **15**, 17273–17282 (2007).
17. A. Melloni, F. Morichetti, C. Ferrari, and M. Martinelli, "Continuously tunable 1-byte delay in coupled-resonator optical waveguides," *Opt. Lett.* **33**, 2389–2391 (2008).
18. F. Morichetti, A. Melloni, C. Ferrari, and M. Martinelli, "Error-free continuously-tunable delay at 10 Gbit/s in a reconfigurable on-chip delay-line," *Opt. Express*, **16**, 8395–8405 (2008).
19. J. B. Khurgin, "Optical buffers based on slow light in electromagnetically induced transparent media and coupled resonator structures: comparative analysis," *J. Opt. Soc. Am. B* **22**, 1062-1074 (2005).
20. L. Yosef Mario and M. K. Chin, "Optical buffer with higher delay-bandwidth product in a two-ring system," *Opt. Express*, **16**, 1796-1807 (2008).
21. J. V. Hryniewicz, P. P. Absil, B. E. Little, R. A. Wilson, and P. T. Ho, "Higher order filter response in coupled microring resonators," *IEEE Photonics Technol. Lett.* **12**, 320-322 (2000).

22. A. Melloni, "Synthesis of a parallel-coupled ring-resonator filter," *Opt. Lett.* **26**, 917–919 (2001).
23. A. E. Little, S. T. Chu, P. P. Absil, J. V. Hryniewicz, F. G. Johnson, F. Seiferth, D. Gill, V. Van, O. King, and M. Trakalo, "Very high-order microring resonator filters the WDM applications," *IEEE Photonics Technol. Lett.* **16**, 2263–2265 (2004).
24. T. Barwicz, M. A. Popović, M. R. Watts, P. T. Rakich, E. P. Ippen, and H. I. Smith, "Fabrication of Add-Drop filters based on frequency-matched microring resonators," *J. Light. Technol.* **24**, 2207- (2006).
25. F. Xia, M. Rooks, L. Sekaric, and Y. Vlasov, "Ultra-compact high order ring resonator filters using submicron silicon photonic wires for on-chip optical interconnects," *Opt. Express*, **15**, 11934-11941 (2007).
26. L. Y. M. Tobing, P. Dumon, R. Baets, and M.-K. Chin, "Boxlike filter response based on complementary photonic bandgaps in two-dimensional microresonator arrays," *Opt. Lett.* **33**, 2512–2514 (2008).
27. L. Yang, T. Carmon, B. Min, S. M. Spillane, and K. J. Vahala, "Erbium-doped and Raman microlasers on a silicon chip fabricated by the sol-gel process," *Appl. Phys. Lett.* **86**, 1–3 (2005).
28. L. Yang, D. K. Armani, and K. J. Vahala, "Fiber-coupled erbium microlasers on a chip," *Appl. Phys. Lett.* **83**, 825–826 (2003).
29. H. B. Lin, A. J. Campillo, "CW nonlinear optics in droplet microcavities displaying enhanced gain," *Phys. Rev. Lett.* **73**, 2440–2443 (1994).
30. T. J. Kippenberg, S. M. Spillane, D. K. Armani, and K. J. Vahala, "Ultralow-threshold microcavity Raman laser on a microelectronic chip," *Opt. Lett.* **29**, 1224-1226 (2004).

31. B. Min, L. Yang, and K. Vahala, “Controlled transition between parametric and Raman oscillations in ultrahigh- Q silica toroidal microcavities,” *Appl. Phys. Lett.* **87**, 181109 (2005).
32. S. M. Spillane, S. M. Spillane, T. J. Kippenberg, T. J. Kippenberg, and K. J. Vahala, “Ultralow-threshold Raman laser using a spherical dielectric microcavity,” *Nature*, **415**, 621–623 (2002).
33. J. Vučković and Y. Yamamoto, “Photonic crystal microcavities for cavity quantum electrodynamics with a single quantum dot,” *Appl. Phys. Lett.* **82**, 2374–2376 (2003).
34. Y. F. Xiao, C. L. Zou, P. Xue, L. Xiao, Y. Li, C. H. Dong, Z. F. Han, and Q. Gong, “Quantum electrodynamics in a whispering-gallery microcavity coated with a polymer nanolayer,” *Phys. Rev. A*. **81**, 053807 (2010).
35. G. Mie, “Beitrage zur optic triiber medien, speziell kolloidaler metallosungen,” *Ann. Phys.* **330**, 377–445 (1908).
36. G. C. Righini and S. Soria, “Biosensing by WGM microspherical resonators,” *Sensors (Switzerland)* **16**, 1–25 (2016).
37. F. Vollmer and S. Arnold, “Whispering-gallery-mode biosensing: Label-free detection down to single molecules,” *Nat. Methods*, **5**, 591–596 (2008).
38. M. Hossein-Zadeh and K. J. Vahala, “Fiber-taper coupling to Whispering-Gallery modes of fluidic resonators embedded in a liquid medium,” *Opt. Express*, **14**, 10800-10810 (2006).
39. T. Reynolds, N. Riesen, A. Meldrum, X. Fan, J. M. M. Hall, T. M. Monro, and A. François, “Fluorescent and lasing whispering gallery mode microresonators for sensing applications,” *Laser Photonics Rev.* **11**, 1–20 (2017).

40. W. Vernooy, V. S. Ilchenko, H. Mabuchi, E. W. Streed, and H. J. Kimble, “High-Q measurements of fused-silica microspheres in the near infrared,” *Opt. Lett.* **23**, 247-249 (1998).
41. M. Soltani, S. Yegnanarayanan, and A. Adibi, “Ultra-high Q planar silicon microdisk resonators for chip-scale silicon photonics,” *Opt. Express*, **15**, 4694-4704 (2007).
42. K. Armani, T. J. Kippenberg, S. M. Spillane, and K. J. Vahala, “Ultra-high-Q toroid microcavity on a chip,” *Nature*, **421**, 925–928 (2003).
43. Q. Xu, D. Fattal, and R. G. Beausoleil, “Silicon microring resonators with 1.5- $\mu\text{m}$  radius,” *Opt. Express*, **16**, 4309-4315 (2008).
44. X. Jin, Y. Dong, and K. Wang, “Selective excitation of axial modes in a high-Q microcylindrical resonator for controlled and robust coupling,” *Appl. Opt.* **54**, 8100-8107 (2015).
45. J. M. Ward, Y. Yang, and S. N. Chormaic, “Highly Sensitive temperature measurements with liquid-core microbubble resonators,” *IEEE Photon. Technol. Lett.* **25**, 2350–2353 (2013).
46. M. Fujii, M. Haraguchi, T. Okamoto, and M. Fukui, “Characteristics of whispering gallery modes in single dielectric spheroid excited by Gaussian beam,” *Japanese J. Appl. Physics*, **44**, 4948–4955 (2005).
47. A. Ahmed, R. Koya, O. Wada, M. Wand, and R. Koga, “Field Analysis of pillbox resonator with radiation loss utilizing finite-element beam propagation method formulation,” *Opt. Rev.* **3**, 109–113 (1996).
48. V. M. N. Passaro and G. Z. Mashanovich, “Investigation of coupling conditions in microgear resonators,” *Opt. Express*, **15**, 998–1005 (2007).

49. A. B. Matsko, A. A. Savchenkov, and L. Maleki, “Vertically coupled whispering-gallery-mode resonator waveguide,” *Opt. Lett.* **30**, 3066–3068 (2005).
50. M. Sumetsky, “Whispering gallery modes in a microfiber coil with an n-fold helical symmetry: classical dynamics, stochasticity, long period gratings, and wave parametric resonance,” *Opt. Express*, **18**, 2413–2425 (2010).
51. X. Sun, K. Y. Fong, C. Xiong, W. H. P. Pernice, and H. X. Tang, “GHz optomechanical resonators with high mechanical Q factor in air,” *Opt. Express*, **19**, 22316–22321 (2011).
52. Y. L. Shang, M. Y. Ye, and X.-M. Lin, “Experimental observation of Fano-like resonance in a whispering-gallery-mode microresonator in aqueous environment,” *Photonics Res.* **5**, 119–123 (2017).
53. A. K. Mallik, D. Liu, V. Kavungal, Q. Wu, G. Farrell, and Y. Semenova, “Agarose coated spherical micro resonator for humidity measurements,” *Opt. Express*, **24**, 21216–21227 (2016).
54. S. Krämmer, S. Rastjoo, T. Siegle, S. F. Wondimu, C. Klusmann, C. Koos, and H. Kalt, “Size-optimized polymeric whispering gallery mode lasers with enhanced sensing performance,” *Opt. Express*, **25**, 7884–7894 (2017).
55. Q. Hua, C. Yang, X. Jiang, M. Xiao, and A. S. Preparation, “High-order filters based on three high- Q microtoroid cavities,” in 2017 Opto-Electronics and Communications Conference (OECC) and Photonics Global Conference (PGC) (IEEE Xplore), pp. 2–3.
56. M. Mariano, F. J. Rodríguez, P. Romero-Gomez, G. Kozyreff, and J. Martorell, “Light coupling into the Whispering Gallery Modes of a fiber array thin film solar cell for fixed partial Sun tracking,” *Sci. Rep.* **4**, 4959 (2014).

57. M. Sumetsky, "Mode localization and the Q-factor of a cylindrical microresonator," *Opt. Lett.* **35**, 2385-2387 (2010).
58. A. W. Poon, R. K. Chang, and J. A. Lock, "Spiral morphology-dependent resonances in an optical fiber: effects of fiber tilt and focused Gaussian beam illumination," *Opt. Lett.* **23**, 1105–1107 (1998).
59. M. White, H. Oveys, and X. Fan, "Liquid-core optical ring-resonator sensors," *Opt. Lett.* **31**, 1319-1321 (2006).
60. N. Oraevsky, "Whispering-gallery waves," *Quantum Electron.* **32**, 377–400 (2002).
61. Y. V. Prokopenko, Y. F. Filippov, and I. A. Shipilova, "Distribution of the field of whispering-gallery modes in a radially nonuniform two-layer cylindrical dielectric resonator," *Radiophys. Quantum Electron.* **51**, 561–570 (2008).
62. R. Yang, A. Yun, Y. Zhang, and X. Pu, "Quantum theory of whispering gallery modes in a cylindrical optical microcavity," *Optik (Stuttg.)* **122**, 900–909 (2011).
63. N. Okada and J. Cole, "Simulation of whispering gallery modes in the Mie regime using the nonstandard finite-difference time domain algorithm," *J. Opt. Soc. Am. B.* **27**, 631–639 (2010).
64. N. Lin, L. Jiang, S. Wang, H. Xiao, Y. Lu, and H.-L. Tsai, "Design and optimization of liquid core optical ring resonator for refractive index sensing," *Appl. Opt.* **50**, 3615-3621 (2011).
65. A. Meldrum and F. Marsiglio, "Capillary-type microfluidic sensors based on optical whispering gallery mode resonances," *Rev. Nanosci. Nanotechnol.* **3**, 193–209 (2014).

66. A. E. Little, J. P. Laine, and H. A. Haus, “Analytic theory of coupling from tapered fibers and half-blocks into microsphere resonators,” *J. Lightwave Technol.* **17**, 704–715 (1999).
67. A. J. W. Klunder, M. L. M. Balistreri, F. C. Blom, H. J. W. M. Hoekstra, A. Driessen, L. Kuipers, and N. F. Van Hulst, “High-resolution photon-scanning tunneling microscope measurements of the whispering gallery modes in a cylindrical microresonator,” *IEEE Photonics Technol. Lett.* **12**, 1531–1533 (2000).
68. A. J. W. Klunder, M. L. M. Balistreri, F. C. Blom, H. J. W. M. Hoekstra, A. Driessen, L. Kuipers, and N. F. Van Hulst, “Detailed analysis of the intracavity phenomena inside a cylindrical microresonator,” *J. Light. Technol.* **20**, 519–529 (2002).
69. M. L. M. Balistreri, D. J. W. Klunder, F. C. Blom, A. Driessen, H. W. J. M. Hoekstra, J. P. Korterik, L. Kuipers, and N. F. van Hulst, “Visualizing the whispering gallery modes in a cylindrical optical microcavity,” *Opt. Lett.* **24**, 1829–1831 (1999).
70. M. L. M. Balistreri, D. J. W. Klunder, F. C. Blom, A. Driessen, J. P. Korterik, L. Kuipers, and N. F. Van HULST, “Experimental analysis of the whispering-gallery modes in a cylindrical optical microcavity,” *J. Opt. Soc. Am. B.* **18**, 465–471 (2001).
71. A. Lock, “Morphology-dependent resonances of an infinitely long circular cylinder illuminated by a diagonally incident plane wave or a focused Gaussian beam,” *J. Opt. Soc. Am. A.* **4**, 653–661 (1997).



72. G. Guimaraes and J. P. R. Furtado de Mendonca, "Analysis of the resonant scattering of light by cylinders at oblique incidence," *Appl. Opt.* **36**, 8010-8019 (1997).
73. J. A. Lock, "Scattering of a diagonally incident focused gaussian beam by an infinitely long homogeneous circular cylinder," *J. Opt. Soc. Am. A.* **14**, 653–661 (1997).
74. J. C. Knight, G. Cheung, F. Jacques, and T. A. Birks, "Phase-matched excitation of whispering-gallery-mode resonances by a fiber taper," *Opt. Lett.* **22**, 1129-1131 (1997).
75. G. Adamovsky and S. Wrbanek, "Coupling of low-order LP modes propagating in cylindrical waveguides into whispering gallery modes in microspheres," *Opt. Express*, **21**, 2279–2286 (2013).
76. N. Dubreuil, J. C. Knight, D. K. Leventhal, V. Sandoghdar, J. Hare, and V. Lefevre, "Eroded monomode optical fiber for whispering-gallery mode excitation in fused-silica microspheres," *Opt. Lett.* **20**, 813–815 (1995).
77. J. S. W. and M. N. Z. G. S. Murugan, "Selective excitation of whispering gallery modes in a novel bottle microresonator," *Opt. Express*, **17**, 11916–11925 (2009).
78. Y. Le Pan and R. K. Chang, "Highly efficient prism coupling to whispering gallery modes of a square  $\mu$  cavity," *Appl. Phys. Lett.* **82**, 487–489 (2003).
79. V. S. Ilchenko, X. S. Yao, and L. Maleki, "Pigtailling the high-Q microsphere cavity: a simple fiber coupler for optical whispering-gallery modes," *Opt. Lett.* **24**, 723–725 (1999).

80. J. C. Knight, G. Cheung, F. Jacques, and T. A. Birks, "Phase-matched excitation of whispering-gallery-mode resonances by a fiber taper," *Opt. Lett.* **22**, 1129-1131 (1997).
81. M. Cai, O. Painter, and K. J. Vahala, "Observation of critical coupling in a fiber taper to a silica-microsphere whispering-gallery mode system," *Phys. Rev. Lett.* **85**, 74-77 (2000).
82. T. A. Birks and Y. W. Li, "The shape of fiber tapers," *J. Light. Technol.* **10**, 432-438 (1992).
83. A. Yariv, "Universal relations for coupling of optical power between microresonators and dielectric waveguides," *Electron. Lett.* **36**, 321-322 (2000).
84. D. H. Smithgall, L. S. Watkins, and R. E. Frazee, Jr, "High-speed noncontact fiber-diameter measurement using forward light scattering," *Appl. Opt.* **16**, 2395-2402 (1977).
85. B. van der Mark and L. Bosselaar, "Noncontact Calibration of Optical Fiber Cladding Diameter Using Exact Scattering Theory," *J. Light. Technol.* **12**, 1-5 (1994).
86. J. F. Owen, P. W. Barber, B. J. Messinger, and R. K. Chang, "Determination of optical-fiber diameter from resonances in the elastic scattering spectrum," *Opt. Lett.* **6**, 272-274 (1981).
87. M. Young, P. D. Hale, and S. E. Mechels, "Optical Fiber geometry: Accurate measurement of cladding diameter," *J. Res. Natl. Inst. Stand. Technol.* **98**, 203-216 (1993).

88. F. Warken and H. Giessen, “Fast profile measurement of micrometer-sized tapered fibers with better than 50-nm accuracy,” *Opt. Lett.* **29**, 1727-1729 (2004).
89. A. W. Poon, R. K. Chang, and D. Q. Chowdhury, “Measurement of fiber-cladding diameter uniformity by use of whispering-gallery modes: nanometer resolution in diameter variations along millimeter to centimeter lengths,” *Opt. Lett.* **26**, 1867–1869 (2001).
90. T. A. Birks, J. C. Knight, and T. E. Dimmick, “High-resolution measurement of the fiber diameter variations using whispering gallery modes and no optical alignment,” *IEEE Photonics Technol. Lett.* **12**, 182–183 (2000).
91. A. Boleininger, T. Lake, S. Hami, and C. Vallance, “Whispering gallery modes in standard optical fibres for fibre profiling measurements and sensing of unlabelled chemical species,” *Sensors*, **10**, 1765–1781 (2010).
92. M. Sumetsky and Y. Dulashko, “Radius variation of optical fibers with angstrom accuracy,” *Opt. Lett.* **35**, 4006–4008 (2010).
93. D. C. Kim and R. C. Dunn, “Integrating whispering gallery mode refractive index sensing with capillary electrophoresis separations using phase sensitive detection,” *Anal. Chem.* **88**, 1426–1433 (2016).
94. S. Lane, F. Marsiglio, Y. Zhi, and A. Meldrum, “Refractometric sensitivity and thermal stabilization of fluorescent core microcapillary sensors: theory and experiment,” *Appl. Opt.* **54**, 1331 (2015).
95. T. Ling and L. J. Guo, “A unique resonance mode observed in a prism-coupled micro-tube resonator sensor with superior index sensitivity,” *Opt. Express*, **15**, 17424–17432 (2007).

96. H. Zhu, I. M. White, J. D. Suter, P. S. Dale, and X. Fan, “Analysis of biomolecule detection with optofluidic ring resonator sensors,” *Opt. Express*, **15**, 9139–9146 (2007).
97. L. Bo, “Tapered optical microfibre based structures for sensing applications,” Ph. D. Thesis, Dublin institute of Technology (2015).

## Chapter 2

---

---

### **Excitation of WGMs from silica fiber based cylindrical microresonators and its application in geometrical profiling**

---

---

The primary aim of the research in this thesis is to study the WGM effect in cylindrical micro-resonators for applications in novel sensors and optical tunable devices with the particular focus on the practical aspects of their design and fabrication. This chapter contributes to achieving this aim by presenting and analysing the results of experimental studies of WGMs in silica fiber micro-cylinders. Silica fiber micro-resonators with different diameters are investigated to establish the influence of the micro-cylinder's diameter on the properties of WGMs, such as their quality factor and free spectral range. The chapter also investigates the optimum conditions for effective excitation of WGMs in such resonators, including the optimal tapered fiber diameter and the influence of its tilt angle with respect to the micro-resonator on achieving good quality WGM spectra. This study underpins the basic techniques for excitation of WGMs in a variety of cylindrical micro-resonators types considered in the following chapters.

Utilizing the established relationship between the micro-cylinders' diameters and properties of WGMs as a foundation, this chapter also proposes and demonstrates a new technique for geometrical profiling of thin microfiber tapers. As a demonstration of the proposed method, samples of tapered optical fibers with

different waist diameters and shapes are fabricated and profiled using both the WGM spectroscopy and scanning electron microscope imaging confirming the accuracy of the proposed method. The new WGM profiling method is a promising non-destructive tool for monitoring and troubleshooting of fiber taper during fabrication, and subsequently characterisation of their asymmetries and geometrical profiles.

## **2.1 A comprehensive experimental study of whispering gallery modes in a cylindrical micro-resonator excited by a tilted fiber taper<sup>1</sup>**

**Abstract:** Whispering gallery modes (WGMs) excitation in a cylindrical micro-resonator formed by a section of silica optical fiber has been studied. Evanescent light coupling into the micro-resonator is realized using a tapered optical fiber, fabricated by a micro-heater brushing technique. Several types of silica fibers with different diameters are studied as micro-resonators, and the influence of the resonator's diameter on the excitation of WGMs is investigated. The excitation of WGMs in a cylindrical fiber resonator were studied with changes to the tilt angle between the micro-cylinder and the fiber taper in the range of angles from a perpendicular position ( $0^0$ ) to large tilt angles ( $24^0$ ). The evolution of the fiber taper transmission spectrum with the change of the tilt angle results in changes in the intensity, broadening of and a blue shift in the WGM resonance spectra. Overall

---

<sup>1</sup> V. Kavungal, G. Farrell, Q. Wu, A. K. Mallik and Y. Semenova, "A comprehensive experimental study of whispering gallery modes in a cylindrical micro-resonator excited by a tilted fiber taper," *Microwave and Optical Technology Letters*, **60**, 1495-1504 (2018).

losses in the taper transmission spectrum decrease with the increase of the taper tilt angle from its perpendicular position, followed by a complete disappearance of the WGM resonances at large tilt angles greater than  $20^\circ$ .

**Keywords:** Whispering gallery modes; Tapered fiber; Microcavities; Optical microresonators; Fiber optic sensors.

### **2.1.1 Introduction**

Whispering gallery modes (WGMs) are electromagnetic surface oscillations formed in dielectric micro resonators with a circular structure such as spheres, cylinders or disks. WGMs arise as a result of trapping of light within the micro-resonator by total internal reflections from the resonator's curved surface. Such reflections force the light to take on a polygonal path within the curved structure, effectively confining its energy to a very small volume.

Optical micro-resonators supporting WGMs are attractive photonic devices due to their small mode volumes, very high power densities, narrow spectral linewidths and high  $Q$  factors. Such micro-resonators have been shown to have potential use in many areas, including studies of nonlinear optical effects and quantum electrodynamics, low threshold micro-lasers and very sensitive micro-sensors. WGMs can be supported by a variety of resonator geometries and the choice of the particular resonator for a given application is usually influenced by three major factors: the achievable value of the  $Q$ -factor; ease of fabrication and ease of integration [1–4]. The most common micro resonators are spherical; they are relatively easy to fabricate and usually have very high  $Q$ -factors:  $\sim 10^9$  at  $1.55 \mu\text{m}$  for silica [5] and  $\sim 10^5$  at  $1.55 \mu\text{m}$  for chalcogenide glass [6].

Cylindrical WGM resonators have the disadvantage that due to the longitudinal degree of freedom in such structures a coupled beam can spread along the cylinder length and eventually vanish even if there is no material loss. However, Sumetsky *et al.* [7] theoretically reported an infinitely long cylindrical micro-resonator with its Q-factor as high as that of spherical and spheroid counterparts.

There are a number of potential advantages that make fiber-based cylindrical resonators worth exploring. Some of these have been pointed out previously by Farca *et al.* [8]: optical fibers are highly uniform in diameter, allowing large numbers of identical resonators to be fabricated easily and providing a high degree of repeatability; fiber micro cylinders are easy to handle, and the alignment for optimal coupling of the excitation light into the fiber resonator depends on only one angular degree of freedom, as opposed to two for experiments involving microspheres. Due to this the optical setup for fiber-based experiments is more straightforward. Moreover, previously reported experiments showed that micro-cylindrical resonators demonstrate narrow peaks for both the microfiber taper/micro-cylinder configuration [9] and for free Gaussian beam scattering [10]. The authors in [11–13] demonstrated that excitation of WGMs in cylindrical fiber resonators can be applied to high-resolution measurements of the fiber diameter variations. More recently, authors in [14] reported a tunable high Q-factor cylindrical micro resonator based on a tapered silica micro-fiber.

There are several methods of light coupling in and out of a WGM resonator that includes free space coupling and guided wave coupling. In free space coupling WGMs are excited using focused laser pump to the resonator and the transmitted light is collected using a collimator to a detector [15–17]. In guided wave coupling, the most commonly used method is based on evanescent-wave coupling



either from an adjacent guiding structure such as a tapered optical fiber coupler, a polished fiber half block coupler [18,19] or a channel waveguide coupler [20], and coupling under frustrated total internal reflections such as a prism [21] or an angle-polished fiber [22]. Among them tapered fiber is an excellent and easy to align coupling approach with a demonstrated ultra-high coupling efficiency of up to 99% [23]. The phase matching condition in the tapered fiber coupling can also be controlled by the diameter of the taper and the gap between the fiber taper and the resonator [24].

In order to maintain stable coupling conditions and to protect the micro resonator-tapered fiber system from environmental perturbations many techniques have been developed. These include packaging of the resonator-coupler system with a low refractive index UV curable [6,25–27] and moisture curable [28] polymer glue, fabrication of silica side walls close to the resonator for mechanical support of the tapered fiber [27–29] and the use of special resonator shapes such as an inverted wedge silica resonator [29] and an octagonal silica toroid [30]. Maintaining perfect alignment of the light coupling tapered optical fiber and the micro-resonator during packaging is a challenging task since perturbations can lead to a misalignment or tilting of the tapered fiber with respect to the resonator.

Tilting, where the cylindrical micro-resonator is not perpendicular to the coupling fiber, has an effect on WGM excitation in a cylindrical micro-resonator. This was studied by J. A. Lock *et al.* [31,32] and A. W. Poon *et al.* [10]. In their experiments, spiral morphology dependent resonances in an optical fiber were excited by elastic scattering of both focused and unfocused laser beams on a tilted optical fiber with small angles from perpendicular to the incident beam propagation directions. A. Boleininger *et al.* [13] reported an investigation of tilting effect of cylindrical

micro-resonator on the excitation of WGMs by the evanescent field of a tapered optical fiber. However, in their work the range of tilt angles of the micro-resonator with respect to the perpendicular position of the tapered fiber was limited to  $13^\circ$  and several significant aspects of tilting, such as its influence on the overall transmission losses and resonance wavelength shift were not considered.

To the best of our knowledge this work is the first comprehensive experimental investigation of the influence of the fiber taper tilt on the excitation of WGMs in a fiber cylindrical micro-resonator. We report on changes in the evolution of the WGM transmission spectrum of the tapered fiber with the increase of the tilt angle between the fiber resonator and the taper in the range of tilt angles from the perpendicular position of the taper ( $0^\circ$ ) to  $60^\circ$  tilt angle and analyze the influence of the tilt on the spectral positions of the WGM resonances and the effect of tilting on light transmission in the taper.

In addition, we investigate and analyze the optimum fiber taper waist diameter to achieve the most efficient light coupling into the micro-resonator and the influence of the resonator radius on the parameters of the WGM spectrum, such as Q-factor and the free spectral range.

### **2.1.2 Properties of WGM resonances**

WGM resonances excited in the cylindrical cavity can be characterized by their quality factor (Q), a figure of merit generally used to describe all kinds of resonators. In our case the WGM resonant modes are formed in the transmission spectrum of the tapered fiber due to the destructive interference between the light propagating in the tapered fiber and the light circulating inside the cylindrical cavity. The transmission spectrum of the fiber taper typically displays a periodic pattern of Lorentzian dips corresponding to the WGM resonances. The separation

of successive resonances is referred as the free spectral range (FSR).

A simple approximation can be obtained for the FSR from the propagation constant, starting with [33,34]

$$\frac{\partial\beta}{\partial\lambda} = \frac{-\beta}{\lambda} + k \frac{\partial n_{\text{eff}}}{\partial\lambda} \quad (2.1)$$

Neglecting the wavelength dependency of the refractive index [33] yields

$$\frac{\partial\beta}{\partial\lambda} = \frac{-\beta}{\lambda} + \frac{2\pi}{\lambda} \frac{\partial n_{\text{eff}}}{\partial\lambda} \approx \frac{-\beta}{\lambda} \quad (2.2)$$

The FSR of the resonator is then given by the equation:

$$\text{FSR} = \frac{-2\pi}{L} \left( \frac{\partial\beta}{\partial\lambda} \right)^{-1} = \frac{-2\pi}{L} \left( \frac{-\lambda}{\beta} \right) \approx \frac{\lambda^2}{n_{\text{eff}} L} \quad (2.3)$$

Where  $L$  is the circumference of the resonator. Thus, the FSR is given by:

$$\text{FSR} = \frac{\lambda^2}{2\pi R_{\text{eff}} n_{\text{eff}}} \quad (2.4)$$

From this approximate relationship between the FSR and the radius of the resonator, it is clear that the WGMs spectral spacing decreases with an increase of the resonator radius and thus a larger cavity can accommodate a higher number of modes. The WGMs spectral positions follow a simple approximation:

$$\lambda_m = \frac{2\pi R n}{m} \quad (2.5)$$

Where  $R$  is the radius of the resonator,  $n$  is the refractive index of the resonator,  $\lambda_m$  is the resonance wavelength and  $m$  is the integer called the azimuthal mode number. This approximation is more accurate when the path taken by the light is close to a circle, which is true for larger radius resonators. This is because, based on a ray optics model, the total internal reflection path around the curved surface is polygonal in nature, so the true path taken by the light is slightly shorter than

the circumference of the resonator and thus the resonance wavelength is slightly shorter than the predicted by the Eq. (2.5) value [13].

Using a wave optics model one can get more accurate values for the resonance wavelength by solving the respective eigenvalue equation inside the cavity. WGMs in a cylindrical cavity are defined by three mode numbers: the radial mode number ( $l$ ), the azimuthal mode number ( $m$ ) and the slab mode number ( $p$ ). For a WGM with a mode number  $m$  there are  $2m$  field maxima around the circumference of the cylinder (cylinder azimuth),  $(l-1)$  nodes along the radial coordinate of the cylinder and  $p$  nodes along the axis of the cylinder [13].

As stated above, the azimuthal mode number ( $m$ ) is related to the number of field maxima distributed along the circumference of the resonator, so for a larger cylinder radius the azimuthal number of the resonant modes increases but this also leads to a reduction of the spectral spacing between the WGM resonances. Spectra with well separated WGMs are desirable for sensing applications, since in this case spectral shifts are easier to discern. Thus, for example, the authors in [35,36] increased the FSRs of their sensors by reducing the diameter of the sensor structures.

The sharpness of the WGM spectral dips greatly impacts the resolution of sensors based on WGM micro-resonators, since a sharper peak allows for the detection of smaller spectral shifts in the resonance wavelength. This sharpness can be characterized by the value of Q-factor of the micro-resonator. The Q-factor is a dimensionless parameter related to loss of energy in an oscillatory system. It is defined as the ratio of the central resonance wavelength ( $\lambda_m$ ) to the full width at half depth ( $\Delta\lambda_m$ ) of the same resonance:

$$Q = \frac{\lambda_m}{\Delta\lambda_m} \quad (2.6)$$

In an resonant optical structure, the Q-factor is proportional to the decay time of the mode, which in turn is inversely related to the sum of losses from the various loss mechanisms. The quality factor in WGM resonators is limited by various factors such as intrinsic radiative (curvature) losses, scattering losses due to residual surface inhomogeneities, losses due to surface contaminants and material losses [37]. When WGMs in a resonator are excited using a tapered fiber in contact with the resonator, the corresponding Q- factor is referred to as a loaded Q-factor. Due to physical contact of the fiber taper, coupling will cause additional losses in the resonator. The unloaded or intrinsic Q-factor of the resonator is the Q-factor calculated in the absence of coupling losses. The loaded Q-factor is always smaller than the unloaded Q-factor [34].

### 2.1.3 Experimental arrangement, results, and discussion

#### a) Fabrication of tapered optical fibers

Light propagation inside a standard optical fiber with a diameter greater than the propagating light wavelength is guided by total internal reflection and the light is localized inside the core. When light hits the interface between the core and cladding layers, a small portion of the light energy infiltrates the cladding as an evanescent field that exponentially decays into the cladding region. The penetration depth of the evanescent field into the cladding is given by the formula [38]

$$d_p = \frac{\lambda}{2\pi(n_1^2 \sin^2 \theta - n_2^2)^{1/2}} \quad (2.7)$$

Where  $\lambda$  is the wavelength of light and  $n_1$  and  $n_2$  are the refractive indices of the core and cladding respectively.  $\theta$  is the incident angle measured from the normal at the interface of the core and cladding. The reflected beam from the interface is returned to the core with a phase shift along its axial propagation direction.

When the diameter of the optical fibre is greatly reduced to a micron scale by tapering, the original boundary between the fibre core and cladding at the waist region is no longer significant. The refractive index contrast between the core and cladding becomes very small. In this case, an optical micro-fiber can be considered as a cylindrical waveguide with a homogeneous refractive index profile. In a thin fiber taper light is guided by the total internal reflection at the cladding-air interface (if the surrounding medium is air). Under these conditions a significant portion of light propagates outside of the microfiber. The presence of a large evanescent field outside of the tapered portion of the fiber can be used for coupling the light into another fiber acting as the micro-cylinder by placing both fibers in direct physical contact.

The optical properties of the tapered micro-fibers strongly depend on the geometry of both their transition and waist regions. If the tapering process is carried out in such a way that the fiber diameter within its transition region changes smoothly and can be adiabatically slow as a function of fiber length, the taper is considered adiabatic. This condition ensures low transmission loss and small inter-mode coupling. In our experiments, we used adiabatic tapers for excitation of WGMs from cylindrical micro-resonators [39,40].

The fiber taper for light coupling was fabricated using the micro-heater brushing technique. A short length of a coating-stripped standard single mode fiber (SMF 28, Corning) with core and cladding diameters of 8.3 and 125  $\mu\text{m}$  respectively was

cleaned with isopropyl alcohol. The stripped and cleaned fiber section was fixed horizontally between two computer controlled XYZ translational stages. The tapered fiber was then fabricated by means of a customized micro-heater brushing technique described in [41]. A ceramic micro heater (CMH-7019, NTT-AT) was used to heat the fiber up to approximately 1300°C, making the silica material soft enough for tapering. A customized PC program allowed for an accurate control of the diameter, the length and the shape of the fabricated tapers.

In our experiment, the tapered waist diameter is approximately 1.3  $\mu\text{m}$ , the waist length is around 3.5 mm and the full taper length is circa 30 mm. The fabricated fiber taper was then fixed on a glass slide at a height of  $\sim 1$  mm from the slide surface using two drops of UV curable epoxy (Norrland). The total length of the fiber between the cured epoxy droplets was 40 mm. Figure 8 shows the schematic diagram of the optical fiber tapering setup.

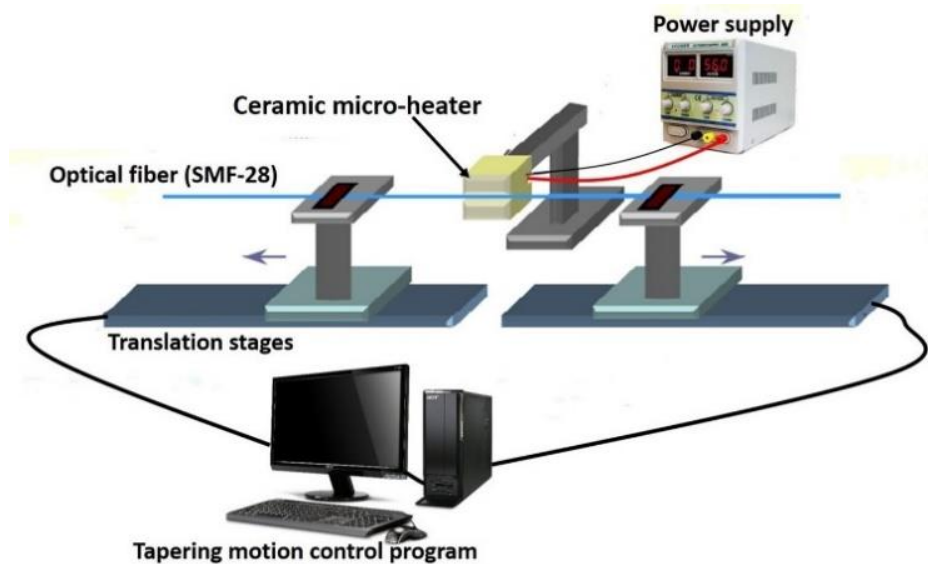


**Figure 8.** Schematic diagram of the micro-fiber fabrication setup based on the microheater brushing technique.

The fabricated fiber taper with waist diameter of circa  $\sim 1.3$   $\mu\text{m}$  was experimentally determined to be the optimal diameter choice to balance the need for effective light

coupling against mechanical fragility. Initially the transmission loss of the tapered fiber was measured as a function of wavelength, with reference to the un-tapered fiber. It was found that the fiber taper shows an increased 1.3 dB loss over the spectral range from 1500 to 1600 nm, compared with the un-tapered fiber,

### b) Experimental setup

In our experiment a short (circa 3 cm) section of a silica optical fiber with its buffer coating removed using a fiber stripper was used as the micro-cylinder. Evanescent light coupling to the micro-cylinder was achieved by a full fiber taper placed in physical contact with the micro-cylinder. Figure 9 illustrates schematically the experimental setup for recording the transmission spectrum of the micro-fiber taper and observation of the WGMs of the cylindrical micro-resonator.

The input end of the fiber taper was connected to a Super luminescent diode (SLD) (Thorlabs), with a wavelength range of 1500-1600 nm followed by a three-paddle manual polarization controller (Thorlabs). The output of the fiber taper is connected to an Optical Spectrum Analyser (OSA) (86142B, Agilent).

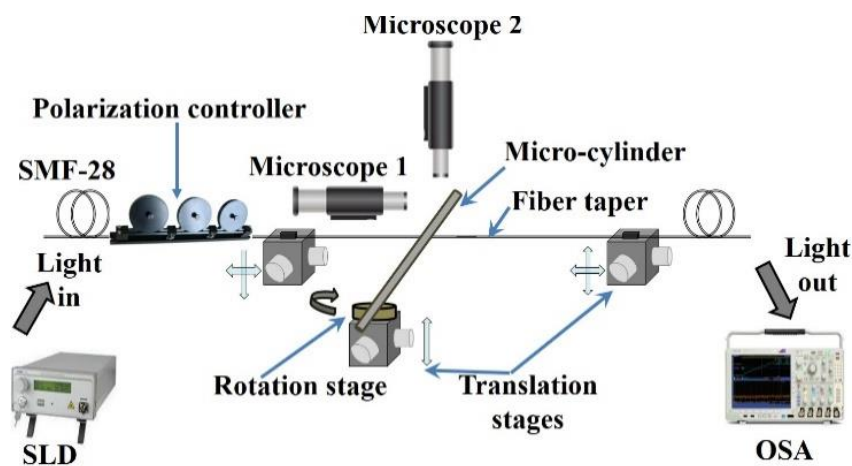


**Figure 9.** Experimental setup for observation of the transmission spectrum of WGMs in a cylindrical micro-resonator excited by a fiber taper.



Figure 10 is a microphotograph of the micro-cylinder resonator in perpendicular position with respect to the tapered fiber. Here  $Z_{\text{fiber}}$  is the micro-cylinders meridional axis with the laboratory coordinates system  $(X_{\text{lab}}; Z_{\text{lab}})$ ,  $X_{\text{lab}}$  is the axis of the tapered fiber and  $Z_{\text{lab}}$  is the normal to the tapered fiber.

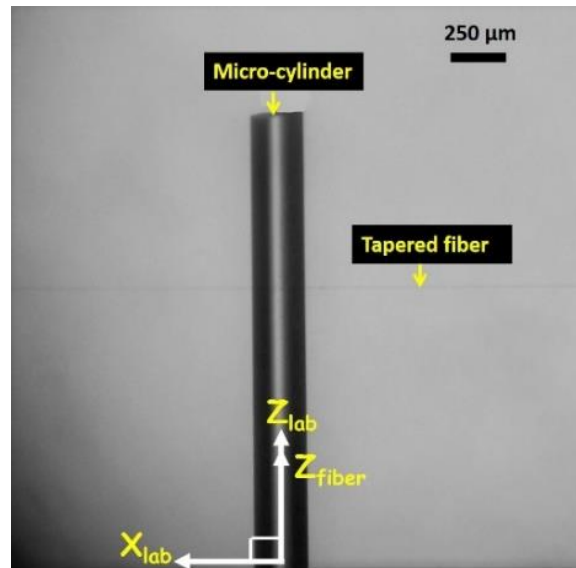


**Figure 10.** Microphotograph of the micro-cylinder resonator in perpendicular position with respect to the tapered fiber.

### c) Selection of the optimal tapered fiber diameter

For selecting the optimum tapered fiber diameter for the excitation of WGMs for a particular diameter microcylinder, fine tuning of the phase matching was performed by moving the microcylinder along the taper relative to the waist region while keeping both the micro-cylinder and tapered fiber perpendicular relative to each other.

Figure 11 shows the WGM spectra recorded by placing a 240  $\mu\text{m}$  cylindrical micro-resonator in direct contact with a tapered fiber at different positions along its axial direction corresponding to the varying diameters of the taper waist region. The waist diameter of the fabricated tapered fiber at its thinnest part is circa  $\sim 1.3$

$\mu\text{m}$ . It can be seen from the figure that no WGM resonances were observed in the spectra recorded at the positions along the fiber taper when the waist diameter was  $\sim 5 \mu\text{m}$  and larger, indicating that in those cases the power re-coupled from the micro-resonator into the fiber taper due to evanescent field was much lower than that of transmitted power along the fiber taper. At the position corresponding to the diameter of  $\sim 3.34 \mu\text{m}$  WGM resonances are observed with a small (0.82 dB) extinction ratio and an overall average spectral loss of -4.34 dB.

As the taper diameter decreases, the extinction ratio of the WGM spectrum gradually improves and the overall transmission loss grows, indicating that more light is coupled into the resonator. When the taper diameter reaches  $1.3 \mu\text{m}$ , the extinction ratio is 5.43 dB and an average spectral loss is 15.8 dB.

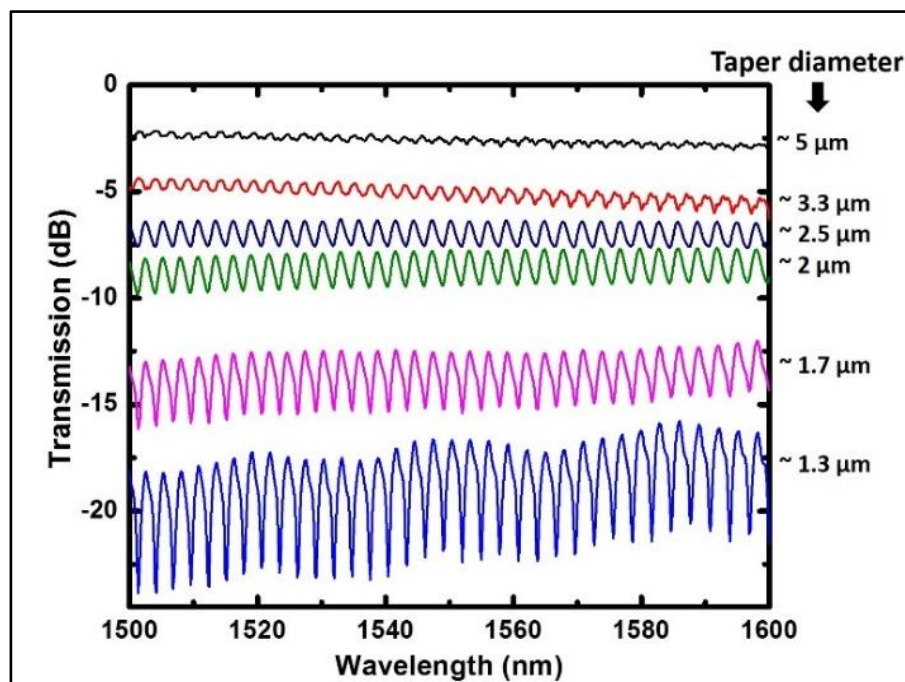


**Figure 11.** WGM transmission spectra excited in the cylindrical fiber resonator with a diameter of  $240 \mu\text{m}$  for different tapered fiber diameters.

Since in the proposed coupling method involves placing the fiber taper in direct physical contact with the micro-resonator, further decreases in the fiber taper waist

diameter beyond 1  $\mu\text{m}$  is undesirable as it may result in a fiber taper bend and an associated bend loss, while also being more susceptible to breakage. In our experiments, therefore the fiber taper with the waist diameter of 1.3  $\mu\text{m}$ , whose SEM image is shown in Figure 12, was employed for light coupling into a 240  $\mu\text{m}$  fiber micro-resonator.

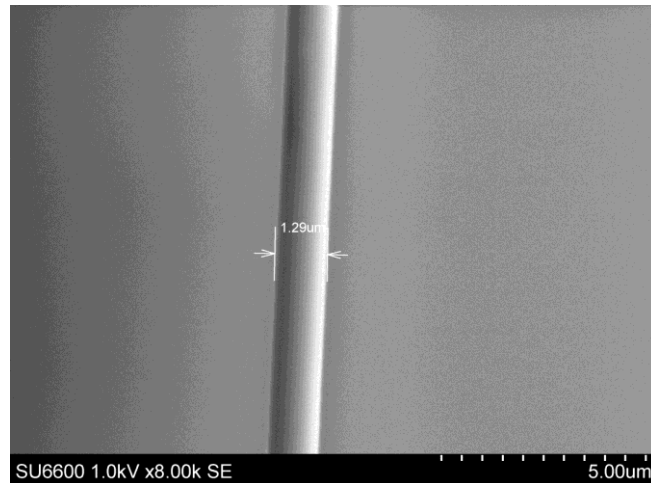


**Figure 12.** SEM image of the waist portion of the tapered optical fiber.

#### **d) Dependence of the WGM spectrum on the diameter of the resonator**

For the purpose of the experiment, fourteen micro cylinders with different diameters from 8  $\mu\text{m}$  to 125  $\mu\text{m}$  were fabricated from SMF28 fibre using a fiber tapering technique to produce different fiber diameters. Additionally, a single 240  $\mu\text{m}$  micro cylinder was fabricated from a multimode fiber, type BFL 22-200,  $\varnothing$ 240  $\mu\text{m}$ .

For illustration purposes, Figure 13(a-d) shows the experimental WGM spectra of different diameter cylindrical micro-resonators excited by the same tapered fiber with the waist diameter of  $\sim$ 1.3  $\mu\text{m}$ . Figures 13(a), (b), (c), and (d) show the WGMs spectra for 240  $\mu\text{m}$ , 125  $\mu\text{m}$ , 36  $\mu\text{m}$ , and 8  $\mu\text{m}$  diameter cylindrical silica fiber micro-resonators.

As shown in Figure 13, for a 240  $\mu\text{m}$  diameter cylindrical micro-resonator 34 resonance modes are observed within the range of 1500-1600 nm with an average spectral spacing of 2.89 nm. Decreasing the diameter of the resonator means that the number of modes in a given wavelength range also decreases leading to an increased spectral spacing. The number of modes for cylindrical micro-resonators with diameters of 125  $\mu\text{m}$ , 36  $\mu\text{m}$  and 8  $\mu\text{m}$  are 21, 7, and 2 respectively with corresponding spectral spacings of 4.64 nm, 14.37 nm, and 71 nm. It is noted that the overall transmission loss of the spectrum decreases as the diameter of the micro-resonator reduces.

Figures 14(a) & (b) illustrates the experimental dependencies of different spectral parameters versus the diameter of the micro-cylinder in the range of diameters from 8 to 240  $\mu\text{m}$ . Figure 14(a) shows the variation of the FSR of the WGM spectrum versus the resonator diameter. As was shown previously in Figure 13, with a decrease in the diameter of the resonator, the possible number of WGM resonances visible within the specified wavelength range becomes smaller and the spectral separation between the resonance modes increases, consistent with the theory presented earlier.

The widths of the WGM dips increase with the decrease in the size of the resonator. Figure 14(b) shows the full width at half maximum (FWHD) and Q-factor of selected WGM resonance dips of various cylindrical resonators versus the resonator's diameter. One can see that as the diameter of the resonator decreases, the WGMs resonances broaden. The broadening of the resonance dips is due to the increased curvature loss, and thus a lower Q, when the resonator's diameter becomes smaller.

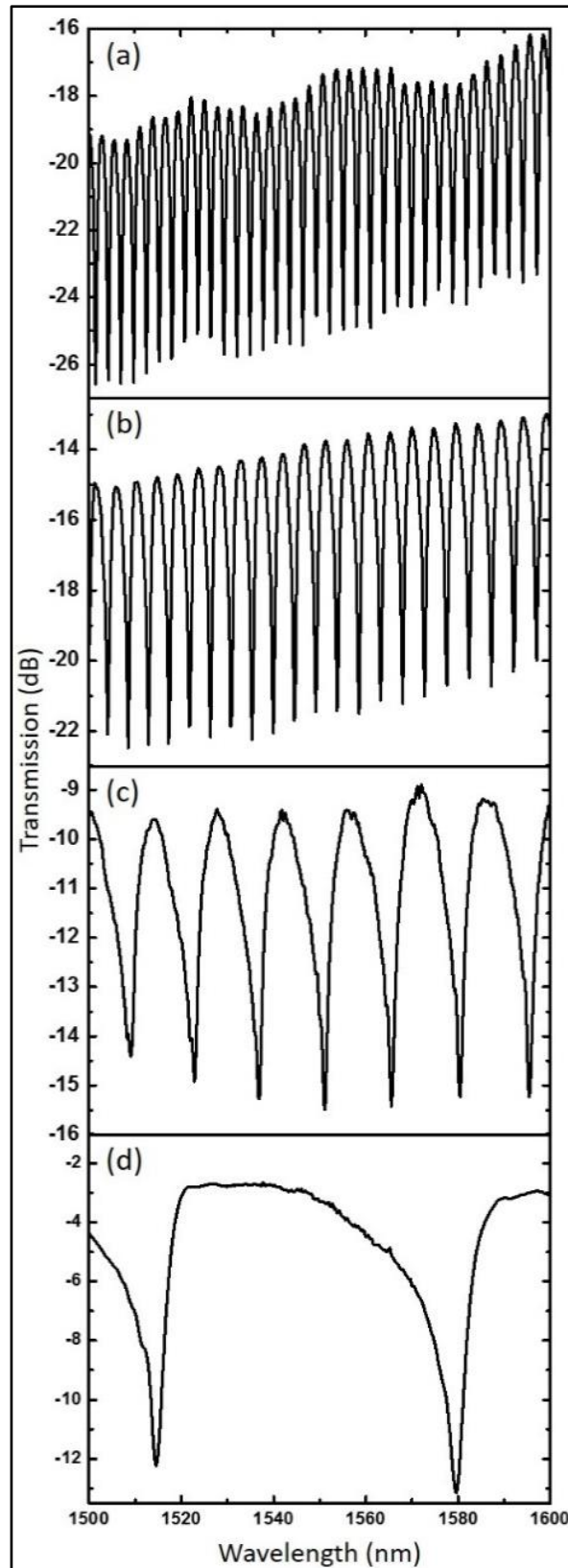


**Figure 13.** WGM spectra for cylindrical micro-resonators with different diameters: (a) 240  $\mu\text{m}$  (b) 125  $\mu\text{m}$  (c) 36  $\mu\text{m}$  and (d) 8  $\mu\text{m}$ .

The Q-factor of the WGMs increases with an increase in the diameter of the resonator. In practical experiments, the Q-factor of WGM resonators may be limited by various factors such as irregularities on the surface of the micro-cylinder, losses due to surface contaminants, etc.

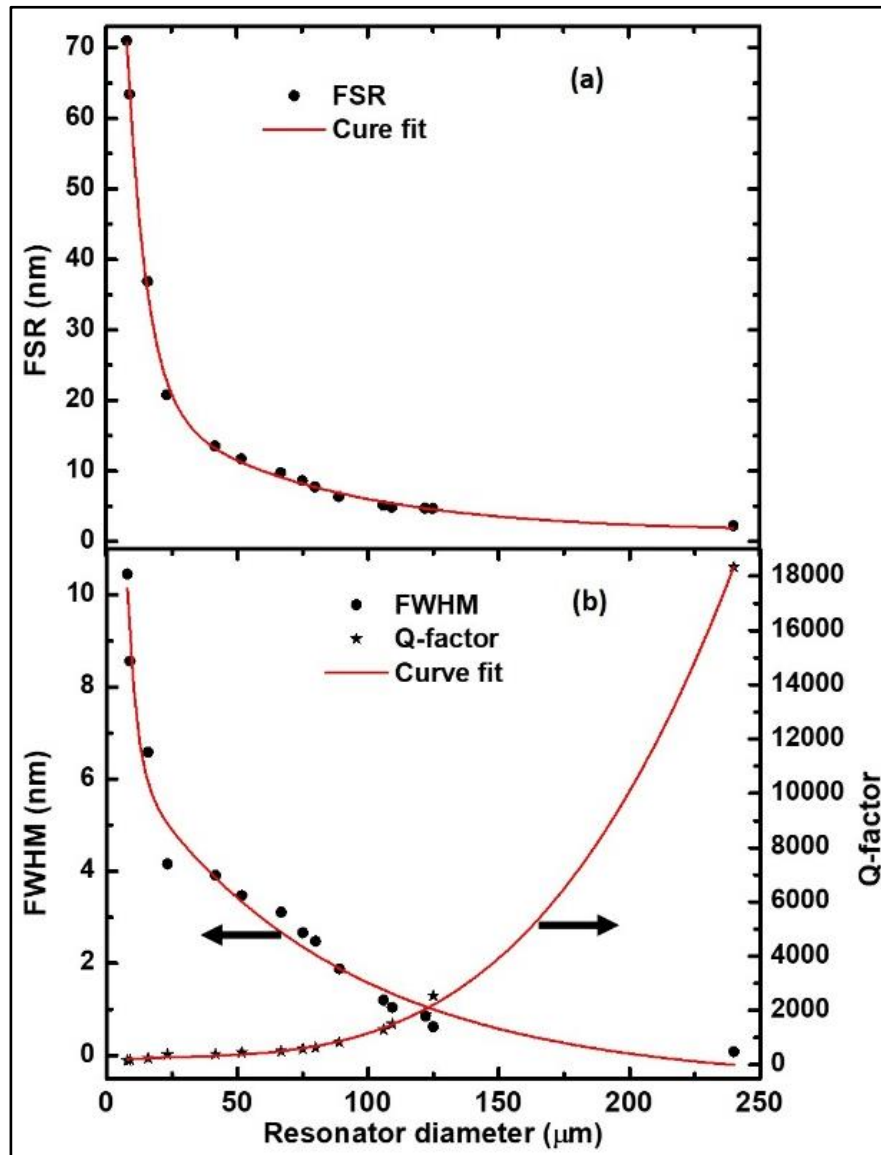


**Figure 14.** Variation of (a) free spectral range (FSR), (b) full width at half minimum (FWHM) and quality factor (Q-factor) of the WGM resonances for different diameter resonators with curve fit.

Reducing the diameter of the resonator eventually leads to a violation of the total internal reflection (TIR) for the light propagating inside the curved surface of the

cavity. Below a certain radius of the cavity,  $R_{min}$  the resonator loses its capability to trap light by means of TIR. Considering the WGM path inside a polygon with a side of length  $\lambda$  [35]:

$$R_{min} = \frac{\lambda}{n_c} \frac{1}{\pi - \theta_{crit}} \quad (2.8)$$

Where  $\theta_{crit}$  (in radian) is the critical angle,  $n_c$  is the refractive index of the cavity, and  $\lambda$  is the vacuum wavelength of the circulating light. Using the above equation, one can predict  $R_{min} = 0.45 \mu\text{m}$  by assuming  $\lambda = 1550 \text{ nm}$  and  $n_c = 1.44$ . However, in practical conditions other loss mechanisms add to this fundamental limitation. There are reports on the excitation of WGMs in  $1.5 \mu\text{m}$  [35] and  $2 \mu\text{m}$  [42] polystyrene micro-spheres. The smallest reported whispering gallery optical resonator is an individual hexagonal ZnO nano-cone whose diameter gradually reduces from bottom to top in the range of 700 to 50 nm and at a wavelength of 380 nm [43]. In our experiments with silica cylindrical micro-resonators we were able to observe WGMs excited in a resonator with a minimum radius of  $3 \mu\text{m}$  at a wavelength of 1550 nm.

#### e) **WGMs in a cylindrical micro-resonator excited by a tilted fiber taper**

Here we present the results of our experimental investigations of WGMs in a cylindrical micro resonator formed by a short length of a multimode fiber, with a diameter of  $240 \mu\text{m}$ , as a function of the tilt angle of the micro resonator with respect to the fiber taper, used for coupling the light in the resonator. This work is motivated by the need to understand the tolerance of the excitation of WGMs in a cylindrical fiber resonator with respect to changes in the tilt angle.

Figure 15 is a microphotograph of the micro-cylinder tilted from its perpendicular position with respect to the tapered fiber. Here  $Z_{fiber}$  is the micro-cylinder axis,

creating angle  $\theta$  (tilt angle) with the laboratory coordinates system ( $X_{lab}$ ,  $Z_{lab}$ ).  $X_{lab}$  is the axis of the tapered fiber and  $Z_{lab}$  is the normal to the tapered fiber.

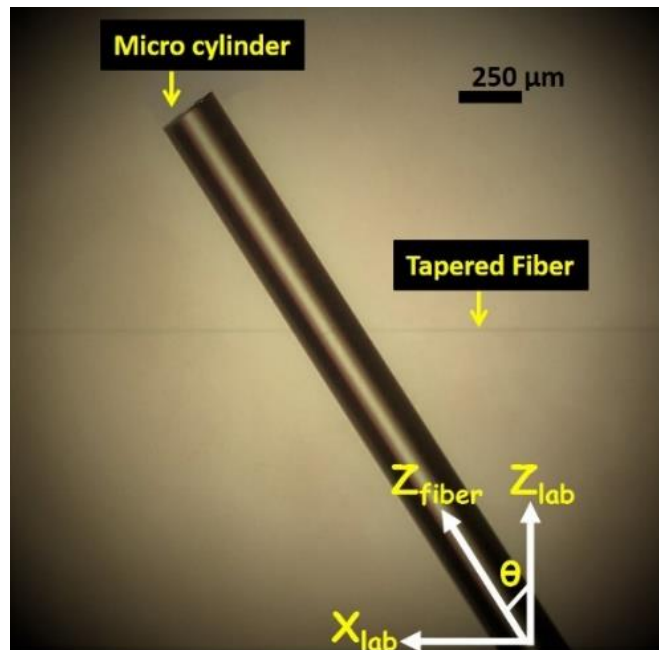


**Figure 15.** Microscopic image of the micro-cylinder with the tapered optical fiber.

As it was shown in the Figure 9, the fabricated fiber taper is straightened and fixed between two translation stages which supports three-dimensional movement for precise alignment. One end of the resonator under test (labeled as “micro-cylinder” in the figure) is fixed on a rotating stage with an angular scale for measurement of the tilt angle and is also mounted on the top of the second translation stage with adjustable vertical position to allow for the light coupling and for an accurate control of the tilt angle between the micro-cylinder and the fiber taper. Due to the short length (~3 cm) and relatively large diameter of the fiber micro-cylinder it should be noted there is no visible bending of the fiber micro-cylinder observed during the experiment. The choice of a 240 μm diameter resonator was used as this



has the highest Q-factor and was also the cylinder which suffered the least bending, when supported at one end only.

This process of micro-alignment is repeated for a number of tilt positions of the micro-cylinder with respect to the fiber taper assisted by two optical microscopes, which provide both top and side views of the micro-cylinder-tapered fiber system.

In our experimental setup polarization of the input light was controlled by a three-paddle polarization controller FPC030, with adjustment applied to achieve maximum coupling for a tilt angle of  $0^\circ$ .

Figure 16(a) shows the transmission spectrum of the fiber taper aligned perpendicularly to the  $240\ \mu\text{m}$  diameter fiber cylinder (in the adopted coordinate system this corresponds to  $\theta = 0^\circ$ ).

WGM resonances are clearly present at wavelengths of 1532.55 nm (p1), 1534.84 nm (p2), 1537.09 nm (p3), 1539.38 nm (p4), 1541.67 (p5) and 1544.21 nm (p6). The average extinction ratio, FWHM for the observed resonances and FSR of the spectrum are estimated as 7.76 dB, 0.08 nm and 2.27 nm, respectively. The maximum Q factor is measured as circa  $1.83 \times 10^4$ . Figure 16(b) illustrates a selected narrow portion of the experimental spectrum around 1534.8 nm and its Lorentzian fit used to derive the estimated value of the Q factor.

The micro-cylinder was then tilted progressively in  $2^\circ$  steps from the perpendicular position to  $24^\circ$  and the spectrum was recorded for each tilt angle. Figure 17(a) shows the WGM spectra for different tilt angles of the micro cylinder for a representative number of spectra at  $0^\circ$ ,  $2^\circ$ ,  $16^\circ$  and  $20^\circ$ . Not all of the measured spectra between  $0^\circ$  and  $24^\circ$  are shown in Figure 17(a) for the sake of clarity.

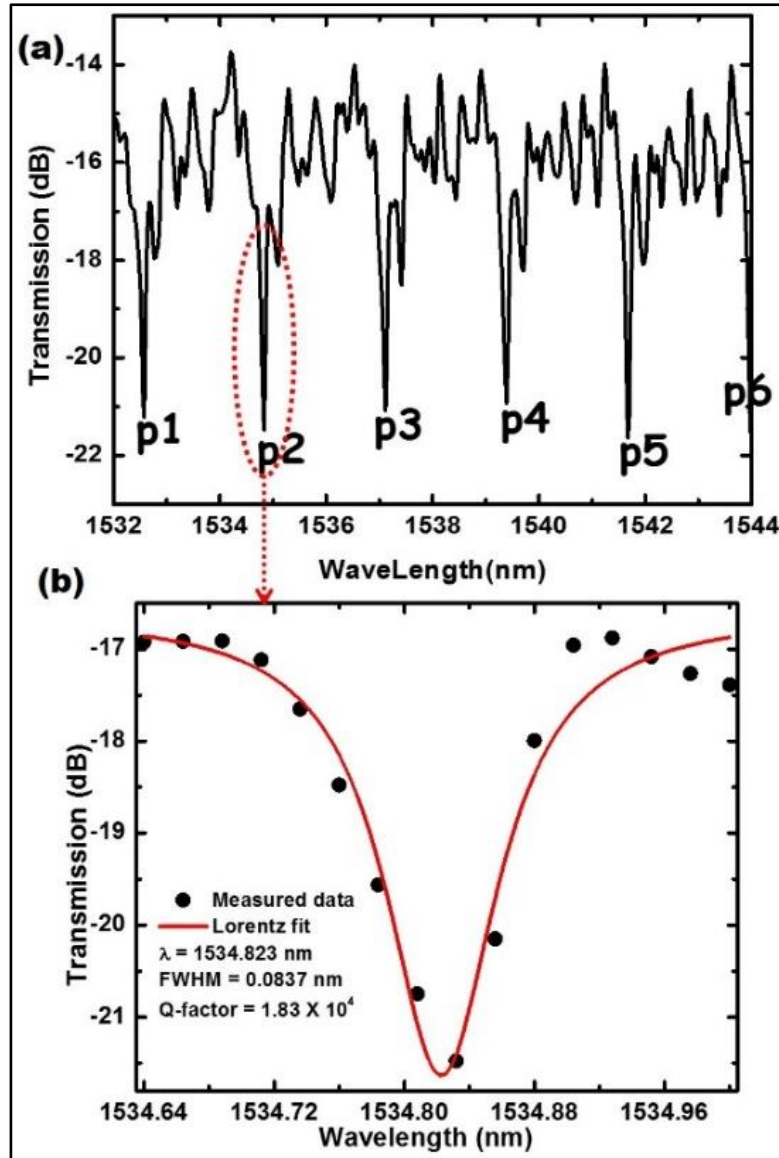


**Figure 16.** (a) WGM spectrum generated by a 240  $\mu\text{m}$  diameter cylindrical micro-resonator (normal to the taper,  $\theta = 0$ ). (b) Lorentzian fit of one of the WGM peaks, estimated Q factor is  $1.83 \times 10^4$ .

One can see from the figures that increasing the tilt angle results in an increase in the average loss for the spectrum associated with that tilt angle and the decrease in the extinction ratio for the dips associated with the WGMs. Also, some broadening of the WGM resonant dips is observed, accompanied with by a slight blue shift of the dip wavelengths. At tilt angles greater than  $24^\circ$ , no resonance peaks are observed in the measured WGM spectrum.

The observations above could be interpreted as follows: The efficiency of the light coupling from the tapered fiber to a particular WGM inside the micro-cylinder depends on the overlap between the evanescent field of the fiber taper and the corresponding mode field. The overlap is at its maximum when the two fibers are perpendicular to each other. As the tilt angle increases and the micro-cylinder moves away from the perpendicular position ( $\theta = 0^\circ$ ), the fundamental mode field decreases. At the same time with an increase in the tilt angle, the overlap with helical, higher order, WGMs of the resonator improves [13] and as a result coupling into these modes becomes more efficient, which causes the spectral broadening of WGM peaks observed in our experiment.

Figures 17(b) illustrates the measured variation of the overall average transmission loss of the spectrum and the extinction ratio of the WGMs for different tilt angles. With an increase in the micro resonator tilt angle away from the perpendicular position, the overall average loss of the spectrum increases and a monotonic decrease in the extinction ratio of the WGMs is observed.

It is found that the extinction ratio for the spectral dips reaches a half of its original value in dB when the tilt angle increases to  $16^\circ$  and a quarter of its original value when the tilt angle is equal to  $20^\circ$ . An average reduction of  $\sim 0.95$  dB in the extinction ratio is observed for each  $2^\circ$  increases in the tilt angle.

Finally Figure 17(c) illustrates the increasing FWHM and the blue shift experienced on a selected WGM resonance dip with an increase in the tilt angle  $\theta$ . The broadest WGM resonances in our experiment were observed at the tilt angle of  $24^\circ$  with a FWHM greater by 1.6 nm compared with that corresponding to the micro-cylinder which is perpendicular to the fiber taper.

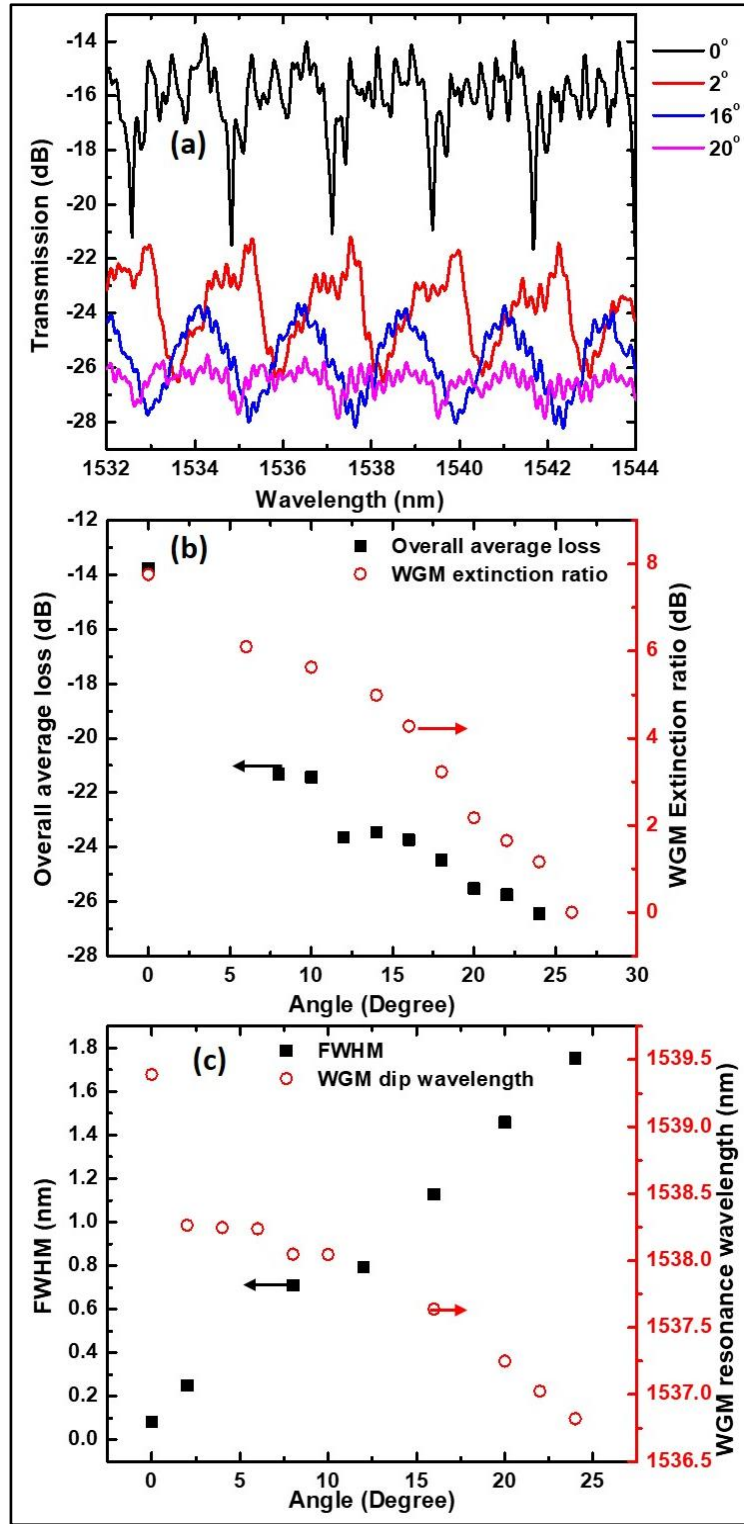


**Figure 17.** (a) Transmission spectra of the tapered fiber in contact with the micro-cylinder for different tilt angles with respect to the perpendicular position; (b) overall average loss of the transmission spectrum and extinction ratio of the WGM dip (for peak p2) with the increase in the tilt angle; (c) The broadening of the WGM dip and blue shift experienced on a selected WGM dip with the increase of the tilt angle.

The selected WGM dip (p4 in Figure 16(a)) experienced a 2.6 nm blue shift from the resonance wavelength 1539.38 to 1536.82 nm with the corresponding increase in the tilt angle from 0° to 24°. The significant application of this work is, it is a new method to tune the wavelength and linewidth of WGM of a cylindrical micro-resonator.

#### **2.1.4 Conclusions**

In summary, we have experimentally investigated the excitation of WGMs in cylindrical micro-resonators formed by silica optical fibers. The light was evanescently coupled into the micro-cylinder from a tapered optical fiber. The results of our studies allow for experimental determination of the optimum diameter of the tapered optical fiber for efficient evanescent light coupling into the fiber micro-cylinder. The influence of the micro-resonator radius on the WGM spectral parameters, such as the Q-factor and FSR has been experimentally investigated and analyzed. The optimum conditions for generating WGMs in a cylindrical micro-resonator are observed when the tapered fiber is perpendicular to the micro-cylinder. Evolution of the WGM spectrum with the increase of the tilt angle away from its initial perpendicular position resulted in changes in the intensity, broadening and blue shift of the WGM resonant wavelengths. Overall spectral losses increases with the increase of the tilt angle, and a complete disappearance of the WGM resonances occurred at large tilt angles above 24 °.

The results of this work are useful for an understanding of the optimum conditions for excitation of WGMs in cylindrical fiber resonators and can be applied to expand the range of practical applications of cylindrical fiber micro-resonators.

## **2.2 Studies of geometrical profiling in fabricated tapered optical fibers using whispering gallery modes spectroscopy<sup>2</sup>**

**Abstract:** This paper experimentally demonstrates a method for geometrical profiling of asymmetries in fabricated thin microfiber tapers with waist diameters ranging from ~10 to ~50  $\mu\text{m}$  with submicron accuracy. The method is based on the analysis of whispering gallery mode resonances excited in cylindrical fiber resonators as a result of evanescent coupling of light propagating through the fiber taper. The submicron accuracy of the proposed method has been verified by SEM studies. The method can be applied as a quality control tool in fabrication of microfiber-based devices and sensors or for fine-tuning of microfiber fabrication set-ups.

**Keywords:** Fibers; Fiber optics sensors; Microcavity devices; Microstructured optical fibers; Resonators; Surface waves; Fiber characterization; Fiber properties

### **2.2.1 Introduction**

Precise measurement of the outside diameter of standard optical fibers is important in both the manufacturing and quality control of such fibers. Fiber diameter measurements are used to understand and dynamically control the fiber drawing process and to select fibers suitable for commercial use. Other areas where a highly accurate fiber diameter measurement technique is required are related to improving the quality of fiber Bragg gratings [44], fabrication of special fibers,

---

<sup>2</sup> V. Kavungal, G. Farrell, Q. Wu, A. K. Mallik, and Y. Semenova, "Studies of geometrical profiling in fabricated tapered optical fibers using whispering gallery modes spectroscopy," *Optical Fiber Technology*, **41**, 82-88 (2018).

fiber-based devices, and more recently, microfiber based resonant devices [45]. Many of the fiber diameter measurement techniques developed to date are based on an analysis of interference fringes or diffraction patterns produced as a result of light scattering by an optical fiber under test [46–54]. The accuracy of these techniques is in the order of a few tens of nanometers, but complex equipment is required utilising spatial optics which involves complex measurement and signal processing. Birks *et al.* [11] suggested a simple and accurate method for the measurement of the variations in the diameter of an optical fiber based on the use of a microfiber. In their experiment, a guided mode of a microfiber was evanescently coupled into whispering-gallery modes (WGMs) propagating around the circumference of the fiber under test, which itself served as a cylindrical micro-resonator.

WGMs are electromagnetic surface oscillations which arise in dielectric micro-resonators with a circular structure as a result of the trapping of light within the micro-resonator by total internal reflections from the resonator's curved surface with a near-glancing incidence (angle of incidence ( $i$ )  $\sim 90^\circ$ ) [1]. Such reflections force the light to take on a polygonal path within the curved structure, very close to the surface of the resonator, and effectively confine its energy within very small volumes. The exceptional sensitivity of such resonances to the shape and size of the resonator make WGM spectroscopy a promising tool for geometrical profiling that can measure diameter variations at a sub-wavelength scale.

In Birks's experiments a microfiber with a guided light mode was used to accurately measure the relative diameter variations of less than one part in  $10^4$ , as a possible means to implement accurate diameter control for fibre drawing. In that scheme, the microfiber and fibre under test moved relative to each other and were

also in physical contact with each other. The fibre under test acted as a cylindrical WGM resonator and the fiber diameter variation was calculated from the shift of a WGM resonance detected in the transmission spectrum of the microfiber. This technique was further developed by Sumetsky and Dulashko in [12] by addressing some problems in Birks's method that arose because only a single resonance was tracked. This problem was resolved in Sumetsky's method by increasing the number of WGM resonances whose spectral positions were traced leading to the demonstration of reliable angstrom fiber diameter measurement accuracy.

Another alternative method of fiber characterization is by calculating the effective diameter of the resonator using the information from the WGMs spectral spacing. The fundamental WGMs are localized close to the surface of the cylindrical resonator and thus the FSR can be linked to the microresonator's effective diameter [33, 34]. Using this approach, Boleininger *et al.* [13] experimentally demonstrated WGM profiling of a 3 mm long tapered optical fiber with a diameter  $>80 \mu\text{m}$ , and verified the accuracy of their method using optical microscopy data.

Tapered optical fibers themselves have been intensively studied in the recent years for applications as sensors for temperature, strain and biomedical measurands as well as various devices for optical communications due to their simple fabrication, configurability and excellent performance [45, 55–58]. More recently asymmetric fiber tapers have attracted a lot of attention as high sensitivity sensors, narrow-line optical comb filters [59–62] and surface nano-scale axial photonics devices [63–67]. The growing popularity of tapered fiber-based devices requires the development of a simple and accurate taper profiling and a-/symmetries characterization method which would be useful for better understanding of such devices fabrication and quality control.



In this paper, we for the first time explore and experimentally demonstrate applicability of WGM spectroscopy for characterization of asymmetries in thin fiber tapers with waist diameters ranging from  $\sim 10$  to  $\sim 50$   $\mu\text{m}$  where a submicron resolution is required.

Our WGM spectroscopy method is based on calculations of effective diameters using the experimentally measured FSR of the WGMs spectra. The technique is nondestructive, and the measurements can be carried out in situ as opposed to measurements with an optical microscope. In addition, the proposed technique is a better alternative to optical microscopy since its resolution is not limited by the diffraction limit. To verify the submicron accuracy of our proposed method effective diameters of the tapered fibers calculated using the WGM spectroscopy were verified by scanning electron microscopy (SEM).

## 2.2.2 Theoretical background

### a) Tapered fiber transmission spectra

The transmission characteristics of a tapered optical fiber, coupled with a cylindrical micro resonator and the coupled power circulating inside the cylindrical micro-resonator, can be described using universal coupled microcavity theory [68]. In Figure 18, the field amplitudes at the input and output of the tapered optical fiber are denoted as  $a_1$  and  $b_1$  respectively.

The coupled field amplitudes in the cylindrical micro-resonator immediately before and after the coupling region are  $a_2$  and  $b_2$  respectively. The circulation loss factor inside the cylinder is denoted by  $\alpha$ , which can be found from [68]:

$$\frac{a_2}{b_2} = \alpha e^{i\theta} \quad (2.9)$$

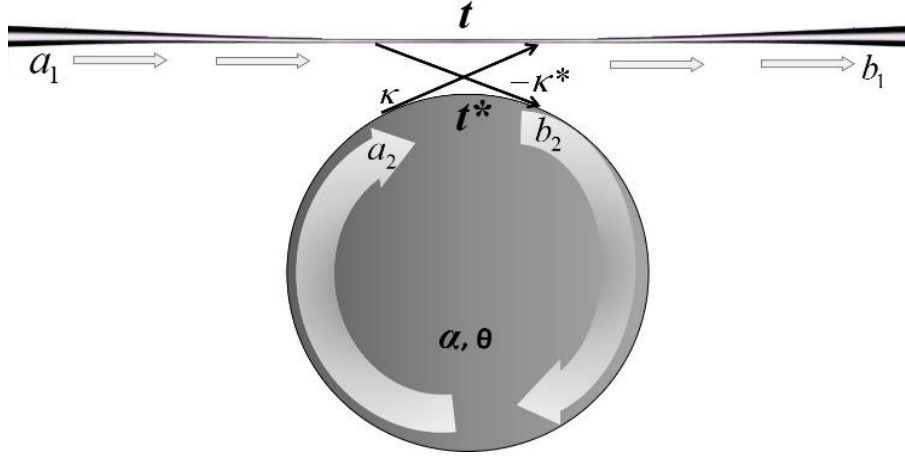


**Figure 18.** Schematic diagram of tapered fiber coupled cylindrical resonator.

Where  $\theta$  is the circulation phase shift given by:

$$\theta = \frac{4\pi^2 R n_{eff}}{\lambda} \quad (2.10)$$

Here  $n_{eff}$  is the effective refractive index of the mode that propagates along a circular path within the cavity,  $R$  is the radius of the cylindrical micro-cavity, and  $\lambda$  is the resonance wavelength.

By setting  $a_1 = 1$ , the normalized transmission power of the tapered optical fiber is given by [68]:

$$|b_1|^2 = \frac{\alpha^2 - 2\alpha|t|\cos(\theta - \varphi_t) + |t|^2}{1 - 2\alpha|t|\cos(\theta - \varphi_t) + \alpha^2|t|^2} \quad (2.11)$$

Here  $t$  represents the transmission coefficient of the system, which is related to the coupling coefficient ( $\kappa$ ) by the equation:

$$|t|^2 = 1 - |\kappa|^2 \quad (2.12)$$

Where  $\varphi_t$  is the phase offset due to coupling to the tapered optical fiber. When the resonance condition is satisfied,  $\varphi_t$  is zero [69].

Based on Eq. (2.11), the typical curves of the loss factor ( $\alpha$ ) due to circulation versus transmission power for a cylindrical resonator-tapered fiber system are simulated and shown in Figure 19(a). The simulated plots are for three different values of  $|t|$  equal to 0.999, 0.980, and 0.960 respectively.

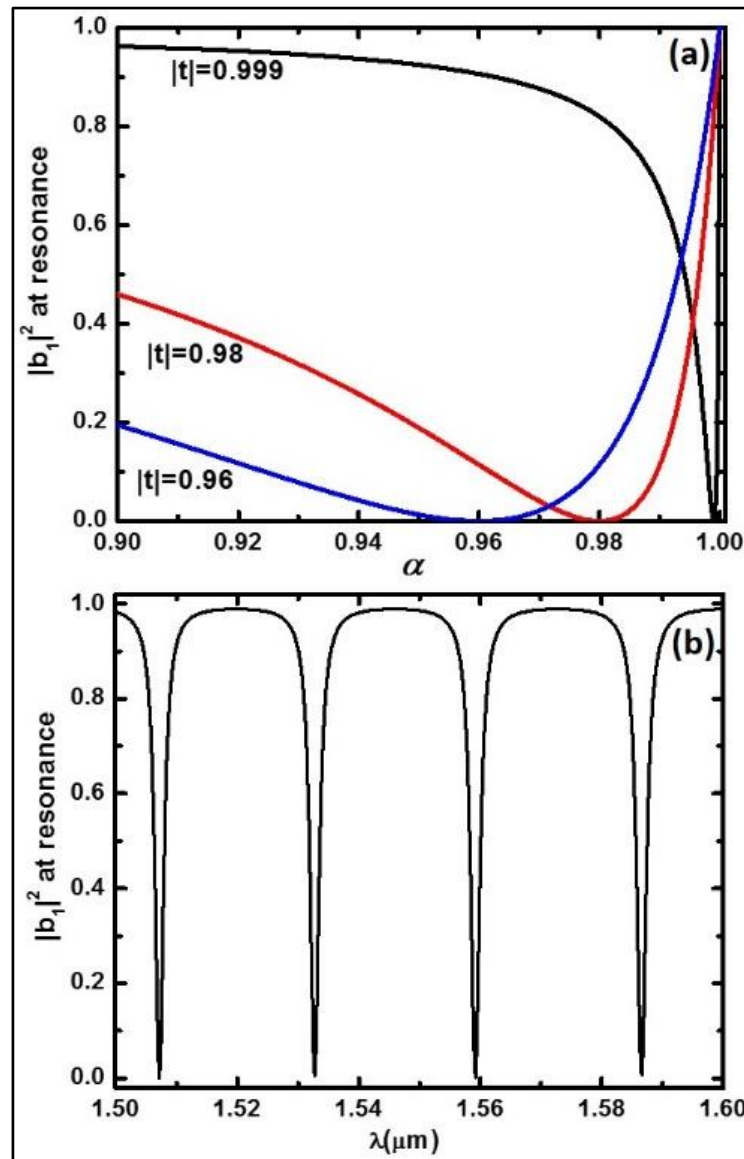


**Figure 19.** (a) Relationship between the transmission powers of the tapered fiber coupled with the cylindrical microresonator with the resonator internal loss coefficient ( $\alpha$ ) and, transmission loss coefficient ( $|t|$ ) with its transmission power. (b) The simulated transmission spectrum of the tapered fiber at critical coupling.

From Eq. (2.11) it can be seen that when  $|t| = \alpha$ , there is no light power in the transmission spectrum ( $|b_1|^2 = 0$ ). This is due to the fact that when the internal loss is equal to the transmission loss there is a perfect destructive interference in the tapered fiber between the power transmitted through the fiber taper and the circulating power leaked from the cylindrical resonator. This condition is referred to as the critical coupling [68].

For illustration purposes, Figure 19(b) shows the simulated transmission spectrum of the tapered fiber (based on Eq. 2.11) coupled with a 20  $\mu\text{m}$  diameter cylindrical micro resonator at critical coupling by setting both the cavity's internal loss coefficient ( $\alpha$ ) and the transmission loss coefficient ( $|t|$ ) equal to 0.90.

### b) Effective radius of the resonator and the FSR of its WGM spectrum

A simple approximation can be obtained for the FSR from the propagation constant and neglecting the wavelength dependency of the refractive index [33, 34].

The light wave propagation constant is given by:

$$\beta(\lambda) = \frac{2\pi}{\lambda} n_{\text{eff}} \quad (2.13)$$

Differentiate Eq. (2.5) with respect to  $\lambda$ ,

$$\begin{aligned} \frac{\partial\beta(\lambda)}{\partial\lambda} &= -\frac{2\pi}{\lambda^2} n_{\text{eff}} + \frac{2\pi}{\lambda} \frac{\partial n_{\text{eff}}}{\partial\lambda} \\ \frac{\partial\beta(\lambda)}{\partial\lambda} &= -\frac{2\pi}{\lambda^2} \left( n_{\text{eff}} - \frac{\partial n_{\text{eff}}}{\partial\lambda} \lambda \right) \approx \frac{-2\pi n_g}{\lambda^2} \end{aligned} \quad (2.14)$$

Where,  $n_g = n_{\text{eff}} - \frac{\partial n_{\text{eff}}}{\partial\lambda} \lambda$  is the group refractive index

FSR of the resonator is given by the equation [33]:

$$\text{FSR} = \frac{-2\pi}{L} \left( \frac{\partial\beta}{\partial\lambda} \right)^{-1} = \frac{-2\pi}{L} \left( \frac{-\lambda^2}{2\pi n_g} \right) \approx \frac{\lambda^2}{n_g L} \quad (2.15)$$

Where  $L$  is the circumference of the resonator.

It should be noted that the group refractive index varies with the change of the mode order. But for the lowest order modes this variation is small and can be neglected [16]. When calculating the FSR we are only considering the fundamental modes of the WGM spectrum, which have the lowest radial mode number. Hence

neglecting the  $\frac{\partial n_{eff}}{\partial \lambda} \lambda$  term from the expression for  $n_g$ , an approximate expression

for the FSR is obtained as [33, 34]:

$$\text{FSR} = \frac{\lambda^2}{Ln_{eff}} = \frac{\lambda^2}{2\pi Rn_{eff}} \quad (2.16)$$

Eq. (2.16) represents the main approximation that underpins the approach presented in this paper. It assumes that the wavelength dependence of  $n_{eff}$  is negligibly small and the variation of the FSR of a resonator depends only on the micro-resonator radius.

As was shown in reference [70], Eq. (2.16) is not only useful for finding the spectral spacing between the modes within the uniform diameter portion of the resonator but can also be used for calculating the spectral spacing in the conical portion of the tapered fiber transition region.

### 2.2.3 Experiments and discussion

#### a) Fabrication of tapered optical fibers

Light propagation inside a standard optical fiber with a diameter greater than the propagating light wavelength is based on total internal reflection where the light is trapped inside the core. When light hits the interface between the core and cladding layers, a small amount of the light infiltrates the boundary as an evanescent field that exponentially decays into the cladding region. The penetration depth of the

evanescent field into the surrounding region is given by the relation [38]:

$$d_p = \frac{\lambda}{2\pi(n_1^2 \sin^2 \Theta - n_2^2)^{1/2}} \quad (2.17)$$

Here  $\lambda$  is the wavelength of incident light,  $n_1$  and  $n_2$  are the refractive indices of the core and cladding respectively.  $\Theta$  is the incident angle measured from the normal at the interface of the core and cladding. The reflected beam from the interface is returned to the core with a phase shift along its axial propagation direction.

When the diameter of a tapered optical fiber is greatly reduced, the original fiber core dimensions are so small at the waist region that they are no longer significant. In this case, an optical fiber can be considered as a cylindrical waveguide with a homogeneous refractive index profile. In a thin (micron order) fiber taper light is guided by the total internal reflection at the cladding-air interface (if the surrounding medium is air). Thus, a significant portion of light propagates outside of the microfiber. The presence of a large evanescent field outside of the tapered portion of the fiber can be used for coupling the light into another fiber acting as the WGM micro-resonator by placing both fibers in direct physical contact.

A typical optical fiber taper consists of a non-tapered portion followed by a fiber taper transition region where the radius of the fiber decreases with distance. The uniform thin portion after the transition region is known as the taper waist. This is followed by a second fiber transition region of increasing diameter and ends with another non-tapered region. The optical properties of the tapered micro-fibers strongly depend on the geometry of both the transition and waist regions. If the tapering process is carried out in such a way that the fiber diameter within its transition region changes smoothly and can be adiabatically slow as a function of

fiber length, the taper is considered adiabatic [39,40]. This condition ensures low transmission loss and small inter-mode coupling. In our experiments, only adiabatic tapers were studied.

The fiber tapers both for light coupling and as the microfibers under test, were fabricated using the micro-heater brushing technique [71,72]. The technique involved stripping the coating off a short length of a standard single mode optical fiber (SMF 28, Corning), with core and cladding diameters of 8.3 and 125  $\mu\text{m}$  respectively, and its subsequent cleaning with isopropyl alcohol. The stripped and cleaned fiber section was then fixed horizontally between two computer controlled XYZ translational stages. A ceramic micro heater (CMH-7019, NTT-AT) was used to heat the fiber up to approximately 1300°C, making the silica material soft enough for tapering. A customized PC program allowed for the control of the diameter, the length and the shape of the fabricated tapers. Figure 20 illustrates a schematic diagram of the fiber tapering setup.

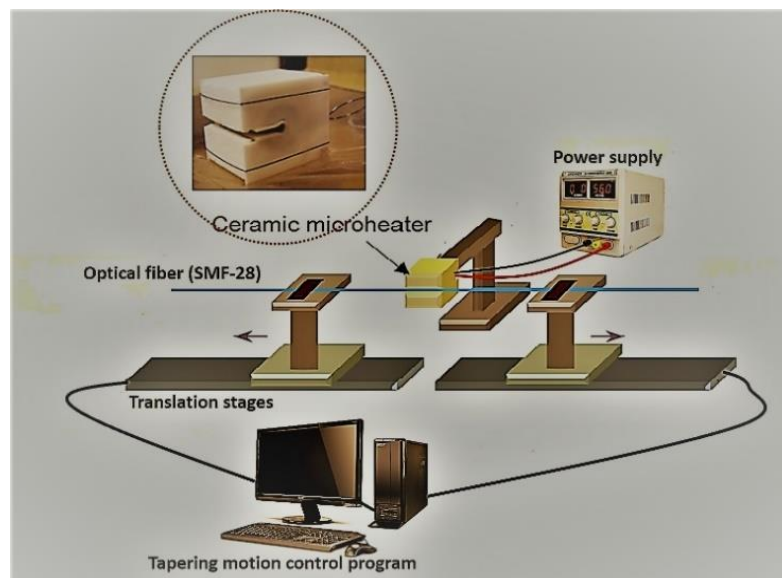


**Figure 20.** Schematic diagram of the micro-fiber fabrication setup using the microheater brushing technique.

## b) Experimental set up for geometrical profiling of fabricated tapered optical fibers

For geometrical profiling in our experiment a fiber taper under test was moved in small steps, in a manner similar to the technique described in [12], perpendicularly to a fixed “delivery” microfiber, the ends of which were connected to the optical source (SLD, Thorlabs) and the optical spectrum analyzer (86142B, Agilent) as shown in Figure 21. Both fibers were placed in physical contact at 90° to each other so that the tapered fiber under test acted as a cylindrical WGM micro-resonator.

The fabricated fibers tested in our experiments were set to be fabricated with uniform taper waist diameters varying from ~10 to ~50  $\mu\text{m}$ . The delivery microfiber had a waist diameter of circa ~1.3  $\mu\text{m}$ . This value of the taper waist diameter was chosen as optimal to allow for an effective evanescent coupling while providing sufficient mechanical stability during the experiments.

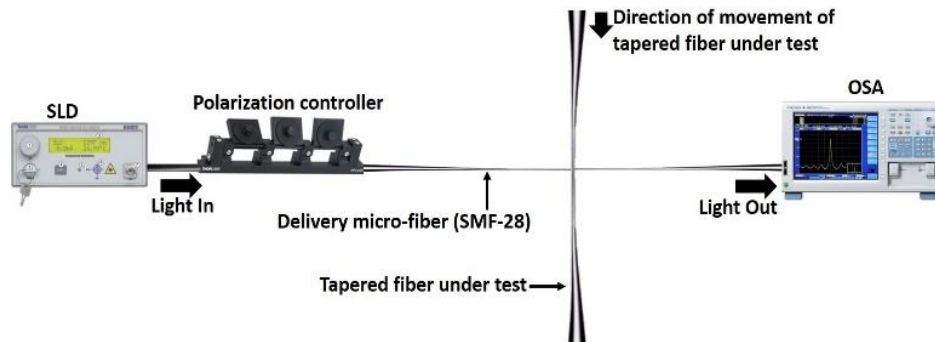


**Figure 21.** Schematic of the experimental setup for whispering gallery mode spectroscopy.

Narrow WGM resonances are observed in the transmission spectrum of the delivery microfiber with a maximum  $Q$  factor of  $\sim 2.55 \times 10^3$  (for a 125  $\mu\text{m}$  fiber/cylinder).



In the geometrical profiling experiment the transmission spectra of the light through the delivery microfiber was recorded for multiple positions of the “delivery” microfiber along the length of the taper under test with a step size of 0.5 mm along its axis. After each measurement, the fiber under test was lifted off the delivery fiber by approximately 1 mm, moved along the “delivery” fiber and placed in contact with it at the next point to take the subsequent measurement. This approach reduces the distortion of both the delivery fiber and the fiber under test and the possible damage from abrasion of the fiber surfaces. The FSR of the measured transmission spectrum is a function of the effective diameter of the tapered fiber under test (Eq. 2.16).

As an initial test, a recorded WGM spectrum for a micro-fiber cylindrical resonator with a known nominal 35.5  $\mu\text{m}$  diameter was measured. Figure 22 shows the experimentally measured spectrum along with the theoretically calculated spectrum using Eq. 2.11. The experimental and simulated FSRs are estimated as 14.37 nm and 14.63 nm respectively for the 35.5  $\mu\text{m}$  diameter micro-fiber resonator. Using Eq. (2.11) and assuming  $n_{eff} \approx 1.4677$  for the resonator from the manufacturer’s data, the corresponding effective diameter of the fiber under test from the experimental FSR is estimated as 36.28  $\mu\text{m}$ . For the theoretical plot in Figure 22, the cavity loss and transmission loss are set as 0.9 and 0.86 respectively allowing to achieve a close fit for transmission loss between the theoretical and experimental spectra. The light circulation phase shift ( $\theta$ ) was calculated from Eq. (2.10).

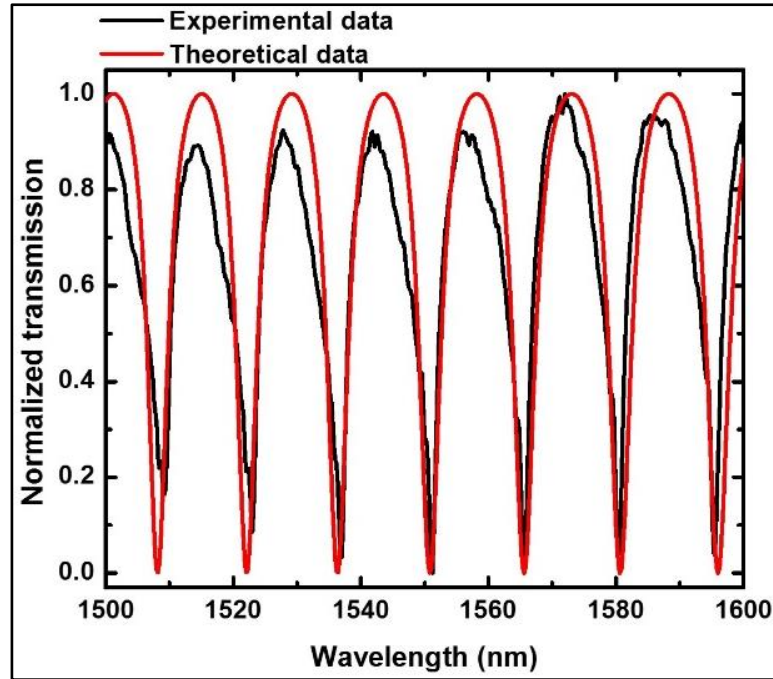


**Figure 22.** Experimental WGM spectrum of the delivery fiber and a simulated spectrum using Eq. 2.11.

### c) Geometrical profiling of optical fiber tapers

Before considering the experimental geometrical profiling results, it is worth noting that the shape of a tapered fiber is important and the requirements to the taper transition length, diameter of the uniform section and taper angle vary depending on the applications. For example, in many applications the fiber taper shape must be sufficiently gradual to satisfy the criterion for adiabaticity, so as to ensure minimum loss of light for the fundamental mode [39]. In some applications it is desirable for the transition region to be as short as possible, allowing the fiber taper to be compact. The shape of a taper is also important in situations where the taper is to be controllably deformed; for example, by bending, to fabricate miniature devices. Special shape considerations may also apply if the taper is to be used as a sensor. Many of the fiber tapering techniques developed to date allow for fabrication of the fiber tapers with specific shapes.

For the geometrical profiling experiments, two tapered fiber samples were used with nominal minimum waist diameters determined by SEM of  $\sim 11.2 \mu\text{m}$  (Taper 1) and  $35.5 \mu\text{m}$  (Taper 2) respectively. SEM measurements were undertaken using a variable pressure FESEM (SU 6600) with a Schottky field emission electron gun which enables excess of 200 nA probe current. The attainable SEM image resolution is 1.2 nm/30 kV. Figure 23 shows the SEM images of the minimum waist sections for the two tapered fiber samples.

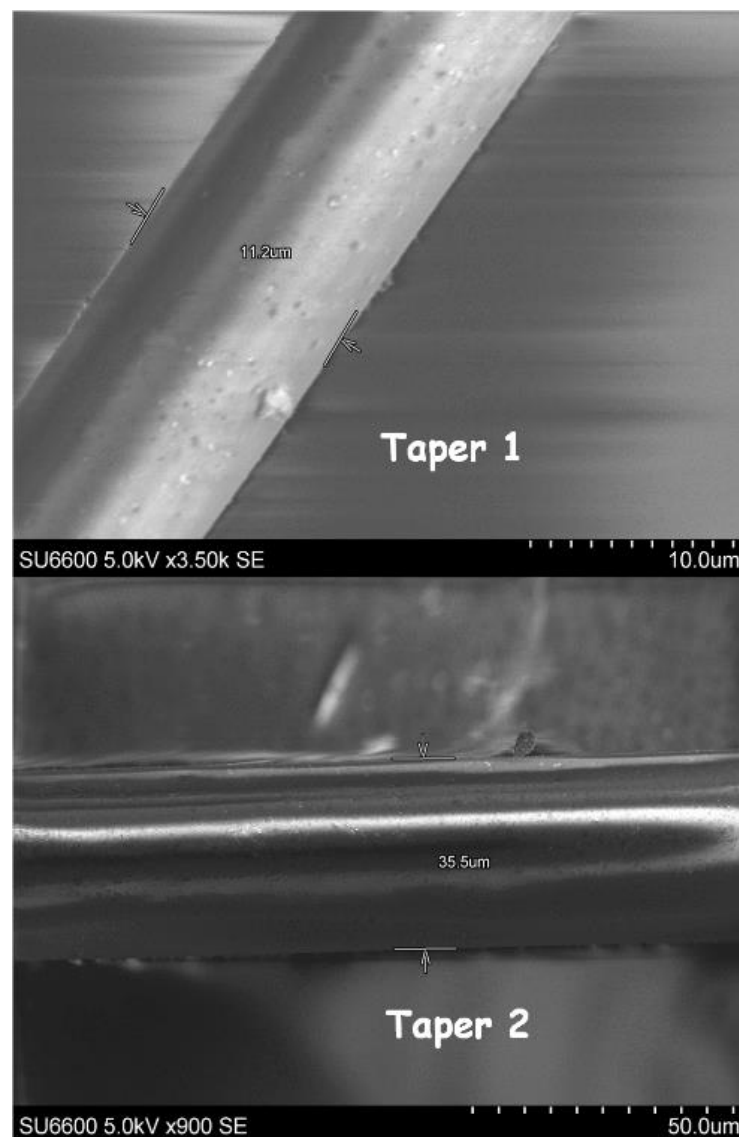


**Figure 23.** SEM images of the uniform waist portions of the tapered optical fibers.

Figure 24 shows the FSR and measured diameter versus position of the delivery fiber for the two tapered fiber samples. The minimum waist diameters recorded are estimated as 10.43  $\mu\text{m}$  and 36.28  $\mu\text{m}$ , taken at position zero in Figure 24.

Table 1 shows the comparison between different fiber diameter measurements using WGM spectroscopy and SEM microscopy. The maximum error between the two measurements methods is 0.77  $\mu\text{m}$  (6.8 %). The disparity between nominal diameters (measured from a SEM image) and the experimentally measured diameters may be due for example to inaccuracies in the SEM determined diameter of the resonator under test or small variations in actual position of the delivery tapered fiber and the tapered fiber under test.

It should be noted that profiling of the tapered fibers using WGM spectroscopy allows one to easily obtain accurate information not just about the taper effective diameter at a certain point but also to fully evaluate the shape of the taper along its length and determine the lengths of the taper transition regions and the uniform tapered portion. For example, from Figure 24 it can be determined that Taper 1 has transition regions 11 mm long on the left-hand side and 10 mm long on the right-hand side and that the uniform tapered portion is about 3.5 mm long. Taper 2 has transition region lengths of 9.5 mm and 10 mm on the left and right-hand sides respectively and the uniform tapered portion is about 2.5 mm long.

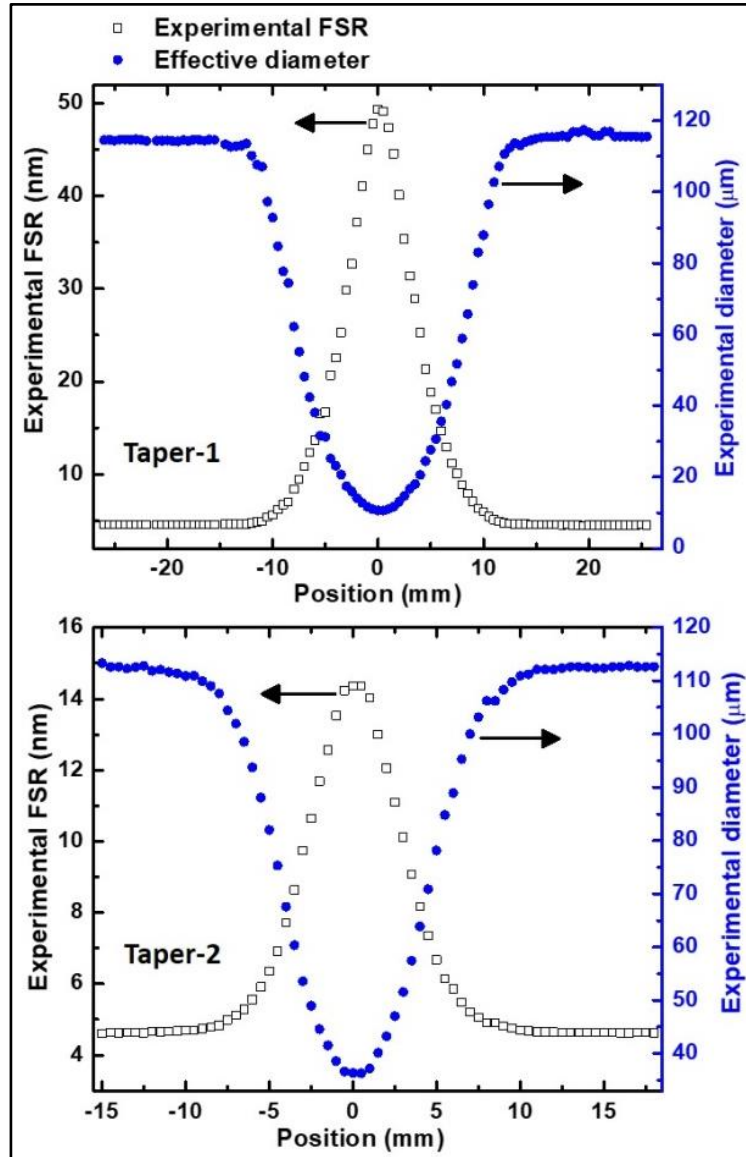


**Figure 24.** Experimentally calculated FSR and diameter vs position of the delivery fiber for a taper with a nominal waist diameter of 11.2  $\mu\text{m}$  (Taper 1) and 35.5  $\mu\text{m}$  (Taper 2) measured by WGM spectroscopy. Zero position corresponds to the center of the taper.

**Table 1.** Comparison of measured fiber diameter using WGMs and SEM microscopic methods

Diameter ( $\mu\text{m}$ ) from WGM Spectroscopy (a)	Diameter ( $\mu\text{m}$ ) from SEM microscopy (b)	Error ( $\mu\text{m}$ ) (a)-(b)
48.66	48.4	0.26 (0.54 %)
45.51	45.6	0.09 (0.2 %)
38.52	38.8	0.28 (0.72 %)
36.26	35.5	0.76 (2.1 %)
10.43	11.2	0.77 (6.8 %)

**d) Application of the WGM spectroscopy to studies of taper symmetry**

In an ideal case, a fiber taper is formed symmetrically. This means that the ends of the taper are pulled apart at equal and opposite speeds relative to the center of the heat source so that the two transition regions are identical. In practice however various factors, such as misalignments within the tapering setup, vibration or temperature fluctuations within the heating zone of the source may result in uneven conditions at the opposite sides of the taper and lead to asymmetries of the fiber taper shape. One important parameter in the model of the fiber tapering process developed in [39] is the constant which determines the relative rates of the hot-zone change and taper elongation  $\Psi^3$  the value of  $\Psi$  must satisfy the condition  $\Psi \leq 1$  and it determines the length of the uniform waist region along with the shape of the transition regions.

To provide a set of non-ideal tapers for test purposes, a fabrication configuration was used that was known to produce increasingly asymmetrical tapers for larger  $\Psi$  values, due to mechanical limitations caused by vibration. This setup, although flawed in principle, was deliberately used to fabricate non-ideal tapers for testing

---

<sup>3</sup> In the original reference paper (Ref [38]), the constant which determines the relative rates of the hot-zone change and taper elongation is represented by ' $\alpha$ '. To avoid the possibility of confusion

of the WGM spectroscopy method presented here. Figure 25(a) illustrates the experimental WGM spectroscopic profiles of a highly asymmetric taper (Taper-3) fabricated using the above mentioned setup. Figure 25(b) shows the comparison of the fabricated asymmetric taper with a symmetric taper, in this case Taper-2.

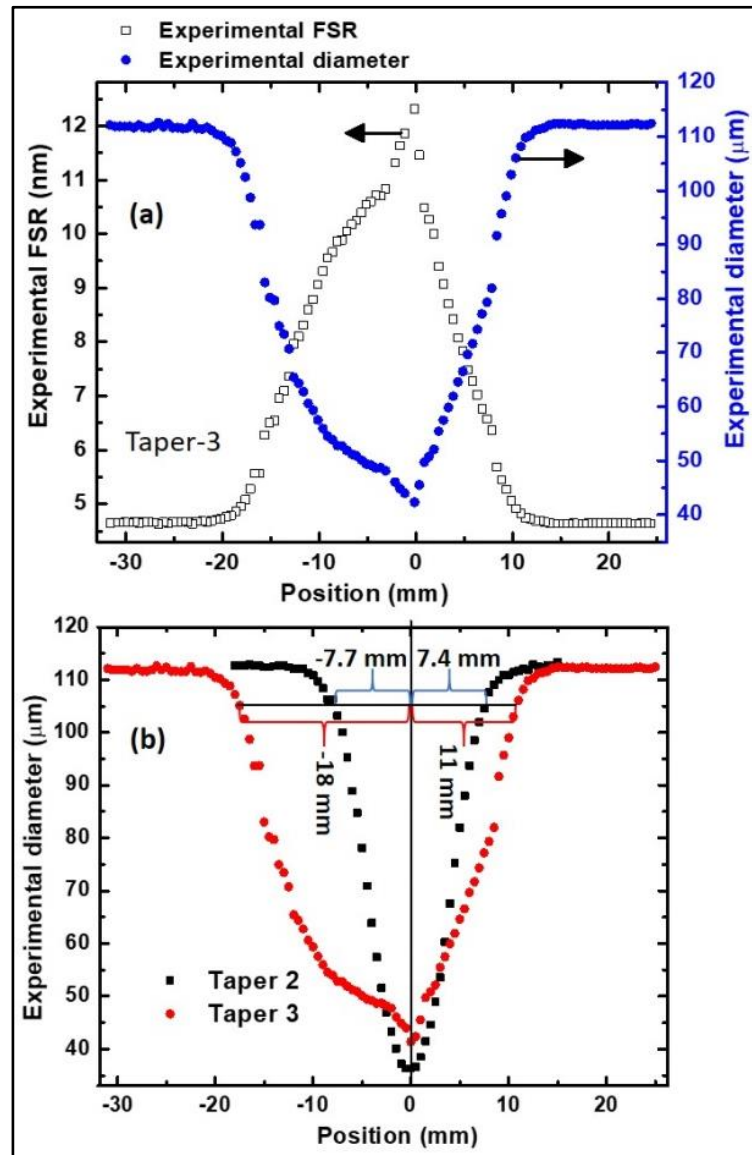


**Figure 25.** (a) FSR and experimental diameter vs position of the delivery fiber for an asymmetrical taper with a minimum waist region effective diameter  $\sim 41 \mu\text{m}$ . The experimental diameter is calculated by the WGM spectroscopy method. (b) Comparison of two experimental profiles for tapered optical fibers drawn under different conditions.

Both fiber tapers were fabricated using the same fabrication unit with different configurations. The symmetrical Taper-2 is fabricated by setting the  $\Psi$  parameter to zero ( $\Psi = 0$ ). Since Taper-2 has the smaller  $\Psi$  value, it is expected to be close to symmetrical. Thus, the two transition regions should have almost the same length. Taper-3 is fabricated by setting  $\Psi$  to 1 and because of the larger  $\Psi$  value is expected to have a more asymmetrical profile. The estimated minimum waist diameters are  $\sim 36.26 \mu\text{m}$  as before for Taper-2, and  $\sim 41.7 \mu\text{m}$  for Taper-3. From inspection of Figure 25(b) the waist region of Taper-3 is much less uniform and it is clear the left and right hand-side transition regions have very different lengths.

In order to systematically examine the measured asymmetry, a detailed comparison of the symmetric (Taper-2) and asymmetric taper (Taper-3) profiles is shown in Figure 26.

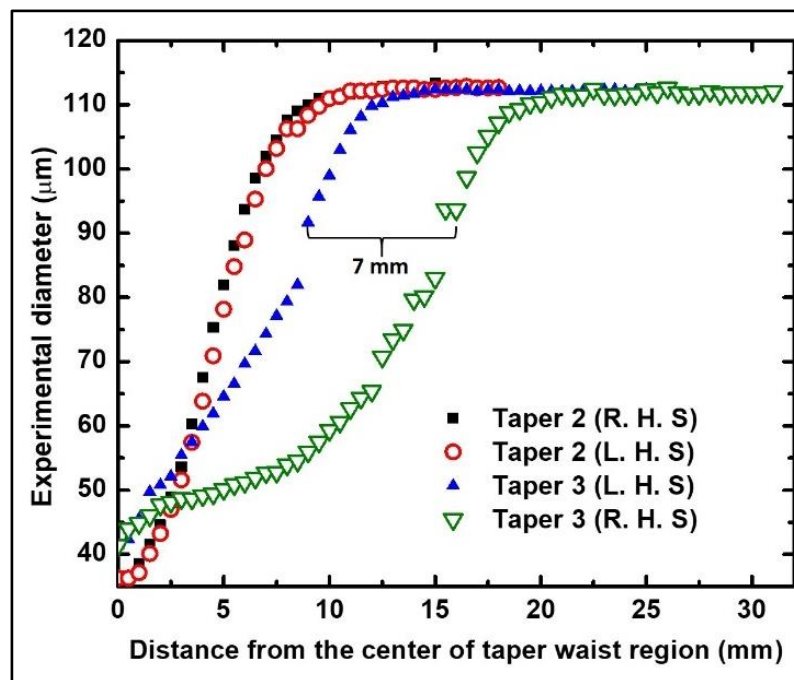


**Figure 26.** Comparison of variation in left and right-hand side transition regions of a symmetrical and an asymmetrical fiber taper.

Here the horizontal axis represents the distance from the center of the uniform



waist region towards left and right-hand side transition regions of the fiber tapers. The vertical axis illustrates the corresponding experimental diameter of the tapered region. From Figure 26, the profiles for the left and right-hand sides of Taper-2 almost overlap, indicating a high degree of symmetry. Taper-3 on the other hand is highly asymmetrical. Both the left and right-hand side transition regions are at maximum 7 mm apart with respect to the center of the uniform waist. The lengths of the transition regions are 12.5 mm and 9.5 mm.

The proposed method of diameter profiling requires accurate calculation of an FSR of the WGM spectrum within the wavelength range determined by the bandwidth of the broadband source used in the experiment. For the calculation of the spectrum's FSR, at least two WGM resonances must be observable in the given wavelength range, and since the FSR of a WGM spectrum is inversely proportional to the microresonator's diameter, the minimal measurable diameter is limited by the bandwidth of the optical source. In our experiment the broadband superluminescent diode source had a bandwidth of 1500-1600 nm, resulting in a minimal measurable diameter of the cylindrical microresonator of 6  $\mu\text{m}$ .

#### **2.2.4 Conclusions**

In conclusion, we have experimentally demonstrated a method for geometrical profiling of thin microfiber tapers with waist diameters ranging from  $\sim 10$  to  $\sim 50$   $\mu\text{m}$  with submicron accuracy. The method is based on the analysis of WGM resonances excited in cylindrical fiber resonators as a result of evanescent coupling of light propagating through the fiber taper under test. Tapered fibers with different shapes were fabricated deliberately to demonstrate the capabilities of the proposed method. It has been demonstrated that the proposed method allows for investigation of the tapers' symmetry and the length of the uniform waist region.

Measurement results have been verified by SEM microscopy with a maximum error of  $0.77\ \mu\text{m}$ . The proposed method can be applied in fabrication of fiber micro tapers as the means of accurate feedback of the taper diameter as a less expensive alternative with similar accuracy to microscopic measurements. It can also be used to detect flaws in a taper fabrication setup. Finally, the method could also be potentially applied to sensing of biochemical species on the surface of the microfiber, where the effective diameter and refractive index of the resonator fiber can be increased due to adsorption of biochemical species on the fiber surface.

### 2.3 References

1. G. C. Righini, Y. Dumeige, P. Féron, M. Ferrari, G. N. Conti, D. Ristic, and S. Soria, "Whispering Gallery Mode microresonators: Fundamentals and applications," *Riv. del Nuovo Cim.* **34**, 435–488 (2011).
2. A. B. Matsko and V. S. Ilchenko, "Optical resonators with whispering-gallery modes - Part I: Basics," *IEEE J. Sel. Top. Quantum Electron.* **12**, 3–14 (2006).
3. V. S. Ilchenko and A. B. Matsko, "Optical resonators with whispering-gallery modes - Part II: Applications," *IEEE J. Sel. Top. Quantum Electron.* **12**, 15–32 (2006).
4. M. Beresna, M. Gecevičius, and P. G. Kazansky, "Ultrafast laser direct writing and nanostructuring in transparent materials," *Adv. Opt. Photon.* **6**, 293-339 (2014).
5. D. W. Vernooy, V. S. Ilchenko, H. Mabuchi, E. W. Streed, and H. J. Kimble, "High-Q measurements of fused-silica microspheres in the near infrared," *Opt. Lett.* **23**, 247-249 (1998).

6. P. Wang, M. Ding, T. Lee, G. Senthil Murugan, L. Bo, Y. Semenova, Q. Wu, D. Hewak, G. Brambilla, and G. Farrell, "Packaged chalcogenide microsphere resonator with high Q-factor," *Appl. Phys. Lett.* **102**, 131110 (2013).
7. M. Sumetsky, "Mode localization and the Q-factor of a cylindrical microresonator," *Opt. Lett.* **35**, 2385-2387 (2010).
8. G. Farca, S. I. Shopova, and A. T. Rosenberger, "Cavity-enhanced laser absorption spectroscopy using microresonator whispering-gallery modes," *Opt. Express* **15**, 17443-17448 (2007).
9. X. Jin, Y. Dong, and K. Wang, "Selective excitation of axial modes in a high-Q microcylindrical resonator for controlled and robust coupling," *Appl. Opt.* **54**, 8100-8107 (2015).
10. A. W. Poon, R. K. Chang, and J. A. Lock, "Spiral morphology-dependent resonances in an optical fiber: effects of fiber tilt and focused Gaussian beam illumination," *Opt. Lett.* **23**, 1105–1107 (1998).
11. T. A. Birks, J. C. Knight, and T. E. Dimmick, "High-resolution measurement of the fiber diameter variations using whispering gallery modes and no optical alignment," *IEEE Photonics Technol. Lett.* **12**, 182–183 (2000).
12. M. Sumetsky and Y. Dulashko, "Radius variation of optical fibers with angstrom accuracy," *Opt. Lett.* **35**, 4006–4008 (2010).
13. A. Boleininger, T. Lake, S. Hami, and C. Vallance, "Whispering gallery modes in standard optical fibres for fibre profiling measurements and sensing of unlabelled chemical species," *Sensors* **10**, 1765–1781 (2010).
14. A. Yin, J. Gu, M. Li, and Y. Song, "Tunable high-Q tapered silica microcylinder filter," *Chin. Opt. Lett.* **11**, 082302 (2013).

15. X. F. Jiang, Y. F. Xiao, Q. F. Yang, L. Shao, W. R. Clements, and Q. Gong, “Free-space coupled, ultralow-threshold Raman lasing from a silica microcavity,” *Appl. Phys. Lett.* **103**, 101102 (2013).
16. X. F. Jiang, Y. F. Xiao, C. L. Zou, L. He, C. H. Dong, B. B. Li, Y. Li, F. W. Sun, L. Yang, and Q. Gong, “Highly unidirectional emission and ultralow-threshold lasing from on-chip ultrahigh-Q microcavities,” *Adv. Mater.* **24**, 1–5 (2012).
17. Q. F. Yang, X. F. Jiang, Y. L. Cui, L. Shao, and Y. F. Xiao, “Dynamical tunneling-assisted coupling of high-Q deformed microcavities using a free-space beam,” *Phys. Rev. A.* **88**, 1–8 (2013).
18. D. R. Rowland and J. D. Love, “Evanescent-wave coupling of whispering-gallery modes of a dielectric cylinder,” *IEEE Proceedings-J Optoelectron.* **140**, 177–188 (1993).
19. J. C. Knight, G. Cheung, F. Jacques, and T. A. Birks, “Phase-matched excitation of whispering-gallery-mode resonances by a fiber taper,” *Opt. Lett.* **22**, 1129–1131 (1997).
20. Y. Panitchob, G. S. Murugan, M. N. Zervas, P. Horak, S. Berneschi, S. Pelli, G. Nunzi Conti, and J. S. Wilkinson, “Whispering gallery mode spectra of channel waveguide coupled microspheres,” *Opt. Express* **16**, 11066–11076 (2008).
21. M. L. Gorodetsky and V. S. Ilchenko, “High-Q optical whispering-gallery microresonators: precession approach for spherical mode analysis and emission patterns with prism couplers,” *Opt. Commun.* **113**, 133–143 (1994).
22. V. S. Ilchenko, X. S. Yao, and L. Maleki, “Pigtailing the high-Q microsphere cavity: a simple fiber coupler for optical whispering-gallery modes,” *Opt. Lett.* **24**, 723–725 (1999).

23. M. Cai, O. Painter, and K. J. Vahala, "Observation of critical coupling in a fiber taper to a silica-microsphere whispering-gallery mode system," *Phys. Rev. Lett.* **85**, 74–77 (2000).
24. M. J. Humphrey, E. Dale, A. T. Rosenberger, and D. K. Bandy, "Calculation of optimal fiber radius and whispering-gallery mode spectra for a fiber-coupled microsphere," *Opt. Commun.* **271**, 124–131 (2007).
25. F. Monifi, J. Friedlein, S. K. Ozdemir, and Y. Lan, "A robust and tunable Add-Drop filter using whispering gallery mode microtoroid resonator," *J. Light. Technol.* **30**, 3306–3315 (2012).
26. Y. Dong, K. Wang, and X. Jin, "Packaged microsphere-taper coupling system with a high Q factor," *Appl. Opt.* **54**, 277-284 (2015).
27. F. Monifi, S. K. Ozdemir, J. Friedlein, and L. Yang, "Encapsulation of a fiber taper coupled microtoroid resonator in a polymer matrix," *IEEE Photonics Technol. Lett.* **25**, 1458–1461 (2013).
28. G. Zhao, Ş. K. Özdemir, T. Wang, L. Xu, E. King, G. L. Long, and L. Yang, "Raman lasing and Fano lineshapes in a packaged fiber-coupled whispering-gallery-mode microresonator," *Sci. Bull.* **62**, 875–878 (2017).
29. F. Bo, S. H. Huang, S. K. Ozdemir, G. Zhang, J. Xu, and L. Yang, "Inverted-wedge silica resonators for controlled and stable coupling," **39**, 1841–1844 (2013).
30. T. Kato, W. Yoshiki, R. Suzuki, and T. Tanabe, "Octagonal silica toroidal microcavity for controlled optical coupling," *Appl. Phys. Lett.* **101**, 121101 (2012).

31. J. A. Lock, "Morphology-dependent resonances of an infinitely long circular cylinder illuminated by a diagonally incident plane wave or a focused Gaussian beam," *J. Opt. Soc. Am. A.* **14**, 653–661 (1997).
32. J. A. Lock, "Scattering of a diagonally incident focused gaussian beam by an infinitely long homogeneous circular cylinder," *J. Opt. Soc. Am. A.* **14**, 653–661 (1997).
33. D. G. Rabus, "Integrated ring resonator," (Springer, 2007).
34. W. Bogaerts, P. de Heyn, T. van Vaerenbergh, K. de Vos, S. Kumar Selvaraja, T. Claes, P. Dumon, P. Bienstman, D. van Thourhout, and R. Baets, "Silicon microring resonators," *Laser Photonics Rev.* **6**, 47–73 (2012).
35. A. Weller, F. C. Liu, R. Dahint, and M. Himmelhaus, "Whispering gallery mode biosensors in the low-Q limit," *Appl. Phys. B.* **90**, 561–567 (2008).
36. W. Lin, H. Zhang, B. Liu, B. Song, Y. Li, C. Yang, and Y. Liu, "Laser-tuned whispering gallery modes in a solid-core microstructured optical fibre integrated with magnetic fluids," *Sci. Rep.* **5**, 1–10 (2015).
37. M. L. Gorodetsky, A. A. Savchenkov, and V. S. Ilchenko, "Ultimate Q of optical microsphere resonators," *Opt. Lett.* **21**, 453-455 (1996).
38. M. Ahmad and L. L. Hench, "Effect of taper geometries and launch angle on evanescent wave penetration depth in optical fibers," *Biosens. Bioelectron.* **20**, 1312–1319 (2005).
39. T. A. Birks and Y. W. Li, "The shape of fiber tapers," *J. Lightwave. Technol.* **10**, 432–438 (1992).
40. M. Sumetsky, "How thin can a microfiber be and still guide light?" *Opt. Lett.* **31**, 870-872 (2006).

41. N. Okada and J. Cole, "Simulation of whispering gallery modes in the Mie regime using the nonstandard finite-difference time domain algorithm," *J. Opt. Soc. Am. B.* **27**, 631–639 (2010).
42. T. Mukaiyama, K. Takeda, H. Miyazaki, Y. Jimba, and M. Kuwata-Gonokami, "Tight-binding photonic molecule modes of resonant bispheres," *Phys. Rev. Lett.* **82**, 4623–4626 (1999).
43. Y. H. Yang, Y. Zhang, N. W. Wang, C. X. Wang, B. J. Li, and G. W. Yang, "ZnO nanocone: Application in fabrication of the smallest whispering gallery optical resonator," *Nanoscale* **3**, 592–597 (2011).
44. M. Ibsen and R. I. Laming, "Fibre non-uniformity caused Bragg grating imperfections," *OFC/IOOC 1999 - Opt. Fiber Commun. Conf. Int. Conf. Integr. Opt. Opt. Fiber Commun.* **4**, 2–4 (1999).
45. L. Tong, and M. Sumetsky, "Subwavelength and nanometer diameter optical fibers" (Springer, 2010).
46. A. W. Poon, R. K. Chang, and D. Q. Chowdhury, "Measurement of fiber-cladding diameter uniformity by use of whispering-gallery modes: nanometer resolution in diameter variations along millimeter to centimeter lengths," *Opt. Lett.* **26**, 1867–1869 (2001).
47. J. Jasapara, E. Monberg, F. DiMarcello, and J. W. Nicholson, "Accurate noncontact optical fiber diameter measurement with spectral interferometry," *Opt. Lett.* **28**, 601-603 (2003).
48. F. Warken and H. Giessen, "Fast profile measurement of micrometer-sized tapered fibers with better than 50-nm accuracy," *Opt. Lett.* **29**, 1727-1729 (2004).

49. M. Young, P. D. Hale, and S. E. Mechels, "Optical Fiber Geometry: Accurate Measurement of Cladding Diameter," *J. Res. Natl. Inst. Stand. Technol.* **98**, 203–216 (1993).
50. J. F. Owen, P. W. Barber, B. J. Messinger, and R. K. Chang, "Determination of optical-fiber diameter from resonances in the elastic scattering spectrum," *Opt. Lett.* **6**, 272-274 (1981).
51. M. B. van der Mark and L. Bosselaar, "Noncontact calibration of optical fiber cladding diameter using exact scattering theory," *J. Lightwave. Technol.* **12**, 1–5 (1994).
52. D. H. Smithgall, L. S. Watkins, and R. E. Frazee, Jr., "High-speed noncontact fiber-diameter measurement using forward light scattering," *Appl. Opt.* **16**, 2395-2402 (1977).
53. J. C. Knight, H. S. T. Driver, G. N. Robertson, and M. Spie, "Measurement of capillary core size and taper using whispering-gallery-mode laser emission," *Opt. Eng.* **33**, 2838–2842 (1994).
54. E. Frins, H. Failache, J. Ferrari, G. D. Costa, and A. Lezama, "Optical-fiber diameter determination by scattering at oblique incidence," *Appl. Opt.* **33**, 7472–7476 (1994).
55. H. Y. Lin, C. H. Huang, G. L. Cheng, N. K. Chen, and H. C. Chui, "Tapered optical fiber sensor based on localized surface plasmon resonance," *Opt. Express*, **20**, 21693–21701 (2012).
56. Y. Tian, W. Wang, N. Wu, X. Zou, and X. Wang, "Tapered optical fiber sensor for label-free detection of biomolecules," *Sensors*, **11**, 3780–3790 (2011).



57. C. Bariáin, I. R. Matías, F. J. Arregui, and M. López-Amo, “Optical fiber humidity sensor based on a tapered fiber coated with agarose gel,” *Sensors Actuators, B Chem.* **69**, 127–131 (2000).
58. W. Jin, H. L. Ho, Y. C. Cao, J. Ju, and L. F. Qi, “Gas detection with micro- and nano-engineered optical fibers,” *Opt. Fiber Technol.* **19**, 741–759 (2013).
59. M. Deng, D. Liu, and D. Li, “Magnetic field sensor based on asymmetric optical fiber taper and magnetic fluid,” *Sensors Actuators, A Phys.* **211**, 55–59 (2014).
60. R. Radzali, Y. M. Kamil, M. A. Mahdi, and M. H. A. Bakar, “Asymmetric fiber taper for temperature sensing applications,” *IBP 2015 - 2015 IEEE Int. Broadband Photonics Conf.* 76–81 (2015).
61. N. H. M. Halip, N. S. Isa, A. A. Latif, M. A. Mahdi, M. H. A. Bakar, “Asymmetric fiber taper for narrow linewidth comb filter,” *J. Teknol. Sciences Eng.* **3**, 117–121 (2016).
62. C.-L. Lee, W.-C. Shih, J.-M. Hsu, and J.-S. Horng, “Asymmetrical dual tapered fiber Mach-Zehnder interferometer for fiber-optic directional tilt sensor,” *Opt. Express* **22**, 24646–24654 (2014).
63. M. Sumetsky, “Surface nanoscale axial photonics sensors,” *Opt. Express*, **19**, 26470-26485 (2015).
64. M. Sumetsky, D. J. DiGiovanni, Y. Dulashko, J. M. Fini, X. Liu, E. M. Monberg, and T. F. Taunay, “Surface nanoscale axial photonics: robust fabrication of high-quality-factor microresonators,” *Opt. Lett.* **36**, 4824-4826 (2011).

65. M. Sumetsky and Y. Dulashko, “SNAP: Fabrication of long coupled microresonator chains with sub-angstrom precision,” *Opt. Express*, **20**, 27896-27901 (2012).
66. M. Sumetsky, “Theory of SNAP devices: basic equations and comparison with the experiment,” *Opt. Express*, **20**, 22537 (2012).
67. F. Shen, A. Dmitriev, N. Gordon, L. Zhang, X. Shu, and M. Sumetsky, “Surface nanoscale axial photonics (SNAP) structures introduced with a femtosecond laser,” *Conf. Lasers Electro-Optics, CLEO 2016 41*, 2795–2798 (2016).
68. A. Yariv, “Universal relations for coupling of optical power between microresonators and dielectric waveguides,” *Electron. Lett.* **36**, 321–322 (2000).
69. X. Zhang, T. Liu, J. Jiang, K. Liu, Z. Yu, M. Feng, W. Liu, and W. Chen, “Ultraprecise resonance wavelength determination for optofluidic sensing applications,” *IEEE Photonics Technol. Lett.* **27**, 399–402 (2015).
70. Y. V. Alekseenko, A. M. Monakhov, and I. V. Rozhanskii, “Whispering gallery modes in a conical resonator,” *Tech. Phys.* **54**, 1633–1638 (2009).
71. G. Brambilla, V. Finazzi, and D. J. Richardson, “Ultra-low-loss optical fiber nanotapers,” *Opt. Express*, **12**, 2258-2263 (2004).
72. L. Bo, P. Wang, Y. Semenova, and G. Farrell, “High sensitivity fiber refractometer based on an optical microfiber coupler,” *IEEE Photonics Technol. Lett.* **25**, 228–230 (2013).

## Chapter 3

---

---

# WGMs of polymer cylindrical microresonators for strain tunable devices and strain sensors

---

---

As discussed in Chapter 1, the exceptional sensitivity of the WGM spectrum to the diameter of the cylindrical micro-resonator and its refractive index can be utilized for strain sensing and strain-induced tuning of WGM resonances. It should be noted however that due to their relatively high elastic modulus, traditional silica fiber based microcylinders have limited sensitivity to strain or force. This chapter explores the use of polymer fibers and polymer wires with smaller elastic modulus as a basis for microcylindrical WGM resonators that can provide higher sensitivity to strain and wider tuning range in the above applications.

This chapter also aims to address one of the main objectives of the thesis by proposing a novel robust packaging method for practical WGM sensors and tunable devices, based on cylindrical fiber micro-resonators and investigating the influence of the packaging on the devices' performance. The mechanical stability of the packaging has been confirmed by vibration tests using a vertical vibration generator. The influence of the ambient temperature on the performance of the packaged device has also been investigated and its temperature cross-sensitivity is estimated. The proposed novel polymer wire based packaged strain sensor/tunable device possesses several desirable features such as ease of fabrication, small

footprint, and large dynamic range of strains.

### **3.1 Strain induced spectral tuning of the whispering gallery modes in a cylindrical micro-resonator formed by a polymer optical fiber<sup>4</sup>**

**Abstract:** A mechanical strain assisted technique for spectral tuning of whispering gallery modes (WGM) in a cylindrical micro-resonator formed by a polymer optical fiber (POF) is investigated. WGMs in the POF based micro-cylinder are excited by evanescent light coupling using a tapered single mode silica fiber. WGMs observed in the transmission spectrum of the silica fiber taper have a high extinction ratio of up to 19 dB and a Q-factor of up to  $2.64 \times 10^4$ . The application of tensile axial strain ( $\mu\epsilon$ ) in the range from 0 to 1746  $\mu\epsilon$  (0.17 %) to the POF micro-resonator results in a linear shift of the WGM spectrum with a sensitivity of 0.66 pm/ $\mu\epsilon$ . Under the influence of the applied strain the WGMs undergo a blue shift and return to their initial spectral positions after the strain is decreased. The proposed strain-tunable POF micro-resonator has potential applications in fiber optic sensing and tunable micro lasers.

**OCIScodes:** (140.3945) Microcavities; (140.3948) Microcavity devices; (060.2370) Fiber optics sensors; (250.5460) Polymerwaveguides.

---

<sup>4</sup> V. Kavungal, A. K. Mallik, G. Farrell, Q. Wu, and Y. Semenova, "Strain-induced spectral tuning of the whispering gallery modes in a cylindrical micro-resonator formed by a polymer optical fiber" *Applied Optics*. **56**, 1339-1345 (2017).

### 3.1.1 Introduction

Whispering gallery mode (WGM) micro-resonators (MRs) are attractive photonic devices due to their small mode field volume, narrow spectral linewidths and high Q-factors [1–3]. Such MRs have found applications in numerous fields, including studies of nonlinear optical effects [4], in quantum electrodynamics [5] and for low threshold miniature scale lasers [6]. One of the most promising applications of WGM MRs is in the area of optical sensing [3,7,8], where such resonators exhibit a higher sensitivity than their macro-fiber counterparts. WGMs can be supported by a variety of resonator geometries, such as spheres [9], spheroids [10], disks [11], rings [7] and cylinders [12]. The choice of the specific resonator for a given application is typically impacted by the three main considerations such as the maximum achievable Q-factor, simplicity of fabrication and ease of interconnection [13].

For cylindrical resonators based on a section of optical fiber there are a number of potential advantages that make such resonators worth exploring: (1) a very simple fabrication process since optical fibers are highly uniform in diameter, allowing large numbers of identical resonators to be fabricated and providing a high degree of repeatability; (2) optical fibers can be easily manipulated and mounted, and (3) the alignment for optimal coupling of the excitation light into the fiber MR has on only one angular degree of freedom, as opposed to two for experiments involving microspheres [14]. As a result, the optical setup for the cylindrical fiber-based microresonator experiments is more straightforward.

Spectral positions of WGM resonances can be tuned by various external stimuli. Numerous reports demonstrate tuning WGM resonant wavelengths of spherical MRs by changing surrounding refractive index [15], applying mechanical strain to

the resonator [16], changing internal pressure [17], applying external electric field [18], *etc.* Self-tuning of WGM resonances has been demonstrated for a standalone silica microsphere by changing its temperature under the influence of the gas flow surrounding the resonator [19]. In a cylindrical MR tuning of WGM resonances using mechanical strain was demonstrated for the first time by A. L. Huston *et al.* [20]. In this work the morphology dependent resonance properties were studied in the elastic scattering spectra of a 1 mm long section of a 125  $\mu\text{m}$  diameter single mode silica optical fiber.

Due to their relatively high elastic modules, silica WGM resonators-based sensors have limited sensitivity to strain or force. Measurement sensitivity can be improved by using dielectric materials with smaller elastic modulus, such as polymers. For example, Ioppolo *et al.* [21–24] have demonstrated that solid, as well as hollow Polymethyl-methacrylate (PMMA) microspheres have higher strain sensitivity compared to that made of silica.

More recently tuning of WGM lasing modes in a polymer optical fiber (POF) based resonator under tensile strain was reported in [25]. The experiment was carried out by scattering of focused laser beams on a section of Rhodamine B doped POF. The spectral shift of WGMs excited in a photonic crystal fiber MR infiltrated with magnetic fluid under the influence of external magnetic fields is investigated in [26] and laser assisted tuning method for WGMs in a cylindrical MR based on magnetic-fluids infiltrated microstructured optical fibers is reported in [27]. This paper presents the findings of a comprehensive investigation of mechanical strain tuning of WGMs for a POF based cylindrical micro resonator. Cross-coupling takes place between the evanescent fields of the guided modes from a tapered single mode silica optical fiber in close physical contact with a

micro-cylinder with an outer diameter of 490  $\mu\text{m}$ . The transmission spectrum of the silica taper coupled to the POF MR shows very high extinction ratio dips corresponding to the WGM eigenmodes. Spectral tuning of the WGM dips is investigated under the influence of increasing and decreasing axial tensile strain applied to the POF micro-cylinder. The influence of the input light polarization on the WGMs tuning is also studied by carrying out the experiments for different input light polarization states.

The proposed POF cylindrical micro-resonator possesses several desirable features such as highly sensitive strain assisted tunability, high linear strain dependence and ease of fabrication, which make it a good candidate for applications in optical fiber sensing and for tunable micro-fiber lasing.

### **3.1.2 Experimental arrangements**

The experimental setup for studies of the influence of strain on the WGMs excited in the cylindrical MR is shown schematically in Figure 27. The cylindrical MR was formed by a section of a  $490\pm 5$   $\mu\text{m}$  (outer diameter) graded index POF (GIPOF 50, Thorlabs). The evanescent light coupling to the micro cylinder was achieved by a full fiber taper placed in close contact with the POF micro-cylinder [28]. The optical fiber tapering is undertaken using the micro heater brushing technique [29]. The fabricated fiber taper has a waist diameter of circa 1.3  $\mu\text{m}$ . The input end of the fiber taper was connected to a super luminescent diode (SLD) (Thorlabs), with a wavelength range of 1500-1600 nm. Light from the SLD was passed through a three-paddle manual polarization controller and the output of the fiber taper was connected to the Optical Spectrum Analyzer (OSA) (86142B, Agilent).

As illustrated in Figure 27, in order to apply the strain to the resonator, one end of the POF micro-cylinder was immobilized with a fiber holder and the other end was attached to the micro translation stage with a resolution of 10  $\mu\text{m}$ . The length between the two fixed points is considered as the sensing length. Here the sensing length of the POF MR was set to 63 mm for ease of mounting. The strain is applied to the POF micro-cylinder by moving the translation stage with a step size of 10  $\mu\text{m}$  (corresponding to an applied tensile strain step of 159  $\mu\epsilon$  (0.016 %)) in a direction away from the fixed end.

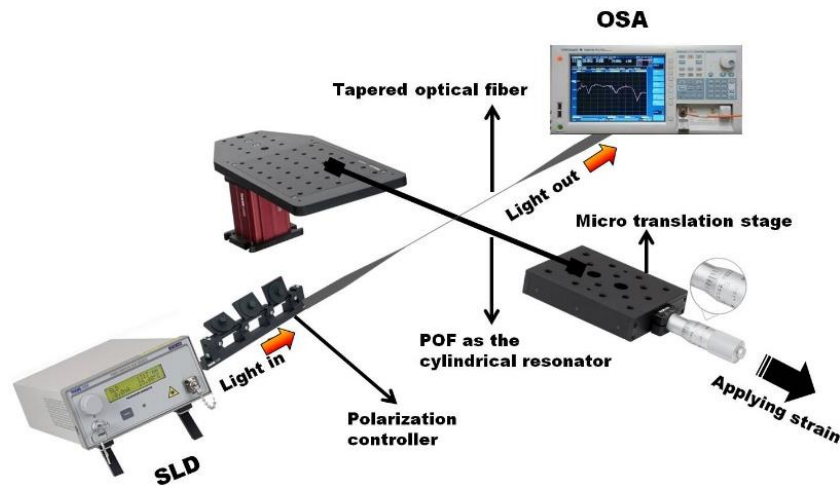


**Figure 27.** Schematic diagram of the experimental setup for studies of the tunability of WGMs in the POF resonator under the influence of applied strain.

During each experiment, the polarization state of the input light was controlled by the three-paddle polarization controller (FPC030, Thorlabs). For investigation of the effect of the input light polarization on the WGMs tuning properties, we compare our results for three different linear polarization states, as described later in the paper. During each measurement of the shift of the WGM spectrum with respect to the applied strain, the input polarization state was fixed. All the measurements were carried out at a constant laboratory temperature (20  $^{\circ}\text{C}$ ).



### 3.1.3 The effect of strain on the WGM resonance wavelength

Figure 28(a) shows the whispering gallery mode spectrum of the unstrained POF micro-cylinder with a diameter of 490  $\mu\text{m}$ .

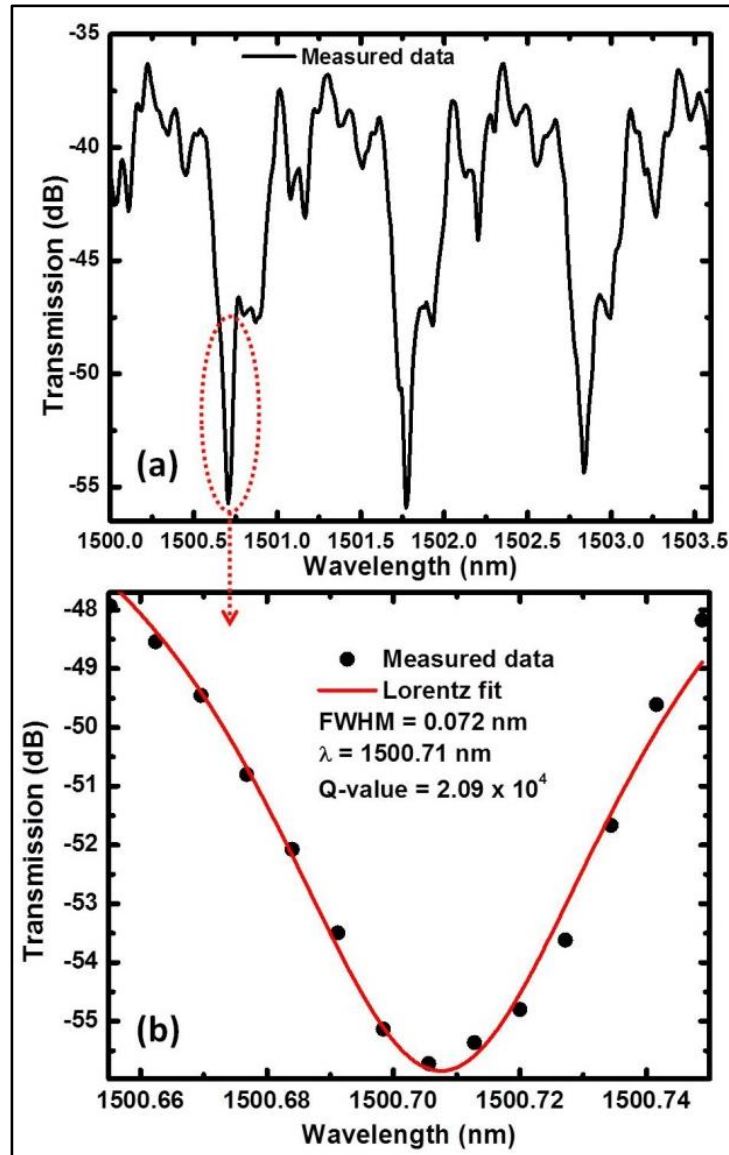


**Figure 28.** (a) Whispering gallery modes spectrum generated by the POF MR, (b) Lorentzian fittings of the spectral dips p1. The dip has the central wavelength at 1500.71 nm, and its FWHM and the corresponding Q-factor are 0.072 nm and  $2.09 \times 10^4$  respectively.

Three WGM resonance dips are observed within the selected 3.6 nm-wide wavelength band. The full widths at half maxima (FWHMs) of the observed resonance dips are measured and their Q factors are calculated using the equation

$Q = \lambda/\Delta\lambda$ , where  $\lambda$  is the resonance wavelength and  $\Delta\lambda$  is the corresponding FWHM. All the Q-factors of the resonance dips in the selected range are approximately equal to  $2 \times 10^4$ . For example, Figure 28(b) shows the Lorentz fit of a selected resonance dip (p1). The dip has the central wavelength at 1500.71 nm, and its FWHM and the corresponding Q-factor are 0.072 nm and  $2.09 \times 10^4$  respectively. The extinction ratios of all the three resonant dips are larger than 18 dB. The average free spectral range associated with the resonant pattern in the specified wavelength range is 1.07 nm.

We experimentally investigated the strain tuning of the POF based micro-resonator using the experimental setup schematically illustrated in Figure 27. Figure 29 shows the evolution of the WGM spectrum of the POF MR as the axial strain is increased from zero to 1746  $\mu\epsilon$  and then decreased back to zero.

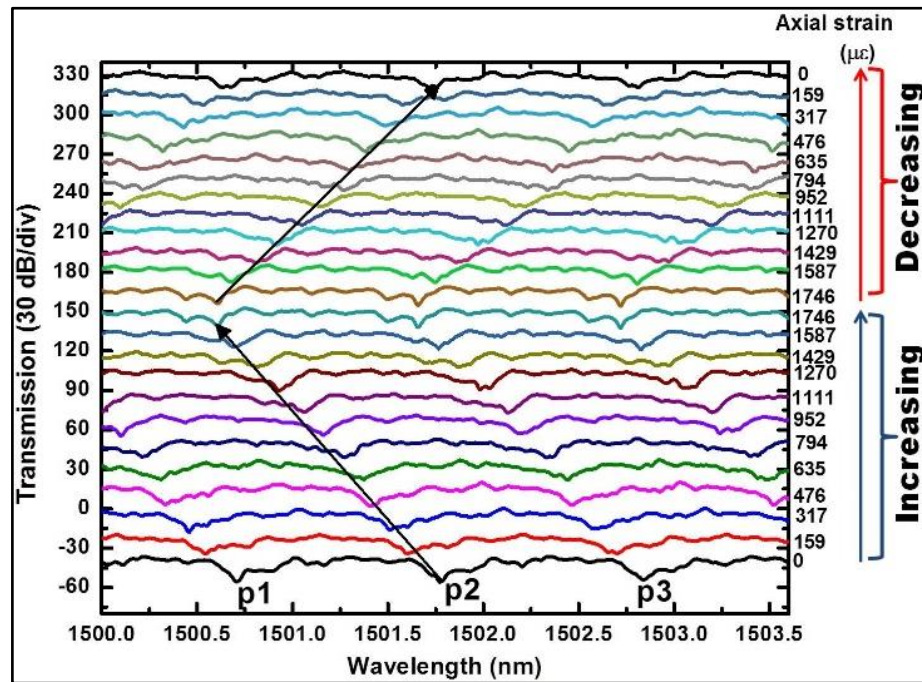


**Figure 29.** Evolution of the tapered fiber transmission spectrum under the influence of the increasing axial strain, followed by the strain decrease back to the unstrained position. For illustrative purposes each consecutive spectrum is plotted with an artificial offset of 30 dB compared to the prior spectrum. The arrows indicate the resonant wavelength shift direction.

As the axial strain increases, the resonant dips exhibit a linear blue shift. When the applied tensile strain is decreased back to zero, the resonance dips linearly red-shift back to their initial positions, which indicates a good reversibility of the proposed WGM tuning approach.

Before considering the wavelength tuning in more detail, it is useful to analyze the expected tuning effect of strain. For this a simple model to predict the tuning of the WGM resonances was developed, based on the two primary assumptions as follows. The first one is the fact that the micro-resonator diameter can be related to the value of the applied axial tensile strain. The second assumption is that there is a measurable change in the refractive index brought about by the different mechanical stress and strain components within the resonator material. Taken together the fractional change in the wavelength of the WGMs is [21–25, 30–33]:

$$\frac{\Delta\lambda}{\lambda} = \frac{\Delta D}{D} + \frac{\Delta n}{n} \quad (3.1)$$

Where  $\Delta D/D$  is the fractional change in the MR diameter ( $D$ ) due to the deformation of the micro-cavity and  $\Delta n/n$  is the fractional change in the refractive index ( $n$ ) due to the induced stress. The transverse deformation ( $\Delta D/D$ ) of the micro-cavity can be related to the axially applied tensile strain ( $\Delta L/L$ ) by Poisson ratio ( $\sigma$ ). The Poisson ratio is the ratio of the lateral contraction strain ( $\Delta D/D$ ) to the axial tensile strain ( $\Delta L/L$ ).

$$\sigma = \frac{\Delta D/D}{\Delta L/L}$$

$$\frac{\Delta D}{D} = \sigma \frac{\Delta L}{L} \quad (3.2)$$

Changes in the fiber dimensions result in changes in the material density with the corresponding induced changes in its refractive index ( $\Delta n$ ). Thus, changes in the refractive index can be expressed as

$$\Delta n = nP_{eff} \frac{\Delta L}{L} \quad (3.3)$$

Where  $P_{eff}$  is the effective strain-optic coefficient [25, 32]. Subsequently the WGM resonance wavelength shift can be expressed as

$$\frac{\Delta \lambda}{\lambda} = -\left(\sigma \frac{\Delta L}{L} + P_{eff} \frac{\Delta L}{L}\right) \quad (3.4)$$

Here the negative sign shows that the axial tensile strain applied to the POF micro-resonator will result in a blue shift of the WGM resonance. The Poisson ratio and the effective strain-optic coefficient of PMMA are 0.35-0.45 and 0.099 ( $\pm 0.0009$ ) respectively [20,25,32,34]. By assuming Poisson's ratio ( $\sigma$ ) of the POF is 0.35, theoretical calculation based on Eq. (3.4) shows that the sensitivity of WGM resonance wavelength shift with respect to increasing and decreasing tensile strain is 0.68 pm/ $\mu\epsilon$ .

Figures 30(a) and (b) correspond to the resonance dips p2 and p3 respectively (as depicted in Figure 29). Here the black dots are the measured data and the solid red line is the linear fit. It is clear that all of the resonance dips move towards the shorter wavelengths in a linear fashion with a good sensitivity to the applied axial tensile strain. For each 10  $\mu\text{m}$  axial elongation (corresponding to a tensile strain of 159  $\mu\epsilon$  (0.016 %)) it is found that the WGMs shift by 0.11 nm on average. Here the second dip of the WGM spectrum, p2, shifts from 1501.77 nm to 1500.605 nm and the third dip, p3, shifts from 1502.84 nm to 1501.66 nm in response to a 110  $\mu\text{m}$  elongation (corresponding to the applied strain of 1746  $\mu\epsilon$  (0.17 %)). Linear fitting of the wavelength response data indicates that the linear regression coefficient is greater than 0.99 for both p2 and p3 dips. It could be also seen that the tuning sensitivities of these WGMs are equal to 0.64 pm/ $\mu\epsilon$  and 0.66 pm/ $\mu\epsilon$  for p2 and p3 dips respectively which is in close agreement with the theoretically

calculated sensitivity of  $0.68 \text{ pm}/\mu\epsilon$ .

The wavelength tuning of the WGM of the POF MR by applying axial tensile strain is also found to be reversible. Figure 31 shows the return of the shifted spectra to their initial positions with the decrease of the applied axial tensile strain.

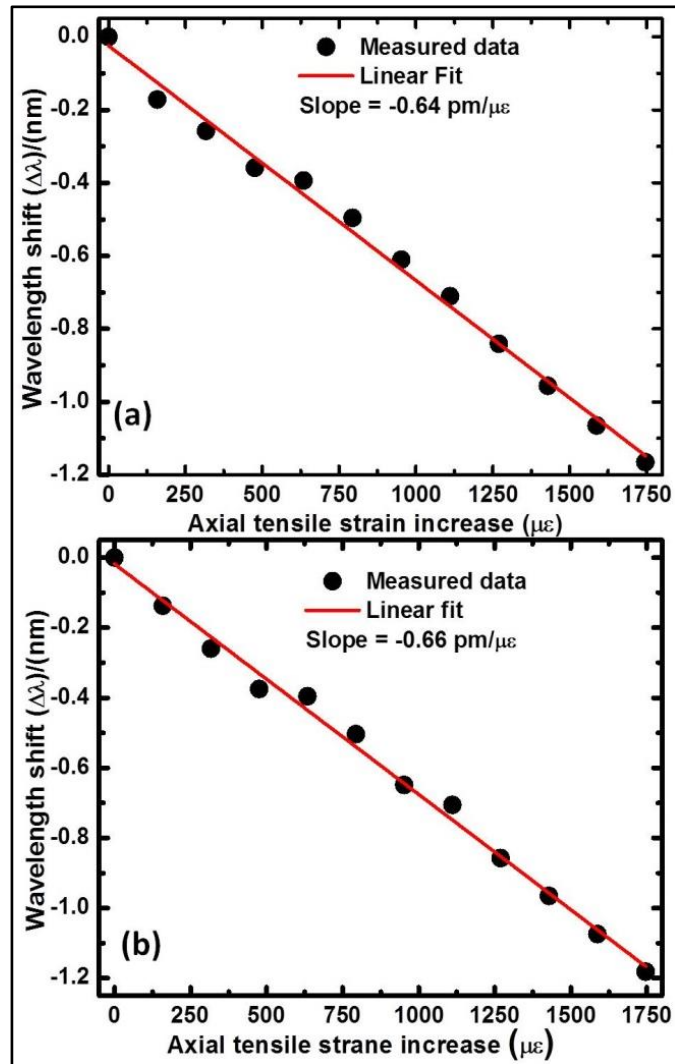


**Figure 30.** Wavelength shift of the selected WGM resonances as a function of increasing axial strain: (a) dip p2 and (b) dip p3 (as depicted in Fig. 29). The measured wavelength shift (scatter data) is linearly fitted (solid line). Linear fitting of the wavelength response data indicates that the linear regression coefficient is greater than 0.99 for both p2 and p3 dips. The slopes of the linear dependencies are  $-0.64 \text{ pm}/\mu\epsilon$  for p2 and  $-66 \text{ pm}/\mu\epsilon$  for p3 respectively.

Figures 31(a) and (b) illustrate the wavelength shift corresponding to the decrease of the applied axial tensile strain for the WGM resonant dips p2 and p3 respectively. Here the black dots are the experimentally measured data and the solid red line is the linear fit.

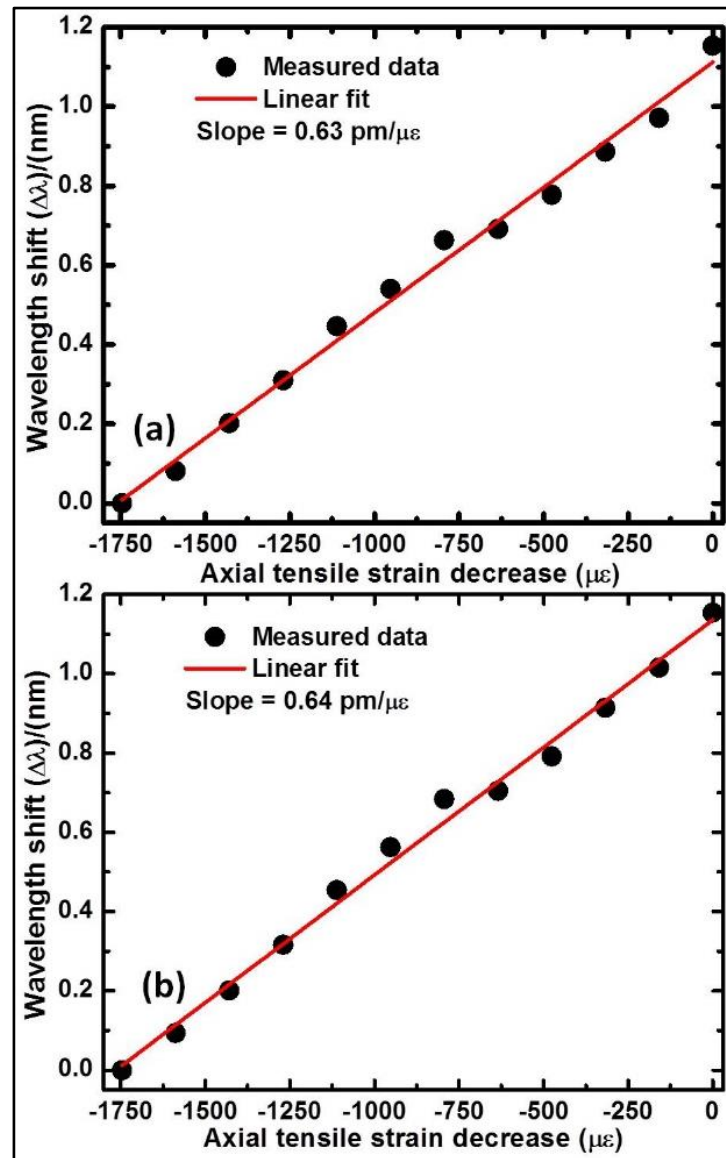


**Figure 31.** Wavelength shifts of the selected WGM resonances as a function of decreasing axial strain: (a) dip p2 and (b) dip p3. The measured wavelength shift (scatter data) is linearly fitted (solid line). Linear fitting of the wavelength response data indicates that the linear regression coefficient is greater than 0.99 for both p2 and p3 dips. The slopes of the linear dependences are 0.63 pm/ $\mu\epsilon$  for p2 and 0.64 pm/ $\mu\epsilon$  for p3 respectively.

Here the linear regression coefficient is greater than 0.99 for both p2 and p3 dips. The negative values of the X-axis illustrate the gradual decrease of the applied axial tensile strain from its maximum value to the initial unstrained state. It is clear that all of the resonance dips move towards the longer wavelengths (initial position) in a linear fashion. For each 10  $\mu\text{m}$  translation (corresponding to the decrease in the applied strain by 159  $\mu\epsilon$  (0.016 %)) in the axial direction, it is found that the WGMs experience an average red shift of 0.11 nm. That means that the spectral shifts of the WGMs are similar in both cases: with the increase and decrease of the applied axial tensile strain. Here the second dip of the WGM spectrum, p2, shifts from 1500.60 nm to 1501.76 nm and the third dip, p3, shifts from 1501.66 nm to 1502.81 nm over the range of strains from the maximum value of 1746  $\mu\epsilon$  (0.17 %) to zero. The strain sensitivity of dip p2 is 0.63 pm/ $\mu\epsilon$  and that of p3 is 0.64 pm/ $\mu\epsilon$ , both in close agreement with the theoretical slope of 0.68 pm/ $\mu\epsilon$ .

Detailed studies of hysteresis of the WGMs tuning with the applied strain and the outcomes are presented in Figure 32. Figure 32(a) and (b) show the WGMs resonance wavelengths of p2 and p3 during the full measurement cycle, including the increase in the applied axial tensile strain and its subsequent complete decrease. Here the black arrows indicate the direction of the WGMs shift during the increase of the applied axial tensile strain and the red arrows show the direction of the spectral shifts during the strain decrease. The inset graphs in Figure 32(a) and (b) illustrate the differences in the WGM dip wavelengths corresponding to the same strain values applied axially during the strain increase ( $\lambda$  (S.I)) and strain decrease ( $\lambda$  (S.D)) cycles. The maximum dip wavelength difference between the increase and decrease cycles of the applied axial strain is estimated as 90 pm.

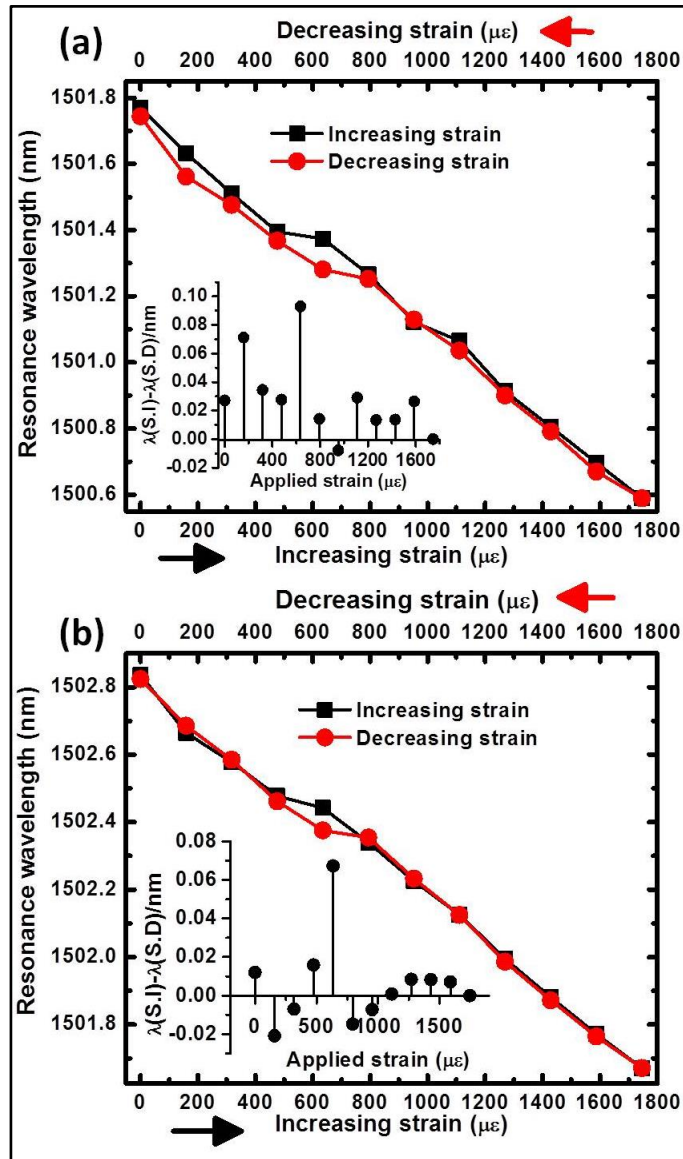


**Figure 32.** Selected WGM resonances during the strain increase (S. I) (black) and strain decrease (S. D) (red) cycles: (a) dip p2 and (b) dip p3. Inset figures show the discrepancies in WGM wavelengths during the increase and decrease cycles.

Such small discrepancies between the WGM wavelengths when increasing and decreasing the strain could be explained by the non-uniform deformations experienced by the POF micro-cylinder during elastic deformation [25].



### 3.1.4 Polarization effects

In order to investigate the impact of the input light polarization and to demonstrate the repeatability of the results presented in the previous section, we carried out the experiments above for different input light polarizations.

As shown previously in Figure 27, the polarization of the light at the input end of the fiber taper is controlled by the three-paddle polarization controller (FPC030, Thorlabs). The working principle of FPC030 is based on the stress-induced birefringence within single mode fiber (SMF 28) created through bending and twisting of the fiber.

The quarter wave plate in the polarization controller transforms the input polarization state into a linear polarization state. The linearly polarized light can then be rotated to a desired angle with respect to the initial state using the middle half wave plate paddle of the polarization controller. The twisting regions of the fiber due to rotating the paddle by an angle ' $\tau$ ' will rotate the polarization by an angle

$$\theta = \alpha\tau \quad (3.5)$$

where  $\alpha = -n^2 p_{44}$  [35]. Here  $p_{44}$  is the elasto-optic coefficient of the fiber and  $n$  is the refractive index of the core. The elasto-optic coefficient of fused silica is given by  $p_{44} = \frac{p_{11} - p_{12}}{2}$ , where numerical values of  $p_{11}$  and  $p_{12}$  respectively given by 0.121 and 0.270 [36].

For the experiments the input polarization state was set as follows: the three paddles had initial vertical positions and then the middle half wave fiber paddle was rotated through its full travel range while the other two quarter wave fiber

paddles remained in their starting, vertical positions. The strain tunability experiments using POF MR were repeated for three more linearly polarized input states by rotating  $0^\circ$ ,  $45^\circ$ , and  $90^\circ$  angle of the central half wave plate of the polarization controller from its initial vertical position. The corresponding rotation of polarization from the initial position is calculated by Eq. (3.5) as  $0^\circ$ ,  $7.22^\circ$ , and  $14.44^\circ$  respectively.

For comparison, Figure 33 shows the WGM resonance spectra excited by a  $490\ \mu\text{m}$  diameter POF MR with the  $0^\circ$ ,  $7.22^\circ$ , and  $14.44^\circ$  angles of the input light polarization.

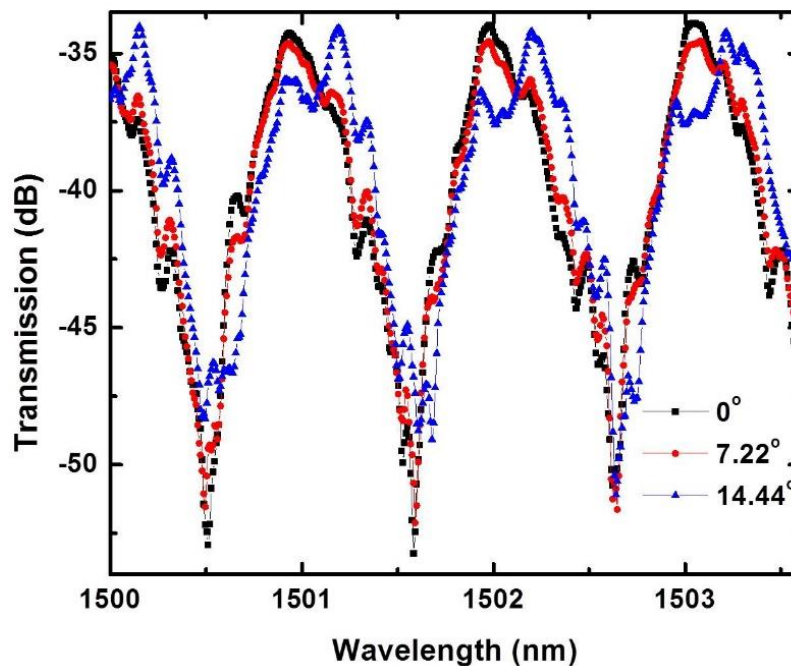


**Figure 33.** WGM resonant spectra from the POF MR with different input light polarizations.

The Q-factors of the resonance dips are of the same order of magnitude in each of the cases ( $\sim 10^4$ ). The maximum extinction ratio of the resonances reaches up to 19 dB. The average free spectral range of the resonances is 1.07 nm. With the changes in the input light polarization, WGM spectra show small differences in the dip

amplitudes and shapes but no significant influence was observed on the tunability of the WGMs spectrum.

Strain sensitivity during the increasing and decreasing cycles of the axial tensile strain shows small differences arising from polarization state changes, possibly because of the non-uniform deformation experienced by the strained POF MR. Figure 34(a), (b), and (c) show the selected WGM resonance wavelengths during increasing and decreasing cycles of the axial tensile strain for different input polarization orientations. Figure 34(d) shows the corresponding strain sensitivity of the POF MR undergoing increasing and decreasing strain cycles.

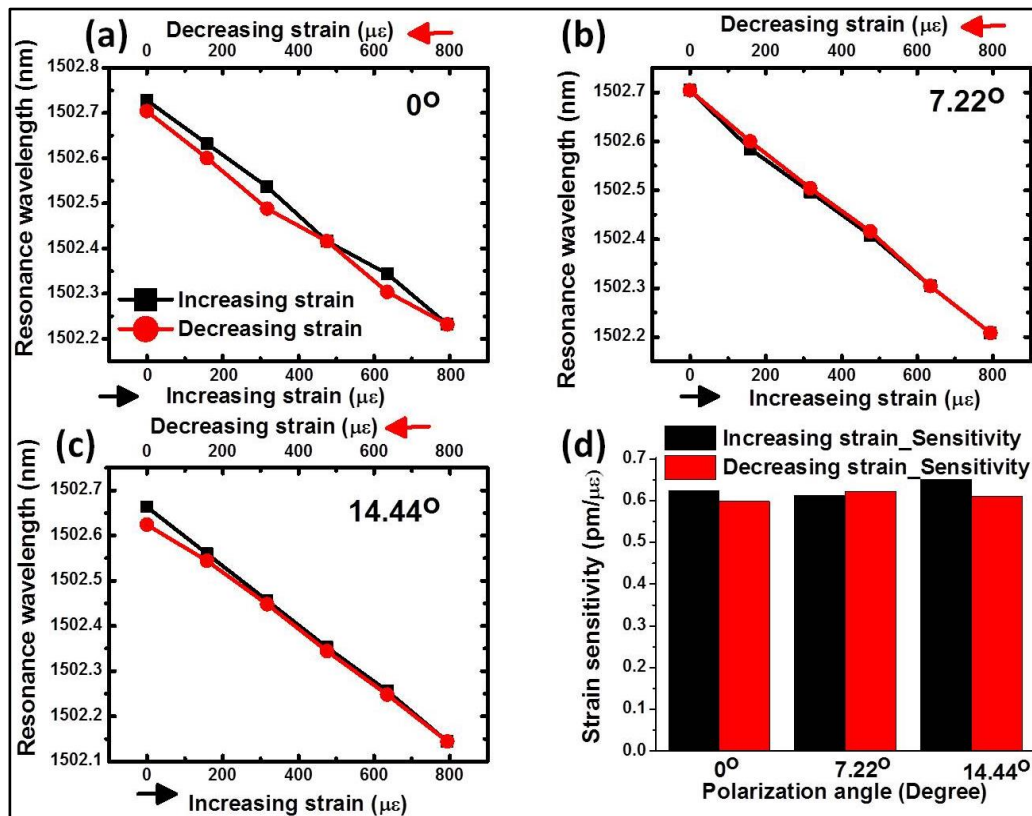


**Figure 34.** Selected WGM resonances during the strain increase (black) and strain decrease (red) cycles with different input light polarization. Here linearly polarized input light is rotated by angle (a)  $0^\circ$ , (b)  $7.22^\circ$ , and (c)  $14.44^\circ$  respectively. (d) Sensitivity of the increase and decrease cycles of the axial tensile strain.

### 3.1.5 Conclusions

In conclusion, we investigated the effect of mechanical strain tuning of the whispering gallery mode resonances excited in a POF cylindrical micro resonator. The light was evanescently coupled into the micro-cylinder from a standard single mode silica optical fiber taper fabricated by the micro heater brushing technique. WGMs observed in the fiber taper's transmission spectrum had a high extinction ratio of up to 19 dB and a Q-factor of up to  $2 \times 10^4$ . We experimentally demonstrated that spectral positions of the WGM resonances shift linearly during the increase and decrease of the axial tensile strain applied to the micro-cylinder in the range of strains from 0 to  $1746 \mu\epsilon$  (0.17 %). The WGMs move toward shorter wavelengths with the increase of the applied strain and return to their initial positions when the strain is decreased. Tuning of the WGMs is observed independently of the input light polarization. The WGMs resonance strain sensitivity reaches  $0.66 \text{ pm}/\mu\epsilon$ . We developed a simple analytical model describing the tuning effect. Strain sensitivity during increasing and decreasing cycles of axial tensile strain shows small differences, possibly due to non-uniform deformation experienced by the strained POF MR. The proposed POF based strain tunable micro resonator possesses several desirable features such as ease of fabrication and modification of the resonator surface for potential applications in fiber optic sensing and tunable micro lasing.

## **3.2 A packaged whispering gallery mode strain sensor based on a polymer-wire cylindrical micro resonator<sup>5</sup>**

**Abstract:** We propose a whispering gallery mode (WGM) strain sensor formed by a polymer-wire cylindrical micro resonator for strain measurement applications. WGMs are generated by evanescently coupling light into the polymer-wire resonator from a silica fiber taper fabricated by the micro heater brushing technique. Accurate and repeatable measurements of a strains up to one free spectral range (FSR) shift of the WGMs (corresponding to 0.33 % of the polymer-wire elongation, 3250  $\mu\epsilon$ ) are demonstrated experimentally with the proposed sensor. Practical packaging method for the proposed strain sensor on a glass microscope slide has also been realized making the sensor portable and easy to handle. The robustness of the packaged coupling system is confirmed by vibration tests. The performance of the packaged strain sensor is evaluated and compared with that for an unpackaged sensor.

**Keywords:** Whispering gallery modes; Optical fiber sensors; Optoelectronic and photonic sensors; Mechanical sensors; Microsensors; Force sensors; Cavity resonators; Resonator filters; Optical tuning.

### **3.2.1 Introduction**

Strain is a measure of the deformation of an object when subject to an applied

---

<sup>5</sup> V. Kavungal, G. Farrell, Q. Wu, A. K. Mallik, and Y. Semenova, "A packaged whispering gallery mode strain sensor based on a polymer-wire cylindrical micro resonator," *Journal of Lightwave Technology*, **36**, 1757-1765 (2018).

force. Specifically, it is the fractional change in dimension (length, width, or height) when subject to a force along that dimension. In a traditional strain gauge, stretching causes a change in the resistance of the metal grid whose value can be related to the value of applied strain. The operation of optical fiber strain sensors is based on measurements of light transmission or wavelength shift resulting from changes in the shape as well as the optical properties of the fiber materials due to the applied strain. The unique advantages of optical fiber strain sensors are high signal-to-noise ratio, light weight, small size, ease of installation, and immunity to electromagnetic interference. Optical fiber strain sensors are intrinsically passive and can be safely utilised in high voltage and potentially explosive environments [37].

However, silica fiber based strain sensors have a limited sensitivity and possess a tensile strain range only up to  $4000 \mu\epsilon$  (limited by the breakage strain threshold corresponding to 0.4% fiber elongation) [38,39] because of the relatively high elastic modulus of silica. Strain sensitivity can be improved by using fiber materials with a smaller elastic modulus such as polymers. Furthermore, flexibility and deformability of the polymer materials makes them capable of surviving larger applied strains without breakage compared to silica. There are many reports on fiber optic strain sensors employing single mode and multimode polymer optical fibers (POFs) as strain sensors including FBGs written in conventional and micro-structured POF [38,40]. A POF multimode interference sensor has also been reported [32]. It should be noted however, that the polymer sensor types above require substantial effort in terms of fabrication and cost (for example FBG writing, photomasks, fiber hetero-structure fabrication, depending on the sensor type).

For over a decade whispering gallery mode (WGM) optical micro-resonators (MRs) have received a lot of attention for application as various forms of sensor because of their high-quality factors and low mode volume [41,42]. There are many reports concerning WGM strain sensing using spherical [16,21–24,30,33] as well as bubble [17,43] MRs based on silica and polymer materials. Typically, an evanescent light coupling technique is used to excite the WGMs in such MRs. This involves placing the MR in physical contact with a thin and often fragile fiber taper. The practical application of such spherical or bubble-shaped MRs for strain sensing is limited due to the need to maintain the precise alignment between the resonator and the fiber taper for optimal and stable coupling, independent of external vibrations. Practical applications are also hindered by the absence of a suitable packaging technique which would allow the sensor to reliably sense strain whilst maintaining long term alignment of the sensor elements. One approach to reducing the difficulty of maintaining alignment accuracy is to utilise MRs with a cylindrical shape, since such an MR-taper structure has only one degree of freedom compared to two degrees of freedom for the case of spherical symmetry [14].

Recently we reported a study of a strain-induced spectral tunability of WGMs excited in a coating-stripped POF cylindrical MR [44], fabricated from a short section of commercially available POF with the outer diameter of 490  $\mu\text{m}$ . That study demonstrated that such resonators are potentially very suitable as highly sensitive strain sensors due to the good stability and repeatability of their performance and also due to the excellent elastic properties of the polymer materials, leading to a large dynamic range for strain sensing.

In this paper, we report the development and experimental demonstration of a practical packaged strain sensor based on the strain tunability of WGMs in a

polymer cylindrical resonator. To avail of greater flexibility in terms of cylindrical MR sizes, in this work we replaced a commercial POF (available only in a few standard diameters) with a laboratory drawn wire made from a polymethylmethacrylate (PMMA) rod as a cylindrical MR for strain sensing. It should be noted, that fabrication of such a wire is significantly simpler in comparison with the commercial POF drawing process, since the MR does not require formation of the fiber core. Similar to the previous work [44], the WGMs in the MR were evanescently excited using a tapered silica optical fiber. In the following sections of this paper, we present the results of the characterization of the strain sensor performance. Furthermore, the packaging of the proposed sensor is demonstrated based on a glass slide acting as a substrate, which results in a portable and easy to handle sensor. The entire proposed packaging process is also simple and takes less than 10 minutes to complete. After the packaging, the robustness of the strain sensing micro-resonator and tapered fiber coupling system is confirmed by vibration tests. To the best of our knowledge this work is a first comprehensive demonstration of a packaged WGM cylindrical strain sensor formed by a polymer wire cylindrical micro resonator packaged on a glass substrate. Our proposed method offers higher strain sensitivity compared to similar sensors based on silica fibers, and in addition offers higher mechanical stability (compared with spherical, bottle, and bubble microresonators) making it a suitable candidate for strain/stress and displacement sensing, especially in applications where a small sensor footprint is required.

### **3.2.2 Sensing principle, operation and fabrication**

The operating principle of the sensor is based on the measurement of the spectral shift of WGM resonances excited in the cylindrical MR as a result of changes in



its diameter due to the applied axial strain or stress. The resonance condition for the light circulating within the MR is fulfilled if the light wave reaches the point of its origin with the same phase after traveling one full circle of the resonator. The resonant wavelengths for which the resonance condition is satisfied are “trapped” within the resonator resulting in the appearance of the spectral dips in the transmission spectrum of the coupled fiber taper. Typically, WGM resonances excited in a fiber cylindrical MR have Q-factors in the order of  $\sim 10^4$ . Under the influence of the axial strain or stress applied to the MR, both its diameter and the effective refractive index of its material change, resulting in a spectral shift of the WGM resonances.

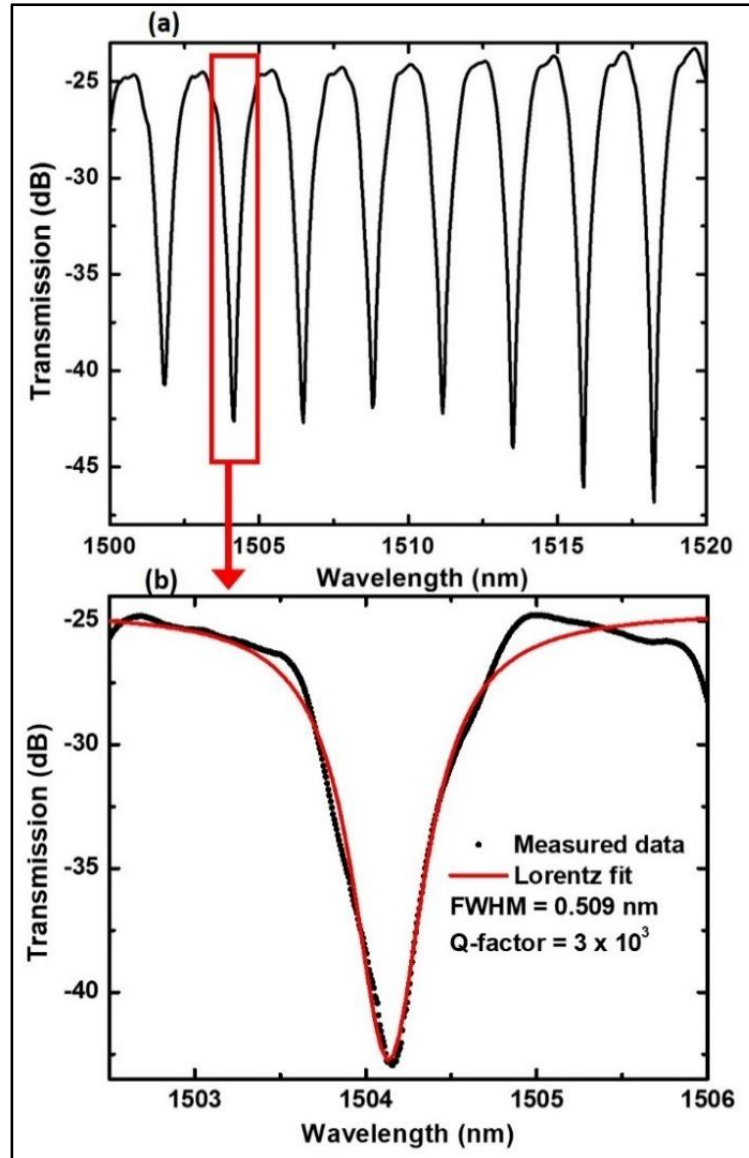
In our experiment, we used a short section of a polymer wire as the strain sensing MR. The polymer wire was fabricated by heating and stretching of a polymethyl methacrylate (PMMA) rod to a diameter of 230  $\mu\text{m}$  at a temperature of 180°C.

For the fabrication of the tapered fiber, a short length of a coating-stripped standard single mode telecommunication optical fiber (SMF 28, Corning) with core and cladding diameters of 8.3  $\mu\text{m}$ , and 125  $\mu\text{m}$  respectively was stripped of its coating and cleaned with isopropyl alcohol. The coating-stripped section then was fixed horizontally between two computer controlled XYZ translational stages. The tapered fiber was then fabricated by means of the customized micro-heater brushing technique described in [2]. A ceramic micro heater (CMH-7019, NTT-AT) was used to heat the fiber up to approximately 1300°C, making the silica material soft enough for tapering. A customized PC program allowed for an accurate control of the diameter, the length, and the shape of the fabricated tapers. In our experiment the fabricated tapered fiber waist diameter is approximately 1.3  $\mu\text{m}$ , the waist length is around 6 mm and the full taper length is circa 50 mm.

A 40 mm length of the polymer wire resonator was fixed with one of its ends clamped to a holder and the other end connected to a micro-translation stage with 10  $\mu\text{m}$  movement resolution. Broadband light from a super luminescent diode (SLD) was launched into the fabricated tapered single mode silica optical fiber, which was placed in contact with the polymer MR similarly to the setup described in [44], and the resulting WGM spectrum was recorded at the output of the taper using an optical spectrum analyzer (OSA) with a 10 pm spectral resolution.

Figure 35(a) & (b) show the transmission spectrum of the tapered fiber of waist diameter 1.3  $\mu\text{m}$  coupled with a cylindrical polymer wire resonator with the diameter of 230  $\mu\text{m}$ . Periodic narrow resonance peaks with a quality factor of circa  $\sim 10^3$  and average free spectral range (FSR) of 2.35 nm are observed in the wavelength range from 1500 to 1520 nm. The maximum extinction ratio for the resonant dips reaches 23 dB. The relatively high transmission loss of the spectrum is due to the high optical absorption by the polymer material in the infrared region, coupling losses, scattering losses on residual surface inhomogeneities, losses introduced by surface contaminants and the slight microbend loss arising in the thin microfiber due to its contact with a relatively thicker cylindrical resonator [2,45].

To characterize the strain sensing performance of the setup, strain was applied to the polymer wire resonator axially by moving the translation stage with a step of 10  $\mu\text{m}$  (corresponding to an axial strain of 250  $\mu\epsilon$  (0.03% fiber elongation)) in a direction away from the fixed end. During each measurement of the shift of the WGM spectrum with respect to the applied strain, the input polarization state was remained unchanged. All the measurements were carried out at a constant laboratory temperature (20  $^\circ\text{C}$ ).



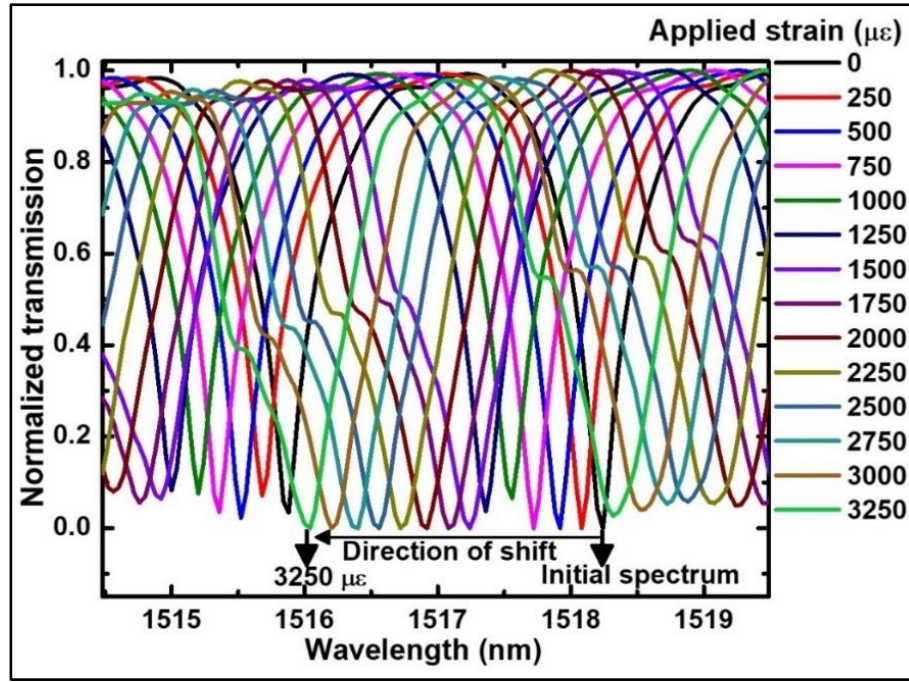
**Figure 35.** (a) Transmission spectrum of tapered fiber coupled with a 230  $\mu\text{m}$  diameter cylindrical polymer wire resonator. (b) Selected single resonance dip along with the Lorentzian fit.

Figure 36 illustrates the effect of axial strain on the selected WGM dip (1518.2 nm at zero strain) in the transmission spectrum. As the axial strain increases from zero to 3250  $\mu\epsilon$  (0.33% polymer-wire elongation), the resonant dip exhibits a progressively larger blue shift close to the FSR range (2.33 nm). As can be seen from the figure, the selected WGM resonance shifts towards shorter wavelengths

with the increase of applied strain. It should be noted that at high tensile strains ( $> 1250 \mu\epsilon$ ), additional side-lobes appear in the selected WGM spectra, possibly due to strain-induced deformations and deviation of the resonator from its cylindrical shape [46].

A 40-mm long polymer-wire used in the experiment is capable of sustaining an axial elongation of 3 to 3.5 mm (corresponding tensile strain is  $7.5 - 8.8 \times 10^4 \mu\epsilon$ ). In the polymer-wire resonator-tapered fiber coupling arrangement, a 6% of its axial elongation (corresponding tensile strain is  $6 \times 10^4 \mu\epsilon$ ) can be applied by without the need of fiber taper realigning. Beyond this estimated strain value, by continuing the elongation, the chance of breakage of the polymer-wire is increased and WGMs coupling efficiency is significantly degraded.

As demonstrated by Klitzing *et al.* [31], designing a useful device for a specific strain sensing application it is desirable to limit the range of the applied strains so that the corresponding WGMs spectral shift occurs within the FSR range of the spectrum in order to avoid ambiguities in identifying the position of a strained modes with respect to the unstrained modes. It is also important to avoid changes in modal components order due to strain induced deformations of the polymer wire. Therefore, in our experiments the strain range is limited so that WGMs shift is less than one FSR corresponding to 0.33% ( $3250 \mu\epsilon$ ) axial elongation of the polymer wire.



**Figure 36.** Shift in the selected dip of WGM transmission spectrum with increasing axial strain.

The spectral shift of the WGM resonant wavelength due to axial strain can be described as a combined effect of changing diameter and the changing refractive index of the resonator [16,21–25,30–33]:

$$\frac{\Delta\lambda}{\lambda} = \frac{\Delta D}{D} + \frac{\Delta n}{n} \quad (3.1)$$

Where  $\Delta D/D$  is the fractional change in the MR diameter ( $D$ ) due to the deformation of the micro-cavity and  $\Delta n/n$  is the fractional change in the refractive index ( $n$ ) due to the strain-optic effect. The transverse deformation ( $\Delta D/D$ ) of the micro-cavity can be related to the axially applied tensile strain ( $\Delta L/L$ ) by the Poisson ratio ( $\sigma$ ). The Poisson ratio is the ratio of the lateral contraction strain ( $\Delta D/D$ ) to the axial tensile strain ( $\Delta L/L$ ) given by:

$$\sigma = \frac{\Delta D/D}{\Delta L/L}. \quad (3.2)$$

Changes in the fiber dimensions result in changes in the material density with the corresponding induced changes in its refractive index ( $\Delta n$ ). Thus, changes in the refractive index can be expressed as

$$\Delta n = n P_{eff} \frac{\Delta L}{L} \quad (3.3)$$

where  $P_{eff}$  is the effective strain-optic coefficient [32,34,47]. The total WGM resonance wavelength shift can be expressed as

$$\frac{\Delta \lambda}{\lambda} = - \left( \sigma \frac{\Delta L}{L} + P_{eff} \frac{\Delta L}{L} \right) \quad (3.4)$$

Here the negative sign shows that the axial tensile strain applied to the POF micro-resonator will result in a blue shift of the WGM resonance. The Poisson's ratio and the effective strain-optic coefficient of PMMA are 0.35-0.45 and 0.099 ( $\pm 0.0009$ ) respectively [25, 32, 34, 44].

Figure 37 shows the theoretically calculated and experimentally measured wavelength shift as a function of axial strain for a selected WGM dip. Here the solid red line is the strain dependence of WGM wavelength shift calculated using equation (3.4) by setting the Poisson's ratio ( $\sigma$ ) of the PMMA wire resonator to 0.35, and the resonance wavelength to 1550 nm. The slope of the calculated linear dependence indicates a theoretical strain sensitivity of  $-0.69 \text{ pm}/\mu\epsilon$ . The theoretically calculated total shift of the WGMs in response to strain associated with a 0.33 % polymer wire elongation is 2.26 nm.

The scattered data in figure 37 shows the experimentally measured wavelength shift for a selected WGM dip versus the applied strain. The slope of the linear dependency of the measured data is calculated as  $-0.68 \text{ pm}/\mu\epsilon$ , which agrees well with the theoretically calculated value. There is an average 0.2 nm blue shift for

the WGMs dip for each 10  $\mu\text{m}$  elongation (250  $\mu\epsilon$ ). From the experimental results one can see that the resonance wavelength shift is quite in line with the theoretically calculated shift thus the proposed system offers good potential as a strain sensor. The total shift of WGMs is 2.2 nm in response to the 0.33% strain, which agrees with the theoretically calculated shift.

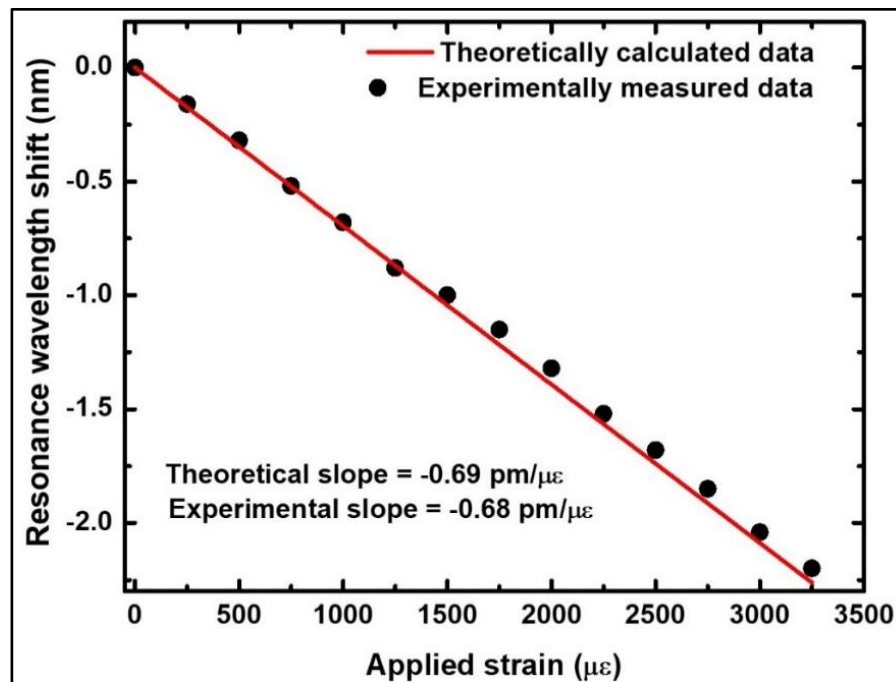


**Figure 37.** Theoretically calculated and experimentally measured wavelength shift as a function of axial strain for a selected WGM dip.

### 3.2.3 Strain sensor packaging experiment

In laboratory conditions, evanescent coupling of light from a fiber taper into a spherical, bottle or bubble MR is typically realized by means of high-resolution 3D micro-positioning stages and optical microscopes, to permit precise alignment of the tapered fiber waist region along the MR equator at a close distance to the resonator surface. As mentioned above, evanescent light coupling to a cylindrical MR is somewhat simpler since only 2D alignment is necessary. However, in real world applications even the least complex scenario becomes impractical if it

demands bulky and heavy micro-positioning equipment as an integral part of the system. Therefore, for practical applications the development of a simple and reliable packaging method is required for WGM based sensors which allows precise alignment of the sensor elements to be initially achieved using micro-positioning equipment but then ensures that precise alignment can be maintained without the continued use of the micro-positioning equipment. This in turn enables the fabrication of portable and miniature devices without degrading their laboratory performance.

Recently Ilchenko *et al.* reported the realization of a compact packaged narrow-linewidth laser based on a WGM resonator with a prism coupler [47]. Yan *et al.* [48] and Wang *et al.*[49] demonstrated a packaging method for a tapered fiber-coupled spherical micro resonator utilizing low refractive index UV curable glue as the coating material. The authors also carried out temperature and photosensitivity studies to evaluate the device performance after packaging. More recently Dong *et al.* proposed a packaging technique for spherical [50], and cylindrical [51] microresonators coupled with a tapered fiber. In their packaging technique, the resonator rested on the thin portion of the tapered optical fiber like a cantilever to achieve light coupling and generate WGMs, utilizing the force of gravity instead of glue. The same authors also confirmed the robustness of the coupling system by a vibration test. A special kind of packaging for a tapered fiber-microsphere system was demonstrated by K. Milenko *et al.* [52], where a silver iodide metaphosphate glass microsphere was thermally melted and attached on to a tapered optical fiber. Temperature characterization of the packaged device was also performed.



In this work, we propose and demonstrate a packaging method based on three simple steps which involves gluing the resonator and the light coupling tapered fiber on to glass substrate. The robustness of the coupling system is confirmed by testing the packaged device under strong vibration conditions.

The proposed packaging process can be completed in three steps: (a) preparation of the tapered fiber and polymer wire resonator arrangement, (b) maximizing the coupling efficiency between the tapered optical fiber and the polymer wire resonator and (c) immobilizing the coupled system on a glass substrate using UV curable epoxy.

#### **a) Preparation of the polymer wire resonator for coupling**

In order to prepare the polymer micro-cylinder for packaging, a short section of silica capillary tube was attached on to a glass substrate using UV- curable glue (Loctite AA 358) as shown in Figure 38(1). Then a flexible polymer wire with a uniform outer diameter of 230  $\mu\text{m}$  was inserted into the attached silica capillary tubing as illustrated in Figure 38(2). The capillary tube's inner diameter must be slightly larger than the polymer wire's outer diameter. In the last step, shown in Figure 38(3), one end of the polymer wire was attached on to the glass substrate using UV- curable glue. The capillary tube has a significant role in the packaging process as it allows attachment of the polymer wire resonator to the glass substrate while ensuring free axial movement of the polymer wire due to applied strain. The total length of the polymer wire in our experiment was 80 mm. The inner diameter and the length of the capillary tubing were circa 240  $\mu\text{m}$  and 5 mm respectively. To achieve a tighter fit between the inner diameter of the tubing and the outer diameter of the polymer wire resonator, the silica tubing's diameter may be

reduced by tapering using the same technique used for fabrication of the tapered fiber.

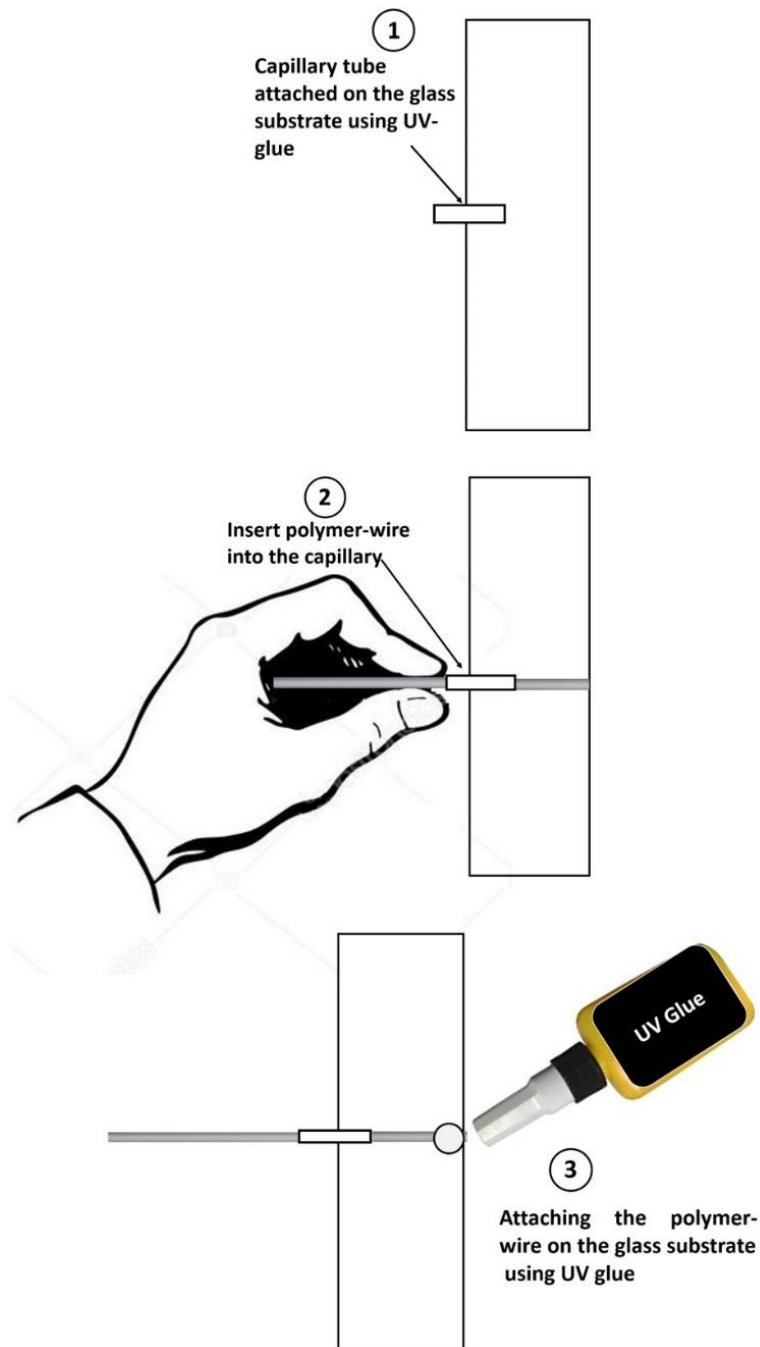


**Figure 38.** Schematic of the packaging process: (1) Capillary tube attached on the glass substrate, (2) inserting polymer-wire into the capillary tube, and (3) attaching the polymer wire on to the glass substrate using UV glue.

## **b) Maximizing the coupling efficiency**

The presence of large evanescent field outside of the tapered portion of the fiber makes it possible to couple the light into the strain sensing polymer wire acting as the micro-cylinder by placing both in direct physical contact.

Figure 39(a) illustrates schematically the experimental setup for optimizing the coupling efficiency between the tapered optical fiber and the polymer wire sensor probe. The prepared strain sensing polymer wire resonator shown in Figure 38(3) is fixed on a translation stage with an adjustable 3D- positioner. Using the vertical positioner, the polymer wire was brought in contact with the tapered fiber to excite the WGMs. It should be noted that due to the difficulty of manipulating the thin and fragile tapered silica fiber, this step was carried out while the fiber taper was still secured horizontally between the two translational stages of the taper-drawing setup after its fabrication.

This process of micro-alignment is assisted by a fiber coupled He-Ne laser radiating at 632.8 nm, connected to the input of the tapered fiber. The leaked red light made the taper waist region clearly visible and helped to align it perpendicularly with the polymer wire resonator. When the alignment process was completed, the He-Ne laser at the input end of the fiber taper was replaced with a super luminescent diode (SLD) (Thorlabs), with a wavelength range of 1500-1600 nm and the output of the fiber taper was connected to the OSA (86142B, Agilent).

After achieving the physical contact with the tapered fiber, the polymer wire was slowly moved along the taper axis while maintaining physical contact and mutually orthogonal orientation. During this operation, the transmission spectrum of the taper was observed at the OSA screen to determine the optimal position of

the contact point, corresponding to the phase match between the propagating mode of the fiber taper and the fundamental WGM of the polymer wire resonator [53] .

**c) Immobilizing the coupled system on a glass substrate**

After achieving the desired WGM spectrum quality, vis-à-vis a high extinction ratio and Q-factor, the tapered fiber was glued to the glass slide using UV curable epoxy. Before applying the glue, the physical contact between the fiber taper and the polymer wire was ensured using spacers with an appropriate thickness attached to the glass substrate serving as the basis for the coupling arrangement. The entire packaging process took less than 10 minutes.

Figure 39(b) shows the schematic diagram of a packaged strain sensor. The photograph of the packaged strain sensor is shown in Figure 40.

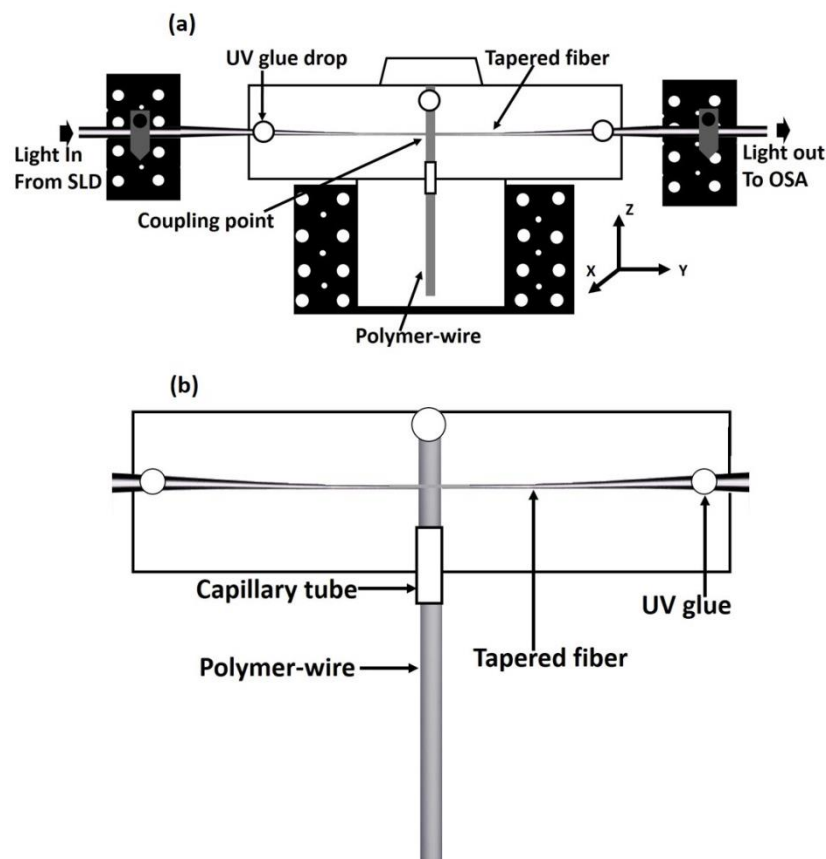


**Figure 39.** (a)- (b) Illustration of the packaging process.

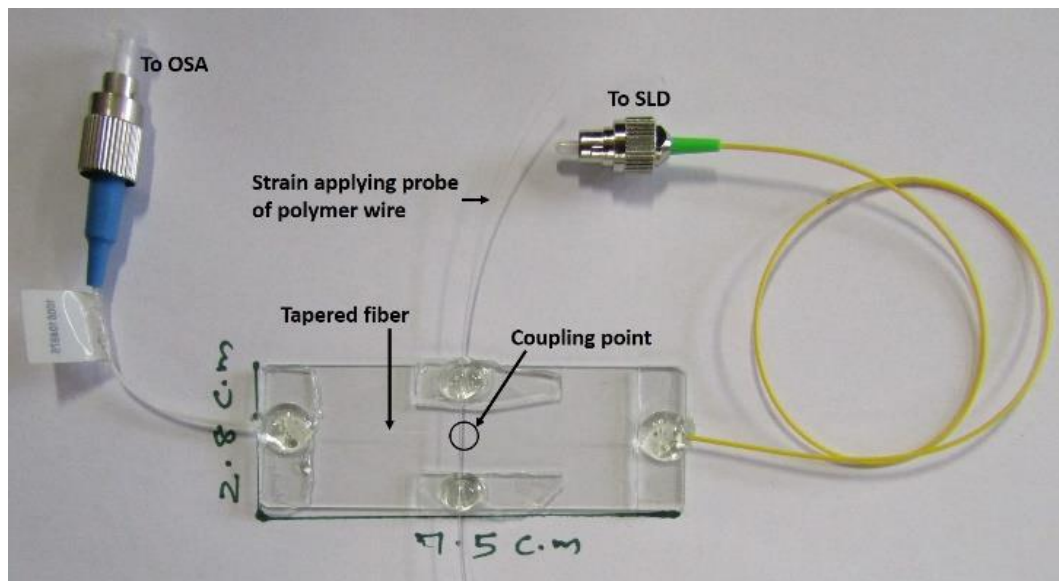


**Figure 40.** Photograph of the packaged strain sensor.

### **3.2.4 Before/after packaging performance comparison**

Figures 41(a, b) show the transmission spectra of the tapered fiber before and after the packaging. Narrow resonances with a Q-factor in the order of  $\sim 10^3$  were observed in both spectra. There is a change in the extinction ratio of the WGM spectrum before and after packaging also accompanied by a small spectral shift in the order of picometer. This is possibly due to the increased coupling loss and changing polarization of the input light.

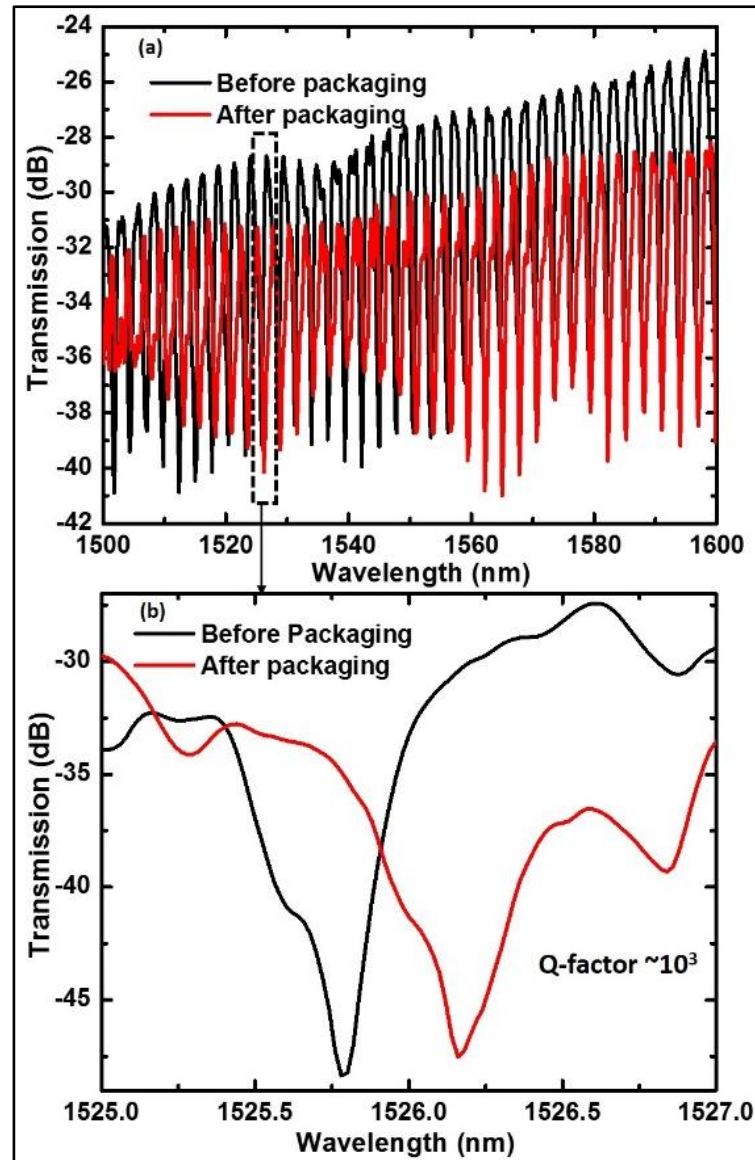


**Figure 41.** (a) Transmission spectrum of the tapered fiber before and after packaging (b) selected single resonance dip.

### 3.2.5 Analysis of the performance of the packaged strain sensor

To evaluate the performance of the packaged device, strain sensing experiments were carried out at a constant laboratory temperature (20 °C). Figure 42 illustrates the experimental setup used for characterization of the packaged WGM based strain sensor. Similar to the previous experiments, one end of the tapered fiber is connected to the SLD through a three-paddle polarization controller and the output end is connected to an OSA with a 10 pm resolution. The packaged strain sensor

is clamped onto an optical platform. The free end of the polymer wire is fixed on a micro translation stage with a 10  $\mu\text{m}$  movement resolution. The distance between the two fixed points (A and B) of the polymer wire is considered as the sensing length. Here the sensing length was set to 40 mm for consistency.

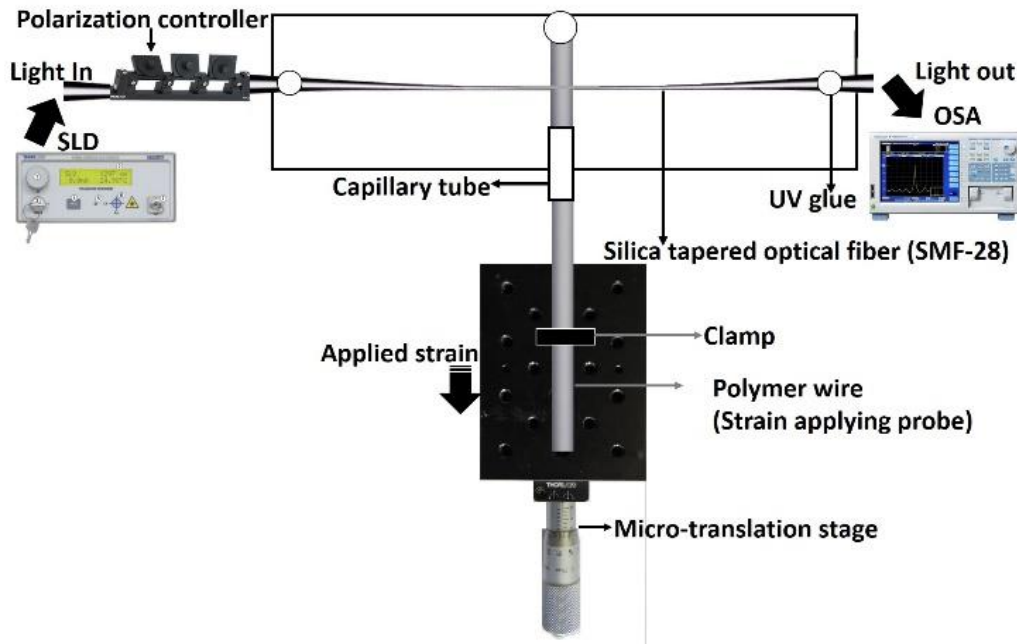


**Figure 42.** Schematic diagram of the strain sensing experiments using the packaged strain sensor.

Strain is applied to the polymer wire by moving the translation stage with a step of 10  $\mu\text{m}$  (corresponding to an axial tensile strain of 250  $\mu\epsilon$ ) in a direction away from the fixed end. Figures 43 (a) show the spectral shift experienced by a selected WGM dip as the axial strain is increased from zero to 2500  $\mu\epsilon$ . Similar to the previous experiments, when the axial strain increases, the resonant dips exhibit a linear blue shift. For testing the repeatability of the packaged sensor performance, we carried out a reversed cycle of measurements where the applied axial strain was decreased back to zero, during which the resonance dips linearly red-shifted back to their initial positions with a relatively low level of hysteresis.

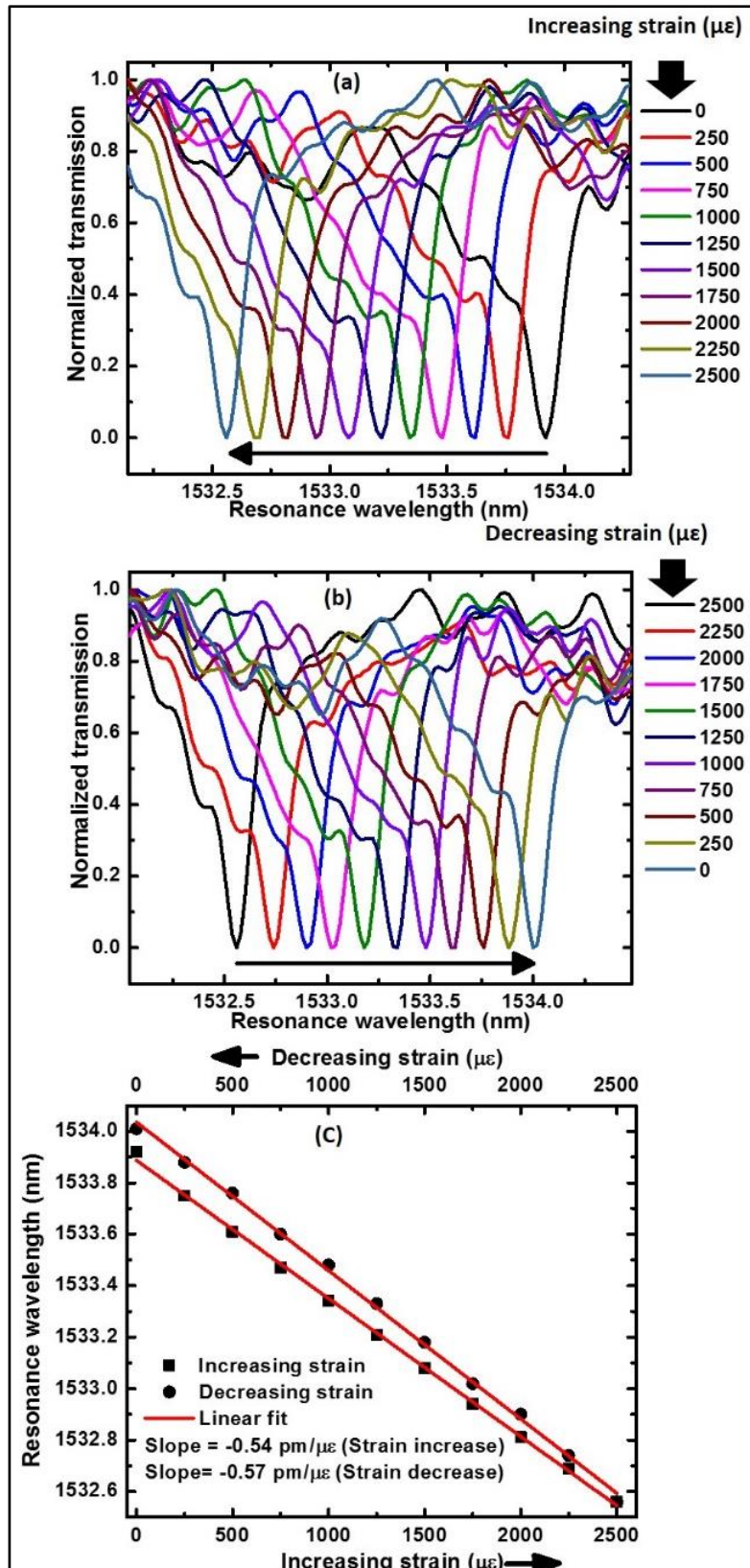


**Figure 43.** Experimental results for the packaged sensor: (a) & (b) wavelength shift of a selected WGM resonance versus applied increasing (decreasing) strain and (c) & (d) corresponding WGM resonance shifts versus applied strain.



Figure 43(b) shows the resonance wavelength shift with the decreasing applied strain and Figure 43(c) illustrates the hysteresis between the two opposite cycles, where the bottom axis represents the increasing strain and the top axis represents a gradual decrease of the applied axial strain from its maximum value to the initial unstrained state. The maximum difference between the shifted resonance wavelengths in the unstrained position is 0.15 nm.

It should be noted that in the case of the packaged sensor, the slope of the linear fit is less than that of the unpackaged sensor, indicating a lower sensitivity to strain (-0.54 pm/ $\mu\epsilon$ ). This is possibly due to the decrease in the efficiency of strain transfer to the polymer wire induced by the frictional forces from the capillary tube. In the packaged sensor, strain sensitivity can be improved by using more flexible capillary tube as holder.

### **3.2.6 Studies of factors affecting the performance of packaged sensor**

#### **a) Mechanical stability**

The robustness of the packaged device is evaluated by observing the effect on the transmission spectrum of strong vibrations. For this test, the packaged sensor is placed on the vibration platform (shown in Figure 44) operated with a function generator which can produce various frequency vibrations. A single WGM resonance dip in the transmission spectrum before vibration and after the vibration is shown in Figure 45. One can see from the figure that this resonance dip with a central wavelength of 1526.8 nm does not experience significant changes as a result of vibration. There is a slight decrease in the extinction ratio after the

application of vibration but the shape and the Q- factor ( $\sim 10^3$ ) of the resonance dip remain almost constant, indicating that the packaged sensor possesses good resistance to vibration.

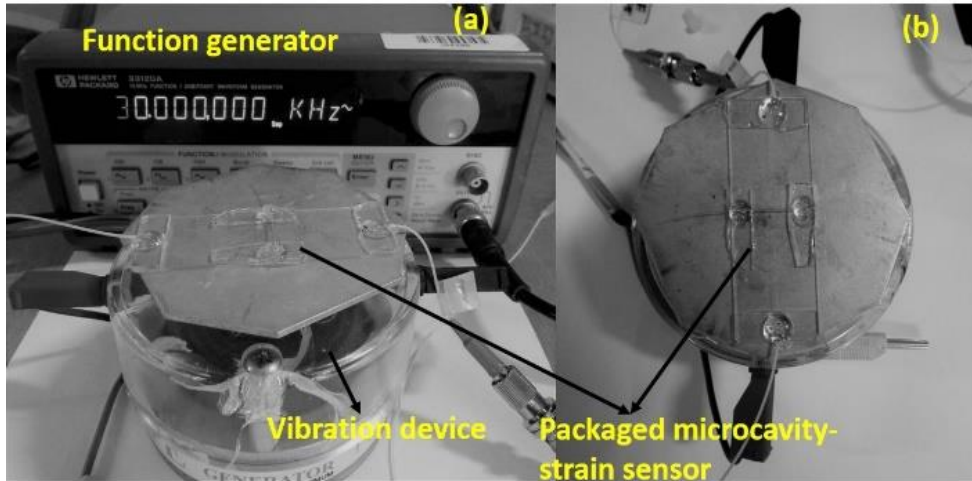


**Figure 44.** Experimental setup for vibration tests (a) General view; (b) Top view of the vibrational platform.

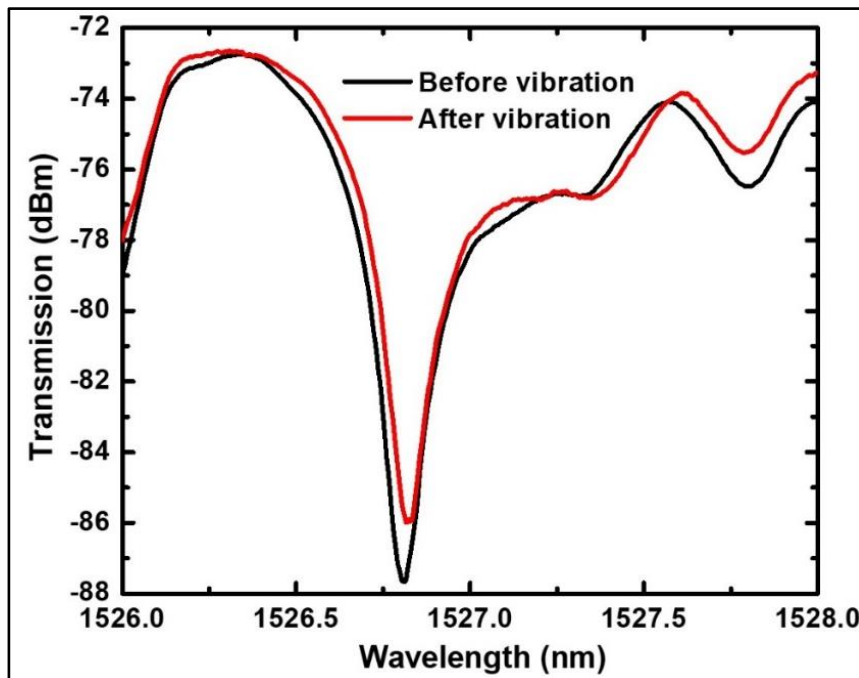


**Figure 45.** Selected single transmission WGM dip of the packaged strain sensor at before and after vibration.

## b) Temperature stability

Temperature sensitivity is an issue for all optical fiber sensors operating in an environment with a varying temperature. The thermal drift of a resonant wavelength in an optical microresonator results from thermal expansion and thermo-optic effects of its material. Fused silica has positive thermal expansion and thermo-optic coefficients. As a result, WGM resonances in a silica microresonator shift towards longer wavelengths with an increase in temperature. The reason behind the red shift is that, when the temperature increases, both the diameter and the refractive index of the material also increase. This leads to the increase in effective optical path for light within the resonator. To accommodate the larger circumference, the WGM resonance will shift to a longer wavelength.

In the case of optical microresonators made from polymers (PMMA, PDMS), calcium fluoride (CaF<sub>2</sub>), or athermal glasses that exhibit negative thermo-optical effect, the refractive index of the material decreases with the increase of the temperature reducing the optical circumference. This leads to the resonance wavelengths shift towards the shorter wavelength side of the spectrum [54]. The temperature induced resonance wavelength shift can be determined from the equation [55],

$$\Delta\lambda = \lambda_0 \left( \frac{1}{n} \frac{dn}{dT} \Delta T + \frac{1}{D} \frac{dD}{dT} \Delta T \right) \quad (3.5)$$

where  $\frac{dn}{dT}$  is the thermo-optic coefficient and  $\frac{1}{D} \frac{dD}{dT}$  is the thermal expansion coefficient. The negative thermo-optic coefficient of PMMA is  $10^{-4} \text{ K}^{-1}$ , one order of magnitude higher than the thermo-expansion coefficient, which is equal to  $10^{-5} \text{ K}^{-1}$  [56].

To investigate the temperature response of the packaged strain sensor experimentally, sensor's ambient temperature was varied by placing it on a hot stage capable of realizing temperature changes in the range from 20 to 50 °C in 1 °C steps. A reference thermocouple probe with 0.1°C resolution was attached to the surface of the hot stage near the sensor under test. The temperature of the heater then was gradually increased in 2 °C steps and the corresponding changes in the resonance wavelength were recorded using the OSA along with the temperature readings of the thermocouple.

Figure 46(a) shows the position of a selected WGM resonance at different applied temperatures and Figure 46(b) analyses the experimental data. Here the scatter data points represent the measured resonance wavelength shifts with increasing temperature and the solid line is a linear fit of the measured data. From the figure one can see that, when the temperature is increased the WGM resonance experiences a blue shift. The slope of the linear fit to the experimental data gives an estimated temperature sensitivity of 40.8 pm/°C. Thus, the estimated temperature cross sensitivity of the strain sensor while operating at increase in temperature conditions is 54  $\mu\epsilon$ /°C.

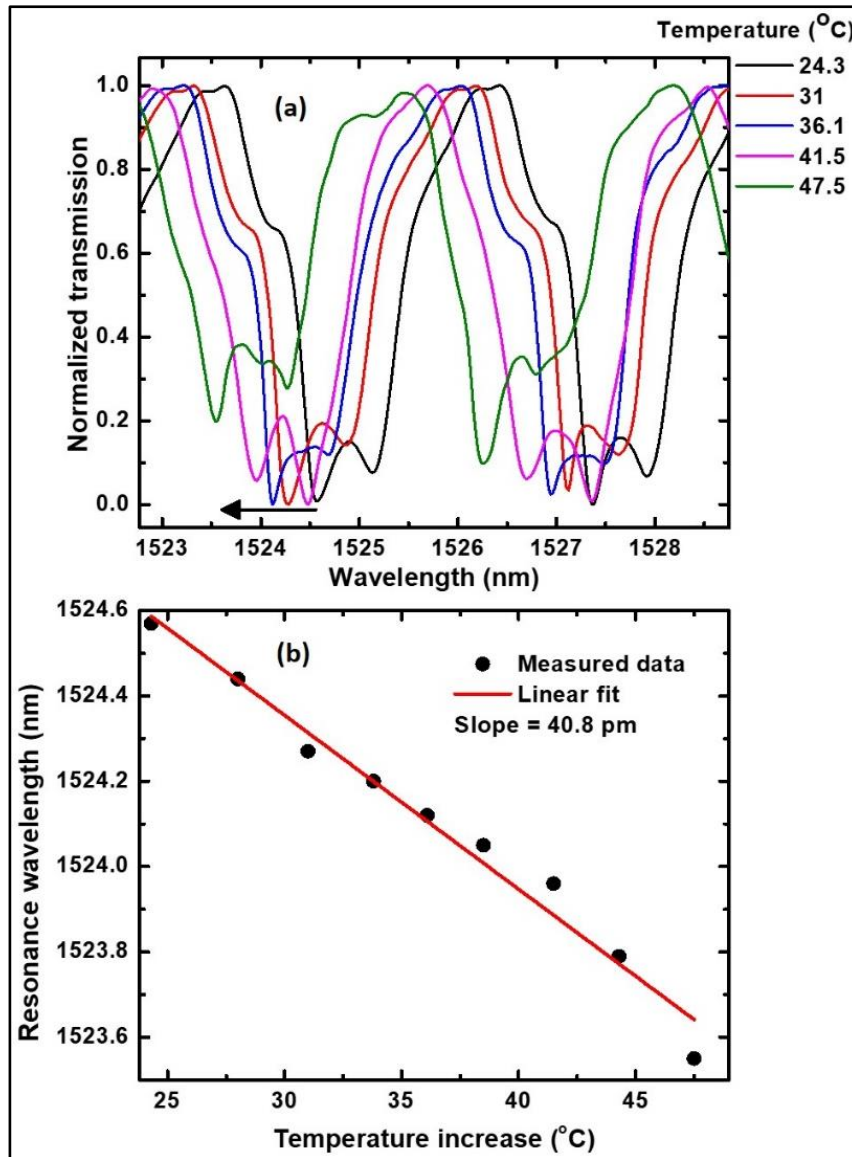


**Figure 46.** (a) Selected WGM resonance with different applied temperature, and (b) linear fit of the measured resonance wavelength shift data.

### 3.2.7 Conclusions

In conclusion, we have proposed a strain sensor based on WGMs excited in a polymer wire cylindrical micro resonator for applications requiring a large dynamic range for strain measurements. The sensitivity of the proposed strain sensor to the increasing axial tensile strain in the range of wavelengths from 1500 to 1600 nm is  $-0.68 \text{ pm}/\mu\epsilon$  (unpackaged), and  $-0.58 \text{ pm}/\mu\epsilon$  (packaged) respectively. The light was evanescently coupled into the polymer wire resonator

from a standard single mode silica optical fiber taper fabricated by the micro heater brushing technique. Narrow WGM resonances were observed in the fiber taper's transmission spectrum with a Q-factor in the order of  $10^3$ . WGMs are shifted towards shorter wavelengths with increasing axial strain on the resonator. Measurements of axial strains up to  $3.25 \times 10^3 \mu\epsilon$  (corresponding to 0.33 % elongation) have been demonstrated, without the need for re-adjustment of the coupling setup due to the impact of applying strain. Furthermore, we proposed and demonstrated a packaging method for the strain sensor on a glass microscope slide which will make the sensor portable and easy to use. The packaging process is simple and robust. Strain sensing experiments were carried out using the packaged sensor at a constant laboratory temperature to demonstrate the sensor performance. The spectral positions of the WGM resonances for the packaged strain sensor shift linearly to shorter wavelengths during the increase in axial tensile strain. The return of WGMs to their original positions with small hysteresis as the decrease of the applied axial strain demonstrates the repeatability of the packaged strain sensor performance. The package sensor was subjected to a range of vibration to determine the sensitivity of the sensor to external vibration. It was found that external vibrations had little or no effect on the sensor performance. The spectral response of the sensor in increasing ambient temperature condition is studied. The estimated temperature cross sensitivity of the strain sensor while operating at increase in temperature conditions is  $54 \mu\epsilon/^\circ\text{C}$ . The proposed polymer wire based packaged strain sensor possesses several desirable features such as ease of fabrication, small footprint, portability and large dynamic range of strains.

### 3.3 References

1. K. Vahala, "Optical microcavities," *Nature*. **424**, 839–846 (2003)
2. M. L. Gorodetsky, A. A. Savchenkov, and V. S. Ilchenko, "Ultimate Q of optical microsphere resonators," *Opt. Lett.* **21**, 453-455 (1996).
3. M. R. Foreman, J. D. Swaim, and F. Vollmer, "Whispering gallery mode sensors," *Adv. Opt. Photon.* **7**, 168-240 (2015).
4. V. B. Braginsky, M. L. Gorodetsky, and V. S. Ilchenko, "Quality-factor and nonlinear properties of optical whispering-gallery modes," *Phys. Lett. A*. **137**, 393–397 (1989).
5. Y. Loyer, D. Meschede, and A. Rauschenbeutel, "Tunable Whispering Gallery Mode Resonators for Cavity Quantum Electrodynamics," *Phys. Rev. A*. **72**, 031801(2005).
6. V. Sandoghdar, F. Treussart, J. Hare, V. Lefèvre-Seguin, J. M. Raimond, and S. Haroche, "Very low threshold whispering-gallery-mode microsphere laser," *Phys. Rev. A* . **54**, R1777–R1780 (1996).
7. A. Ksendzov and Y. Lin, "Integrated optics ring-resonator sensors for protein detection," *Opt. Lett.* **30**, 3344-3346 (2005).
8. T. Yoshie, L. Tang, and S. Y. Su, "Optical microcavity: Sensing down to single molecules and atoms," *Sensors* **11**, 1972–1991 (2011).
9. S. Arnold, M. Khoshshima, I. Teraoka, S. Holler, and F. Vollmer, "Shift of whispering-gallery modes in microspheres by protein adsorption," *Opt. Lett.* **28**, 272-274 (2003).
10. A. E. Fomin and M. L. Gorodetsky, "Spheroidal microresonators for the optoelectronics," *Proc. SPIE* **5948**, 594818 (2005).
11. J. U. Fürst, D. V. Strekalov, D. Elser, A. Aiello, U. L. Andersen, C. Marquardt,

- and G. Leuchs, “Quantum light from a whispering gallery mode disk resonator,” *Phys. Rev. Lett.* **106**, 1–4 (2011).
12. M. Sumetsky, “Mode localization and the Q-factor of a cylindrical microresonator,” *Opt. Lett.* **35**, 2385-2387 (2010).
  13. A. Boleininger, T. Lake, S. Hami, and C. Vallance, “Whispering gallery modes in standard optical fibres for fibre profiling measurements and sensing of unlabelled chemical species,” *Sensors* **10**, 1765–1781 (2010).
  14. G. Farca, S. I. Shopova, and A. T. Rosenberger, “Cavity-enhanced laser absorption spectroscopy using microresonator whispering-gallery modes,” *Opt. Express.* **15**, 17443-17448 (2007).
  15. R. S. Moirangthem and A. Erbe, “Interfacial refractive index sensing using visible-excited intrinsic zinc oxide photoluminescence coupled to whispering gallery modes,” *Appl. Phys. Lett.* **103**, 051108 (2013).
  16. V. S. Ilchenko, P. S. Volikov, V. L. Velichansky, F. Treussart, V. Lefèvre-Seguin, J. M. Raimond, and S. Haroche, “Strain-tunable high-Q optical microsphere resonator,” *Opt. Commun.* **145**, 86–90 (1998).
  17. R. Henze, T. Seifert, J. Ward, and O. Benson, “Tuning whispering gallery modes using internal aerostatic pressure,” *Opt. Lett.* **36**, 4536-4538 (2011).
  18. T. Ioppolo, U. Ayaz, and M. V Otugen, “Tuning of whispering gallery modes of spherical resonators using an external electric field,” *Opt. Express.* **17**, 16465–16479 (2009).
  19. M. Agarwal and I. Teraoka, “Mode latching and self tuning of whispering gallery modes in a stand-alone silica microsphere,” *Appl. Phys. Lett.* **101**, 1–5 (2012).
  20. A. L. Huston and J. D. Eversole, “Strain-Sensitive Elastic Scattering from



- Cylinders,” *Opt. Lett.* **18**, 1104–1106 (1993).
21. U. K. Ayaz, T. Ioppolo, and M. V. Ötügen, “Wall shear stress sensor based on the optical resonances of dielectric microspheres,” *Meas. Sci. Technol.* **22**, 075203-075212 (2011).
  22. T. Ioppolo, U. K. Ayaz, and M. V. Ötügen, “High-resolution force sensor based on morphology dependent optical resonances of polymeric spheres,” *J. Appl. Phys.* **105**, 1–9 (2009).
  23. T. Ioppolo, M. Kozhevnikov, V. Stepaniuk, M. V. Ötügen, and V. Sheverev, “Micro-optical force sensor concept based on whispering gallery mode resonators,” *Appl. Opt.* **47**, 3009–30014 (2008).
  24. T. Ioppolo and M. V. Ötügen, “Pressure tuning of whispering gallery mode resonators,” *J. Opt. Soc. Am. B.* **24**, 2721-2726 (2007).
  25. C. L. Linslal, M. Kailasnath, S. Mathew, T. K. Nideep, P. Radhakrishnan, V. P. N. Nampoori, and C. P. G. Vallabhan, “Tuning whispering gallery lasing modes from polymer fibers under tensile strain,” *Opt. Lett.* **41**, 551-554 (2016).
  26. A. Mahmood, V. Kavungal, S. S. Ahmed, G. Farrell, and Y. Semenova, “Magnetic-field sensor based on whispering-gallery modes in a photonic crystal fiber infiltrated with magnetic fluid,” *Opt. Lett.* **40**, 4983–4986 (2015).
  27. W. Lin, H. Zhang, B. Liu, B. Song, Y. Li, C. Yang, and Y. Liu, “Laser-tuned whispering gallery modes in a solid-core microstructured optical fibre integrated with magnetic fluids,” *Sci. Rep.* **5**, 1–10 (2015).
  28. J. C. Knight, G. Cheung, F. Jacques, and T. A. Birks, “Phase-matched excitation of whispering-gallery-mode resonances by a fiber taper,” *Opt. Lett.* **22**, 1129-1131 (1997).
  29. G. Brambilla, V. Finazzi, and D. J. Richardson, “Ultra-low-loss optical fiber

- nanotapers,” *Opt. Express*, **12**, 2258-2263 (2004).
30. Z. H. Zhou, F. J. Shu, Z. Shen, C. H. Dong, and G. C. Guo, “High-Q whispering gallery modes in a polymer microresonator with broad strain tuning,” *Sci. China Physics, Mech. Astron.* **58**, 114208-114213 (2015).
31. W. von Klitzing, R. Long, V. S. Ilchenko, J. Hare, and V. Lefèvre-Seguin, “Frequency tuning of the whispering-gallery modes of silica microspheres for cavity quantum electrodynamics and spectroscopy,” *Opt. Lett.* **26**, 166–168 (2001).
32. J. Huang, X. Lan, H. Wang, L. Yuan, T. Wei, Z. Gao, and H. Xiao, “Polymer optical fiber for large strain measurement based on multimode interference,” *Opt. Lett.* **37**, 4308–4310 (2012).
33. R. Madugani, Y. Yang, J. M Ward, J. D. Riordan, S. Coppola, V. Vespini, S. Grilli, A. Finizio, P. Ferraro, and S. Nic Chormaic, “Terahertz tuning of whispering gallery modes in a PDMS stand-alone, stretchable microsphere,” *Opt. Lett.* **37**, 4762-4764 (2012).
34. G. N. Greaves, A. L. Greer, R. S. Lakes, and T. Rouxel, “Poisson’s ratio and modern materials,” *Nat. Mater.* **10**, 823–837 (2011).
35. R. Ulrich and, A. Simon, “Polarization optics of twisted single-mode fibers,” *Appl. Opt.* **18**, 2241-2251 (1979).
36. D. C. Brown and H. J. Hoffman, “Thermal, stress, and thermo-optic effects in high average power double-clad silica fiber lasers,” *IEEE J. Quantum Electron.* **37**, 207–217 (2001).
37. H. Gross, “Handbook of Optical Systems”, (Wiley-VCH, 2005), Vol. 2.
38. H. Y. Liu, G. D. Peng, and P. L. Chu, “Polymer fiber Bragg gratings with 28-dB transmission rejection,” *IEEE Photonics Technol. Lett.* **14**, 935–937

- (2002).
39. V. Bhatia, and A. M. Vengsarkar, "Optical fiber long-period grating sensors," *Opt. Lett.* **21**, 692-694 (1996).
  40. Y. J. Rao, Y. P. Wang, Z. L. Ran, and T. Zhu, "Novel fiber-optic sensors based on long-period fiber gratings written by high-frequency CO<sub>2</sub> laser pulses," *J. Light. Technol.* **21**, 1320–1327 (2003).
  41. V. S. Ilchenko and A. B. Matsko, "Optical resonators with whispering-gallery modes - Part II: Applications," *IEEE J. Sel. Top. Quantum Electron.* **12**, 15–32 (2006).
  42. A. B. Matsko and V. S. Ilchenko, "Optical resonators with whispering-gallery modes - Part I: Basics," *IEEE J. Sel. Top. Quantum Electron.* **12**, 3–14 (2006).
  43. M. Sumetsky, Y. Dulashko, and R. S. Windeler, "Super free spectral range tunable optical microbubble resonator," *Opt. Lett.* **35**, 1866-1868 (2010).
  44. V. Kavungal, A. K. Mallik, G. Farrell, Q. Wu, and Y. Semenova, "Strain-induced spectral tuning of the whispering gallery modes in a cylindrical microresonator formed by a polymer optical fiber," *Appl. Opt.* **56**, 1339-1345 (2017).
  45. M. Sumetsky, Y. Dulashko, J. M. Fini, A. Hale, and J. W. Nicholson, "Probing optical microfiber nonuniformities at nanoscale," *Opt. Lett.* **31**, 2393–2398 (2006).
  46. M. Hossein-Zadeh and K. J. Vahala, "Fiber-taper coupling to Whispering-Gallery modes of fluidic resonators embedded in a liquid medium," *Opt. Express*, **14**, 10800-10810 (2006).
  47. V. S. Ilchenko, E. Dale, W. Liang, J. Byrd, D. Eliyahu, A. A. Savchenkov, A. B. Matsko, D. Seidel, and L. Maleki, "Compact tunable kHz-linewidth

- semiconductor laser stabilized with a whispering-gallery mode microresonator,” Proc. SPIE. **7913**, 79131G (2011).
48. Y.-Z. Yan, C.-L. Zou, S.-B. Yan, F.-W. Sun, Z. Ji, J. Liu, Y.-G. Zhang, L. Wang, C.-Y. Xue, W.-D. Zhang, Z.-F. Han, and J.-J. Xiong, “Packaged silica microsphere-taper coupling system for robust thermal sensing application,” Opt. Express, **19**, 5753-5759 (2011).
49. P. Wang, M. Ding, T. Lee, G. Senthil Murugan, L. Bo, Y. Semenova, Q. Wu, D. Hewak, G. Brambilla, and G. Farrell, “Packaged chalcogenide microsphere resonator with high Q-factor,” Appl. Phys. Lett. **102**, 131110 (2013).
50. Y. Dong, K. Wang, and X. Jin, “Packaged microsphere-taper coupling system with a high Q factor,” Appl. Opt. **54**, 277-284 (2015).
51. Y. Dong, X. Jin, and K. Wang, “Packaged and robust microcavity device based on a microcylinder–taper coupling system,” Appl. Opt. **54**, 4016-4022 (2015).
52. K. Milenko, I. Konidakis, and S. Pissadakis, “Silver iodide phosphate glass microsphere resonator integrated on an optical fiber taper,” Optics Lett. **41**, 2185–2188 (2016).
53. M. Cai, O. Painter, and K. J. Vahala, “Observation of critical coupling in a fiber taper to a silica-microsphere whispering-gallery mode system,” Phys. Rev. Lett. **85**, 74–77 (2000).
54. M. Han and A. Wang, “Temperature compensation of optical microresonators using a surface layer with negative thermo-optic coefficient,” Opt. Lett. **32**, 1800-1802 (2007).
55. C. H. Dong, L. He, Y. F. Xiao, V. R. Gaddam, S. K. Ozdemir, Z. F. Han, G. C. Guo, and L. Yang, “Fabrication of high- Q polydimethylsiloxane optical microspheres for thermal sensing,” Appl. Phys. Lett. **94**, 231119 (2009).

56. L. Shi, T. Zhu, D. Huang, and M. Liu, "Thermo-Optic tuning of integrated polymethyl methacrylate sphere whispering gallery mode resonator," *IEEE Photonics J.* **8**, 2701307-2701314 (2016).

# Chapter 4

---

---

## Temperature and magnetic field sensors based on LCORR cylindrical microresonators

---

---

In the previous chapters the strong dependence of the WGM spectra on the resonator diameter was explored for the development of a new geometrical profiling method and highly sensitive strain sensors where the change in refractive index was negligible as compared to the diameter change of the resonator due to the applied strain. The primary research goal in this chapter is to utilize the refractive index tunability of the WGM spectra for the development of novel high sensitivity temperature and magnetic field sensors and tunable electro-optic devices.

It is well known that the optical properties of silica are practically independent on electro-magnetic fields and display a relatively weak temperature dependence making this material unsuitable for sensing of the above parameters. In this chapter, in order to achieve its main objective, combining cylindrical silica microresonators with suitable sensitivity-improving materials or liquids is proposed and investigated. Hollow cylindrical microresonators with different geometries, also known as liquid core optical ring resonators (LCORRs) have been chosen as basic structures allowing easy infiltration with liquid materials, having strong thermo-, electro- and magneto-optic dependencies, such as liquid crystals

and magnetic fluids.

## **4.1 Thermo-optic tuning of a packaged whispering gallery mode resonator filled with nematic liquid crystal<sup>6</sup>**

**Abstract:** Thermo-optic tuning of whispering gallery modes (WGMs) in a nematic liquid crystal-filled thin-walled capillary tube resonator is reported. WGMs were excited by the evanescent field from a tapered optical fiber. Tapered optical fiber fabrication and reduction of wall thickness of the capillary tube was carried out by ceramic micro-heater brushing technique. A simple and robust packaging technique is demonstrated to ensure stable and repeatable operation of the device. Tunability of WGMs with temperature was demonstrated with a sensitivity of  $267.5 \pm 2.5$  pm/°C. The demonstrated thermo-optic method for WGMs tuning is potentially useful for many tunable photonic devices and sensors.

**OCIS codes:** (060.2370) Fiber optics sensors; (140.3945) Microcavities; (140.3948) Microcavity devices.

### **4.1.1 Introduction**

Optical whispering gallery modes (WGMs) are the electromagnetic resonances supported by open dielectric resonators with the dimensions in the order of few

---

<sup>6</sup> V. Kavungal, G. Farrell, Q. Wu, A. K. Mallik, and Y. Semenova, "Thermo-optic tuning of a packaged whispering gallery mode resonator filled with nematic liquid crystal," *Optics Express*, **26**, 8431-8442 (2018).

millimeters or smaller and a circular shape, *e.g.*, spherical, cylindrical, disk, ring, toroidal etc. WGM resonances can be used in many applications, including optical sensors for biological and chemical compounds, as electro-optical oscillators and modulators, all optical switches, tunable optical filters, or in quantum electrodynamic applications. The versatility of WGM resonators arises from their many advantages, such as high Q-factors, low mode volumes, and the exceptional sensitivity of the optical properties of the resonator to its size as well the nature of the surrounding medium [1,2]. The exceptional sensitivity of the WGM resonators' optical properties to the changes in their geometry and refractive index may lead to significant temperature dependence due to thermo-optic and thermal expansion properties of the resonator's material.

Several authors reported different approaches to eliminate the temperature cross-sensitivity of sensors based on WGM resonators, such as liquid core optical ring resonators (LCORR) [3,4], micro-spheres [5–12], micro-ring [13], micro-toroid [14–16] and fluorescent core micro-capillary (FCM) [17], allowing to improve their performance. At the same time several studies reported applications of the temperature induced spectral shift in WGM resonators for temperature sensing or in tunable devices based on micro-spheres [18–20], micro-bubble [21], micro-rings [22,23], bent optical fiber [24], dye doped hollow polymer optical fiber [25], micro-fiber knot resonator [26], and spherical droplets [27–29].

Silica glass is one of the most popular materials used for fabrication of optical WGM micro-resonators (MRs) due to its low loss and the simplicity of fabrication of high quality resonators by melting the material into circular shapes. However, silica has relatively low thermo-optic and thermal expansion coefficients, so if a silica resonator device is used for sensing of environmental parameters or utilizes



thermo-optic tuning, a means to enhance its temperature sensitivity is required. Such an enhancement is often achieved by coating of the resonator surface with suitable functional materials. For example, authors in [30] used a conjugated polymer coated silica micro-sphere with an improved temperature sensitivity to design a thermo-optical switch. Li *et al.* [22] used a polydimethylsiloxane (PDMS) coating on a toroidal silica micro resonator to enhance its thermal sensitivity. However, combinations of sensitivity improving liquids with micro-resonator devices and sensors results in multiple design challenges, since applying fluids onto the surface of the resonator may lead to poor mechanical stability, the need to protect the fluids from evaporation *etc.* An alternative approach to integration of liquids with WGM resonators is encapsulation of the fluid inside the resonator, fabricated in the shape of a tube, a bubble, or photonic crystal fiber. In this scenario, a thin-walled capillary tube resonators, also referred to as LCORR [31] are especially promising. LCORRs have been used in various sensing applications including the detection of DNA, viruses, proteins and cancer biomarkers [32].

In this manuscript, we propose to enhance the temperature sensitivity of a silica capillary tube resonator with a submicron wall thickness by filling it with a nematic liquid crystal (LC) for thermo-optic tuning applications. The light is evanescently coupled to the resonator using a tapered silica optical fiber. Apart from traditional display applications, LCs are suitable candidates for many photonic applications in which active light manipulation is required. The optical, electrical and magnetic properties of liquid crystals are defined by the orientational order of the constituent anisotropic molecules. The orientational order can be influenced by many factors, such as temperature and electro-magnetic fields. For example, temperature dependence of the refractive indices and optical anisotropy of LCs are often

utilized in many LC based tunable devices for various applications [33]. Nematic liquid crystals are attractive temperature tunable materials due to their large negative thermo-optic coefficients and low absorption at the infrared and visible wavelengths. The thermo-optic coefficient of a typical nematic liquid crystal is significantly larger ( $-9 \times 10^{-4}/^{\circ}\text{C}$  for 5 CB [34]) than those of many common materials such as deionized water ( $-0.7 \times 10^{-4}/^{\circ}\text{C}$  [35]), ethanol ( $-3.7 \times 10^{-4}/^{\circ}\text{C}$  [35]), isopropanol ( $-4 \times 10^{-4}/^{\circ}\text{C}$  [36]) *etc.* The temperature sensitivity of WGMs excited in nematic liquid crystal droplets embedded in polymer matrix has been demonstrated by Humar *et al.* [37] and recently Y. Wang *et al.* [27] reported thermo-optical tuning of optically pumped WGM lasing emission from dye-doped emulsion microdroplets of cholesteric liquid crystals (CLCs) suspended in an aqueous environment. More recently, temperature tuning in a tapered fiber coupled LC droplet WGM resonator was reported by Y. Wang *et al.* [29]. However, individual LC droplets have never been considered as a tunable optical device. Moreover, in laboratory conditions, evanescent field coupling of light into spherical, bottle or bubble MRs using a fiber taper is typically realized by means of high-resolution 3D micro-positioning stages and optical microscopes for a precise alignment of the tapered fiber waist along the MR equator at a close distance to the resonator surface. Evanescent light coupling is somewhat simpler in the case of cylindrical micro-resonators since only the 2D alignment is necessary. However, in real world applications even the least complex scenario becomes impractical due to the need for bulky and heavy micro-positioning equipment. Therefore, for practical applications development of a simple and reliable packaging method is required for such WGM devices, which would enable their fabrication in a portable and miniature shape without degrading in their

laboratory performance. Therefore, in this work we also propose and demonstrate a suitable packaging method for our proposed WGM device. Such a packaged device can be used as a narrow-band thermo-optic tunable filter. The tapered fiber, thin walled silica capillary resonator, and the substrate supporting the resonator, are made from silica, which is good for reducing the temperature expansion imbalance in the packaged device. Additionally, the simplicity, mechanical stability, and the direct interaction of the coupling region with the surroundings (the coupling region is not embedded in a polymer) are the advantages of the proposed packaging technique.

#### **4.1.2 Experimental details, results and discussions**

##### **a) Packaging of the coupled system.**

The operating principle of the proposed tunable device relies on the interaction between higher order WGMs penetrating into the capillary and the LC inside the capillary whose refractive index is strongly influenced by the applied temperature. In order to increase the efficiency of such interaction, the capillary walls should be sufficiently thin [38]. The thin-walled capillary tube resonator in our experiment was prepared from a short section of a coating-stripped silica capillary tube with inner diameter of 700  $\mu\text{m}$  and outer diameter of 850  $\mu\text{m}$  (Polymicro Technologies). In order to reduce the wall thickness down to the submicron scale, the capillary tube was tapered using a ceramic micro-heater and the fiber pulling setup [39]. Heating and stretching of the capillary tube resulted in the reduction of the capillary wall thickness as well as its external diameter. Resulting external diameter and wall thickness of the uniform tapered portion of the resonator were 41  $\mu\text{m}$  and 0.5  $\mu\text{m}$  respectively. As a first step of the resonator packaging process, the prepared thin-walled capillary tube was attached on to a glass substrate at a

height of ~1 mm above the glass surface using a UV- curable glue [Figure 48(a)].

The total length of the capillary tube was 20 mm.

The tapered optical fiber for light coupling was fabricated using the same fiber pulling setup as for the capillary fabrication and the micro-heater brushing technique described in [39]. The diameter of a uniform waist portion of the fabricated fiber taper was ~1.3  $\mu\text{m}$ . The ends of the tapered fiber were connected to a superluminescent diode (SLD) (Thorlabs) with a wavelength range of 1500–1600 nm and an optical spectrum analyzer (OSA) (Advantest, Q8384) with a resolution of 0.01 nm. To maximize the light coupling efficiency, the uniform tapered portion of the capillary tube acting as the micro-cylinder must be placed perpendicularly and in direct physical contact with the fiber taper waist. Figure 48(b) illustrates schematically the experimental setup for optimizing the coupling efficiency between the fabricated tapered optical fiber and the capillary tube resonator. After achieving the physical contact with the tapered fiber, the capillary tube was slowly moved along the taper axis using a micro-translation stage while maintaining physical contact and a mutually orthogonal orientation. During this process, the transmission spectrum of the taper was observed at the OSA screen to determine the optimal position of the contact point, corresponding to the phase match between the propagating mode of the fiber taper and the fundamental WGM of the capillary tube resonator. A manual three-paddle polarization controller (FPC030) placed between the SLD and fiber taper was used to control the polarization and maximize the light coupling efficiency. After achieving the desired WGM spectrum quality, both ends of the tapered fiber were glued to the glass substrate using a UV curable epoxy as shown in Figure 48(c). The entire packaging process took less than 10 minutes.

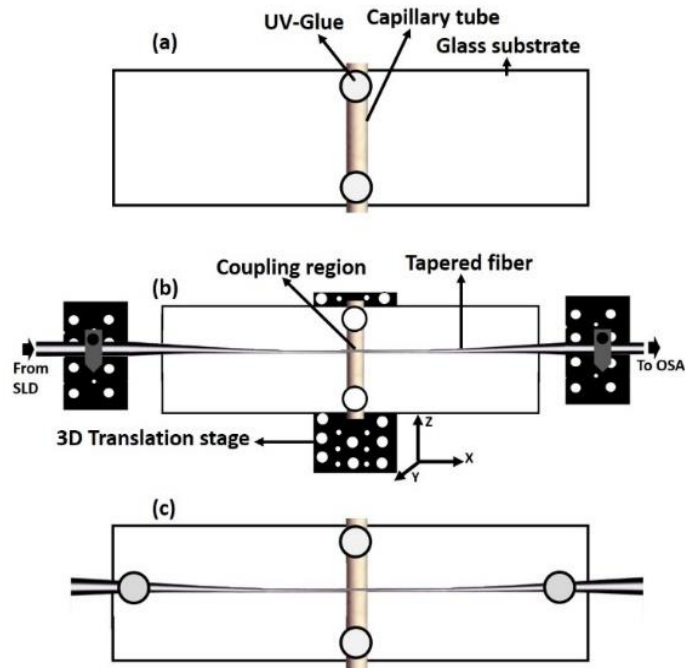


**Figure 47.** Schematic of the packaging process: (a) Capillary tube attached to the glass substrate, (b) Maximizing the coupling efficiency between the tapered optical fiber and capillary tube resonator, and (c) Immobilizing the coupled system on a glass substrate.

Robustness of the packaged device was evaluated by observing the effect of vibration on the transmission spectrum. For this test, the packaged sensor was placed on a simple vibration generator driven by a signal generator with a maximum peak-to-peak amplitude of 6 V, as shown in Figure 48(b). The packaged device was subjected to vibrations at a frequency of 10 Hz for 30 minutes. Spectra of a single WGM resonance dip in the transmission spectrum before and after the vibration test are shown in Figure 48(a). One can see from the figure that this resonance dip with a central wavelength of 1515.78 nm does not show any changes, and any possible discrepancies are less than the resolution of the OSA employed in the experiment (10 pm).

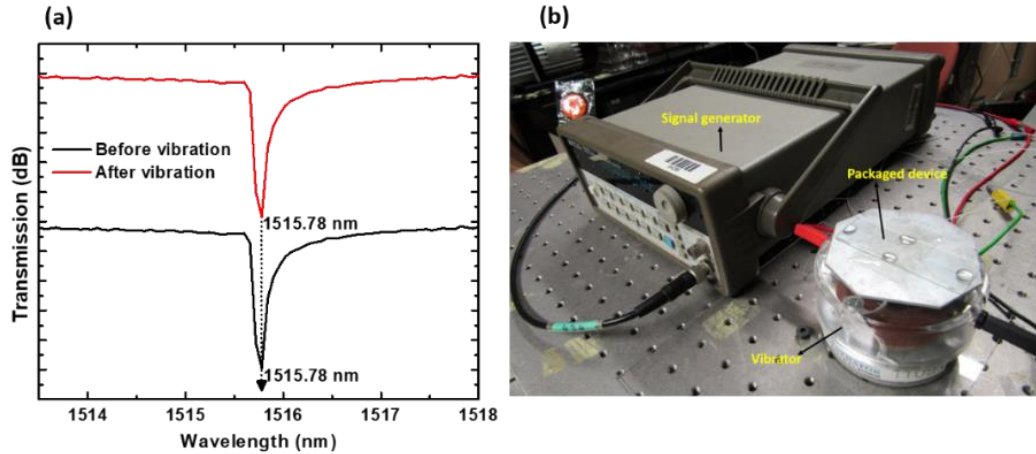


**Figure 48.** (a) Selected WGM resonance dip of the packaged device before and after the vibration test. (b) Experimental set up for vibration tests.

### **b) Thermo-optic tuning experiments using the packaged device**

After packaging, the capillary micro-resonator was filled with a nematic liquid crystal (MLC 7012, Licrystal) using a micro-syringe pump. Subsequently both ends of the capillary tube were sealed using a UV curable epoxy. The WGM spectrum experienced dramatic changes due to the significant increase in the effective refractive index inside the resonator. Figure 49 shows the WGM spectra of the packaged capillary tube resonator before and after it was filled with the liquid crystal. One can see from the figure that the average transmission loss of the spectrum, corresponding to the resonator filled with the LC, is much higher. The extinction ratio of the WGM resonances increased from 6 dB to 13 dB (about 60 % increase). It should be noted that additional side-lobes appear in the WGM spectra, possibly due to the excitation of non-degenerated WGMs after infiltrating the resonator with higher birefringent LCs. The shift experienced by the WGMs after infiltration is difficult to calculate since the shift is higher than that of the FSR value of the spectrum. The average Q-factor of the highest extinction troughs decreased from  $\sim 1.9 \times 10^4$  to  $\sim 0.9 \times 10^3$ , suggesting an increased loss within the

resonator. The increase in the average loss of the transmission spectrum of the taper after infiltrating the resonator with the LC is probably due to a number of factors such as scattering and absorption of light by the liquid crystal medium. In addition, it can be seen that the free spectral range (FSR) of the WGMs increased for the LC-filled resonator from 11.5 nm to 13.35 nm leading to the reduction of a number WGM resonances observed in the wavelength range from 1500 to 1600 nm.

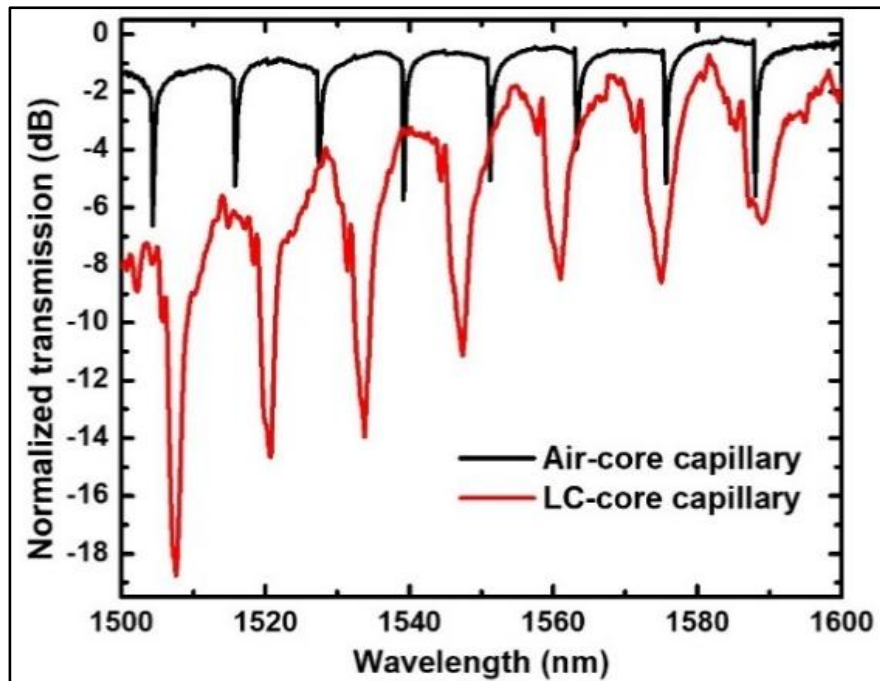


**Figure 49.** Experimental WGM spectra of the air core and liquid crystal filled thin-walled micro-capillary.

Analysis of the experimental results allows one to determine and compare the so-called effective diameter of the capillary tube resonator before and after its infiltration with LC, using the approximate equation [40]:

$$D_{eff} = \frac{\lambda^2}{\pi n_{eff} FSR} \quad (4.1)$$

Where  $\lambda$  is the resonance wavelength and  $n_{eff}$  is the effective refractive index of the

capillary tube resonator.

As can be seen from the above formula, the increase in the effective refractive index of the capillary tube and the increase in experimental FSR due to the infiltration with a higher refractive index LC, should lead to a reduction in the resonator's effective diameter. The notion of effective diameter relates to the localization of WGMs inside the resonator. As was discussed previously by Sumetsky *et al.* in [38] for liquid ring resonator optical sensor (LRROS), and in our previous study of the photonic crystal fiber resonators [41], an increase in the effective refractive index of the resonator core leads to the WGMs moving away from the capillary wall toward the higher refractive index core.

In order to demonstrate thermo-optic tuning of the WGM resonances in the fabricated capillary tube resonator we carried out a series of experiments increasing the temperature from room temperature 25°C up to 50°C in 1°C steps by placing the packaged device on a controlled hot stage. Later the temperature was decreased in 1°C steps back to room temperature with all changes in the transmission spectrum recorded using an OSA. The temperature of the hot stage was measured by a thermocouple with 0.1°C measurement resolution. Figure 50 shows the transmission spectra of the packaged LC filled capillary tube resonator with increasing and decreasing temperature in a selected wavelength range. With the increase in temperature, all the WGM resonances experienced monotonic blue shifts and the decrease in temperature resulted in their return back to their initial spectral positions.



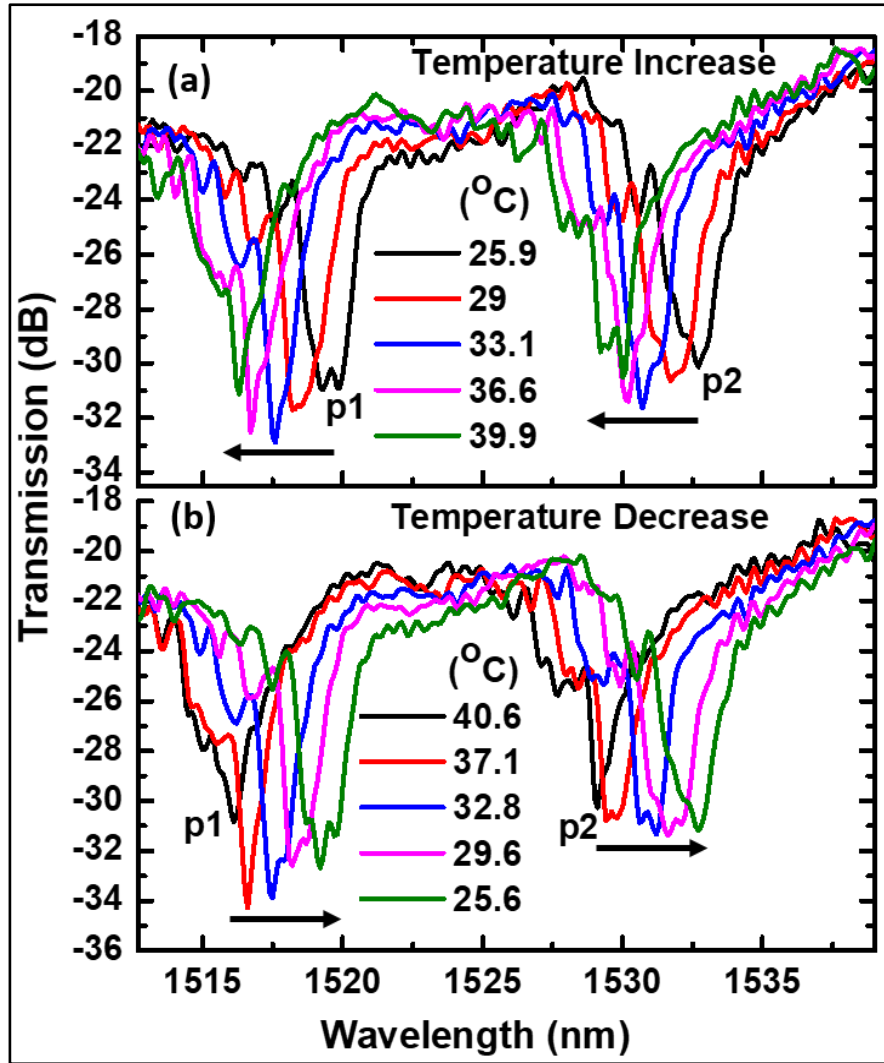


**Figure 50.** Transmission spectra of the LC-filled WGM resonator with (a) increasing and (b) decreasing temperature. There is an average spectral shift of 3.23 nm for the temperature change from of 26 to 40 °C.

An average spectral shift of 8.3 nm was observed for the temperature change from of 26°C to 50.8°C with a rate of 270 pm/°C. By way of justification it is well known that both, ordinary and extraordinary refractive indices of nematic LCs depend on the orientational order of the LC molecules. An increase in the LC temperature causes orientational fluctuations leading to the decrease of refractive index of both components [33]. This decrease of the liquid crystal’s refractive index leads to the decrease in the WGM resonant wavelengths to satisfy the

resonance phase matching condition ( $Ln_{eff} = m\lambda_m$ , where  $\lambda_m$  is the  $m^{\text{th}}$  order resonance wavelength,  $n_{eff}$  the effective refractive index of the resonator,  $L$  is the cavity's round trip length, and  $m$  is the integer number of wavelengths along the optical round-trip length termed as the azimuthal mode number) [40].

An increase in temperature also causes a decrease in the Q-factor of the resonance and appearance of additional secondary spectral dips near the main resonance, most likely due to the fact that the liquid crystal core is a birefringent medium and thus has different RIs for different polarizations. The exact position of the resonance minimum was determined by fitting of the primary (highest extinction ratio) spectral trough corresponding to the fundamental mode with Lorentz function. For greater clarity, Figure 51 illustrates the dip wavelength shift of a single WGM resonance [marked p2 in Fig. 50] with increasing and decreasing temperatures in the range from 25.6 to 51°C. The measured wavelength shift (scatter data) is linearly fitted (solid line). Linear fitting of the wavelength response data indicates that the linear regression coefficient is 0.97 for both the temperature increase and temperature decrease cases. The slopes of the linear dependencies are -270 pm/°C (temperature increase) and -265 pm/°C (temperature decrease). The mean value of the slope for the heating and cooling experiments is -267.5 pm/°C. The uncertainty in the slope is calculated as  $\pm 2.5$  pm/°C. Thus, the temperature sensitivity of the proposed device is  $267.5 \pm 2.5$  pm/°C. At higher temperatures, the resonance wavelength undergoes stronger fluctuations due to the increasing fluctuations of the hot stage temperature.

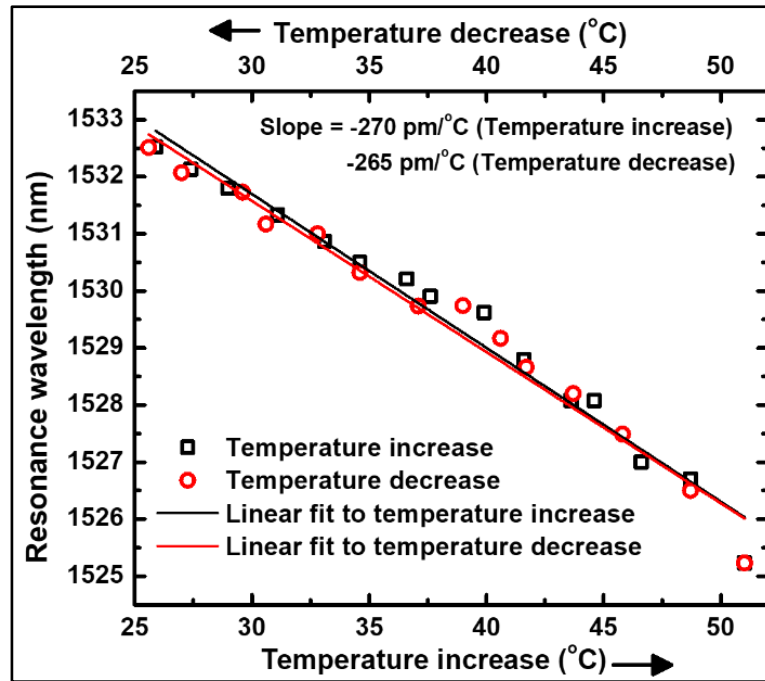


**Figure 51.** Spectral shift experienced by a selected WGM resonance [p2 in Figure 50] with increasing and decreasing temperature.

To test the repeatability of the thermo-optic tuning of the packaged LC filled resonator, two additional experiments were carried out by setting a specific temperature of the hot stage, allowing for a certain time interval to reach the setting and then turning the stage off allowing it to cool down to room temperature. The WGM spectra were recorded continuously and the spectral shift experienced by the modes were analyzed. In the experiment the temperature of the sensor was altered from room temperature (26 °C) to one of two elevated temperatures, 35 °C and 45 °C, by a controlled heating stage.

To understand the evolution of the spectrum as temperature changes with time, the spectral shifts of a selected resonance [marked p2 in Figure 50] were measured as the temperature was cycled at intervals of 10 minutes between room temperature and an elevated temperature. The WGM spectra of the packaged device were sampled with a fixed time interval of 80 seconds during the experiments. The temperature of the controlled heating stage is monitored using a thermocouple attached to the heater. Figure

52 shows the resonance wavelength plotted against time as the temperature was cycled, for both elevated temperatures. Temperature cycling was repeated for 110 minutes for both elevated temperatures. As can be seen from Figure 52, the spectral shifts in response to a temperature change are consistent with time. It was found that after temperature cycling of the sensor to an elevated temperature, the resonance wavelength always returned to its room temperature value, with only very minute variations, demonstrating that the sensor is unaffected by repeated temperature cycling. It should be noted that small fluctuations observed in the WGM spectral positions at the constant but elevated temperatures are most likely due to instabilities of the temperature of the hot stage. The heater used in the experiments had a maximum instability of  $\pm 1.5^{\circ}\text{C}$ , measured using a thermocouple attached to its surface.

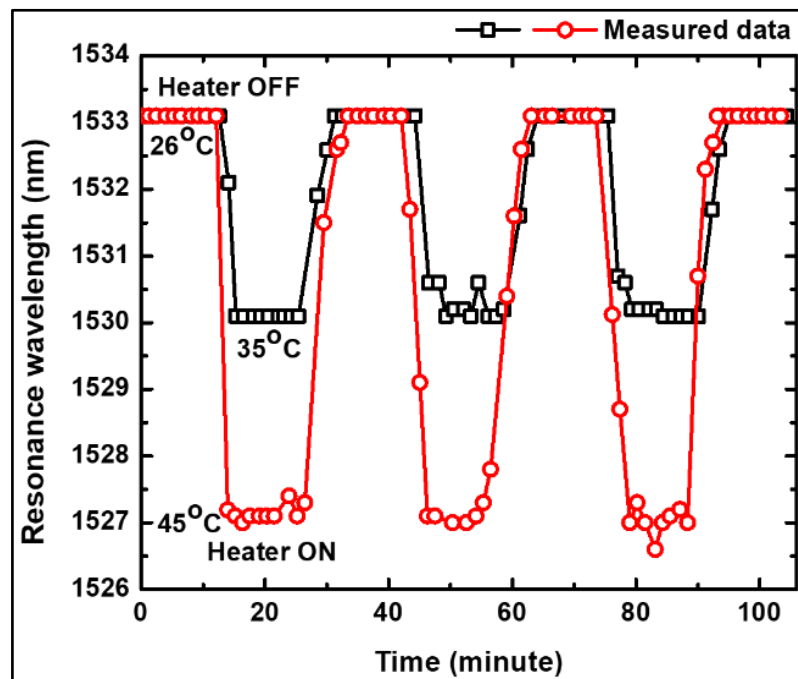


**Figure 52.** The resonance wavelength [p2] plotted against time as the temperature was cycled, for elevated temperatures of  $35^{\circ}\text{C}$  and  $45^{\circ}\text{C}$  from room temperature.

In order to obtain better understanding of the role of LC core within the proposed thermo-optic tunable device, we have conducted a set of experiments for

characterization of temperature response of an empty (air core) capillary tube resonator, fabricated using the same method and thus with a similar geometry.

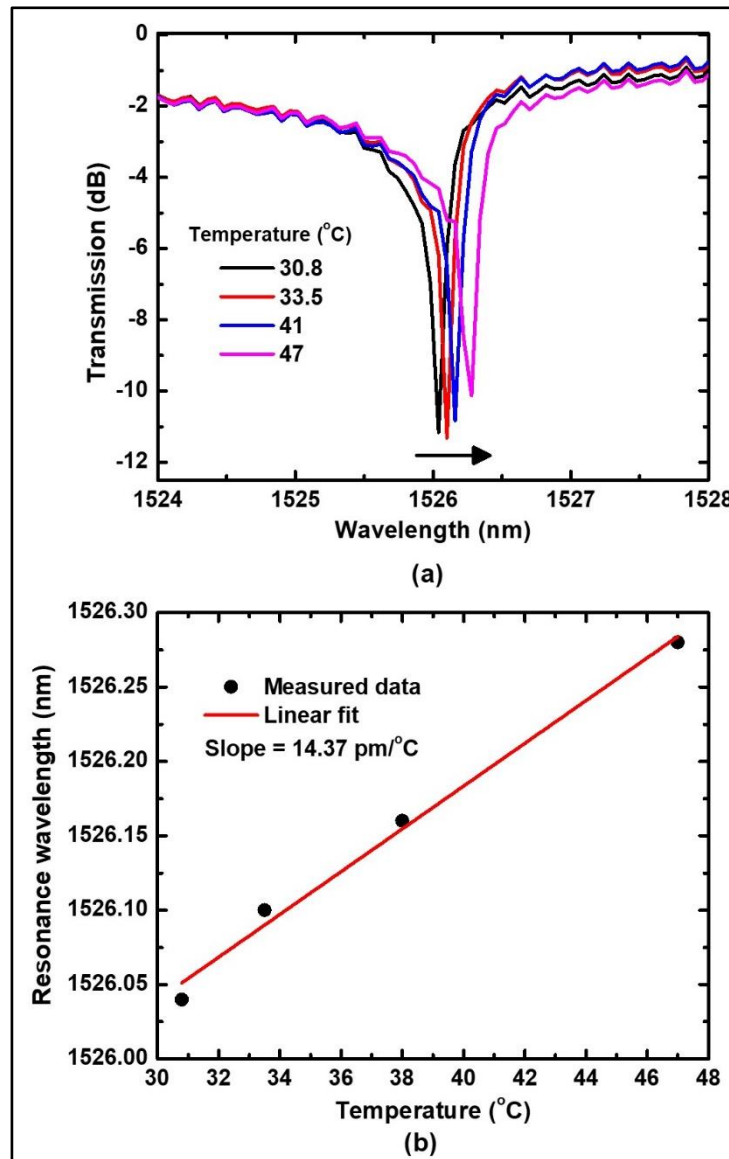


**Figure 53.** (a) Selected WGM resonance dip of an air-core capillary tube resonator with increasing temperature. (b) Linear fit of the measured resonance wavelength data with increasing temperature.

The temperature was increased from room temperature 31°C up to 47°C with 2°C steps by placing the packaged air-core capillary tube resonator on a temperature controlled hot stage while all changes in the transmission spectrum were recorded

using an OSA. The temperature of the hot stage was measured by a thermocouple. Figure 54 illustrates the results of these experiments.

As can be seen from Figure 53(a), the WGM spectrum experiences red shift of 0.24 nm with the increase in temperature, resulting in sensitivity of 14.4 pm/°C. Figure 53(b) shows the linear fit to the measured resonance wavelength shift data with increasing temperature. The redshift of the WGMs with increasing temperature is due to the positive thermo-optic and the thermal expansion coefficients (in the order of  $\sim 10^{-5}/^{\circ}\text{C}$ ) of the silica glass [42]. The thermo-optic coefficient of air is even lower than that of the fused silica ( $\sim 10^{-6}/^{\circ}\text{C}$ ). The sensitivity of the air core silica capillary tube resonator is about 19 times lower than that for the LC filled capillary tube resonator.

### c) Temperature detection Limit

The temperature detection limit (DL) of the proposed device can be calculated using the following formula [43]:

$$DL = \frac{R}{S} \quad (4.2)$$

Here  $R$  is the sensor's resolution and  $S$  is the sensitivity. The sensor's resolution depends upon the various sources of noise involved in the measurement and determined by the equation [43]:

$$R = 3\sigma = \sqrt{\sigma_{\text{ampl-noise}}^2 + \sigma_{\text{temp-induced}}^2 + \sigma_{\text{spect-res}}^2} \quad (4.3)$$

where  $\sigma$  is the total system noise variance, which can be expressed in terms of all the individual noise variances for amplitude noise ( $\sigma_{\text{ampl-noise}}$ ), temperature induced spectral noise ( $\sigma_{\text{temp-induced}}$ , and the spectral resolution noise limit ( $\sigma_{\text{spect-res}}$ ). The standard deviation of the amplitude noise can be calculated as [43]:

$$\sigma_{\text{ampl-noise}} \approx \frac{\Delta\lambda}{4.5(\text{SNR})^{1/4}} \quad (4.4)$$

where  $\Delta\lambda$  is the full-width half maximum of the mode amplitude derived from the Q factor ( $Q = \lambda/\Delta\lambda$ ). The Q-factor of the LC-filled, and the air-core capillary tube resonators were calculated by fitting the resonance dips with Lorentz equation. The corresponding Q-factors of the selected WGMs of the LC-filled and the air-core capillary tube resonators were 807, and 10263 respectively. We assumed the SNR of the system as 60 dB (equivalent to a ratio of  $10^6$ ), then the corresponding  $\sigma_{\text{ampl-noise}}$  were calculated as 13.25 and 1.04 respectively for the LC-filled and the air-core capillary tube resonators. We also assumed the standard deviation due to the temperature stabilization ( $\sigma_{\text{temp-induced}}$ ) as 0.01 pm. The spectral resolution of the OSA used in our experiment is  $10 \text{ pm} \pm 3\%$ . The error in determining the position of the resonant mode is uniformly distributed between  $-0.3 \text{ pm}$  to  $+0.3 \text{ pm}$  and the resulting standard deviation of  $\sigma_{\text{spect-res}}$  is 0.173 pm. The overall sensor resolutions obtained by Eq. (4.3) are 39.84 pm and 3.25 pm respectively for the LC-filled and the air-core capillary tube resonators. Then the corresponding temperature DLs can be calculated by Eq. (4.2) as  $0.148^\circ\text{C}$  and  $0.23^\circ\text{C}$  respectively for the LC-filled and empty (air core) resonators. From the study it is clear that even though the Q- factor of the LC-filled capillary tube resonator is lower than that for the empty (air core) resonator, the temperature detection limit is slightly better for the LC-filled capillary tube than for the empty one.

Finally, we carried out a comparison of the temperature sensitivity of the proposed tunable device with a number of WGM temperature sensors reported previously, and the results are summarized in Table 2.

**Table 2.** Sensitivity comparison of WGM temperature sensors.

Type of sensor	Sensitivity (pm/°C)
Water filled thick (thin) walled fused silica micro-capillary resonator [3]	7.6 (5.4)
Dye-doped hollow polymer optical fiber [25]	11
Water filled thick (thin) walled aluminosilicate capillary micro-resonator [3]	17.2 (13.8)
PMMA wire microcylinder [44]	40.8
PMMA microsphere inserted in a hollow fiber [20]	50
Silica microfiber knot resonator [26]	52
Silicon micro-ring [23]	110
PDMS-coated silica micro-ring [45]	151
Microbubble filled with ethanol [46]	200
Bent optical fiber [24]	212
PDMS microsphere [19]	245
PMMA microfiber knot resonator [26]	266
Tapered optical fiber coupled liquid crystal microdroplet [29]	267.6
<b>Liquid crystal infiltrated LCORR [This work]</b>	<b>267.5±2.5</b>
DCM-doped oil droplet [28]	377
Integrated PMMA microsphere [18]	460
Dye-doped cholesteric liquid crystal microdroplets [27]	1500

As one can see from the Table 2, the device described in this paper offers competitive temperature sensitivity compared to many of the similar WGM devices. Only the dye-doped cholesteric liquid crystal microdroplets [27], DCM-doped oil droplet [28], and the integrated PMMA microsphere resonator [18] show higher temperature sensitivity than the tunable device proposed in this work. It should be noted however that as mentioned in the introduction, individual droplet resonators are difficult to implement as a tunable device due to light coupling and



packaging issues. Moreover, the integrated PMMA microsphere sensor described in [18] demands more effort in terms of fabrication and its wavelength tunability range is four times less (1.93 nm) than that of the proposed here tunable device (8.3 nm).

### **4.1.3 Summary**

In summary, thermo-optic tuning of a nematic liquid crystal filled thin-walled silica capillary tube resonator was demonstrated experimentally with a sensitivity of  $-267.5 \pm 2.5$  pm/°C. An evanescent field from a tapered optical fiber was used to excite the WGMs in the capillary resonator and record its WGM spectrum in the wavelength range from 1500 to 1600 nm. Fabrication of the tapered fiber and the thin-walled capillary tube was carried out by the micro-heater brushing technique. A simple and robust packaging technique for the proposed tunable device was also developed and demonstrated. Thermo-optic tuning experiments were carried out using the LC filled packaged resonator. An increase in the resonator temperature leads to a blue shift of the WGM resonances observed in the transmission spectrum of the fiber taper with a rate of  $-270$  pm/°C and the decrease in temperature resulted in their return back to the initial spectral positions with a rate of  $-265$  pm/°C. The calculated temperature detection limit of the proposed LC filled capillary tube resonator is  $0.15$ °C. The proposed device shows good mechanical stability and repeatability of performance. Initial study indicates that the demonstrated thermo-optic tuning of the WGMs in a nematic liquid crystal thin-walled capillary tube resonator is promising for many photonic applications, for example in tunable filters, switches and sensors.

## **4.2 Magnetic-field sensor based on whispering gallery modes in a photonic crystal fiber infiltrated with magnetic fluid<sup>7</sup>**

**Abstract:** In this work, a magnetic-field sensor was designed to take advantage of the tunability of the resonance wavelengths of a cylindrical whispering-gallery-mode microresonator. The microresonator is based on a 1.3 cm length of photonic crystal fiber infiltrated with a magnetic fluid containing nanoparticles with diameters of either 5 or 10 nm. The Q-factor achieved for the microresonators was  $4.24 \times 10^3$  or higher. When a magnetic field is applied, the whispering-gallery-mode resonances shift toward longer wavelengths. The experimentally demonstrated sensitivity of the proposed sensor was as high as 110 pm/mT in the magnetic field range from 0 to 38.7 mT.

**OCIS codes:** (060.2310) Fiber optics; (060.2370) Fiber optics sensors; (060.4005) Microstructured fibers; (140.4780) Optical resonators.

### **4.2.1 Introduction**

Magnetic field sensors are required in a wide range of applications including navigation, speed and distance measurements, geophysical research, non-contact switching and current measurement [47]. Compared with traditional electrical sensors, fiber optic magnetic field sensors are advantageous because of their immunity to electromagnetic interference, low weight, small size, and the possibility of remote operation.

---

<sup>7</sup> A. Mahmood, V. Kavungal, S. S. Ahmed, G. Farrell, Y. Semenova, "Magnetic field sensor based on whispering gallery modes in photonic crystal fiber infiltrated with magnetic fluids," *Optics Letters*, **40**, 4983-4986 (2015).

Most of the fiber optic magnetic field sensors reported to date utilise either the Faraday effect [48] or magnetostrictive perturbation. Sensors of the former category are often problematic due to the intrinsic birefringence of the sensing fibers, while the latter type of sensor employing magnetostrictive materials in conjunction with optical fiber structures, face the challenge of combining two types of materials within the sensor. Using bulk magnetostrictive materials is also problematic for space limited applications and coating the fibers with magnetostrictive layers often requires a complex fabrication process [49].

Recently many researchers have turned their attention to the use of magnetic fluids for fiber optic sensing. Magnetic fluids are colloidal materials based on surfactant-coated magnetic nanoparticles dispersed in a suitable liquid carrier. Due to their fluidity they can be easily combined with optical fibers and due to their magnetic properties, such as tunable refractive index, magneto-volume variation, magneto-viscosity and magneto-dielectric anisotropy they are good potential candidates to form the basis of magnetic field sensors. Several examples of such sensors have been reported including sensors based on infiltration of magnetic fluids into the air holes of photonic crystal fibers (PCF) [50–54] or using magnetic fluids as claddings in combination with special fiber structures [55], such as fiber tapers [56, 57], and microfiber structures [58, 59]. Depending on the interrogation method used, the sensitivity of these sensors is either in units of wavelength shift per magnetic field unit (pm/mT) or in units of transmission loss per magnetic field unit (dB/mT). Good magnetic field sensitivities have been achieved by several groups. For example, Thakur *et al.* reported a sensitivity of 242 pm/mT in the range of 0 to 45 mT [50]. Miao *et al.* used an S-tapered microfiber integrated with a ferrofluid and reported sensitivities as high as 1.3056 dB/mT and 560 pm/mT in

the range of 2.5 to 20 mT [57]. To date the highest magnetic field sensitivity of 15.6 nm/mT has been reported by Zu *et al.* for a sensor based on the magnetic tunability of photonic bandgaps in a PCF infiltrated with a specially designed high-refractive index magnetic fluid [51].

Whispering gallery modes (WGMs) are electromagnetic surface oscillations supported by dielectric micro resonators with circular structures such as spheres, cylinders, disks or toroids. WGMs arise as a result of trapping of light within the micro resonator by almost total internal reflections from the resonator's curved surface. Such reflections force the light to take on a polygonal path within the curved structure, effectively confining its energy to very small volumes and thus leading to high power densities and high quality (Q) factors. WGM resonators have thus found a wide range of applications as filters, lasers, modulators and sensors [60]. WGMs in a circular resonator can be both excited and interrogated using a thin fiber taper placed in close proximity to the resonator. The excitation of WGMs causes a series of dips in the spectrum of the light transmitted through the fiber taper. The spectral positions of the transmission dips are strongly dependent on the geometry of the resonator, the optical properties of the resonator material and on its effective refractive index (RI). Many of the WGM sensors proposed operate by detecting the resonance frequency or wavelength (dip) shift caused by the change of the RI of the medium surrounding the resonator due to the presence of chemical or biological materials on the resonator surface or in the surrounding solution [2, 61]. In addition, due to the fact that many liquids offer tunable RIs and other unique optical properties, integrating such liquids with circular micro resonators creates opportunities for novel WGM devices, *e.g.* liquid crystal tunable filters, modulators, liquid dye lasers *etc.* Such devices and sensors

face multiple design challenges due to the complexity of applying fluids onto the surface of the resonator, poor mechanical stability and the need to protect the fluids from evaporation. An alternative approach to the integration of liquids and WGM resonators is encapsulation of the fluid within a solid cladding in the shape of a tube, a bubble (bubble) or a hollow sphere. Recently White *et al.* introduced a liquid core optical ring resonator based on a thin-walled glass capillary and demonstrated theoretically and experimentally the possibility to detect the change in the RI of the liquid core near the interior surface of the capillary [62,63].

In this work, a novel form of magnetic field sensor is proposed and demonstrated experimentally for the first time, to the best of our knowledge. The sensor utilizes WGMs excited in a short section of PCF infiltrated with a magnetic fluid. The proposed sensor offers a competitive sensitivity to magnetic field measurement compared to fiber optic sensors reported previously but with the advantage of simpler design and fabrication.

#### **4.2.2 Operational principles**

The operating principle of the magnetic field sensor proposed in this work is as follows. A short section of a solid core PCF acts as a cylindrical micro resonator in which the WGMs are excited by evanescent coupling of light propagating through a thin fiber taper placed perpendicularly and in direct contact with the PCF. The cladding air holes of the PCF are infiltrated with a magnetic fluid whose RI is sensitive to magnetic field. It is well known that spectral positions of the WGM resonances for a particular resonator are determined by spatial distribution of the refractive index inside the resonator body [2]. A general analytic solution to describe the WGM spectra is difficult to obtain, although the structure of WGMs have been studied numerically in [64]. Most WGM sensors studied in the literature

are based on perturbation of the WGMs at the surface of the resonator, but in this case the magnetic fluid, which is key to sensing magnetic fields, is within the body of the resonator, not on the surface of the resonator. It has been found that higher frequency WGMs excited in a micro resonator are mainly confined close to the surface of the resonator (in the outer cladding of the PCF in this case), while the lower frequency modes are located further from the surface of the micro resonator [2].

In the proposed configuration the resonator is formed by a section of silica fiber cylinder (LMA-10 PCF from NKT Photonics) which has a solid core with a radius of 5  $\mu\text{m}$ , and a cladding with an outer radius of 62.5  $\mu\text{m}$ . The cladding has an outer region formed by solid silica and an inner holey region formed by a periodic seven-ring lattice of hollow capillaries surrounding the core and running through the entire length of the fiber cylinder parallel to its axis. The hollow capillaries have a diameter ( $d$ ) of 3.04  $\mu\text{m}$  and are arranged in a triangular pattern so that  $d/\Lambda = 0.5$ . Such a configuration can be approximately treated as a ring resonator formed by a cylindrical silica wall with an outer radius of 62.5  $\mu\text{m}$  and inner radius of  $\sim 45$   $\mu\text{m}$ . When such a hollow fiber structure is used as a resonator, the effective refractive index of the inner cladding is lower than that of the outer cladding (silica) and WGMs form within the outer part of the fiber cladding with the evanescent field extending toward the holey region of the cladding as illustrated in Figure 54(a). With the increase of the holey region's effective RI (due to infiltration with a magnetic fluid (MF) or due to a further increase of the MF's RI under the influence of magnetic field), the WGMs are "pulled" towards the holey region (Figure 55(b)). This allows for an interaction between the MF and the WGMs evanescent field, especially for the case of higher order modes.

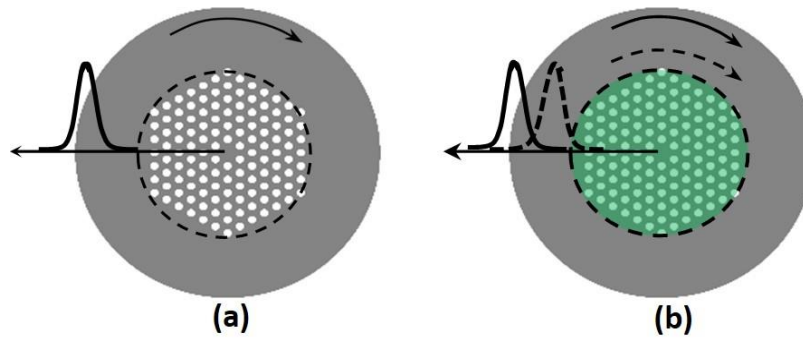


**Figure 54.** Schematic representation of WGMs localization. (a) Inner cladding has low RI - WGMs form at the outer wall and have evanescent field extending toward the inner (holey) cladding region; (b) Inner cladding has higher RI - WGMs exist at both outer surface of the fiber and in the vicinity of the holey cladding.

I. M. White *et al.* [62] and more recently, Y. Liu *et al.* [58] studied optofluidic ring resonators (OFRRs) formed by silica capillaries both theoretically and experimentally showing that while the WGMs were mainly confined in the silica wall (which in the case of the work by Liu *et al.* for example had a wall thickness that approximates the silica outer cladding thickness in this work), the changes in the radial distribution of WGMs are similar to the situation we describe above.

### 4.2.3 Experimental details, results and discussions

In our experiment a  $\sim 1.3$  cm long section of LMA-10 PCF was used as a WGM resonator. The protective polymer coating was removed from the fiber so that the outer diameter was  $125 \mu\text{m}$ .

The air holes of the cladding of the sample were infiltrated with a MF. To allow for comparison, two different MF types were used in two samples of PCF of the same length. The two MFs (from Cytodiagnostics Inc.) contained 10- and 5 nm-diameter water soluble iron oxide magnetic nanoparticles correspondingly, each with a concentration of 5 mg/ml. The refractive indices of the MFs were measured by an Abbe refractometer as 1.337 in both cases. Infiltration of the MF into the

PCF was carried out using capillary forces at room temperature and pressure conditions. For sensor interrogation, a fiber taper with a waist diameter of circa 1  $\mu\text{m}$  was fabricated from a short length of a single mode fiber (SMF-28) using the customized micro-heater brushing technique described in [39].

Figure 55 illustrates experimental setup for the magnetic field sensor characterisation.

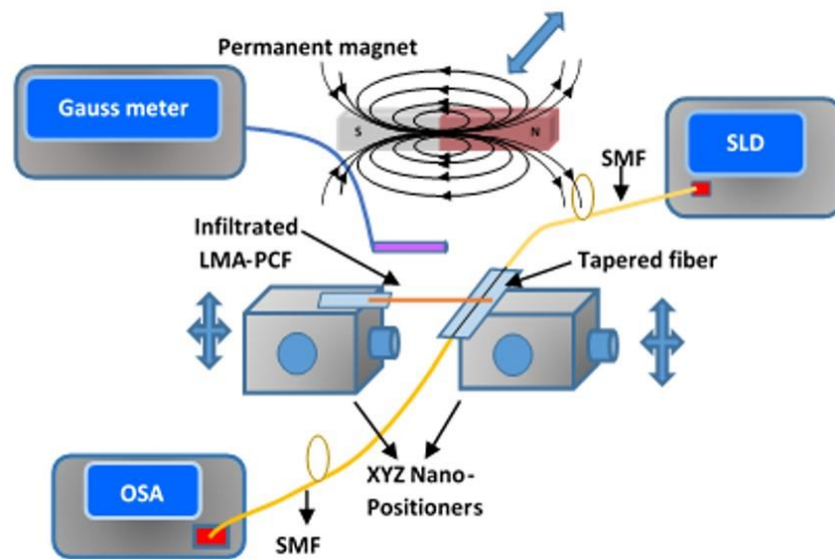


**Figure 55.** Schematic diagram of the experimental setup for the magnetic field sensor characterization.

The ends of the tapered fiber were connected to a superluminescent diode (SLD) (Thorlabs) with a wavelength range of 1500-1600 nm and an OSA (Advantest, Q8384) with a resolution of 0.01 nm. The magnetic field was generated by a rectangular permanent magnet with dimensions of 2"x0.5"x 0.25". Magnetic field strength was varied by changing the distance between the sensor fiber and the magnet as indicated by arrows in Figure 55.

A gauss meter probe (RS, GM08) was used as a reference to measure the magnetic field strength in the vicinity of the sensor fiber. One end of the PCF sensor fiber was fixed on the translation stage with adjustable vertical position to allow for



precise alignment perpendicularly and in direct contact with the tapered fiber to achieve high coupling efficiency.

Figure 56 compares experimental data for a single WGM resonance in the transmission spectra of the LMA-10 resonator recorded before and after its infiltration with the MF containing 10 nm diameter nanoparticles and the corresponding Lorentzian fitting curves allowing an estimate of the resonator's Q-factor. One can see that the value of Q-factor decreases after the infiltration as a result of increased loss due to increased absorption in MF.

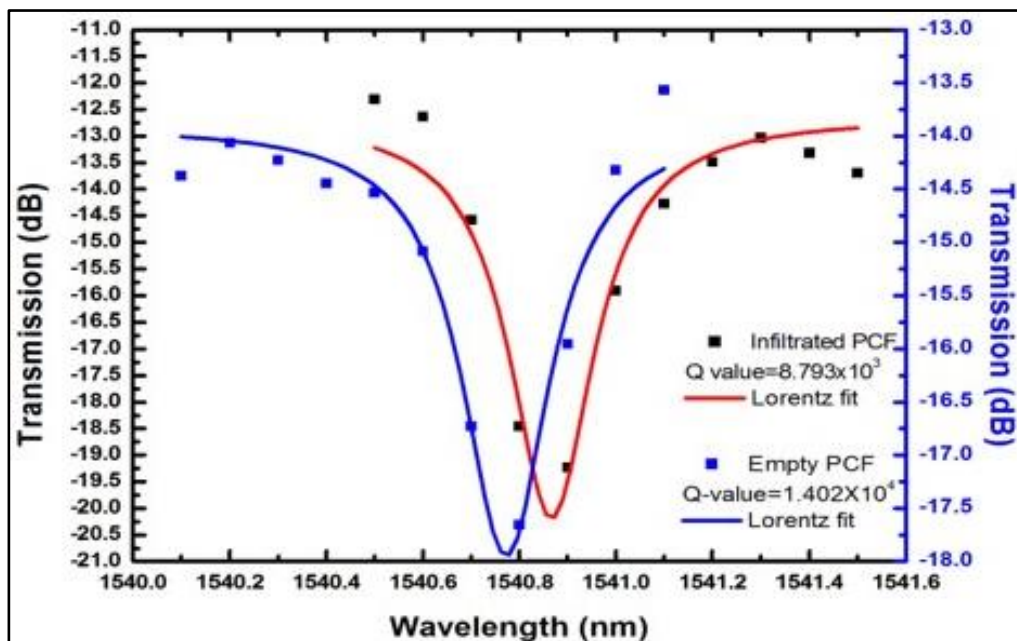


**Figure 56.** Experimental data and their Lorentzian fitting for selected WGM resonances for the spectra generated by an LMA-10 resonator without a ferrofluid and after its infiltration with the MF containing 10 nm diameter nanoparticles in the absence of magnetic field.

The Q-factor, maximum extinction ratio and the free spectral range (FSR) of the WGM spectra were estimated as  $4.24 \times 10^3$ ,  $\sim 10.63$  dB and 4.82875 nm respectively for the sample PCF infiltrated with an MF containing 5 nm diameter nanoparticles. The corresponding values for the sample infiltrated with the 10 nm

nanoparticles solution are  $8.793 \times 10^3$ ,  $\sim 7.61$  dB and 11.6999 nm respectively. The Lorentzian fit used to estimate the Q-factor is illustrated in Figure 56.

Following initial characterization both samples were subjected to varying magnetic fields by changing the distance between the permanent magnet and the sample. Figures 57(a) and 57(b) illustrate the WGM spectra of both samples in the absence of a magnetic field (black) and in the presence of magnetic (red) field in each case. The corresponding magnetic field values were chosen in the higher magnetic field range, close to the saturation.

It can be seen that under the influence of a magnetic field, both spectra experience a red shift and an overall increase of the power level. For clarity only the two extreme spectra corresponding to the minimum and maximum field values are illustrated in Figure 57 for each of the samples with the respective WGM resonances labelled with letters a, b, c, etc. The arrows in the figures indicate the direction of the spectral shift with the increase of the magnetic field. It should be noted that during the experiments changes in the spectral positions of the WGM resonances corresponding to the variations in the applied magnetic field were tracked to eliminate the possibility of ambiguity in the wavelength shift direction. Figures 58(a) and 58(b) illustrate the dependencies of two selected WGM resonances (WGM resonances at 1533.3 nm and 1540.9 nm labelled d in both Figure 57(a) and Figure 57(b) respectively) versus the applied magnetic field. It can be seen that as the applied magnetic field increases the WGM resonance wavelengths increase at first, reaching saturation at values of the magnetic fields above 40 mT and 50 mT respectively. The most likely reason for saturation is the complete alignment of all magnetic nanoparticles with the applied field, which results in no further changes in the refractive index as the field increases further.

The maximum spectral shift values observed for each of the samples are 4.15 nm and 1.66 nm respectively.

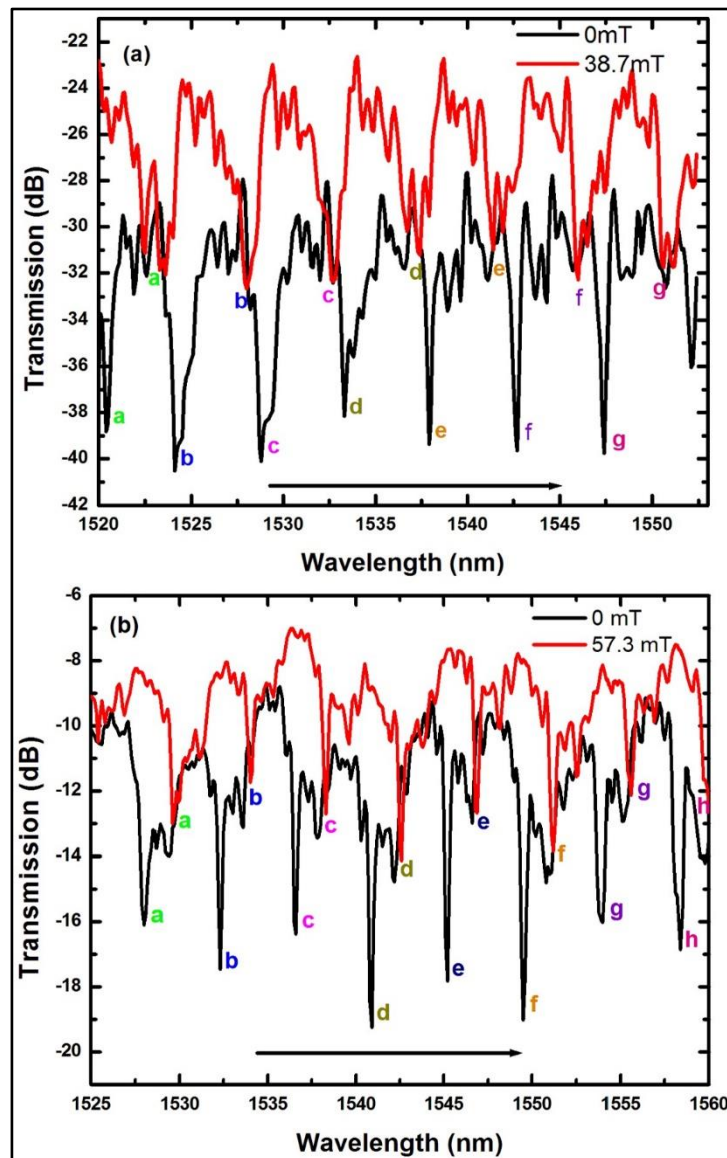


**Figure 57.** (a) WGM spectra generated by the LMA-10 PCF infiltrated with the MF containing 5 nm diameter nanoparticles in the absence of magnetic field (0 mT) and at 38.7 mT; (b) WGM spectra generated by the LMA-10 PCF infiltrated with the MF containing 10 nm diameter nanoparticles in the absence of magnetic field (0 mT) and at 57.3 mT. The arrows indicate the direction of the spectral shift with the increase of the magnetic field.

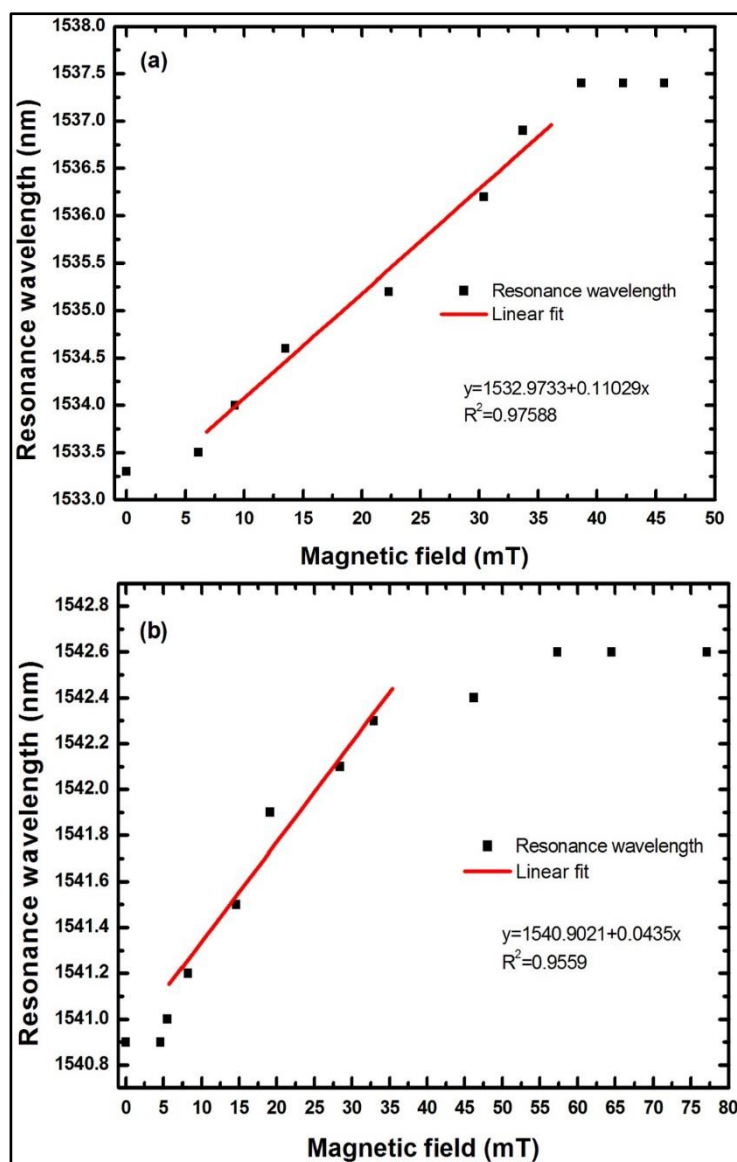


**Figure 58.** Selected WGM resonance wavelength versus applied magnetic field: a) 5 nm diameter nanoparticles sample and b) 10 nm diameter nanoparticles sample.

Variations in the extinction ratio of the WGM spectra versus applied magnetic field are also shown in Figure 57(a) and 57(b). It can be seen that in both experiments higher values of the magnetic field result in the decrease of the extinction ratio of the WGM spectra and both dependencies saturate at higher field values.

The corresponding average sensitivities of the sensor samples estimated from the experimental dependencies in Figure 58 are circa 110 pm/mT for the MF with 5

nm diameter nanoparticles in the magnetic field range 0 to 38.7 mT and circa 43 pm/mT for the 10 nm- particles in the magnetic field range 0 to 57.3mT.

Figure 59 is an enlarged portion of the WGM spectra for a 10 nm-diameter MF sample which illustrates the modes splitting in the vicinity of the fundamental mode dips with the increase of the applied magnetic field [65], resulting from some higher-order modes.

It should also be noted that magnetic field sensitivity depends significantly on the properties of the magnetic fluid, *e.g.*, the size of the nanoparticles. As can be seen from the experiments the magnetic field sensitivity is higher for the sample based on the MF containing smaller diameter nanoparticles. This fact points towards the possibility of improving the sensitivity of the proposed structure by optimising the properties of both the MF and PCF and thus further studies are required in order to address this challenge

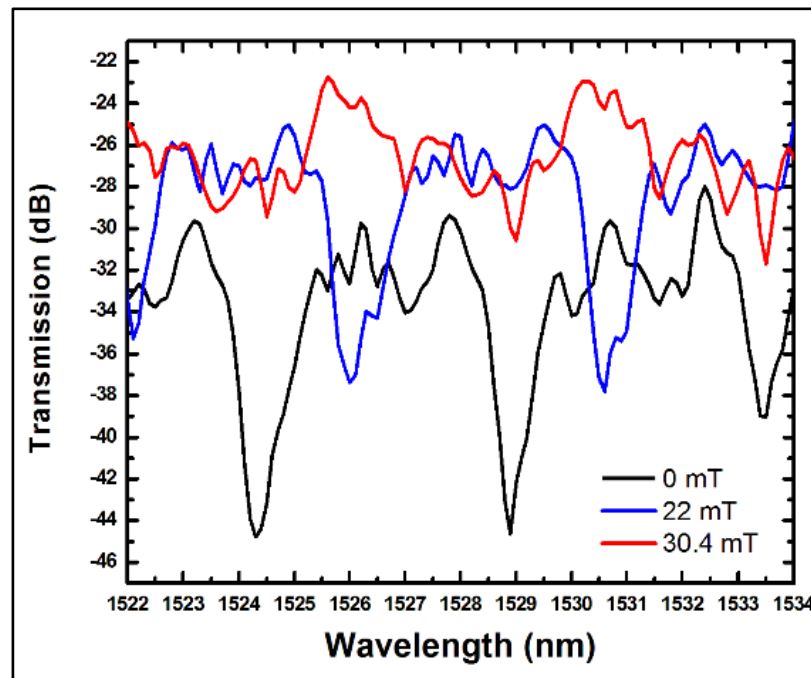


**Figure 59.** Evolution of a single fundamental WGM dip under the influence of magnetic field.

#### **4.2.4 Conclusions**

In conclusion this paper reports for the first time a novel type of magnetic field sensor based on the WGMs excited in a cylindrical micro-resonator formed by a section PCF infiltrated with a MF. Perturbation of the RI of the MF under the influence of the applied magnetic field results in the spectral shift of the WGM resonances detectable in the transmission spectrum of the tapered fiber positioned perpendicularly to the PCF micro resonator. The value of the applied magnetic field is related to the WGM spectral shift assuming a suitable calibration has taken place.

The experimentally demonstrated sensitivity of the proposed sensor is in the order of 110 pm/mT. This value is comparable with the sensitivities of other fiber optic sensors reported previously while the proposed sensor has the advantage of a simpler fabrication.

Further studies are on-going in order to determine the influence of the MF parameters on the proposed sensor performance and to improve the magnetic field sensitivity.

### 4.3 Magnetic field sensing using whispering-gallery modes in a cylindrical microresonator infiltrated with ferronematic liquid crystal<sup>8</sup>

**Abstract:** An all-fiber magnetic field sensor based on whispering-gallery modes (WGM) in a fiber micro-resonator infiltrated with ferronematic liquid crystal is proposed and experimentally demonstrated. The cylindrical microresonator is formed by a 1 cm long section of a photonic crystal fiber infiltrated with ferronematic materials. Both ferronematics suspensions are prepared based on the nematic liquid crystal 1-(trans-4-Hexylcyclohexyl)-4-isothiocyanatobenzene (6CHBT) doped with rod-like magnetic particles in the first case and with spherical magnetic particles in the second case. WGMs are excited in the fiber microresonator by evanescent light coupling using a tapered fiber with a micron-size diameter. The Q-factor of the microresonator determined from the experimentally measured transmission spectrum of the tapered fiber was  $1.975 \times 10^3$ . Under the influence of an applied magnetic field the WGM resonances experience spectral shift towards shorter wavelengths. The experimentally demonstrated sensitivity of the proposed sensor was -39.6 pm/mT and 37.3 pm/mT for samples infiltrated with rod like and spherical like ferromagnetic suspensions respectively for a magnetic field range (0-47) mT. Reducing the diameter of the cylindrical micro-resonator by tapering leads to enhancement of the magnetic field sensitivity up to -61.86 pm/mT and -49.88 pm/mT for samples

---

<sup>8</sup> A. Ibrahim, V. Kavungal, S. Ahmed, P. Kopcanskya, V. Zavisova, G. Farrell, Y. Semenova, "Magnetic field sensing using whispering-gallery modes in a cylindrical microresonator infiltrated with ferronematic liquid crystal," *Optics Express*, **25**, 12195-12202 (2017).

infiltrated with rod like and spherical like ferromagnetic suspensions respectively for the magnetic field range (0-44.7) mT.

**OCIS codes:** (060.2310) Fiber optics; (060.2370) Fiber optics sensors; (060.4005) Microstructured fibers; (140.4780) Optical resonators; (160.3710) Liquid crystals.

### **4.3.1 Introduction**

Optical microresonators are axially symmetric structures that trap light in a small volume in the form of WGMs. This effect occurs when light travels in a dielectric medium of circular geometry. After multiple repeated total internal reflections at the curved boundary, the electromagnetic field can close on itself and give rise to WGM resonances. Such microresonators have been investigated for applications in nonlinear optics, quantum electrodynamics, as optical filters, lasers and sensors for several decades [2]. But only recently have advances in micro- and nano-fabrication techniques made practical applications of micro-resonators with physical dimensions in the order of optical wavelengths feasible. A wide range of optical resonators, such as micro-spheres [66], micro-disks [67], micro-rings [68] and cylindrical micro-cavities [69] have attracted significant interest from researchers worldwide. By using silica which is a highly transparent, low scattering loss material, WGM resonators with extremely high Q-factors and small mode volumes can be realised. Optical micro-resonators have shown many advantages in sensing applications due to their miniature size and high sensitivity allowing for low detection limits [70–72]. Many of the previously reported WGM sensors operate by detecting the shift in the resonant dips caused by the change of the refractive index (RI) of the medium surrounding the resonator due to the presence of chemical or biological materials on the resonator surface or in the surrounding solution [17,61]. Several approaches proposed in the literature utilize



liquid crystals or magnetic fluids to realise novel devices based on the WGMs. Humar *et al.* reported electrically tunable WGM resonators made of nematic liquid crystal droplets, embedded in a polymer matrix with the tunability of approximately two orders of magnitude larger than that achieved in solid-state micro-resonators [73]. Liu *et al.* infused a silica micro-capillary based ring resonator with a magnetic fluid, into which a laser pump light was injected by a fiber taper. Magnetic fluid strongly absorbs pump light which leads to a resonance shift of the silica micro-resonator due to the photothermal effect, resulting in tuning sensitivity of 0.15 nm/mW [58]. In this paper we report a novel magnetic field sensor utilizing WGMs in a cylindrical fiber microresonator infiltrated with a ferronematic LC. The sensor's structure and operating principle are as follows. A short section of a solid core photonic crystal fiber (PCF) acts as a cylindrical micro resonator in which the WGMs are excited by evanescent coupling of light propagating through a thin fiber taper placed perpendicularly and in direct contact with the PCF. The holes of the PCF are infiltrated with a ferronematic liquid crystal whose RI is sensitive to an applied magnetic field. Most WGM sensors reported in the literature are based on perturbation of the WGMs at the surface of the resonator, which in many cases leads to a poor stability of such resonators and often requires additional packaging of the resonator surface. In this work a ferronematic LC, which is key to sensing magnetic fields, lies within the body of the resonator, which leads to an improved stability. It has been found that lower order WGMs excited in such a micro resonator are strongly confined within the surface layer of the fiber resonator (in the outer cladding of the PCF), while the higher order modes expand further from the surface and into the body of the micro-resonator [2].

### 4.3.2 Experimental details

The fiber used in our experiments is the commercially available Polarization Maintaining Photonic Crystal Fiber type PM-1550-01-PCF (Thorlabs). The fiber structure has five rings of air-holes around its asymmetric solid core. The small holes are  $\sim 2.2 \mu\text{m}$  in diameter and the inter-hole spacing is  $\sim 4.4 \mu\text{m}$ . The two large holes defining the birefringent axis of the fibre have a diameter of  $4.5 \mu\text{m}$ . The outside diameter of the fiber is  $122 \mu\text{m}$  and the diameter of the holey region is  $39.7 \mu\text{m}$ . Infiltration of the ferronematics liquid crystal in the 1 cm long section of PM-PCF was carried out by dipping one end of the fiber into the ferronematic suspension so that the liquid infiltrated the PCF holes under the influence of capillary forces. The process was carried out at constant room temperature and pressure conditions. Two samples of ferronematic liquid crystal mixtures have been used in this work. Both ferronematics were based on the nematic liquid crystal 1-(trans-4-Hexylcyclohexyl)-4-isothiocyanatobenzene (6CHBT); which was doped with magnetic nanoparticles of different shapes: spherical and rod-like. Both magnetic suspensions consisted of  $\text{Fe}_3\text{O}_4$  particles coated with oleic acid as a surfactant. The nematic-to-isotropic phase transition temperature (the clearing point) of the studied nematic was  $T_{\text{NI}} = 42.8 \text{ }^\circ\text{C}$ . The mean diameter of the spherical magnetic nanoparticles was  $11.6 \text{ nm}$ . The rod-like magnetic particles had a diameter of  $80 \text{ nm}$ , a mean length of  $1200 \text{ nm}$  and the volume concentration of the nanoparticles in both suspensions was  $2 \times 10^{-4}$ . Figure 60 TEM images for spherical and rod like ferronematic liquid crystal mixtures and optical microscope images of the PCF before and after infiltration [73], and SEM image of the PM-PCF cross section.

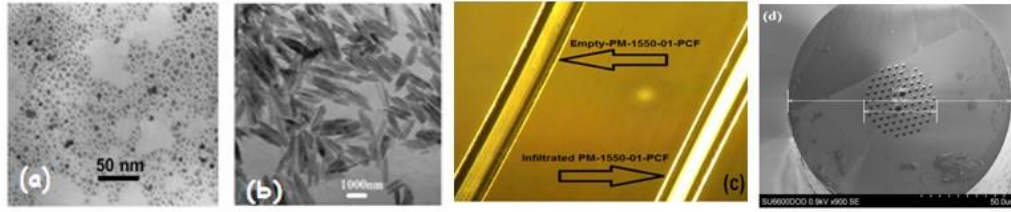


**Figure 60.** TEM images of (a) spherical magnetic nanoparticles, (b) rod-like magnetic nanoparticles, (c) polarizing microscope images of empty and infiltrated PCF in crossed polarizers, and (d) SEM image of the PM-1550-01-PCF cross section.

For the sensor interrogation, a fiber taper with a waist diameter of circa 1  $\mu\text{m}$  was fabricated from a short length of a single mode fiber (SMF-28) using the customised microheater brushing technique [39]. The fiber tapering process was controlled by a customized computer program which realized a synchronized motion of two translation stages with fiber holders applying accurately calculated strain to the SMF. Figure 61 illustrates the experimental setup for the magnetic field sensor characterisation. A superluminescent diode (SLD) (Thorlabs) with a wavelength range of 1500-1600 nm is coupled to a polarization controller (DPC5500; Thorlabs) which in turn is coupled to the input end of tapered fibre, the output of which is coupled to an OSA (Advantest, Q8384) with a wavelength resolution of 0.01 nm. The magnetic field was generated by a rectangular permanent magnet with dimensions of 2"x0.5"x 0.25". The magnetic field strength was varied by changing the distance between the sensor fiber and the magnet as indicated by arrows in Figure 61. A Gauss meter probe (RS, GM08) was used as a reference to measure the magnetic field strength in the vicinity of the sensor fiber. One end of the PCF sensor fiber was fixed on the translation stage with an adjustable vertical position to allow for precise alignment perpendicularly and direct contact with the tapered fiber to achieve high coupling efficiency.

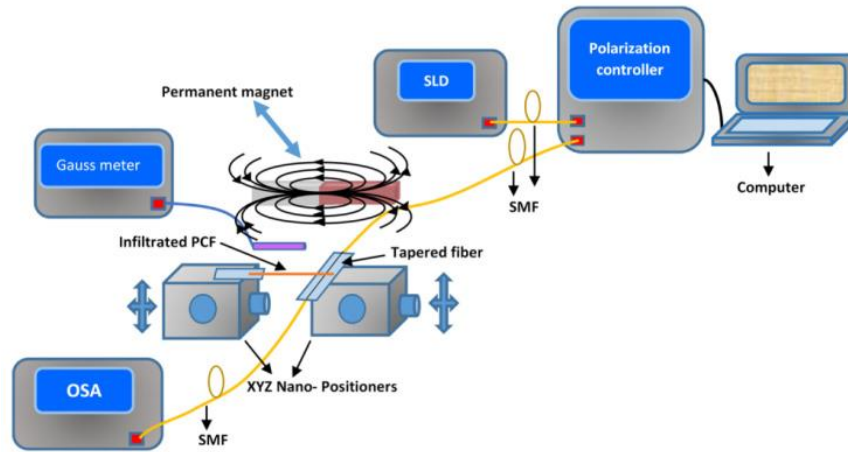


**Figure 61.** Schematic diagram of the experimental setup for the magnetic field sensor characterization.

### 4.3.3 Results and discussion

Figures 62 and 63 show the experimentally measured WGM transmission spectra and the Lorentzian fit used to estimate the Q-factor for the two sample resonators infiltrated with ferronematic LC containing rod-like and spherical particles respectively in the absence of magnetic field and at room temperature.

As can be seen from the figures, the spectra contain periodic narrow dips corresponding to the WGM resonances. The Q-factor for the PCF samples infiltrated with ferronematic LC containing rod-like and spherical like particles are  $1.975 \times 10^3$  and  $1.628 \times 10^3$  respectively. The Q-factors are quite typical for this kind of cylindrical resonators, and their relatively low values are determined by strong scattering by the ferronematics and do not differ for the different kinds of nanoparticles.

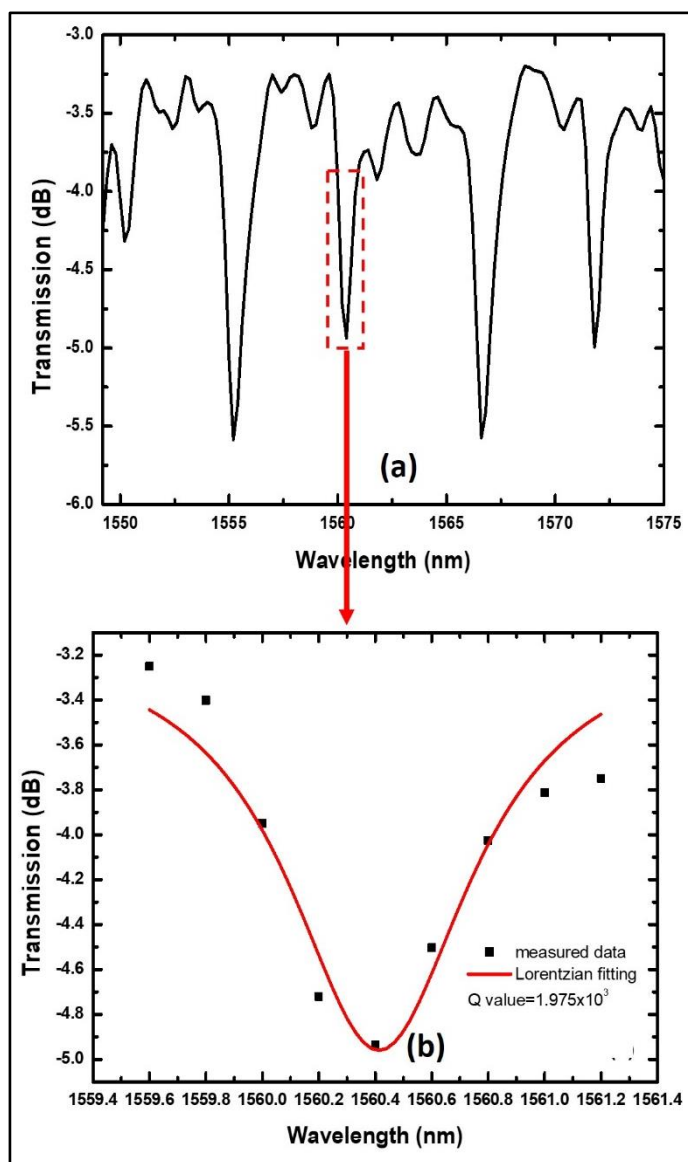


**Figure 62.** Experimental WGM transmission spectra and corresponding Lorentzian fitting to estimate the Q-factor for the sample resonators infiltrated with rod-like particles containing ferronematic LC in the absence of magnetic field and at room temperature.

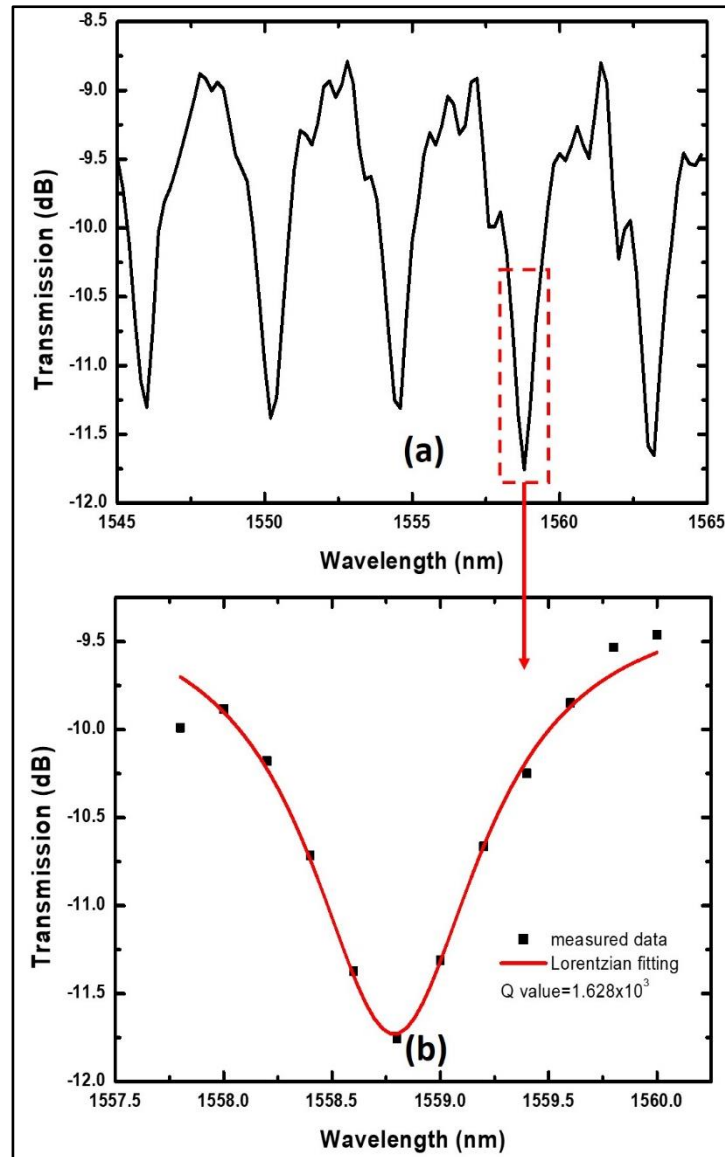


**Figure 63.** Experimental WGM transmission spectra and corresponding Lorentzian fitting to estimate the Q-factor for the sample resonators infiltrated with spherical particles containing ferronematic LC in the absence of magnetic field and at room temperature.

Following initial characterization both samples were subjected to varying magnetic fields by changing the distance between the permanent magnet and the sample, Figures 64(a) and 64(b) illustrate the changes in the WGM spectra for both samples under the influence of different values of the applied magnetic field.

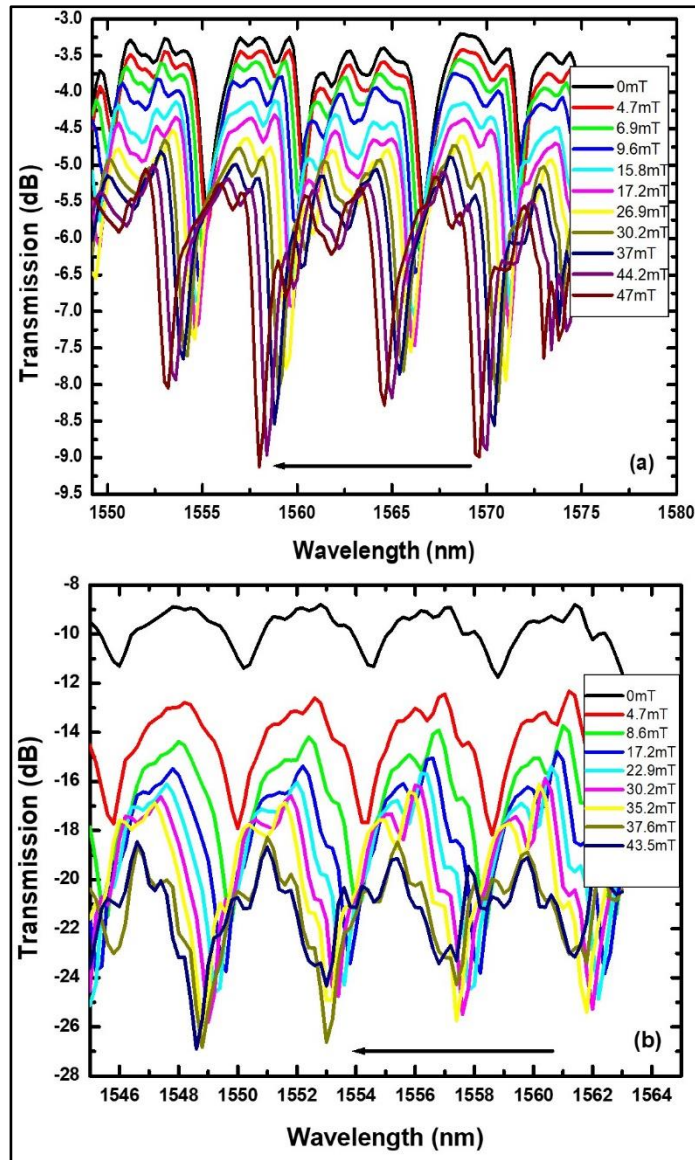


**Figure 64.** WGM spectra at different values of the applied magnetic field for the PM-1550-01-PCF infiltrated samples with (a) rod-like and (b) spherical particles.

It can be seen that with an increase in the magnetic field strength, both spectra experience blue shifts and changes in the overall transmission loss level. The arrows in the figures indicate the direction of the spectral shift with the increase of the magnetic field strength. It should be noted that during the experiments, changes in the spectral positions of the WGM resonances corresponding to the variations in the applied magnetic field were accurately tracked to eliminate the possibility of ambiguity in determining the wavelength shift direction. As expected, an

increase in the applied magnetic field results in the changes of the effective refractive index of the ferronematic-filled fiber cladding, which via interaction with the evanescent field of the WGM leads to the observed blue-shift of the spectral positions of WGM resonances. The apparent increase in the transmission loss for both samples in Figure 64 is likely due to the increased light scattering within the ferronematic LC since at higher values of the magnetic field, greater portion of the WGMs volume overlaps with the ferronematic filled region of the microresonator.

Figures 65(a) and (b) illustrates the dependencies of the two selected WGM resonances (at 1560.4 nm and 1558.8 nm for rod-like and spherical particles containing samples respectively) versus the applied magnetic field value. It can be seen that as the applied magnetic field strength increases the WGM resonant wavelengths decrease linearly at first, reaching saturation at values of the magnetic field above 50 mT and 45 mT for the rod-like and spherical samples respectively. The most likely reason for saturation is the complete re-alignment of all magnetic nanoparticles with the applied field, so that no further changes in the effective index of refraction occur as the magnetic field increases further.

The maximum spectral shift values observed for each of the samples are -2 nm and -1.6 nm for the rod-like and spherical particles samples respectively. The corresponding average sensitivities of the sensor samples estimated from the experimental dependencies in Figure 65 are circa -39.6 pm/mT and -37.3 pm/mT in the magnetic field range 0-50 mT.



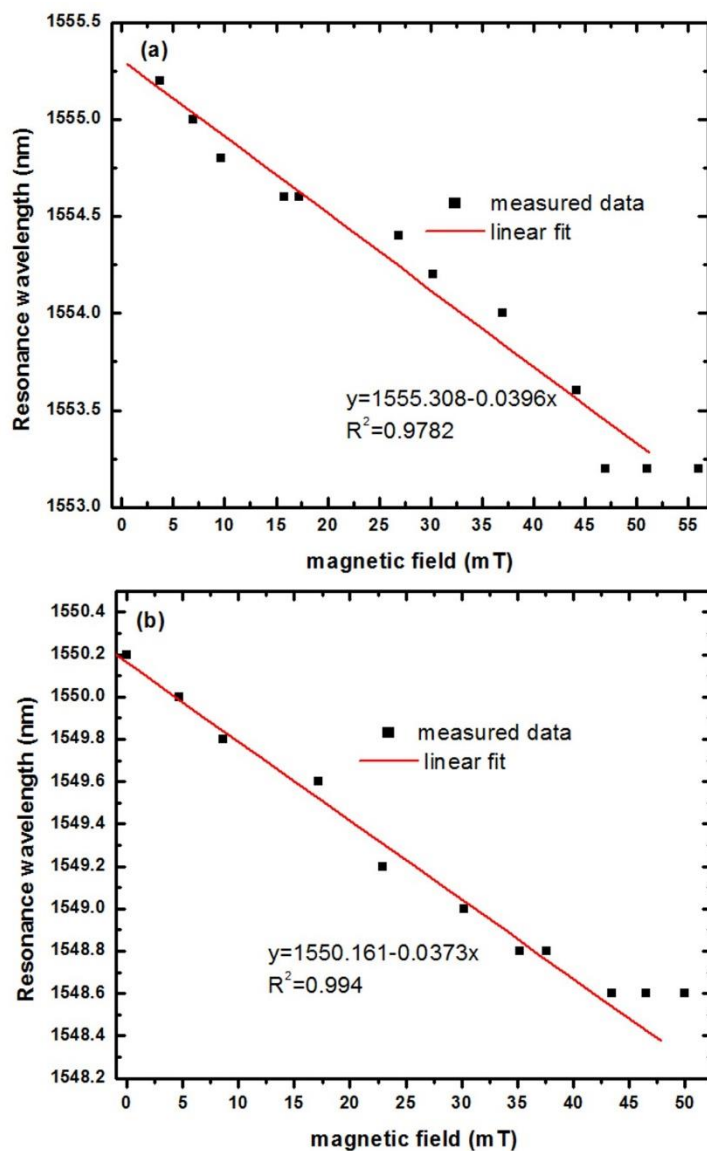


**Figure 65.** Dependence of selected WGM resonant wavelengths and extinction ratio versus applied magnetic field: (a) rod-like particles containing sample and (b) spherical particles containing sample.

From the results we observed that the sensors where the PCF is infiltrated with a rod-like ferronematic liquid crystal sample are more sensitive to a magnetic field than those where the PCF is infiltrated with spherical like ferronematic liquid crystal sample. This is likely due to the dependence of the magnetic susceptibility on the nanoparticles morphology; doping with suspension containing particles with similar shape to the liquid crystal molecules (as in rod-like ferronematic

liquid crystal) will result in lowering of the Fréedericksz transition threshold, as the applied field will more easily rotate the magnetic moments of the magnetic particles inside the ferronematic suspension. This realignment or rotation effect could then be extended to the host nematic through the coupling between the nanoparticles and the liquid crystal molecules. The realignment of the host nematic was assumed to be entirely determined by the ferromagnetic properties of the nanoparticles (not affected by the intrinsic diamagnetic properties of the nematic), since the theory of Brochard and de Gennes predicted a rigid anchoring with  $\mathbf{n} \parallel \mathbf{m}$ , where  $\mathbf{n}$  is the unit vector of the preferred direction of the nematic molecules (director), and  $\mathbf{m}$  is the unit vector of the magnetic moment of the magnetic particles [74]. Since the operating principle of the proposed sensor relies on the influence of the effective index of refraction in the PCF holey region on higher order WGMs excited in such a cylindrical resonator, it is reasonable to assume that decreasing the diameter of the PCF resonator could result in the increase of its sensitivity to the applied magnetic field. To verify this assumption, we carried out an additional experiment for a similar sensor structure but in this case the PCF diameter was reduced down to 50  $\mu\text{m}$  by tapering as shown in Figure 66.

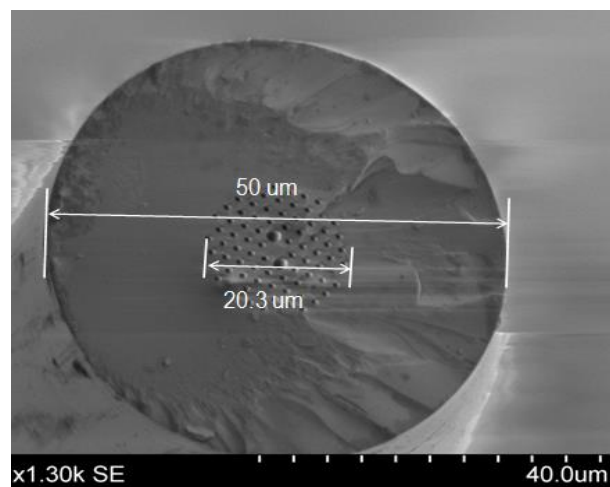


**Figure 66.** The SEM image of the cross section of 50  $\mu\text{m}$  tapered PM- 1550-01-PCFs.

The minimum diameter of 50  $\mu\text{m}$  was chosen in order to prevent collapse of the air holes within the cladding.

Following the tapering the cylindrical resonators were infiltrated with the same ferronematic LC samples as in the previous experiments, Figure 67 illustrates the selected WGM resonances as functions of the applied magnetic field.

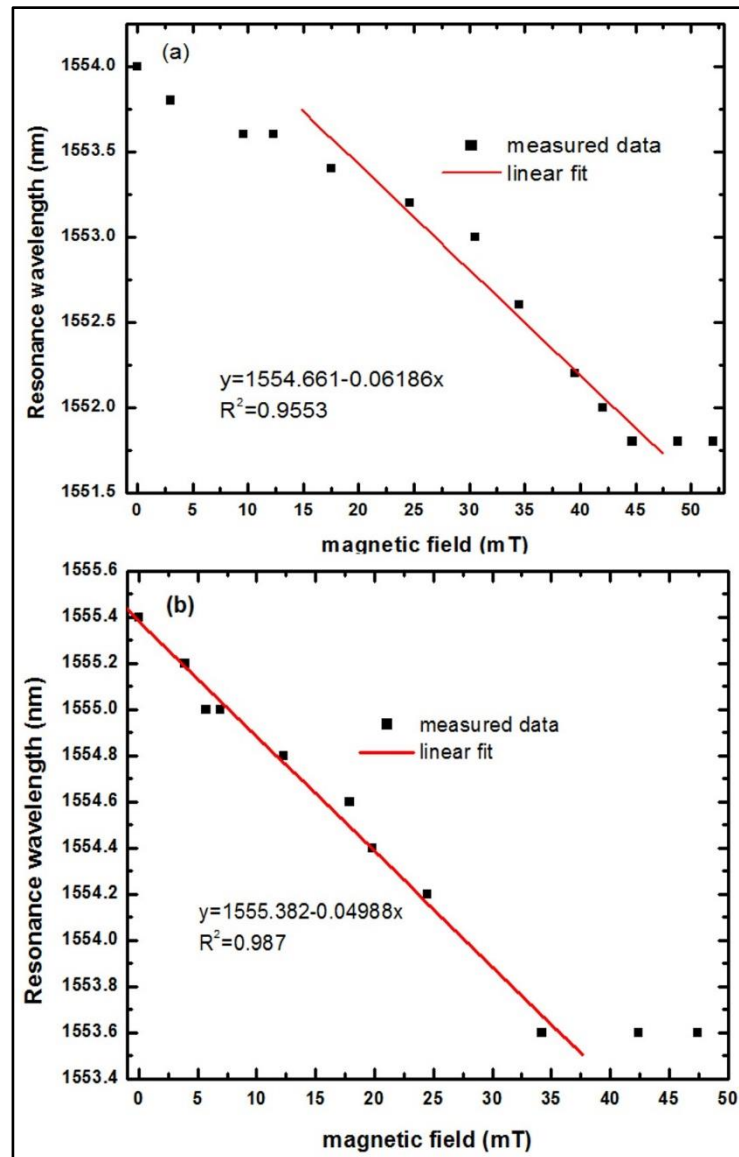


**Figure 67.** Selected WGM resonance wavelength versus applied magnetic field for the tapered sensors (50  $\mu\text{m}$  diameter): (a) rod-like particles sample and (b) spherical particles sample.

Analysis of the obtained results shows an increase in the sensitivity to -61.86 pm/mT for the sensor with the rod-like ferronematic LC and to -49.88 pm/mT for the spherical ferronematic LC sample respectively in the magnetic field range from 0 to 48.8 mT. It should be noted, that a small non-linearity of the resonant wavelength shift at low values of magnetic field for the rod-like sample (Figure 67(a)) could be caused by a small reduction in the fiber cladding holes diameter due to tapering. This in turn may raise the value of the Fréedericksz transition threshold when the length of the rod-like particles becomes comparable with the diameter of cladding holes.

#### **4.3.4 Conclusions**

This paper reports a new type of a magnetic field sensor based on WGMs excited in a cylindrical micro resonator formed by a section of PM-01-1550-PCF infiltrated with a ferronematic LC. Perturbation of the RI of the magnetic fluid under the influence of the applied magnetic field results in the spectral shift of the WGM resonances detectable in the transmission spectrum of the tapered fiber positioned perpendicularly to the micro-resonator. The experimentally demonstrated sensitivity of the proposed sensor is in the order of -39.6 pm/mT for the sensor infiltrated with the rod-like and -37.3 pm/mT for the spherical particles containing ferronematic LC respectively. Reducing the diameter of the cylindrical micro-resonator by tapering leads to enhancement of the magnetic field sensitivity up to -61.86 pm/mT for the sensor infiltrated with the rod-like and -49.88 pm/mT for the spherical particles containing ferronematic LC respectively.

## 4.4 References

1. B. Matsko, A. A. Savchenkov, D. Strekalov, V. S. Ilchenko, and L. Maleki, “Review of applications of whispering-gallery mode resonators in photonics and nonlinear optics,” *IPN Prog. Rep.* **42**, 1–51 (2005).
2. B. Matsko and V. S. Ilchenko, “Optical resonators with whispering-gallery modes - Part I: Basics,” *IEEE J. Sel. Top. Quantum Electron.* **12**, 3–14 (2006).
3. J. D. Suter, I. M. White, H. Zhu, and X. Fan, “Thermal Characterization of Liquid Core Optical Ring Resonators,” *Appl. Opt.* **46**, 389–396 (2007).
4. N. Lin, L. Jiang, S. Wang, H. Xiao, Y. Lu, and H.-L. Tsai, “Design and optimization of liquid core optical ring resonator for refractive index sensing,” *Appl. Opt.* **50**, 3615-3621 (2011).
5. M. R. Foreman, W.-L. Jin, and F. Vollmer, “Optimizing detection limits in whispering gallery mode biosensing,” *Opt. Express.* **22**, 5491–5511 (2014).
6. A. Chijioke, Q. F. Q. Chen, A. A. Y. Nevsky, and S. Schiller, “Thermal noise of whispering gallery resonators,” *Phys. Rev. A.* **85**, 053814 (2012).
7. I. Teraoka, “Analysis of thermal stabilization of whispering gallery mode resonance,” *Opt. Commun.* **310**, 212–216 (2014).
8. A. Savchenkov, A. B. Matsko, V. S. Ilchenko, N. Yu, and L. Maleki, “Whispering-gallery-mode resonators as frequency references II Stabilization,” *J. Opt. Soc. Am. B.* **24**, 2988-2997 (2007).
9. T. Carmon, L. Yang, and K. J. Vahala, “Dynamical thermal behavior and thermal self-stability of microcavities,” *Opt. Express*, **12**, 4742-4750 (2004).
10. M. L. Gorodetsky and I. S. Grudinin, “Fundamental thermal fluctuations in microspheres,” *J. Opt. Soc. Am. B.* **21**, 697–705 (2004).

11. A. B. Matsko, A. A. Savchenkov, N. Yu, and L. Maleki, "Whispering-gallery-mode resonators as frequency references. I. Fundamental limitations Andrey," *J. Opt. Soc. Am. B.* **24**, 1324–1335 (2007).
12. M. Han and A. Wang, "Temperature compensation of optical microresonators using a surface layer with negative thermo-optic coefficient," *Opt. Lett.* **32**, 1800–1802 (2007).
13. B. Guha, J. Cardenas, and M. Lipson, "Athermal silicon microring resonators with titanium oxide cladding," *Opt. Express.* **21**, 26557-26563 (2013).
14. L. He, Y. F. Xiao, C. Dong, J. Zhu, V. Gaddam, and L. Yang, "Compensation of thermal refraction effect in high- Q toroidal microresonator by polydimethylsiloxane coating," *Appl. Phys. Lett.* **93**, 1–4 (2008).
15. J. Zhu, Ş. Kaya Özdemir, L. He, and L. Yang, "Optothermal spectroscopy of whispering gallery microresonators," *Appl. Phys. Lett.* **99**, 2009–2012 (2011).
16. L. He, S. K. Ozdemir, J. Zhu, and L. Yang, "Scatterer induced mode splitting in poly(dimethylsiloxane) coated microresonators," *Appl. Phys. Lett.* **96**, 221101 (2010).
17. S. Lane, F. Marsiglio, Y. Zhi, and A. Meldrum, "Refractometric sensitivity and thermal stabilization of fluorescent core microcapillary sensors: theory and experiment," *Appl. Opt.* **54**, 1331-1340 (2015).
18. L. Shi, T. Zhu, D. Huang, and M. Liu, "Thermo-optic tuning of integrated polymethyl methacrylate sphere whispering gallery mode resonator," *IEEE Photonics J.* **8**, 2701307 (2016).
19. H. Dong, L. He, Y. F. Xiao, V. R. Gaddam, S. K. Ozdemir, Z. F. Han, G. C. Guo, and L. Yang, "Fabrication of high- Q polydimethylsiloxane optical microspheres for thermal sensing," *Appl. Phys. Lett.* **94**, 231119 (2009).

20. B. Özel, R. Nett, T. Weigel, G. Schweiger, and A. Ostendorf, “Temperature sensing by using whispering gallery modes with hollow core fibers,” *Meas. Sci. Technol.* **21**, 094015 (2010).
21. J. M. Ward, Y. Yang, and S. N. Chormaic, “Highly sensitive temperature measurements with liquid-core microbubble resonators,” *IEEE Photonics Technol. Lett.* **25**, 2350–2353 (2013).
22. B. Li, Q. Y. Wang, Y. F. Xiao, X. F. Jiang, Y. Li, L. Xiao, and Q. Gong, “On chip, high-sensitivity thermal sensor based on high- Q polydimethylsiloxane-coated microresonator,” *Appl. Phys. Lett.* **96**, 94–97 (2010).
23. S. Nawrocka, T. Liu, X. Wang, and R. R. Panepucci, “Tunable silicon microring resonator with wide free spectral range,” *Appl. Phys. Lett.* **89**, 7–10 (2006).
24. S. H. Nam and S. Yin, “High-temperature sensing using whispering gallery mode resonance in bent optical fibers,” *IEEE Photonics Technol. Lett.* **17**, 2391–2393 (2005).
25. V. R. Anand, S. Mathew, B. Samuel, P. Radhakrishnan, and M. Kailasnath, “Thermo-optic tuning of whispering gallery mode lasing from a dye-doped hollow polymer optical fiber,” *Opt. Lett.* **42**, 2926-2929 (2017).
26. Y. Wu, Y.-J. Rao, and Y.-H. Chen, “Miniature fiber-optic temperature sensors based on silica/polymer microfiber knot resonators,” *Opt. Express.* **17**, 18142–18147 (2009).
27. Y. Wang, H. Li, L. Zhao, Y. Liu, S. Liu, and J. Yang, “Tunable whispering gallery modes lasing in dye-doped cholesteric liquid crystal microdroplets,” *Appl. Phys. Lett.* **109**, 231906 (2016).

28. Z. Liu, L. Liu, Z. Zhu, Y. Zhang, Y. Wei, X. Zhang, E. Zhao, Y. Zhang, J. Yang, and L. Yuan, "Whispering gallery mode temperature sensor of liquid microresonator," *Opt. Lett.* **41**, 4649-4652 (2016).
29. Y. Wang, H. Li, L. Zhao, Y. Liu, S. Liu, and J. Yang, "Tapered optical fiber waveguide coupling to whispering gallery modes of liquid crystal microdroplet for thermal sensing application," *Opt. Express.* **25**, 918-926 (2017).
30. H. C. Tapalian, J. P. Laine, and P. A. Lane, "Thermo-optical switches using coated microsphere resonators," *IEEE Photonics Technol. Lett.* **14**, 1118–1120 (2002).
31. M. White, H. Oveys, and X. Fan, "Liquid-core optical ring-resonator sensors," *Opt. Lett.* **31**, 1319-1321 (2006).
32. J. Wang, T. Zhan, G. Huang, P. K. Chu, and Y. Mei, "Optical microcavities with tubular geometry: Properties and applications," *Laser Photonics Rev.* **8**, 521–547 (2014).
33. K. Yang and S. T. Wu, "Fundamentals of Liquid Crystal Devices," (John Wiley & Sons, Ltd, 2014).
34. J. N. Ptasinski, I. Khoo, and Y. Fainman, "Nematic Liquid Crystals for Temperature Stabilization of Silicon Photonics," in *Advanced Photonics for Communications*, OSA Technical Digest (online) (Optical Society of America, 2014), paper JT3A.20.
35. C.-L. Lee, H.-Y. Ho, J.-H. Gu, T.-Y. Yeh, and C.-H. Tseng, "Dual hollow core fiber-based Fabry-Perot interferometer for measuring the thermo-optic coefficients of liquids," *Opt. Lett.* **40**, 459–462 (2015).



36. S. Qiu, Y. Chen, F. Xu, and Y. Lu, "Temperature sensor based on an isopropanol-sealed photonic crystal fiber in-line interferometer with enhanced refractive index sensitivity," *Opt. Lett.* **37**, 863–865 (2012).
37. M. Humar, "Liquid-crystal-droplet optical microcavities," *Liq. Cryst.* **43**, 1937–1950 (2016).
38. M. Sumetsky, R. S. Windeler, Y. Dulashko, and X. Fan, "Optical liquid ring resonator sensor," *Opt. Express.* **15**, 14376-14381 (2007).
39. G. Brambilla, V. Finazzi, and D. J. Richardson, "Ultra-low-loss optical fiber nanotapers," *Opt. Express.* **12**, 2258-2263 (2004).
40. W. Bogaerts, P. de Heyn, T. van Vaerenbergh, K. de Vos, S. K. Selvaraja, T. Claes, P. Dumon, P. Bienstman, D. van Thourhout, and R. Baets, "Silicon microring resonators," *Laser Photonics Rev.* **6**, 47–73 (2012).
41. A. Mahmood, V. Kavungal, S. S. Ahmed, G. Farrell, and Y. Semenova, "Magnetic-field sensor based on whispering-gallery modes in a photonic crystal fiber infiltrated with magnetic fluid," *Opt. Lett.* **40**, 4983–4986 (2015).
42. M. Han and A. Wang, "Temperature compensation of optical microresonators using a surface layer with negative thermo-optic coefficient," *Opt. Lett.* **32**, 1800-1802 (2007).
43. X. F. Ian M. White, "On the performance quantification of resonant refractive index sensors," *Opt. Express*, **16**, 1020-1028 (2008).
44. V. Kavungal, G. Farrell, Q. Wu, A. K. Mallik, and Y. Semenova, "A packaged whispering gallery mode strain sensor based on a polymer wire cylindrical micro resonator," *J. Light. Technol.* **36**, 1757-1765 (2017).

45. B. Li, Q. Y. Wang, Y. F. Xiao, X. F. Jiang, Y. Li, L. Xiao, and Q. Gong, "On chip, high-sensitivity thermal sensor based on high- Q polydimethylsiloxane-coated microresonator," *Appl. Phys. Lett.* **96**, 251109 (2010).
46. J. M. Ward, Y. Yang, and S. N. Chormaic, "Highly sensitive temperature measurements with liquid-core microbubble resonators," *IEEE Photonics Technol. Lett.* **25**, 2350–2353 (2013).
47. J. Lenz and S. Edelstein, "Magnetic sensors and their applications," *IEEE Sens. J.* **6**, 631–649 (2006).
48. L. Sun, S. Jiang, and J. R. Marciante, "All-fiber optical magnetic-field sensor based on Faraday rotation in highly terbium-doped fiber," *Opt. Express.* **18**, 5407-5412 (2010).
49. S. M. M. Quintero, C. Martelli, A. M. B. Braga, L. C. G. Valente, and C. C. Kato, "Magnetic Field Measurements Based on Terfenol Coated Photonic Crystal Fibers," *Sensors.* **11**, 11103–11111 (2011).
50. H. V. Thakur, S. M. Nalawade, S. Gupta, R. Kitture, and S. N. Kale, "Photonic crystal fiber injected with Fe<sub>3</sub>O<sub>4</sub> nanofluid for magnetic field detection," *Appl. Phys. Lett.* **99**, 161101 (2011).
51. P. Zu, C. Chiu Chan, T. Gong, Y. Jin, W. Chang Wong, and X. Dong, "Magneto-optical fiber sensor based on bandgap effect of photonic crystal fiber infiltrated with magnetic fluid," *Appl. Phys. Lett.* **101**, 241118 (2012).
52. A. Candiani, M. Konstantaki, W. Margulis, and S. Pissadakis, "Optofluidic magnetometer developed in a microstructured optical fiber," *Opt. Lett.* **37**, 4467-4469 (2012).
53. S. Pu, S. Dong, and J. Huang, "Tunable slow light based on magnetic-fluid-infiltrated photonic crystal waveguides," *J. Opt.* **16**, 045102 (2014).

54. C. Rinaldi, A. Chaves, S. Elborai, X. He, and M. Zahn, “Magnetic fluid rheology and flows,” *Curr. Opin. Colloid Interface Sci.* **10**, 141–157 (2005).
55. H. Wang, S. Pu, N. Wang, S. Dong, and J. Huang, “Magnetic field sensing based on singlemode-multimode-singlemode fiber structures using magnetic fluids as cladding,” *Opt. Lett.* **38**, 3765–3768 (2013).
56. Y. Zhao, D. Wu, and R.-Q. Lv, “Magnetic field sensor based on photonic crystal fiber taper coated with ferrofluid,” *IEEE Photonics Technol. Lett.* **27**, 26–29 (2015).
57. Y. Miao, J. Wu, W. Lin, K. Zhang, Y. Yuan, B. Song, H. Zhang, B. Liu, and J. Yao, “Magnetic field tunability of optical microfiber taper integrated with ferrofluid,” *Opt. Express*, **21**, 29914-29920 (2013).
58. Y. Liu, L. Shi, X. Xu, P. Zhao, Z. Wang, S. Pu, and X. Zhang, “All-optical tuning of a magnetic-fluid-filled optofluidic ring resonator,” *Lab Chip* **14**, 3004–3010 (2014).
59. L. Luo, S. Pu, J. Tang, X. Zeng, and M. Lahoubi, “Highly sensitive magnetic field sensor based on microfiber coupler with magnetic fluid,” *Appl. Phys. Lett.* **106**, 1–6 (2015).
60. G. C. Righini, Y. Dumeige, P. Féron, M. Ferrari, G. N. Conti, D. Ristic, and S. Soria, “Whispering gallery mode microresonators: Fundamentals and applications,” *Riv. del Nuovo Cim.* **34**, 435–488 (2011).
61. D. Zhu, Y. Zhou, X. Yu, P. Shum, and F. Luan, “Radially graded index whispering gallery mode resonator for penetration enhancement,” *Opt. Express*, **20**, 26285–26291 (2012).

62. M. White, J. Gohring, Y. Sun, G. Yang, S. Lacey, and X. Fan, "Versatile waveguide-coupled optofluidic devices based on liquid core optical ring resonators," *Appl. Phys. Lett.* **91**, 2005–2008 (2007).
63. M. White, H. Oveys, X. Fan, T. L. Smith, and J. Zhang, "Demonstration of a liquid core optical ring resonator sensor coupled with an ARROW waveguide array," *Proc. SPIE - Int. Soc. Opt. Eng.* 6475 (2007).
64. S. V. Boriskina, P. Sewell, T. M. Benson, and A. I. Nosich, "Accurate simulation of two-dimensional optical microcavities with uniquely solvable boundary integral equations and trigonometric Galerkin discretization," *J. Opt. Soc. Am. A.* **21**, 393–402 (2004).
65. G. L. J. A. Rikken and B. A. Van Tiggelen, "Observation of magnetically induced transverse diffusion of light," *Nature.* **381**, 54–55 (1996).
66. Y. Lu, J. Q. Yao, P. Wang, and C. Z. Zhang, "An investigation of a tapered fiber-microsphere coupling system with gain and evanescent-field sensing device," *Opt. Lett.* **112**, 475–478 (2001).
67. D. Armani, B. Min, A. Martin, and K. J. Vahala, "Electrical thermo-optic tuning of ultrahigh-Q microtoroid resonators," *Appl. Phys. Lett.* **85**, 5439–5441 (2004).
68. N. Pornsuwancharoen and P. P. Yupapin, "Entangled photon states recovery and cloning via the micro ring resonators and an add/drop multiplexer," *Optik (Stuttg).* **121**, 897–902 (2010).
69. V. Zamora, A. Díez, M. V. Andrés, and B. Gimeno, "Cylindrical optical microcavities: Basic properties and sensor applications," *Photonics Nanostructures - Fundam. Appl.* **9**, 149–158 (2011).

70. A. Yalçın, K. C. Papat, J. C. Aldridge, T. A. Desai, J. Hryniewicz, N. Chbouki, B. E. Little, O. King, V. Van, S. Chu, D. Gill, M. Anthes-Washburn, M. S. Ünlü, and B. B. Goldberg, “Optical sensing of biomolecules using microring resonators,” *IEEE J. Sel. Top. Quantum Electron.* **12**, 148–154 (2006).
71. J. Zhu, S. K. Ozdemir, Y. F. Xiao, L. Li, L. He, D. R. Chen, and L. Yang, “On-chip single nanoparticle detection and sizing by mode splitting in an ultrahigh-Q microresonator,” *Nat. Photonics*, **4**, 46-49 (2010).
72. V. S. Ilchenko and A. B. Matsko, “Optical resonators with whispering-gallery modes - Part II: Applications,” *IEEE J. Sel. Top. Quantum Electron.* **12**, 15–32 (2006).
73. M. Humar, M. Ravnik, S. Pajk, and I. Muševič, “Electrically tunable liquid crystal optical microresonators,” *Nat. Photonics*, **3**, 595–600 (2009).
74. Kopčanský, N. Tomašovičová, T. Tóth-Katona, N. Éber, M. Timko, V. Závášová, J. Majorošová, M. Rajňak, J. Jadzyn, and X. Chaud, “Increasing the magnetic sensitivity of liquid crystals by rod-like magnetic nanoparticles,” *Magnetohydrodynamics*. **49**, 586–591 (2013).

# Chapter 5

---

---

## **Coupling of multiple WGM microresonators for novel sensing applications**

---

---

Optical sensors and tunable devices based on a single WGM micro-resonator were discussed in the previous chapters. This chapter focuses on coupling of multiple WGM micro-resonators to a single optical fiber. Development of an efficient and robust solution to this problem could open the way to multi-parameter and quasi-distributed sensing with WGM micro-resonators. This chapter presents an investigation of the proposed novel configuration based on inline cascaded optical microresonators (ICOMRs). The proposed sensor configuration allows for simultaneous measurement of different parameters (strain, temperature, humidity etc.) using individual WGM resonators coupled to a single optical fiber. The measurement of multiple parameters can be realized by analysing the composite output transmission spectrum. This in turn eliminates the need for multiple light sources and detectors that would be required in a conventional multi-parameter sensor system.

A detailed description of fabrication and packaging of the ICOMRs and demonstration of multi-parameter sensing are presented. Additional micro-resonators in the proposed ICOMR structure can be used to eliminate cross-sensitivity to other environmental influences such as temperature, humidity, air flow *etc.*

## 5.1 Packaged inline cascaded optical micro-resonators for multi-parameter sensing<sup>9</sup>

**Abstract:** A novel design principle and fabrication method for whispering gallery mode optical multiple-resonator arrays have been proposed and demonstrated. The proposed design involves an inline cascade of optical micro-resonators (ICOMRs) coupled to multiple tapered sections along a single optical fiber. The multiple micro-resonators can be used for sensing of several parameters or a single parameter at multiple locations simultaneously. A simple and robust packaging technique has been developed ensuring stable and repeatable operation of the device. In order to demonstrate the capability of simultaneous multi-parameter sensing of the proposed ICOMRs structure, strain and temperature measurements were carried out using an inline cascade of two cylindrical micro-resonators: a tapered polymer optical fiber based micro-cylinder and a polydimethylsiloxane coated silica cylindrical micro-resonator. An Axial tensile strain sensitivity of 1.4 pm/ $\mu\epsilon$  and temperature sensitivity of 330 pm/ $^{\circ}\text{C}$  have been demonstrated experimentally. The proposed ICOMRs design has many potential applications in distributed sensing, lab-on-a-fiber technology and optical communications.

Key words: Microcavity devices; Fiber optics sensors; Microstructured fibers; Multisensor methods.

**OCIS codes:** (140.3948) Microcavity devices; (060.2370) Fiber optics sensors; (060.4005) Microstructured fibers; (150.4232) Multisensor methods.

---

<sup>9</sup> V. Kavungal, G. Farrell, Q. Wu, A. K. Mallik, C. Shen and Y. Semenova, "Packaged inline cascaded optical micro-resonators for multi-parameter sensing," paper in preparation.

### 5.1.1 Introduction

Multiplexing of whispering gallery mode (WGM) micro-resonators has been a field of extensive research for almost three past decades. There have been numerous planar integrated multiple ring resonator devices developed for various applications including optical add/drop multiplexers in optical communications [1-4], optical delay lines [5-7], devices for management of dispersion and pulse distortion [8, 9] *etc.* Free-space WGM microresonators have also become a popular choice in many applications after J. C. Knight *et al.* showed in 1997 that high-Q WGMs could be easily and efficiently excited in micro-spherical resonators by an adiabatic optical fiber taper [10]. Other than tapered fiber coupling to a single free space micro-resonator, other coupling schemes, often involving multiple resonators, have been considered for various applications. For example, a study of induced transparency and absorption was performed using two coupled micro-spheres in [11]; optical pulse propagation experiments were reported with two coupled micro-spheres of different sizes for demonstrating the classical analogy of extremely slow light in [12]; high-Q WGMs in two coupled spheres were used to calculate optically induced attractive and repulsive forces in [13] and an optical waveguide design was reported using chains of dielectric micro-spheres in [14]. More recently, a theoretical study of a serially-coupled double micro-sphere system was carried out with the objective of reducing the number of non-fundamental resonances and achieve higher resonant frequency spacing [15]. However, the above structures suffer disadvantages such as increased attenuation and limited fabrication tolerances.

An experimental study of multi-resonators coupled by a single tapered fiber for optical sensing application was for the first time reported by F. Vollmer *et al.* [16].



In their study, a sensor structure with two spherical micro-resonators coupled to the waist portion of a single tapered fiber was used for multiplexed DNA detection and to discriminate a single nucleotide. M. Sumetsky *et al.* [17] reported a similar structure using double liquid core optical ring resonators to fabricate a temperature and pressure compensated microfluidic optical sensor. Furthermore, achieving optimal phase matching for more than one micro-resonator with the same waist diameter taper is difficult. This results in a limit on the number of micro-resonators in an array with the consequence that such structures had been rarely explored for multi-parameter sensing even though WGM sensors could offer very high measurement resolution due to their high-quality factors, low mode volumes and the high sensitivity of WGMs to external perturbations. In this article we for the first time propose a novel design principle for an inline cascaded optical micro-resonators (ICOMRs). A simple and robust fabrication method for the ICOMRs structure has also been developed and is demonstrated experimentally for simultaneous sensing of strain and temperature.

### **5.1.2 Fabrication of the proposed ICOMRs**

The proposed ICOMRs approach involves fabrication of several tapered sections along the length of a single fiber for coupling of several optical micro-resonators. Evanescent light fields surrounding the fabricated tapered sections of the fiber are utilized for exciting WGMs in the individual resonators. It should be noted that each tapered fiber section is coupled to a single resonator only to allow for the appropriate selection of the diameter of each tapered section so as to achieve phase matching with its corresponding resonator for maximal coupling efficiency. The resulting transmission spectrum of the tapered fiber contains combined WGM spectra for the entire cascade of coupled resonators, so that multiple micro-

resonators can be used for sensing of several parameters simultaneously or sensing of parameters at multiple locations. Since the losses within the untapered portions of the fiber are relatively low, the distances between the cascaded inline resonators have negligible effect on the overall transmission spectrum. The proposed cascaded inline system of coupled micro-resonators offers a quasi-distributed measurement capability along the length of the coupling fiber, whose length could be varied in principle from a few centimeters to several kilometers. A useful packaging technique is also proposed to make the device mechanically stable. The potential applications of the ICOMR are in multi-parametric and distributed sensing, in studies of sensors' cross-sensitivity, for lab-on-a-fiber technology, in optical coding and the design and fabrication of optical logic gates *etc.*

The micro-resonators in our experiments were prepared from short sections of a standard coating-stripped silica fiber (SMF-28) and a polymer optical fiber (POF). The choice of the cylindrical structure as a resonator geometry in our study is due to its simplicity of fabrication and due to the fact that the alignment for optimal coupling of the excitation light with the cylindrical resonator depends on only one angular degree of freedom, as opposed to two for experiments involving microspheres. In practice the original diameters of SMF-28 and POF (125  $\mu\text{m}$  and 490  $\mu\text{m}$  respectively) would result in a very small free spectral range (FSR), but larger FSRs are desired for achieving wide measurement ranges for sensors based on such WGM resonators. Thus, in order to reduce the diameters of the source fibers used for the resonators down to more suitable values, the original commercial fibers were tapered using a customised micro-heater tapering setup [18].

### 5.1.3 Initial Feasibility Experiments

As an initial feasibility experiment, a number of similar cylindrical silica micro-resonators were fabricated and then coupled and packaged with a single multi-taper fiber and subsequently the resulting spectral characteristics were investigated. The purpose of this experiment was not to demonstrate multi-parameter sensing but rather to show that coupling could take place to multiple resonators and that the spectral dips of the individual resonators are distinguishable.

Firstly, as an illustration of the proposed packaging method for an ICOMRs, Figure 68(a-c) shows schematically the main fabrication steps for a cascade of three inline resonators. As a first step of the packaging process, shown in Figure 68(a), the prepared micro-cylinders (MR1, MR2, and MR3) are attached on to three different glass substrates at a height of  $\sim 1$  mm above the glass surface using a UV- curable glue. The lengths of all three microcylinders were  $\sim 20$  mm. The tapered optical fiber used for coupling was fabricated using the same fiber tapering setup used for the SMF-28 based micro-cylinder diameter reduction. Next, to fabricate a triple ICOMR, three tapered portions (Taper-1, Taper-2, and Taper-3) are fabricated along the length of a single optical fiber, as shown in Figure 68(b). The total length of the silica fiber was about 2 meters. Tapering of the silica fiber down to diameter of  $1.3 \mu\text{m}$  at three different positions results in the overall loss of 3.6 dB (measured after the tapering).

In order to maximize the coupling efficiency between the fabricated tapered optical fiber and the cylindrical micro-resonators, each of the prepared cylindrical micro-resonators shown in Figure 68(a) was in turn fixed on a translation stage with an

adjustable 3D-positioner. Using the vertical positioner, the micro-cylinder was brought in contact with the tapered fiber to excite the WGMs. It should be noted that due to the difficulty in manipulating the thin and fragile tapered silica fibers, this step was carried out while the corresponding portion of the fiber containing the tapered section was still secured horizontally between the two translation stages of the taper-drawing setup after its fabrication. The two ends of the tapered fiber were connected to a super luminescent diode (SLD) (Thorlabs) with a wavelength range of 1500–1600 nm and an optical spectrum analyzer (OSA) (Advantest, Q8384) with a resolution of 0.01 nm. To maximize the light coupling efficiency, the micro-cylinder must be placed orthogonally and in direct physical contact with the fiber taper waist. After achieving the physical contact with the tapered fiber, the micro-cylinder was slowly moved along the taper axis using a micro-translation stage while maintaining physical contact and a mutually orthogonal orientation. During this process, the transmission spectrum of the taper was observed at the OSA screen to determine the optimal position of the contact point, corresponding to the phase match between the propagating mode of the fiber taper and the fundamental WGM of the micro-cylinder. After achieving the desired WGM spectrum quality, both ends of the tapered fiber were glued to the glass substrate using a UV curable epoxy as shown in Figure 68(c). The same steps were repeated with the other two micro-cylinder-tapered fiber portions.

In the transmission spectrum of such an array of WGM micro-resonators each resonator must have its own unique family of spectral dips. Therefore, during the second and third resonator coupling steps, spectral overlaps of WGMs due to the previously coupled resonators must be avoided. This can be achieved by either using resonators with deliberately different diameters fabricated by the tapering

process or alternatively relying on the fact that the limitations of the tapering process means that tapers with slightly different diameters are naturally generated anyway, typically differences are less than one micron which is sufficient to ensure adequate spectral separation. Figure 68(c) is a schematic of a packaged triple-cylindrical resonator array. The robustness of the packaged system was confirmed by testing the device in the presence of strong vibrations by placing it on a mechanical vibration generator as explained in [19].

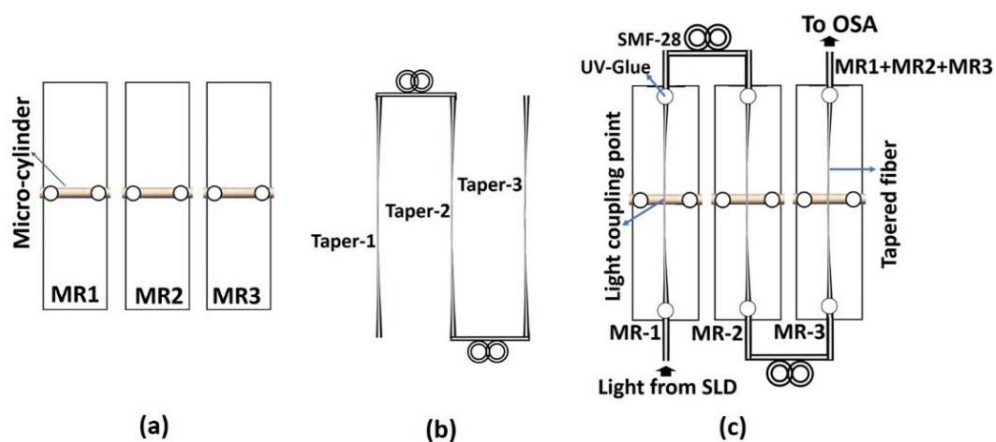


**Figure 68.** Schematic diagrams illustrating the ICOCR packaging steps: (a) cylindrical micro-resonators attached to glass substrates; (b) three tapered sections fabricated along the single optical fiber and (c) packaged ICOMR formed by three resonators.

Finally, the spectral characteristics of the fabricated ICOMRs are investigated. Figures 69(a) & (b) show the WGM spectra for the different packaged ICOMRs, illustrating their additive nature. Figure 69(a) shows the WGMs observed in the transmission spectrum of the double ICOMR. In Figure 69(a), the individual WGM spectra and that for an ICOMR formed by two cylindrical micro-resonators with slightly different external diameters around  $20\ \mu\text{m}$ . The difference in diameter for the two resonators is a natural result of the limitations of the tapering process, as mentioned earlier. Figure 69(b) shows the WGM spectra for the individual

cylindrical micro-resonators in an ICOMR formed by three cylindrical micro-resonators with slightly different external diameters around 15  $\mu\text{m}$  and the resulting composite ICOMR spectrum.

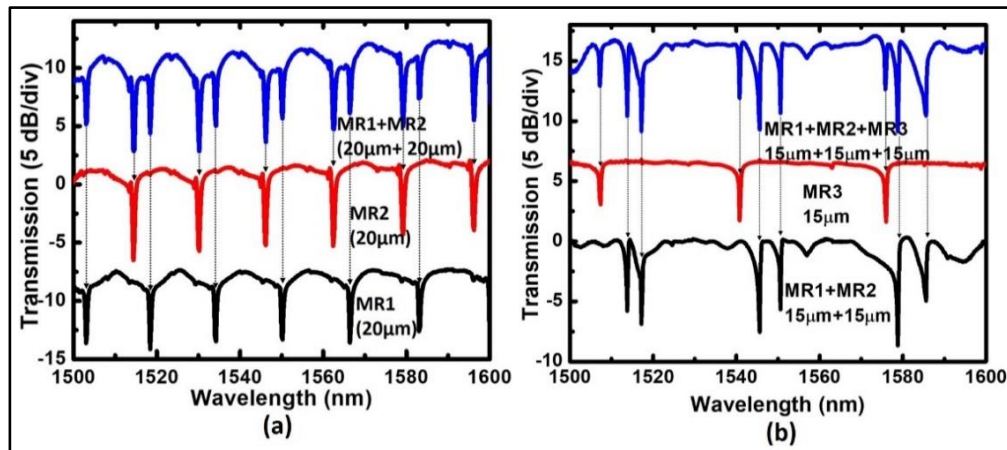


**Figure 69.** Transmission spectra for ICOMRs formed by (a) two  $\sim 20 \mu\text{m}$  diameter resonators and (b) three  $\sim 15 \mu\text{m}$  diameter resonators. Each graph illustrates the individual and combined WGM spectra.

#### 5.1.4 Multi-parameter sensing using ICOMRs

In order to demonstrate sensing of different parameters simultaneously at multiple locations using the proposed ICOMRs structure, a new experimental ICOMRs was fabricated using a polydimethylsiloxane (PDMS) coated silica micro-resonator and a tapered POF micro-resonator, following the method illustrated in Figure 68(a-c). The PDMS coated silica micro-resonator and the tapered POF micro-resonator served for temperature and strain measurements respectively. PDMS material was chosen for the coating of the silica micro-cylinder due to its low attenuation loss, good chemical stability and large thermo-optic coefficient [19], while a POF micro-cylinder was chosen for strain sensing because of its large elastic modulus compared to silica fibers [20-22].

The PDMS coating was prepared as a solution with a base to curing agent ratio of

5:1. Coating a 10  $\mu\text{m}$  diameter silica microcylinder with the prepared PDMS solution resulted in a bottle-shaped structure [23], in effect a cylinder with a distinct bulge toward the cylinders centre point, most probably due to the viscosity and the surface tension of the applied solution. A photo of the structure using an optical microscope is shown in Figure 70. After application of the coating, the micro-resonator was cured at 80  $^{\circ}\text{C}$  for 30 minutes and then at room temperature (20 to 26  $^{\circ}\text{C}$ ) for further 24 hours. The WGM spectrum resulting from coupling to the bulge equator showed densely spaced high Q-factors modes but was highly sensitive to mechanical vibrations and thus was deemed not suitable for packaging. A more stable spectrum resulting from coupling to the neck of the bottle was selected for further packaging of the resonator. The thickness of the PDMS coating layer at the neck region was estimated using optical microscopy to be circa 3.36  $\mu\text{m}$ . The Q-factor of the modes was estimated as  $1.1 \times 10^4$ .

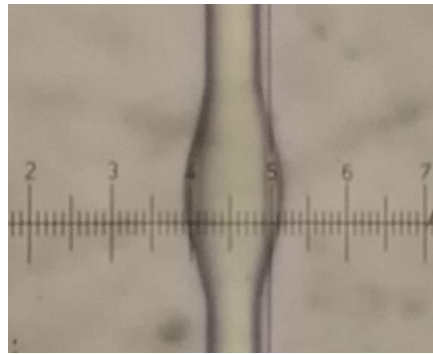


**Figure 70.** Optical microscope image of PDMS coated micro-fiber. One division of the scale in the image is equaling to 1.67  $\mu\text{m}$ .

A POF micro-fiber with a diameter of circa 15  $\mu\text{m}$  was prepared by heat and pull technique from a standard POF (GPOF 62, Thorlabs) of 490  $\mu\text{m}$  diameter. The Q-factor of the resonant modes due the tapered POF cylindrical micro-resonator was  $7 \times 10^2$ . Packaging of the strain sensor based on the POF tapered micro-cylinder was achieved as explained in [20]. Figure 71 shows the WGM spectra excited by

the individual resonators (PDMS-coated and POF) as well as the resulting combined ICOMR spectrum.

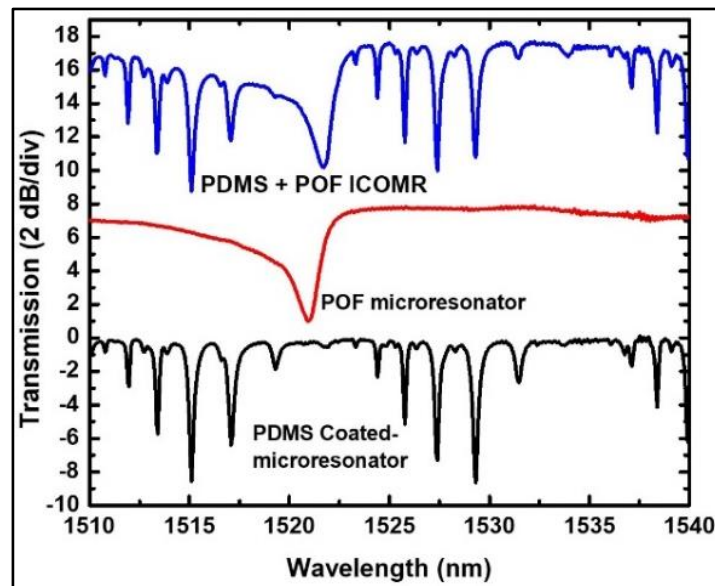


**Figure 71.** WGM spectra for the PDMS-coated micro-resonator, POF micro-resonator and the resulting ICOMRs.

After the ICOMR fabrication, a series of experiments was carried out by placing the two sensors circa one meter apart from each other. The one-meter separation was chosen to demonstrate that sensing can not only take place for two different physical quantities but also at two different points. The PDMS-coated resonator was mounted at the top of a temperature-controlled hot stage, and its temperature was gradually increased from room temperature (25 °C) to 45°C in 2°C steps. The temperature of the hot stage was measured by a thermocouple with a 0.1°C measurement resolution. Tensile strain was applied to the POF micro-resonator by axial elongation with a step of 0.01 mm using a translation stage with a resolution of 10 μm as explained in [20-22]. To avoid the influence of temperature on the POF micro-resonator it was placed inside an environmental chamber maintaining constant room temperature, facilitated also by the 1-meter separation of the sensors. The sensing length of the POF micro-resonator was 70 mm (the distance



between two fixed ends). The resulting spectral changes were recorded using an OSA.

Figure 72 shows the experimental transmission spectra of this ICOMR recorded at different increasing temperatures and strains applied to the respective micro-resonators. In the figure, one of the groups of WGM troughs associated with the PDMS-coated silica micro-resonator is labelled ‘PDMS-WGM’ and the resonant trough due to the POF micro-resonator is marked as ‘POF-WGM’. It can be seen from the figure that an increase in temperature results in a blue shift of the PDMS-WGM troughs and an increase in the applied axial strain also leads to a slight blue shift of the ‘POF-WGM’ spectral dip.

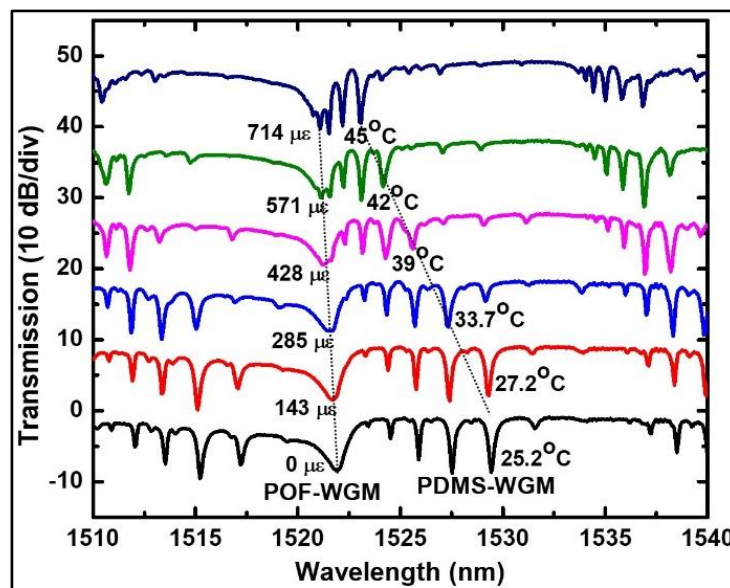


**Figure 72.** Transmission spectra of the ICOMR at different temperatures and applied strain values.

In more detail, Figure 73(a) & (b) illustrate the measured dependences of the spectral positions of selected WGM resonances associated with each of the micro-resonators as functions of the applied axial strain and temperature with the corresponding linear fittings. The PDMS-WGM troughs experienced a total spectral blue shift of 6.47 nm within the given temperature range resulting in

estimated sensitivity of 330 pm/°C. By way of justification, the large blue shift for the PDMS-WGMs is likely due to the large negative thermo-optical coefficient of the PDMS material ( $-1.8 \times 10^{-4}$ ) [19]. The POF-WGM experienced a total spectral shift of 0.99 nm within the studied tensile strain range from 0 to 714  $\mu\epsilon$  with a sensitivity of 1.4 pm/ $\mu\epsilon$  due to the combined effect of the decrease in diameter and changes in the refractive index of the resonator as explained in [20-22].

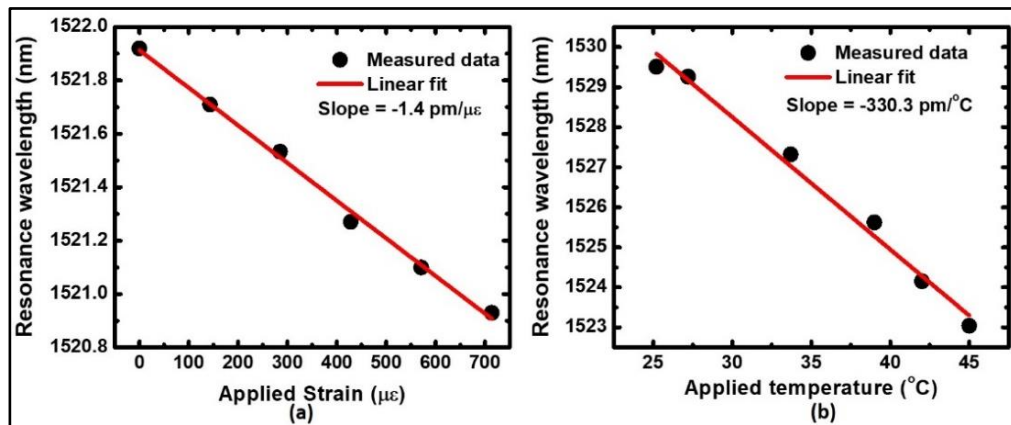


**Figure 73.** Spectral shift of selected resonance troughs for (a) POF micro-cylinder vs. applied strain and (b) PDMS-coated silica micro-cylinder vs temperature.

### 5.1.5 Conclusions

In summary, an ICOMR coupled to a single optical fiber with multiple tapered sections has been proposed and demonstrated for the first time. Evanescent fields from the various tapered portions along the fiber are used to excite the WGMs in the corresponding individual micro-resonators. The inline cascade of multiple “resonator-tapered fiber” pairs has an output transmission spectrum where the families of WGM spectral dips produced by each of the individual coupled resonators can be clearly observed. Fabrication of the tapered fibers and micro-cylinders was carried out by the micro-heater brushing technique. The proposed packaging technique provides mechanical stability and makes the device more portable. To demonstrate multi-parameter sensing using the proposed ICOMR

structure, simultaneous measurements of strain and temperature were carried out for an ICOMR formed by POF based and PDMS-coated silica cylindrical microresonators. An axial tensile strain sensitivity of  $1.4 \text{ pm}/\mu\epsilon$  and a high temperature sensitivity of  $330 \text{ pm}/^\circ\text{C}$  were demonstrated. This initial study indicates that the proposed inline resonator structure is promising for many photonic applications such as distributed sensing, cross-sensitivity studies, lab-on-a fiber technology, optical coding and optical logic gates, etc.

## **5.2 Temperature compensated strain sensor based on an inline cascade of optical microresonators<sup>10</sup>**

**Abstract:** We demonstrate a dual capillary tube based inline cascaded optical microresonator (ICOMR) strain sensor for applications where a small sensor foot print is required. The device is capable of accurate strain measurements with temperature compensation. At constant temperature the strain sensitivity of the device is  $3.3 \text{ pm}/\mu\epsilon$ . The temperature induced red shift of the resonant wavelength during the strain measurement is circa  $0.24 \text{ nm}$  when temperature increases from  $30.8$  to  $47^\circ\text{C}$ . Additional microresonators in the proposed ICOMR structure can be added and used to eliminate cross-sensitivity to other environmental influences (humidity, air flow) or to realise multi-parametric or quasi-distributed sensing.

**OCIS codes:** (140.3945) Microcavities; (140.3948) Microcavity devices; (060.2370) Fiber optics sensors.

---

<sup>10</sup> V. Kavungal, G. Farrell, Q. Wu, A. K. Mallik, and Y. Semenova, "Temperature compensated strain sensor based on an inline cascade of optical microresonators," Proceedings of International Conference on Fiber Sensors (OFS 26) (Poster presentation).

### 5.2.1 Introduction

Optical devices based on whispering gallery modes (WGMs) effect in dielectric micro resonators (MRs) are a promising technology due to the very high sensitivity of the WGMs spectral positions to geometrical dimensions and refractive index of a MR [24]. The WGMs spectrum is sensitive to temperature, strain, pressure, electric, or magnetic fields acting upon the MR since all these factors could influence the cavity's refractive index, or diameter, or both. For example, application of an external stress or strain to the MR leads to changes in the cavity's geometry as well as its refractive index. These changes result in a spectral shift of the optical modes of the device within the range of up to several THz [25]. There are many reports concerning WGM strain sensing using spherical, bubble, and as well as cylindrical MRs based on silica or polymer materials. Unfortunately, the exceptional sensitivity of the WGM resonator's optical properties to the changes in its geometry and refractive index typically leads to significant temperature dependence due to thermo-optic and thermal expansion properties of the resonator's material. So that elimination or compensation of the temperature dependence is usually required for WGM based sensors. Multiple approaches to elimination of the temperature cross-sensitivity in such sensors have been proposed. For example, one technique involves coating a MR made from a polymer with a positive thermo-optic coefficient with a layer of a negative thermo-optic coefficient polymer material [26] or by filling it with a negatively thermo-optic liquid [27]. However, while such methods allow to significantly reduce the temperature dependence, a complete elimination of temperature dependence is not possible. In addition, such methods increase the complexity of sensors design. In this report we propose and experimentally demonstrate a novel

temperature compensated WGMs resonator-based strain sensor fabricated using two inline cascaded optical microresonators (ICOMR).

Cascades of parallelly and serially coupled WGMs microresonators with channel waveguide couplers [28] as well as tapered fiber coupled resonator systems [29] were reported for various applications. We believe that design and fabrication principles proposed here have several advantages in comparison with those for other multi-resonator structures. Firstly, as compared to the channel waveguide light couplers, the tapered fiber coupled system involves simpler fabrication process and potentially lower cost. Secondly, as seen in the reports for channel waveguide and tapered fiber coupled filters, fabrication of closely packed (integrated) microresonators leads to cross coupling between their WGMs, so that this kind of devices is not suitable for applications that require observing independent WGM spectra, such as multiparametric, distributed sensing or cross-sensitivity studies. Finally, as reported by F. Vollmer *et al.* [16] and M. Sumetsky *et al.* [17], two micro-resonators can be coupled using a waist portion of a single tapered fiber, which requires a substantial length of the uniform tapered waist section. Moreover, it is difficult to achieve the phase matching between the tapered fiber and the microresonators of different diameters in a system with more than one resonator and a single fiber taper. All these difficulties can be addressed in the proposed ICOMR structure.

### **5.2.2 Fabrication of the ICOMR based strain sensor**

The proposed ICOMR comprises two cylindrical capillary tube microresonators coupled to two tapered portions of a single fiber separated by un-tapered fiber sections. The transmission spectrum of the coupling fiber contains WGM resonant

dips corresponding to each of the individual resonators. The evanescent light fields surrounding the fabricated tapered sections of the fiber are utilized for exciting the WGMs in the individual capillary tube resonators. It should be noted that each tapered fiber section is coupled to a single resonator only to allow for the appropriate selection of the diameter of each taper to achieve phase matching with its corresponding resonator for maximal coupling efficiency.

The microresonators in our experiments were prepared from short sections of silica capillaries (OD 850  $\mu\text{m}$ , ID 700  $\mu\text{m}$ ; Polymicro Technologies). The choice of the cylindrical capillary tubes in our study was due to their better elastic modulus and strain sensitivity in comparison with solid silica fibers. In practice the 850  $\mu\text{m}$  original diameter of the silica capillary tube would result in a WGM spectrum with a very small free spectral range (FSR). A larger FSR is desirable in order to achieve a wider measurement range for a sensor based on a WGM resonator. Reduction of the silica tube diameter can be realized by heating and stretching of the tube, a process that also reduces the wall thickness of the capillary thus increasing the sensitivity of the outer diameter of the capillary to longitudinal strain. Thus, as a preliminary step, in order to reduce the diameter of the capillary based resonator to a suitable value, the original commercial capillary tubes were tapered using a ceramic micro-heater fiber tapering setup [18].

At the next step two tapered fiber portions were made (Tapered fiber-1, and Tapered fiber-2) along the single optical fiber using the same fiber pulling setup that was used for the MRs' fabrication. The waist diameters of the fabricated fiber tapers were  $\sim 1.3 \mu\text{m}$ . The experimental setup for studies of the temperature compensated WGM strain sensor based on the ICOMR with two resonators is shown schematically in Figure 74(a). The evanescent light coupling to the micro

cylinders (MR1 and MR2) was achieved with the fiber tapers placed in close contact with the capillary tube microresonators. The input end of the fiber was connected to a super luminescent diode (SLD) (Thorlabs), with a wavelength range of 1500-1600 nm. Light from the SLD was passed through a three-paddle manual polarization controller and the output of the fiber was connected to the Optical Spectrum Analyzer (OSA) (86142B, Agilent).

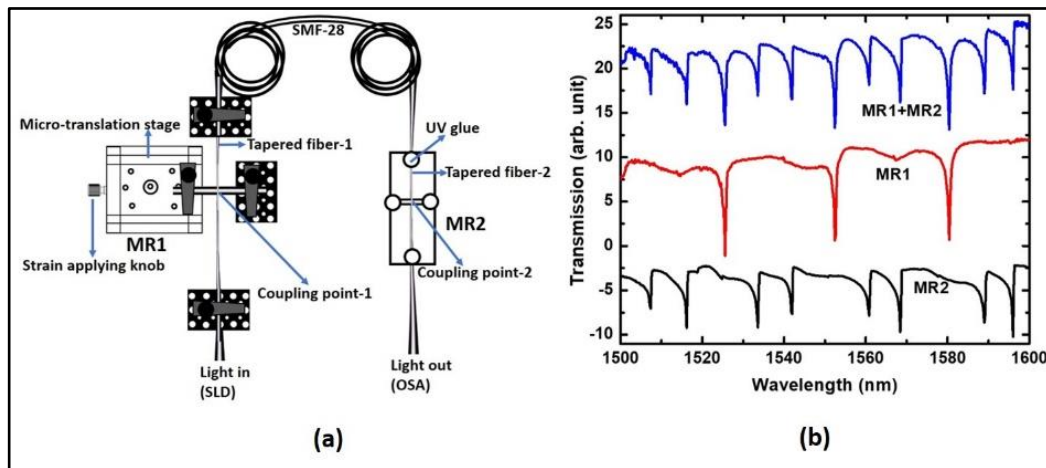


**Figure 74.** (a) Schematic diagram of the experimental setup. (b) Transmission spectra of the ICOCR and each of the MRs separately.

### 5.2.3 Strain measurement

As illustrated in Figure 74(a), in order to apply the strain to one of the resonators in the proposed ICOMR, the MR acting as the strain probe (MR1) was immobilized with a fiber holder with its other end attached to a micro translation stage with a resolution of 10  $\mu\text{m}$ . The length between the two fixed points of the MR1 is considered as the sensing length. Here the sensing length of the resonator was set to 63 mm. The second MR which acts as the temperature probe (MR2) was attached on to a glass substrate at a height of  $\sim 1$  mm above the glass surface using a UV- curable glue (Figure 74(a)) and placed in a close proximity to MR1. The total length of the MR2 was 20 mm. Diameters of both the MRs were circa 20  $\mu\text{m}$ .

To maximize the light coupling efficiency, the MRs must be placed orthogonally and in direct physical contact with the fiber tapers waists. As explained in our previous work [22], after achieving the physical contact with the tapered fiber, the microresonator was slowly moved along the taper axis using a micro-translation stage while maintaining physical contact and a mutually orthogonal orientation. During this process, the transmission spectrum of the taper was observed at the OSA screen to determine the optimal position of the contact point, corresponding to the phase match between the propagating mode of the fiber taper and the fundamental WGM of the capillary tube resonator. After achieving the desired WGM spectrum quality, MR2-Taper 2 coupled system was packaged on the glass substrate by gluing both ends of the Tapered fiber-2 to the glass substrate using a UV curable epoxy. The MR1-Taper 1 coupled system was not packaged since it was used as a strain probe. As shown in Figure 73(b), the resulting transmission spectrum of the ICOMR contains combined WGM spectra for both coupled microresonators. Since one tapered portion is coupled with only one resonator there is no cross coupling between the WGMs of the two resonators.

The breaking point of the capillary tube resonator in the current experimental set up was estimated as circa  $2380\mu\epsilon$  (corresponding to a 0.24% axial elongation). To characterize the strain sensing performance of the proposed sensor structure, the strain was decreased from a pre-strained sensor probe (MR1) by moving the translation stage with a step of  $10\mu\text{m}$  (corresponding to an axial strain decrease of  $159\mu\epsilon$  or 0.016% decrease of the capillary tube elongation) in a direction towards the fixed end. After each step of the strain change, the WGM spectrum of the ICOMR was recorded using the OSA. Figure 75(a) shows the selected part of the ICOMR spectrum which includes the WGM resonances associated with both MR1



and MR2. Here one can see that for each step of the strain decrease, the WGM resonance trough from the resonator MR1 shifts towards the longer wavelengths side of the spectrum (red shift) and the resonance trough from the resonator MR2 remains unchanged during the entire experiment. For better clarity Figure 75(b) shows the plot of experimentally measured WGM resonant wavelengths associated with both resonators (MR1 and MR2), as functions of the applied strain. The maximum shift experienced by the selected WGM trough from MR1 due to axial strain decrease of  $1429 \mu\epsilon$  (0.14% decrease in the axial elongation) was 4.4 nm. The spectral shift of the WGM resonant wavelength is a result of the combined effect of changing diameter and changing refractive index of the resonator. Changes in the fiber dimensions result in changes in the material density with the corresponding induced changes in its refractive index. Since the experiment was conducted at constant temperature, the WGM trough from the MR2 of the ICOMR did not experience any significant fluctuations. The proposed sensor structure is promising for simultaneous measurement of strain and other perturbations such as temperature variation, humidity etc. so that the cross-sensitivity effects can be simply subtracted from the measured experimental data. The measured strain sensitivity of the proposed thin capillary tube-based strain sensor is  $3.3 \text{ pm}/\mu\epsilon$  which is 5 times larger than our previously reported strain sensitivity of a thick polymer fiber [22] and a thick polymer wire-based strain sensor [20].

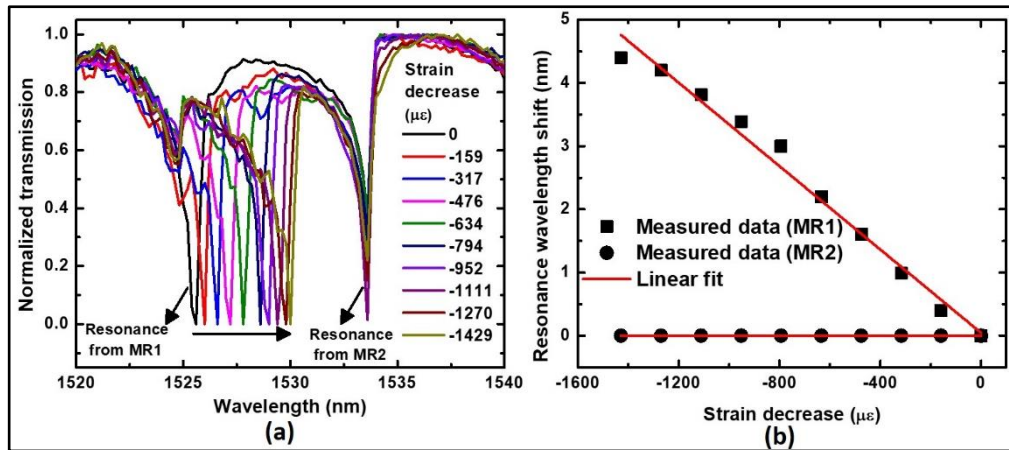


**Figure 75.** Selected part of the transmission spectrum of the ICOMR with strain decrease. (b) Selected WGM resonance wavelength shift as a function of applied strain. The slope of the linear fit to the measured data of the WGM trough from the MR1 resonator is  $3.3 \text{ pm}/\mu\epsilon$ .

In order to characterise the temperature effect of the silica capillary tube resonator, we have conducted another experiment with a capillary tube resonator, fabricated using the same method and thus with a similar geometry. The temperature was increased from room temperature of  $30.8^\circ\text{C}$  up to  $50^\circ\text{C}$  with  $2^\circ\text{C}$  steps by placing the packaged capillary tube resonator on a temperature controlled hot stage while all changes in the transmission spectrum were recorded using an OSA. The temperature of the hot stage was measured by a thermocouple. Figure 76 illustrates the results of this experiment. As can be seen from Figure 76(a), the WGM spectrum experiences red shift of  $0.24 \text{ nm}$  with the increase in temperature from  $30.8^\circ\text{C}$  to  $47^\circ\text{C}$ . The redshift of the WGMs with increasing temperature is due to the positive thermo-optic and the thermal expansion coefficients (in the order of  $\sim 10^{-5}/^\circ\text{C}$ ) of the silica glass. Figure 76(b) shows the resonant wavelength shift with increasing temperature. Here the black dots are the measured data and the solid curve is their polynomial curve fit. The fitting data can be used to eliminate the temperature cross-sensitivity of the strain sensor in the temperature range

relevant to the sensor's application.

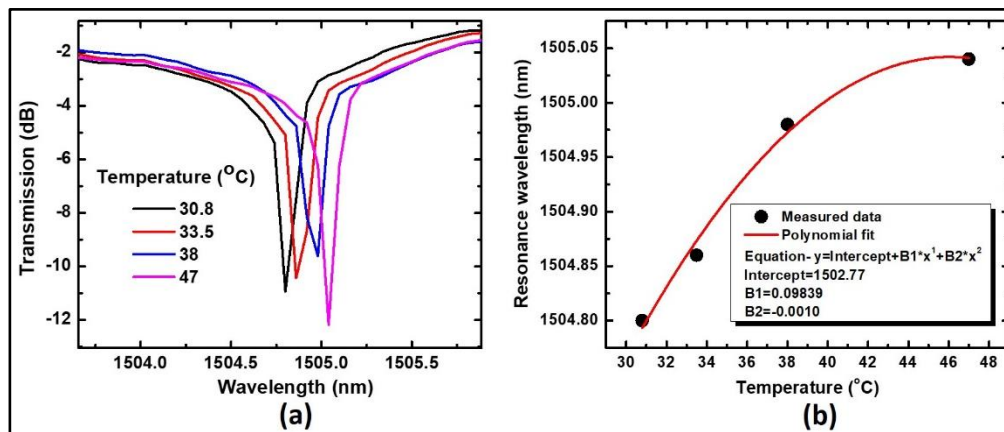


**Figure 76.** Selected resonance wavelength as a function of temperature increase. (b) Resonance wavelength shift with temperature increase. Here the measured wavelength (scatter data) is fitted with polynomial fit (solid curve).

## 5.2.4 Conclusions

In summary, we proposed and experimentally demonstrated a novel temperature compensated WGMs resonator-based strain sensor fabricated using two inline cascaded optical microresonators (ICOMR). We showed that the inline combination of the “resonator-tapered fiber” system results in an output transmission spectrum where WGM spectral dips produced by each of the individual coupled resonators can be clearly observed. In the demonstrated dual resonator configuration one resonator is used for strain measurement and the other resonator can be used for monitoring of the fluctuations in resonance wavelength due to other perturbations such temperature changes, humidity variations, air flow *etc.* At constant temperature the strain sensitivity of the proposed capillary tube based ICOMR strain sensor is 3.3 pm/ $\mu\epsilon$ . The spectral response of the silica capillary tube in increasing ambient temperature conditions is studied. The temperature induced red shift of the resonant wavelength during the strain measurement is circa 0.24 nm when temperature increases from 30.8 to 47°C.

Initial study indicates that the demonstrated inline resonator combination and the additive nature of the resulting WGM spectrum are promising for simultaneous measurement of strain and resonance wavelength fluctuations due to other environmental effects can be simply subtracted from the measured experimental data for accurate strain sensing in applications where a small sensor foot print is required.

### 5.3 References

1. K. Oda, N. Takato, and H. Toba, "A Wide-FSR waveguide double-ring resonator for optical FDM transmission systems," *J. Lightwave Technol.* **9**, 728-736 (1991).
2. Y. Yanagase, S. Suzuki, Y. Kokubun, and S. T. Chu, "Box-like filter response and expansion of FSR by vertically triple coupled microring resonator filter," *J. Lightwave Technol.* **20**, 1525–1529 (2002).
3. B. E. Little, S. T. Chu, H. A. Haus, J. Foresi, J. -P. Laine, "Microring resonator channel dropping filters," *IEEE J. Lightwave Technol.* **15**, 998–1005 (1997).
4. O. Schwelb, I. Frigyes, "Vernier operation of series coupled optical microring resonator filters," *Microwave Opt. Technol.* **39**, 257–261 (2003).
5. J. Adachi, N. Ishikura, H. Sasaki, and T. Baba, "Wide range tuning of slow light pulse in SOI photonic crystal coupled waveguide via folded chirping," *IEEE J. Sel. Top. Quantum Electron.* **16**, 192–199 (2010).
6. J. K. S. Poon, J. Scheuer, Y. Xu, and A. Yariv, "Designing coupled-resonator optical waveguide delay lines," *J. Opt. Soc. Am. B* **21**, 1665-1673 (2004).
7. J. E. Heebner, and R. W. Boyd, "Slow light, induced dispersion, enhanced nonlinearity, and optical solitons in a resonator-array waveguide," *Phys. Rev. E.* **65**, 036619 (2002).

8. V. Van, "Circuit-based method for synthesizing serially coupled microring filters," *J. Lightwave Technol.* **24**, 2912–2919 (2006).
9. L. Y. Mario, and M. K. Chin, "Optical buffer with higher delay-bandwidth product in a two-ring system," *Opt. Express.* **16**, 1796–807 (2008).
10. J. C. Night, G. Cheung, F. Jacques, and T. A. Birks, "Phase-matched excitation of whispering-gallery-mode resonance by a fiber taper", *Opt. Lett.* **22**, 1129–1131 (1997).
11. A. Naweed, G. Farca, S. Shopova, and A. Rosenberger, "Induced transparency and absorption in coupled whispering-gallery microresonators," *Phys. Rev. A.* **71**, 043804 (2005).
12. K. Totsuka, N. Kobayashi, and M. Tomita, "Slow light in coupled resonator induced transparency," *Phys. Rev. Lett.* **98**, 213904 (2007).
13. M. Povinelli, S. Johnson, M. Lončar, M. Ibanescu, E. Smythe, F. Capasso, and J. Joannopoulos, "High-Q enhancement of attractive and repulsive optical forces between coupled whispering-gallery mode resonators," *Opt. Express* **13**, 8286–8295 (2005).
14. Z. Chen, A. Taflove, and V. Backman, "Highly efficient optical coupling and transport phenomena in chains of dielectric microspheres," *Opt. Lett.* **31**, 389–391 (2006).
15. M. Saffari, A. Gholami, and H. Latifi, "Investigation of a serially coupled double microsphere resonator to expand resonance frequency spacing of microsphere resonators" *J. Opt. Soc. Am. B.* **33**, 1993–1999 (2016).
16. F. Vollmer, S. Arnold, D. Braun, I. Teraoka, and A. Libchaber, "Multiplexed DNA quantification by spectroscopic shift of two microsphere cavities", *Biophys. J.* **85**, 1974–1979 (2003).

17. M. Sumetsky, Y. Dulashko, and R. S. Windeler, "Temperature and Pressure Compensated Microfluidic Optical Sensor," in Conference on Lasers and Electro-Optics/Quantum Electronics and Laser Science Conference and Photonic Applications Systems Technologies, OSA Technical Digest (CD) (Optical Society of America, 2008), paper CMJ6.
18. G. Brambilla, V. Finazzi, and D. Richardson, "Ultra-low-loss optical fiber nanotapers," *Opt. Express*. **12**, pp. 2258-2263 (2004).
19. B. B. Li, Q. Y. Wang, Y. F. Xiao, X. F. Jiang, Y. Li, L. Xiao, and Q. Gong, "On chip, high-sensitivity thermal sensor based on high- Q polydimethylsiloxane-coated microresonator," *Appl. Phys. Lett.* **96**, 2008–2011 (2010).
20. V. Kavungal, G. Farrell, Q. Wu, A. K. Mallik, and Y. Semenova, "A packaged whispering gallery mode strain sensor based on a polymer wire cylindrical micro resonator," *J. Light. Technol.* **36**, 1757-1765 (2017).
21. V. Kavungal, A. K. Mallik, G. Farrell, Q. Wu, and Y. Semenov, "Tunable whispering gallery mode cylindrical micro resonator based on a section of a polymer optical fiber," in Optics InfoBase Conference Papers (2014).
22. V. Kavungal, A. K. Mallik, G. Farrell, Q. Wu, and Y. Semenova, "Strain-induced spectral tuning of the whispering gallery modes in a cylindrical micro-resonator formed by a polymer optical fiber," *Appl. Opt.* **56**, 1339-1345 (2017).
23. A. Grimaldi, S. Berneschi, G. Testa, F. Baldini, G. Nunzi Conti, and R. Bernini, "Polymer based planar coupling of self-assembled bottle microresonators," *Appl. Phys. Lett.* **105**, 231114 (2014).
24. B. Matsko and V. S. Ilchenko, " Optical resonators with whispering gallery

- modes I: Basics", *IEEE J. Sel. Top. Quantum Electron.* **12**, PP3-14 (2006).
25. N. Dinyari, R. J. Barbour, D. A. Golter, and H. Wang, "Mechanical tuning of whispering gallery modes over a 0.5 THz tuning range with 140 mhz resolution in a silica microsphere at cryogenic temperatures", *Optics Express* **19**, 17966–17972 (2011).
26. M. Han and A. Wang, "Temperature compensation of optical microresonators using a surface layer with negative thermo-optic coefficient," *Opt. Lett.* **32**, 1800–1802 (2007).
27. D. Suter, I. M. White, H. Zhu, and X. Fan, "Thermal characterization of liquid core optical ring resonator sensors," *Appl. Opt.* **46**, 389–396 (2007).
28. G. Griffel, "Vernier effect in asymmetrical ring resonator arrays", *IEEE Photon. Technol. Lett.* **12**, 1642–1644 (2000).
29. M. Saffari, A. Gholami, and H. Latifi, "Investigation of a serially coupled double microsphere resonator to expand resonance frequency spacing of microsphere resonators," *J. Opt. Soc. Am. B.* **33**, 1993-1999 (2016).

# Chapter 6

---

---

## Conclusions and Future Work

---

---

In this chapter conclusions from across the thesis are reviewed and the contributions to current technology and knowledge from the whole thesis are formulated. Future research as an extension of this PhD thesis is also discussed.

### 6.1 Conclusions from the research

The core aim of this research was *to investigate and address several key aspects related to the development of novel sensors and tunable devices based on cylindrical WGM micro-resonators with the intention of moving such structures closer to practical applications.*

In Chapter 1, a series of objectives were identified to meet the aim stated above. The main findings and conclusions presented and discussed here are divided into six sections based on the different objectives and research strands investigated and reported in this thesis.

#### **I. Conclusions regarding the studies of WGMs in cylindrical micro-resonators.**

In this thesis, one of the objectives was to carry out an in-depth experimental investigation of the WGM effect in different types of cylindrical micro-resonators in order to establish the influence of the resonator's geometry and coupling conditions on the resulting WGM spectrum. For all the experiments, light was evanescently coupled into the micro-cylinders from a tapered optical



fiber. The key conclusions from this study are as follows:

- There is an optimum diameter for the tapered optical fiber for the most efficient evanescent light coupling into the fiber micro-cylinder. The extinction ratio of the WGMs in the transmission spectrum of the tapered fiber increases with the decrease of the taper waist diameter, while the overall transmission loss increases, indicating that more light is coupled into the micro-resonator.
- The WGMs' Q-factor and the number of modes observed within a given wavelength range increase with the increase in the diameter of the micro-cylinder. Consequently, an increase in the micro-resonator diameter leads to a decrease in the free spectral range of the WGM spectrum.
- The optimum conditions for exciting WGMs in a cylindrical micro-resonator are observed when the tapered fiber is placed perpendicularly and in direct physical contact with the micro-cylinder. Evolution of the WGMs spectrum with the increase of the tilt angle away from its perpendicular position results in broadening and blue shift of the WGM resonances.
- Overall transmission losses and extinction ratio of the WGMs increase with the increase of the tilt angle followed by complete disappearance of the WGM resonances at tilt angles  $> 24^\circ$ .

## **II. Development of a new method for non-destructive geometrical profiling of tapered optical fibers with submicron accuracy.**

A new method for geometrical profiling of thin microfiber tapers with submicron accuracy has been proposed. A range of tapered fibers with different shapes were fabricated in order to demonstrate the capabilities of the proposed method. The main conclusions from this research are as follows:

- It has been demonstrated that the proposed method based on the WGM effect

allows for an accurate geometrical profiling of tapered optical micro- fibers including the information regarding their symmetry and the length of the uniform waist region. The measurement accuracy of the proposed method has been verified by SEM microscopy with a maximum error of  $\pm 0.38 \mu\text{m}$ .

- The proposed method is suitable for use in fabrication of tapered fibers as a cost efficient means of the taper diameter control. It can also be used for the detection and troubleshooting of flaws in a taper fabrication setup.
- The method has the potential to also be applied in bio-sensing provided the diameter of the micro-resonator immersed in a bio-analyte increases due to adsorption of bio-chemical species on the fiber surface.

### **III. Development of a simple and robust packaging method for practical WGM sensors and tunable devices.**

As one of the objectives of this thesis, a simple and reliable packaging method for practical applications of the WGM based sensors and tunable devices has been proposed and demonstrated. The proposed packaging method allows for maintaining of precise alignment of the sensor (or tunable device) elements without the continued use of the micro-positioning equipment. This in turn enables the fabrication of portable and miniature devices whose performance is unaffected for example by mechanical vibration. The main conclusions can be summarized as follows:

- The proposed packaging process involves just three sequential steps which include (1) preparation of the tapered optical fiber and micro-resonator, (2) alignment of the “taper-resonator” pair for maximizing the light coupling efficiency and (3) immobilizing the coupled system on a glass substrate using a UV curable epoxy.

- Good mechanical stability of the packaged device is confirmed by vibration tests by placing the packaged sensor on a simple vibration generator driven by a signal generator with a maximum peak-to-peak amplitude of 6 V. The packaged device was subjected to vibrations at a frequency of 10 Hz for 30 minutes.

#### **IV. Conclusions regarding the use of polymer fibers and polymer wires as novel high sensitivity WGM strain sensors and devices with a wide tuning range.**

- Based on a study of the effect of axial mechanical strain on the spectral positions of WGM resonances excited in a POF cylindrical micro-resonator, the WGMs observed in the transmission spectrum of the coupling silica fiber taper have a high extinction ratio of up to 19 dB and a Q-factor of up to  $2 \times 10^4$ .
- The spectral positions of the WGM resonances shift linearly in response to an increase or decrease of the axial tensile strain applied to the micro-cylinder.
- The WGMs move toward shorter wavelengths with the increase of the applied strain and return to their initial positions when the strain is decreased.
- Strain sensitivities (spectral shifts per unit of strain) during the increase and decrease of the applied axial strain differ slightly, possibly due to nonuniform deformations experienced by the strained POF microresonator.
- It is possible to implement a novel strain sensor based on the WGM effect in a cylindrical PMMA wire with a packaging method that allows for large dynamic range strain measurement.
- The sensitivities of the proposed strain sensor to the applied tensile strain are - 0.68 pm/ $\mu\epsilon$  and -0.58 pm/  $\mu\epsilon$  for an unpackaged and packaged device

respectively. Measurements of axial strains of up to  $3.25 \times 10^3 \mu\epsilon$  (corresponding to 0.33 % elongation) have been demonstrated without the need for re-adjustment of the coupling setup.

- The robustness of the proposed method of packaging has been confirmed by subjecting the device to mechanical vibrations. It has been shown that the vibrations had little or no effect on the sensor performance.
- The packaged sensor has good measurement repeatability and the WGM resonances return to their original positions after removing the strain with only a small level of hysteresis.
- The estimated temperature sensitivity for the proposed strain sensor is found to be  $54 \mu\epsilon/^\circ\text{C}$ .
- The proposed polymer wire strain sensor possesses several desirable features such as large dynamic range, ease of fabrication and small footprint.

#### **V. Development of novel magnetic field sensors and a tunable thermo-optic device based on cylindrical LCORR structures.**

A novel type of thermo-optic tunable WGM device based on a thin-walled silica capillary resonator filled with a nematic liquid crystal has been proposed and demonstrated experimentally. A simple and robust packaging technique for the proposed tunable device has also been developed. Furthermore, two novel magnetic-field WGM sensors based on PCF micro-cylindrical micro-resonators filled with a magnetic fluid and a ferronematic liquid crystal have been developed. The key conclusions from this research strand are as follows:

- An increase in the temperature of the nematic liquid crystal-filled resonator leads to a blue shift of the WGMs with a rate of  $-270 \text{ pm}/^\circ\text{C}$ , which is useful in many photonic applications, such as tunable filters and sensors.

- The proposed device shows good mechanical stability and repeatability of performance.
- WGM resonances excited in PCF micro- resonators infiltrated with magnetic fluids or ferronematic liquid crystals, experience spectral shifts proportional to the amplitude of the applied magnetic field due to perturbations of the effective refractive index of the liquids, and this effect can be utilized for the development of magnetic field sensors following a suitable calibration.
- The experimentally confirmed magnetic field sensitivity of the magnetic fluid-infiltrated PCF (LMA-10) sensor was  $\sim 110$  pm/mT.
- For the sensors based on a PCF (PM-01-1550-PCF) filled with ferronematic liquid crystals doped with rod-like and spherical particles, the magnetic field sensitivities were  $-39.6$  pm/mT and  $-37.3$  pm/mT respectively.
- Reducing the diameters of the cylindrical micro- resonators by tapering leads to enhancement of their magnetic field sensitivities: up to  $-61.86$  pm/mT for the sensor containing the rod-like and up to  $-49.88$  pm/mT for the sensor containing the spherical particles respectively. Such magnetic field sensitivities are comparable with the sensitivities of other fiber-optic sensors reported previously, with the advantage of simpler fabrication.

**VI. Development of a new method of coupling of multiple micro- resonators to a single fiber for sensing of multiple parameters.**

A novel approach to coupling of multiple WGM resonators to a single optical fiber has been proposed and demonstrated based on using the evanescent fields from different tapered sections along a single optical fiber to excite the WGMs in the individual micro- resonators. From these studies it can be concluded that:

- The inline combination of the “resonator-tapered fiber” system results in an

output transmission spectrum where the WGM spectral dips produced by each of the individual micro-resonators can be clearly observed.

- Multi-parameter sensing capability of the proposed structure has been confirmed experimentally based on an ICOMR composed of a POF micro-cylinder acting as a strain sensor and a PDMS coated silica micro-cylinder acting as a temperature sensor.
- A strain sensitivity of  $1.4 \text{ pm}/\mu\epsilon$  and a temperature sensitivity of  $330 \text{ pm}/^\circ\text{C}$  have been achieved.
- At a constant temperature, the strain sensitivity of the proposed capillary tube based ICOMR strain sensor is  $3.3 \text{ pm}/\mu\epsilon$ . The temperature-induced red shift of the WGMs during strain measurement is circa  $0.24 \text{ nm}$  when temperature increases from  $30.8$  to  $47^\circ\text{C}$ .
- The demonstrated ICOMR configuration has the potential to be expanded to include a larger number of micro-resonators and is promising in distributed sensing, cross-sensitivity studies, lab-on-a fiber technology, optical coding and optical logic gates.

## **Outcomes of the thesis**

- **A method for stabilizing cylindrical micro-resonator and tapered optical fiber coupled system is successfully demonstrated.**
- **A non-destructive technique for geometrical profiling of tapered optical fibers with submicron precision is proposed.**
- **A polymer cylindrical micro-resonator based WGM strain sensor is demonstrated.**
- **Nematic liquid crystal filled liquid core optical ring resonator (LCORR) thermo-optical tunable device is proposed.**
- **Magnetic field sensors based on magnetic fluid and ferronematic liquid crystal filled LCORR are demonstrated for the first time.**
- **A multi-parameter sensor design has been proposed and demonstrated using an inline cascade of optical micro-resonators (ICOMRs) to the first time.**

## **6.2 Future Work**

### **6.2.1 New method for studies of viscoelastic properties of polymer fibers and polymer wires**

In Chapter 3 the strain- induced WGMs spectral tunability and the fabrication of a strain sensor based on a polymer fiber cylindrical micro-resonator have been discussed. Hysteresis experienced by the WGM resonances with the increasing and decreasing axial tensile strain on the polymer fiber has also been studied. As an extension of this work, a new method for characterization of viscoelastic properties of different polymer fibers could be developed.

When a mechanical strain is applied to a purely elastic material, the latter stretches and immediately returns to its original size once the strain is removed. Whereas viscosity is the property of fluids and it serves as a measure of the fluid's resistance to gradual deformation by a shear stress or tensile strain [1, 2]. Viscoelastic materials, such as polymers, exhibit both of these properties when they are subjected to a time dependent strain. Due to its elasticity, a polymer fiber reacts to an applied strain along the axial direction with an opposing force, which aims to restore the fiber's original shape. If the opposing force is of the same magnitude as the applied strain, the polymer fiber will return to its original shape when the strain is removed. If the applied strain is larger than the opposing force, the polymer fiber may experience permanent molecular rearrangement, referred to as creep [1]. By analysing the value of hysteresis in the spectral shift of WGMs due to increase and decrease of the applied axial strain on the fiber, one could determine the threshold strain resulting in the appearance of creep for a particular material.



### **6.2.2 Optical Voltmeter with temperature compensation**

In Chapter 4 it was shown that a thin-walled capillary resonator filled with a nematic liquid crystal (NLC) can be applied as a thermo-optically tunable device. Due to the high electro-optical coefficients of NLCs, such a resonator can also be used as a sensor of electric field and voltage. Since the NLC filled resonator is very sensitive to changes in ambient temperature, some means for temperature compensation is required, and this should be possible to realize using an ICOMR structure discussed in Chapter 5 of this thesis. The fabrication of a temperature-compensated optical voltmeter could be accomplished in the form of an ICOMR formed by two identical thin-walled micro-capillaries filled with NLC, one of which would serve as a voltage sensor while the other one as a temperature monitor. Both the surrounding temperature changes and the applied electric field lead to the changes in optical properties of the NLC and this will result the shifts on the WGMs associated with corresponding resonators. A temperature compensated voltage measurement can be achieved by subtracting the value of temperature induced WGMs shift (measured using one of the resonators) from the WGMs shift of the voltage sensor.

### **6.2.3 LCORR arrays using ICOMR structure**

A multi- parametric sensor based on an array of LCORRs for sensing of multiple liquid bio- analytes can be realized using the proposed ICOMR design containing several LCORRs. In [3,4] I. M. White *et al.* and X. Fan *et al.* put forward the concept of LCORR array using several waveguides and detectors. This structure can be simplified using the proposed ICOMR design discussed in Chapter 5 of the thesis. In this design several LCORRs are coupled with several tapered portions on a single fiber and a number of light sources and detectors can be reduced

allowing for simpler and less expensive design of the resonators array. Such a structure also can be used for simultaneous determination of refractive index and the flow rate of various liquids flowing through the capillaries serving as microfluidic channels.

### **6.3 References**

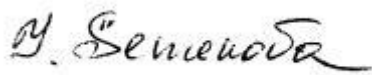
1. M. A. Meyers and K. K. Chawla, “Mechanical Behavior of Materials” (Cambridge University Press, 2009).
2. A. Blinder and H. Rosen, “Mechanical Behaviour of Engineering Materials” (Springer, 1984).
3. X. Fan, I. M. White, H. Zhu, J. D. Suter, and H. Oveys, “Overview of novel integrated optical ring resonator bio/chemical sensors,” Proc. SPIE 6452 (2007).
4. M. White, H. Oveys, and X. Fan, “Liquid-core optical ring-resonator sensors,” Opt. Lett. **31**, 1319-1321 (2006).

# Appendix A

## Statement of Contribution

For the publications presented within this thesis, the co-authors listed below certify that:

1. Vishnu Kavungal is the first author for the six journal publications and second author for the two journal publications.
2. As first author of the six publications, Vishnu Kavungal undertook all aspects of the research described in each publication, including preparation and submission of the publication and the preparation of any revisions requested by referees, with the support and advice of the co-authors. As a second author of two publications, Vishnu Kavungal performed a significant contribution toward the proposed sensor concepts and design of the experiments presented in these publications.
3. The co-authors agree to the use of the publications in this thesis.



**Prof. Yuliya Semenova**



**Prof. Gerald Farrell**



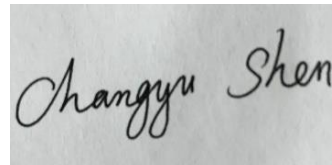
**Dr. Qiang Wu**



**Mr. Arun Kumar Mallik**



**Dr. Aseel Mahmood**



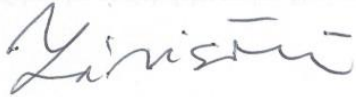
**Prof. Changyu Shen**

Soudad S. Ahmed

**Prof. Soudad Bassam**



**Prof. Peter Kopcansky**



**Dr. Vlasta Zavisova**

## Appendix B

### **Studies of Effective Coupling conditions for a Microsphere- Tapered Fiber System for Generating Whispering Gallery Modes <sup>11</sup>**

**Abstract:** We studied the excitation of whispering gallery modes (WGMs) in a spherical micro resonator by a tapered optical fiber coupled under different excitation conditions. Coupling with the fiber taper positioned at the equator of the microsphere produced the highest quality spectrum in comparison with other positions

#### **Introduction**

Whispering gallery modes (WGMs) are electromagnetic surface oscillations formed in dielectric micro resonators with a circular structure such as spheres, cylinders or disks. WGMs arise as a result of trapping of light within the micro resonator by total internal reflections from the resonator's curved surface. Such reflections force the light to take on a polygonal path within the curved structure, effectively confining its energy to very small volumes [1].

Optical microresonators supporting WGMs are attractive photonic devices due to their small mode volume, very high power density, narrow spectral linewidths and high-Q factors. Such micro resonators have been shown to have potential use in

---

<sup>11</sup> V. Kavungal, Q. Wu, G. Farrell, and Y. Semenova, "Studies of Effective Coupling conditions for a Microsphere-Tapered Fiber System for Generating Whispering Gallery Modes," in 12th International Conference on Fiber Optics and Photonics, OSA Technical Digest (online) (Optical Society of America, 2014), paper S5A.11.

many areas, including studies of nonlinear optical effects and quantum electrodynamics, low threshold micro lasers and very sensitive micro sensors. The most common micro resonators are spherical; they are relatively easy to fabricate and usually have very high Q-factors:  $\sim 10^9$  at 1.55  $\mu\text{m}$  for silica [2] and  $\sim 10^5$  at 1.55  $\mu\text{m}$  for chalcogenide glass [3]. The main difficulty for practical application of WGMs is the problem of efficient coupling of light into resonators. Phase synchronism, optimal overlap of the selected WGM and the coupler mode and selectivity [4] are the main characteristics of every coupling device. Prism couplers with frustrated total internal reflection are one of the oldest methods used to couple light into WGM resonators. Currently wave guide coupling techniques have gained the greatest popularity. Among these, the most efficient coupling is by tapered optical fibers. For example, 99.99% efficiency has been reported for coupling of light into a fused silica resonator using a fiber taper [5]. A tapered optical fiber is a single mode bare cylindrical waveguide with a few microns diameter which is placed in contact with the surface of the resonator allowing evanescent field interaction with the resonator. WGMs can be observed in the output spectrum of the tapered fiber. In this paper we present our studies on the variation of the WGM spectrum with different tapered fiber-microsphere coupling positions.

## **Experimental**

The experimental setup shown in Figure 1 (a) includes a tunable diode laser (Tunic plus, 1500-1600 nm) as the broadband source, a full tapered fiber with a diameter of 1.7  $\mu\text{m}$ , the microsphere sample under studies, a photodetector (PDA 10 CS-EC, InGaAs amplified detector, 700-1800 nm), two optical microscopes and two three-dimensional manually controlled translation stages for the precise alignment

of the microsphere sample with respect to the fiber taper. As a preliminary step, fiber tapering is undertaken using the micro heater brushing technique [6]. The tunable laser is connected to the one end of the fiber taper and the other end of the fiber is connected to the photodetector interfaced with a PC via a Labview program. The tapered fiber is placed on one of the translational stages providing three-dimensional movement of the fiber taper for the precise alignment. The stem of the microsphere is placed on the second translational stage using a fiber holder. Microscopes are placed in appropriate positions in order to view the alignment of the microsphere with the tapered fiber as the microsphere is brought into direct contact with the tapered portion of the fiber as shown in Figure 1 (b) and (c).

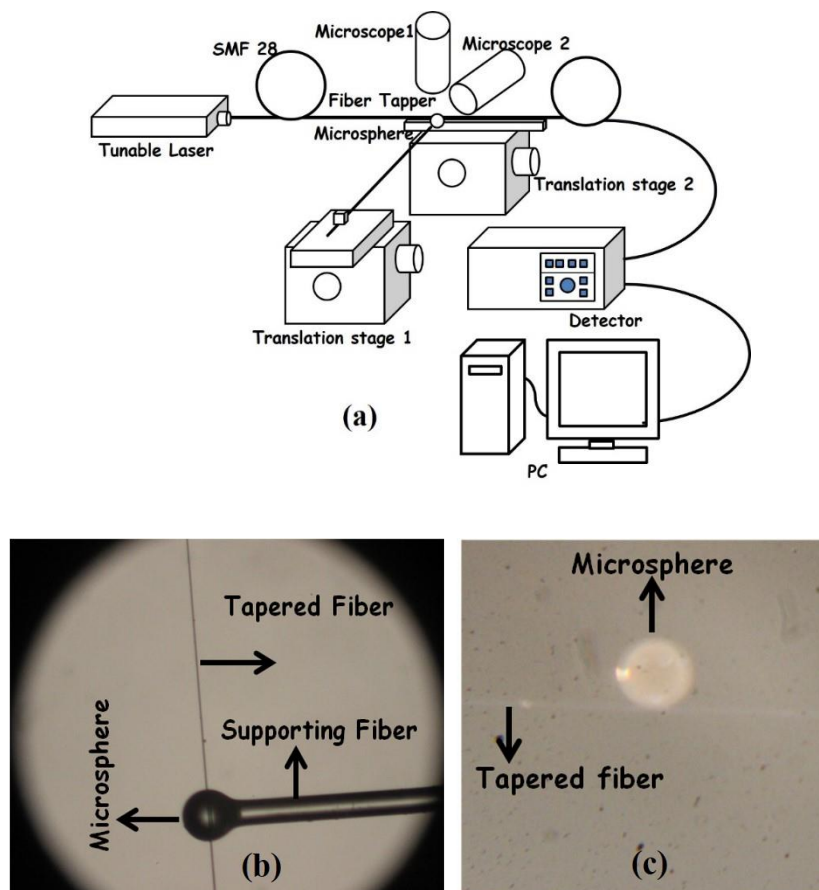


**Figure 1.** (a) Experimental set up for characterizing the microsphere resonator. (b) &(c) Microscope photos of the top and side view of the tapered fiber microsphere system: tapered fiber positioned below (b) the microsphere and parallel (c) to its equator.

The Q factor of the spectrum obtained is estimated to be in the order of  $10^5$ . It was established that the free spectral range (FSR) of the WGM spectrum decreases with the increase of the diameter of the microsphere. The quality factor improves with the increase in size of the microsphere because of the reduction in the intrinsic radiative (curvature) losses. Figure 2 (a) shows the WGM spectrum generated by a  $163 \mu\text{m}$  sphere and Figure 2(b) shows a magnified portion of the spectrum with the corresponding Lorentzian fit in order to estimate the Q-factor value.

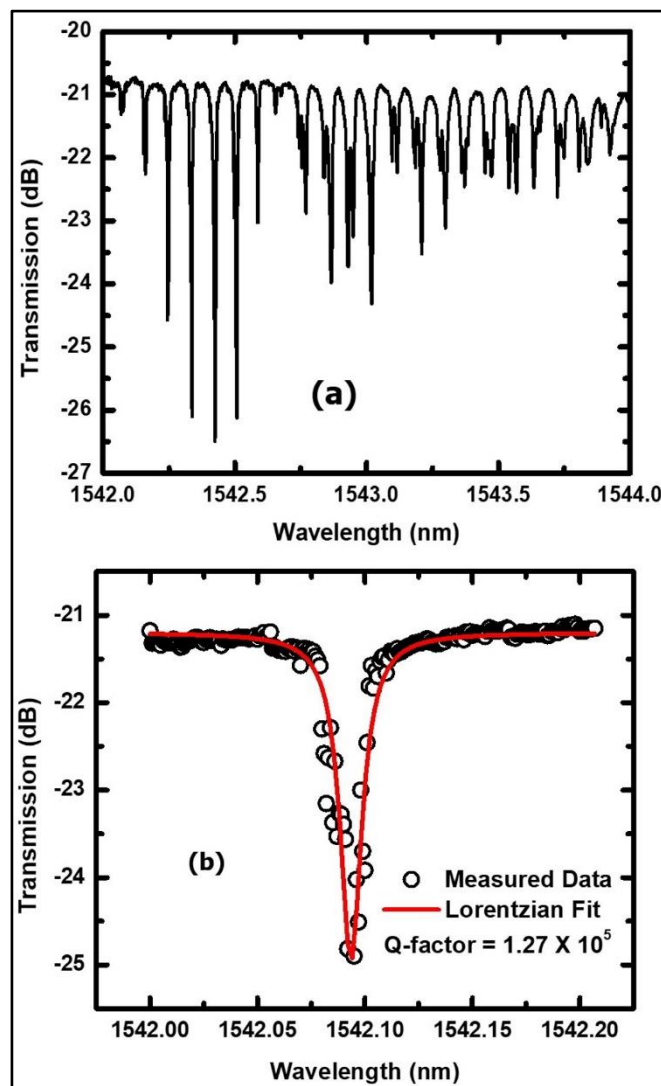


**Figure 2.** (a) Experimental WGM spectrum, when the tapered fiber is along the equator of the microsphere of diameter  $163 \mu\text{m}$  (b) Lorentzian curve fit of one of the dips corresponding to a Q factor of  $1.27 \times 10^5$ .



Figure 3 shows the WGM spectrum of a 163  $\mu\text{m}$  diameter microsphere excited by contact with a tapered fiber of diameter 1.7  $\mu\text{m}$  positioned at different points on the microsphere surface using the micro translation stages. Here the contact position of the tapered fiber with respect to the microsphere is varied from (a) taper at the tip of the sphere, close to the stem; (b) central position, (c) to the left from the equator and (d) near the pole of the microsphere, diametrically opposite to the glass stem. Figure 3 illustrates the above combinations and also shows the corresponding WGM spectrum. At every position the distance between the microsphere and the fiber taper was adjusted to achieve a physical contact with the help of the side view microscope and micro translation stages.

It can be seen that the most pronounced WGM spectrum is observed, when tapered fiber is in contact with the microsphere's equator (Figure 3, (b)). Both extreme left (near the stem) and extreme right (opposite pole) positions result in poor WGM spectra. The maximum extinction ratio of 5.91 dB and the quality factor of  $1.27 \times 10^5$  are obtained when the tapered fiber is placed at the equator of the microsphere. The FSR of the spectrum also shows a slight variation at different contact positions. A minimum FSR value of 0.087 nm was obtained at the equator and a maximum of 0.18 nm was obtained at the point near to the stem of the microsphere. From the experiment it is realized that in the case of the equatorial alignment of the tapered fiber with the microsphere only the symmetric polar modes (even) are excited in the microsphere, while in the case of non-equatorial alignment both symmetric and anti symmetric polar modes (odd) are excited. Therefore, spectral quality can be improved by improving the alignment of the tapered fiber in the equatorial plane of the microsphere. A work by M. J. Humphrey [7] confirms these observations.

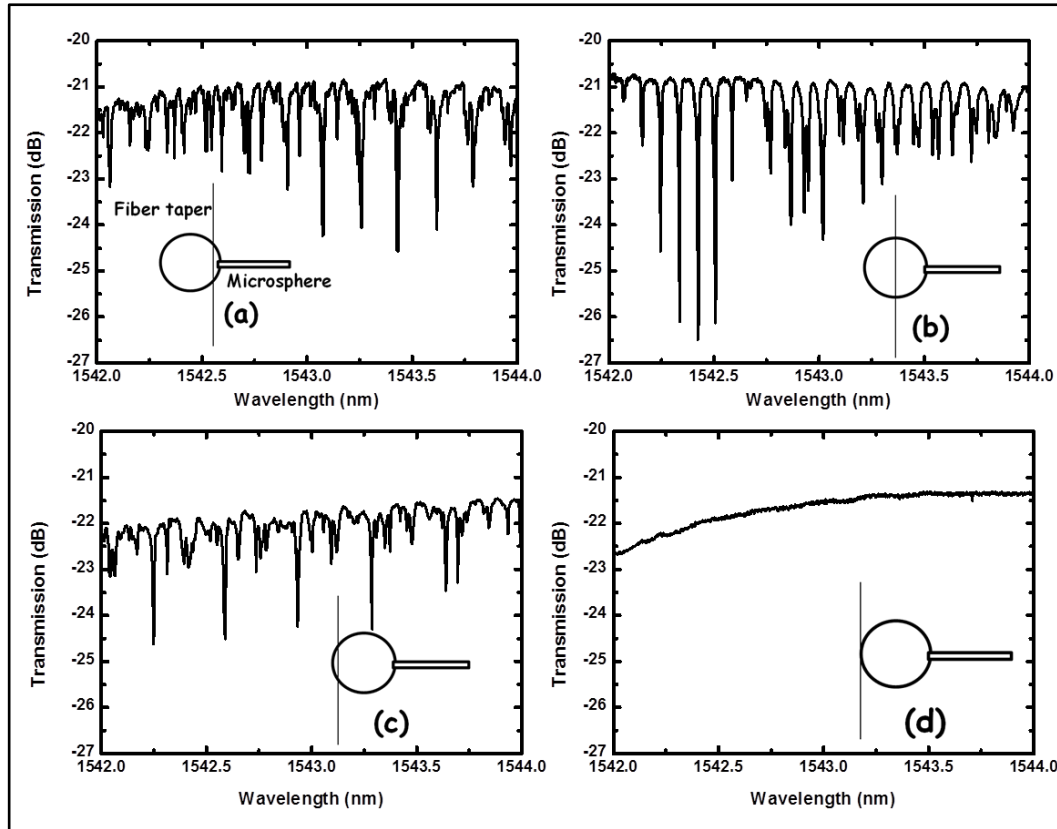


**Figure 3.** WGM spectrum of a 163  $\mu\text{m}$  diameter microsphere excited by a tapered fiber of diameter 1.7  $\mu\text{m}$  positioned at different points of the microsphere surface. Here the contact position of the tapered fiber with respect to the microsphere is varied from (a) taper at the tip of the sphere, close to the stem; (b) central position, (c) to the left from the equator and (d) near the pole of the microsphere, diametrically opposite to the glass stem. The inset diagrams illustrate corresponding positions of the tapered fiber with respect to the microsphere.

## Conclusion

In summary, we have studied the excitation of WGMs in a spherical micro resonator by a tapered optical fiber at different coupling positions on the surface of the microsphere. Narrow WGM resonances are observed in the transmission spectrum of the fiber taper with a maximum estimated Q factor of  $\sim 10^5$ . The evolution of the transmission spectrum with the change in coupling position involved changes in the spectral quality. It is found that a coupling point at the equator of the microsphere produced the highest quality spectrum compared to all

other positions. No WGMs are observed when the coupling point is at the pole (tip) of the microsphere.

## Reference

1. G. C. Righini, Y. Dumeige, P. Feron, M. Ferrari, G. Nunzi Conti, D. Ristic and S. Soria, "Whispering gallery mode microresonators: Fundamentals and applications," *Rivista Del Nuovo Cimento*. **34**, 435 (2011).
2. D. W. Vernooy, V. S. Ilchenko, H. Mabuchi, E. W. Streed, and H. J. Kimble, "High- $Q$  measurements of fused-silica microspheres in the near infrared", *Opt. Lett.* **23**, 247 (1998).
3. P. Wang, M. Ding, L. Bo, Y. Semenova, Q. Wu, and G. Farrell, "Packaged chalcogenide microsphere resonator with high Q-factor," *Appl. Phys. Lett.* **102**, 131110 (2013)
4. A. B. Matsko and V. S. Ilchenko, "Optical resonators with whispering -gallery modes-Part I: Basics" *IEEE J. Sel. Topics Quantum Electron.* **12**, 3(2006).
5. S. M. Spillane, T. J. Kippenberg, O. J. Painter and K. J. Vahala, "Ideality in a fiber taper-coupled microresonator system for application to cavity quantum electrodynamics," *Phys. Rev. Lett.* **91**, 043 (2003).
6. G. Brambilla, V. Finazzi, and D. Richardson, "Ultra-low-loss optical fiber nanotapers," *Opt. Express*, **12**, 2258-2263 (2004)
7. M. J. Humphrey, "Calculation of coupling between fiber modes and whispering gallery modes of a spherical microlaser," (PhD thesis, 2004).